Electronic Thesis and Dissertation Repository

6-20-2018 10:00 AM

Fundamentals of Applied Smouldering Combustion

Marco Zanoni
The University of Western Ontario

Supervisor
Gerhard, Jason I.
The University of Western Ontario Co-Supervisor
Torero, Jose L.
The University of Western Ontario

Follow this and additional works at: https://ir.lib.uwo.ca/etd

🔴 Part of the Environmental Engineering Commons, and the Heat Transfer, Combustion Commons

Abstract

Smouldering combustion is defined as a flameless oxidation reaction occurring on the surface of the condensed phase (i.e., solid or liquid). Traditional research on smouldering was related to economic damages, fire risk, and death, due to the release of toxic gases and slow propagation rates. Recently, smouldering has been applied as an intentional, engineering technology (e.g., waste and contaminant destruction). Smouldering involves the transport of heat, mass, and momentum in the solid and fluid phases along with different chemical reactions. Therefore, numerical models are essential for the fundamental understanding of the process. Smouldering models either neglected heat transfer between phases (i.e., assumed local thermal equilibrium) or employed heat transfer correlations (i.e., under local thermal non-equilibrium conditions) not appropriate for smouldering. Thus, the first step of this thesis was to develop and validate a new heat transfer correlation for air flowing through hot sand at conditions appropriated to smouldering. The new correlation was reliable and predicted well heat transfer between phases. The second step was to apply the new correlation along with appropriate chemistry into a one-dimensional model. The model was calibrated to a smouldering experiment of an organic liquid fuel embedded in sand and then confidence in the model was gained by independent simulations of additional experiments. Local thermal non-equilibrium demonstrated to be essential to correctly simulate smouldering of organic liquid fuels embedded in sand. Moreover, a two-step kinetic mechanism showed to be sufficient to simulate the smouldering chemistry. The third step was to use the one-dimensional model to understand the conditions that lead to self-sustaining smouldering and smouldering extinction. A global energy balance was developed, revealing that self-sustaining and extinction conditions occurred when the net energy balance was positive and negative, respectively. The last step was to use the one-dimensional model to conduct a sensitivity analysis of the key practical model parameters. Moreover, a local energy balance was developed and compared with the global energy balance; both were used to explain the physics of the process. It was found that the local energy balance described the moment of extinction, whereas the global energy balance predicted extinction in advance. Overall, this thesis presented new insights into the interplay between heat transfer and chemical reactions along with the understanding of the conditions that lead to self-sustaining smouldering and smouldering extinction.

Keywords

Co-Authorship Statement

The thesis was written in accordance with the guidelines and regulations for an integrated-article format stipulated by the School of Graduate and Postdoctoral Studies at The University of Western Ontario, Canada. The candidate conducted all simulations and laboratory experiments presented in this thesis, analyzed all data, and formed the conclusions presented. The work was conducted under the supervision of Dr. Jason I. Gerhard and co-supervision of Prof. Jose L. Torero. The candidate wrote the thesis and was the lead author on the manuscript drafts of the following chapters:

Chapter 3: Determination of the interfacial heat transfer coefficient between forced air and sand at Reynold's numbers relevant to smouldering combustion

A version of this chapter has been published: M.A.B. Zanoni, J.L. Torero, J.I. Gerhard, Determination of the interfacial heat transfer coefficient between forced air and sand at Reynold's numbers relevant to smouldering combustion, International Journal of Heat and Mass Transfer, 114 (2017) 90-104. doi.org/10.1016/j.ijheatmasstransfer.2017.06.020

Chapter 4: The Role of Local Thermal Non-Equilibrium in Modelling Smouldering Combustion of Organic Liquids

A version of this chapter has been accepted for presentation at the 37th International Symposium on Combustion in Dublin, Ireland in July, 2018: M.A.B. Zanoni, J.L. Torero, J.I. Gerhard, The Role of Local Thermal Non-Equilibrium in Modelling Smouldering Combustion of Organic Liquids, (2018).

Chapter 5: Determining the Conditions that Lead to Self-Sustained Smouldering Combustion by Means of Numerical Modelling

A version of this chapter has been accepted for presentation at the 37th International Symposium on Combustion in Dublin, Ireland in July, 2018: M.A.B. Zanoni, J.L. Torero, J.I. Gerhard, Determining the Conditions that Lead to Self-Sustained Smouldering Combustion by Means of Numerical Modelling, (2018).

Chapter 6: Smouldering Combustion Explored via Numerical Modelling: Sensitivity to Key Parameters

A version of this chapter will be submitted to a peer-reviewed journal: M.A.B. Zanoni, J.L. Torero, J.I. Gerhard, Smouldering Combustion Explored via Numerical Modelling: Sensitivity to Key Parameters, (2018).

Contributions:

Marco A. B. Zanoni:	initiated research topic; developed the methodology; conducted and analyzed all laboratory experiments and numerical simulations; wrote all manuscript chapters.
Jose L. Torero:	provided guidance on methodology development, experiments, and numerical simulations, assisted in data interpretation and revised/reviewed draft chapters.
Jason I. Gerhard:	initiated research topic, provided the funding and resources for the project, provided guidance on methodology development, experiments, and numerical simulations, assisted in data interpretation and revised/reviewed draft chapters.

Acknowledgments

I would like to express my extreme gratitude to my supervisor Dr. Jason Gerhard. Thank you for your endless support, guidance, patience, and friendship. I will always be grateful to you for believing in me and for being my mentor. I came to Canada 6 years ago, barely speaking English. The opportunity that you gave me literally changed my life. I have learned so much with you. One thing in particular, among many others, is how to be critical. You taught me to always ask "why" and how important the details are. This is something that I will never forget. Also, you gave me the opportunity to work with Prof. Jose Torero, who I have always admired.

Jose, thanks for all your guidance and mentorship. During my undergrad and Master's degree back in Brazil I have always heard about THE Prof. Jose Torero and I have never thought that one day I would have the pleasure to work with you. It was like a dream coming true. Moreover, thanks for inviting me to Australia. It was a great personal and professional experience. I would like to acknowledge the assistance of the Fire Safety Engineering team and the UQ Composites Group at the University of Queensland with the sand thermal properties measurements and thermogravimetric data. Special thanks to Jeronimo Carrascal, Dr. Cristián Maluk, Dr. Luis Yerman, and Dr. Michael Heitzmann.

I am also thankful to Dr. Guillermo Rein, who introduced me to Jason and made this whole thing possible. Thank you very much. I will never forget that. Although we did not have the opportunity to work closely, you had a very special role in this PhD.

Last but not least, I would like to thank Dr. Marcio F. Martins. Marcio was my first mentor and became a close friend. He was the one responsible for introducing me to academia and encouraging me to pursue a doctoral degree. Thanks for all the endless discussions about smouldering and academic life.

Table of Contents

List of Tables

List of Figures

Nomenclature

Typical units are presented in brackets. [-] denotes a dimensionless parameter.

Abbreviations

CVOCs	Chlorinated Volatile Organic Compounds
DSC	Differential Scanning Calorimetry
DT	Dimensionless Time
DTG	Differential Thermogravimetry
ESEM	Environmental Scanning Electron Microscope
GA	Genetic Algorithms
LM	Levenberg-Marquardt
LTE	Local Thermal Equilibrium
LTNE	Local Thermal Non-Equilibrium
MSC	Microgravity Smouldering Combustion
NAPLs	Non-Aqueous Phase Liquids
NASA	National Aeronautics and Space Administration
NRMSD	Normalized Root-Mean-Square Deviation
PCE	Tetrachloroethylene
REV	Representative Elementary Volume
SARA	Saturated, Aromatics, Resins, and Asphaltenes
SS	Self-Sustaining
STAR	Self-sustaining Treatment for Active Remediation
TCE	Trichloroethylene
TG	Thermogravimetry
THAI	Toe to Heel Air Injection
TPS	Transient Plane Source

Latin Letters

a_v	Surface area per unit volume [m^{-1}]
A_b	Bitumen pre-exponential factor [s^{-1}]
A_c	Char pre-exponential factor [s^{-1}]
A_{cs}	Cross-sectional area [m^2]
A_s	Surface area [m^2]
Bi	Biot number [-]
C_p	Specific heat capacity [J kg^{-1} K^{-1}]
D	Diameter of the column [m]
Da	Damköhler number, [-]
D_g	Diffusion coefficient [m^2 s^{-1}]
d_p	Particle diameter [m]
D_s	Difference in the vertical displacement (sand) [m]
D_{st}	Difference in the vertical displacement (standard sapphire) [m]
E	Energy [J]
$\dot{E}$	Energy Rate [J s^{-1}]
E_b	Bitumen activation Energy [kJ mol^{-1}]
E_c	Char activation Energy [kJ mol^{-1}]
fr	Stoichiometric coefficient [-]
g	Gravitational acceleration [m s^{-2}]
h_{sg}	Interfacial heat transfer coefficient [W m^{-2} K^{-1}]
h_m	Mass transfer coefficient [kg m^{-2} s^{-1}]
h_v	Volumetric heat transfer coefficient [W m^{-3} K^{-1}]
H	Height of the column [m]
k	Thermal conductivity [W m^{-1} K^{-1}]

k_a	Arrhenius constant [s^{-1}]
k_p	Intrinsic permeability [m^2]
l	Representative Elementary Volume length scale [m]
L	System length scale [m]
m	Mass [kg]
m_{st}	Mass of the standard sapphire crystal [mg]
M	Molar mass [kg mol^{-1}]
n	Number of independent experiments [-]
Nu	Nusselt number [-]
P	Pressure [Pa]
Pr	Prandtl number [-]
$\dot{q}''$	Heat flux [W m^{-2}]
Q	Source/sink term [W m^{-3}]
Q_g	Volumetric flow rate [m^3 s^{-1}]
r	Radius of the column [m]
R	Reaction rate [s-^{1}]
Ra	Rayleigh number [-]
Re	Reynolds number [-]
R_g	Ideal gas constant [J K^{-1} mol^{-1}]
R_s	Specific Gas Constant [J Kg^{-1} K^{-1}]
S	Objective function [K^2]
S_b	Bitumen saturation [%]
t	Time [s]
t_g	Air-on time [s]
t_h	Heater-off time [s]

T	Temperature [K]
T_b	Adiabatic temperature [K]
T_p	Peak temperature [K]
T_∞	Ambient temperature [K]
u_g	Darcy Air flux [m s^{-1}]
U	Global heat loss coefficient [W m^{-2} K^{-1}]
v	Mass yield/consumption of species per mass of reactant [-]
v_f	Front velocity [m s^{-1}]
V	Volume [m^3]
Y	Mass fraction [-]

Greek Symbols

α	Thermal diffusivity [m^2 s^{-1}]
β	Heating rate [K min^{-1}]
ΔH	Heat of reaction [MJ kg^{-1}]
δ_w	Thickness of the thermal wave [m]
μ	Dynamic viscosity [Pa.s]
ν	Kinematic viscosity [m^2 s^{-1}]
ρ_{bk}	Bulk density [kg m^{-3}]
ρ_s	Particle density [kg m^{-3}]
ϕ	Porosity [-]
σ	Stefan–Boltzmann constant [W m^{-2} K^{-4}]
τ_{REV}	Representative Elementary Volume characteristic time [s]
τ_p	Particle-scale characteristic time [s]

Subscripts/Superscript

av,o	Available for oxidation
av,p	Available for pyrolysis
av	Availabe
avg	Average
b	Bitumen
bk	Bulk
c	Char
cb	Carbon
CO	Carbon monoxide
cl	Cylinder
cond	Conduction
conv	Convection
eff	Effective
exp	Experimental
f	Final
g	Gas
gen	Generation
i	Time step
in	Inlet
j	Thermocouple Number
l	Liquid
max	Maximum
min	Minimum
num	Numerical

0	Initial
O_2	Oxygen
out	Outlet
oxid	Oxidation
p	Pyrolysis
rad	Radiation
s	Solid(Quartz)
sg	Solid/Gas
sp	Sphere
st	Stored
T	Total
w	Wall

Chapter 1

1   Introduction

1.1   Background

Smouldering is a combustion that occurs on the surface of porous organic solids or of liquids embedded in an inert porous matrix (e.g., sand) [1-3]. A permeable porous medium is necessary to allow the transport of oxygen from outside the fixed fuel bed to the reaction zone. Familiar examples of smouldering combustion include charcoal barbeques and cigarettes.

Smouldering is different from flaming combustion. Flaming is governed by homogenous (gas phase) reactions that result in higher temperatures (1500-1800°C) and propagation velocities, when compared to smouldering [1, 4, 5]. Smoldering is classified as a flameless heterogeneous (solid and gas) reaction. Moreover, its lower temperatures produce more incomplete reactions, which can release more carbon monoxide (a toxic gas) [4, 6, 7]. Although smouldering and flaming are distinct processes, smouldering can lead to flaming [4, 8], creating dangerous fires.

In smouldering, the energy released creates a self-sustaining process that propagates through the system without any external energy source, as long as oxygen is provided and energy losses minimized [1, 4]. Moreover, smouldering can propagate under low oxygen concentrations, and therefore can be difficult to extinguish [9]. Thus, for decades, smouldering has been related to economic damages, fire risk, and death, due to the release of toxic gases and slow propagation rates [1, 4, 9, 10].

Recently, smouldering has been applied as an intentional, engineering technology, including enhanced oil recovery and waste and contaminant destruction [2, 3, 11-14]. However, new technologies bring new challenges that require fundamental understanding of the process and optimization of the controlling parameters.

Smouldering is multi-disciplinary, involving heat and mass transfer mechanisms in porous media as well as chemical reactions. Such complex phenomena are challenging to

understand by only conducting laboratory experiments, since most of the processes occurring are very difficult to observe and measure in detail. Therefore, numerical models have long been recognized as important tools in furthering our understanding of smouldering experiments [15-20]. For example, it was recognized that oxygen diffusion from the bulk pores to the fuel surface was an important process that needs further investigation [15-17, 21]. Moreover, Leach et al. [17] identified that heat transfer correlations available in the literature (e.g., Wakao et al. [22]) were not appropriate to correctly predict local heat transfer between solid and gas phases in smouldering. Heat losses were identified as an important mechanism to understand smouldering extinction [19].

Thus, there are knowledge gaps related to applied smouldering and to numerical models for smouldering analysis that need further investigation. This thesis aims to fulfill, in part, this gap by providing novel explanations of how the behavior of a wide variety of applied smouldering scenarios depends on the interaction of heat and mass transfer mechanisms with chemical reactions.

1.2   Research Objectives

The overall objective of this thesis is to improve our understanding of smouldering combustion of an organic liquid embedded in an inert porous medium. Although this work focuses on liquid contaminant destruction, it is expected that such detailed analysis will reveal new knowledge of value to the entire smouldering community. A driver for the main methodology for the work surrounds the question: what is the least complex set of mass, momentum, energy and chemical reaction equations required to describe (i.e., simulate) smouldering combustion in a one-dimensional system?

To achieve the main objective, several specific objectives were accomplished:
1. Develop a new heat transfer correlation in porous media appropriate for air flux and inert sand matrixes associated with liquid smouldering applications.
2. Develop a simple and valid kinetic reaction framework for organic liquid smouldering based on thermogravimetry and differential scanning calorimetry.

3. Develop an appropriate one-dimensional numerical model of organic liquid smouldering utilizing the results of Objectives 1 and 2.

4. Validate the model against vertical column laboratory experiments with organic liquid embedded in sand.

5. Develop a local and global energy balance for organic liquid smouldering and explore their ability to explain self-sustaining and extinction conditions.

6. Explore, with numerical simulations, the sensitivity of organic liquid smouldering to key system parameters.

7. Use the results of Objective 5 and 6 to identify local and global extinction criteria, characterize the robustness of smouldering scenarios, explain observed smouldering behaviour, and guide optimization of smouldering applications.

1.3 Thesis Outline

This thesis is written in "Integrated Article Format". A brief description of each chapter is presented below.

Chapter 1 provides a brief introduction to smouldering combustion and delineates the objectives of this thesis.

Chapter 2 presents a literature review of smouldering combustion, focusing on its occurrence as a hazard and its use as an engineering application. Emphasis was placed on previous experimental and numerical studies that have explored smouldering of solid reactive fuels and liquid fuels embedded in an inert matrix. Moreover, key contributions along with some gaps in the literature are discussed.

Chapter 3 titled "Determination of the interfacial heat transfer coefficient between forced air and sand at Reynold's numbers relevant to smouldering combustion" is a manuscript that developed a new heat transfer correlation in porous media appropriate for air flux and inert sand matrixes associated with liquid smouldering applications. The new Nusselt versus Reynold's and Prandtl empirical correlation was obtained via optimization of the interfacial heat transfer coefficient between sand and air by inverse modelling. This chapter was published on June 20th 2017 in the International Journal of Heat and Mass Transfer. doi.org/10.1016/j.ijheatmasstransfer.2017.06.020

Chapter 4 titled "The Role of Local Thermal Non-Equilibrium in Modelling Smouldering Combustion of Organic Liquids" is a manuscript that developed a simple and valid kinetic reaction framework for organic liquid smouldering and applied both the kinetic framework and the new heat transfer correlation developed in Chapter 3 into a one-dimensional numerical model to simulate smouldering of organic liquids. The model was validated against vertical column experiments at different conditions. This chapter was accepted for presentation at the 37th International Symposium on Combustion (2018).

Chapter 5 titled "Determining the Conditions that Lead to Self-Sustained Smouldering Combustion by Means of Numerical Modelling" is a manuscript that uses the one-dimensional numerical model validated in Chapter 4 to explore how a global energy balance controls the self-sustainability and extinction of a forward smouldering reaction. This chapter was accepted for presentation at the 37th International Symposium on Combustion (2018).

Chapter 6 titled "Smouldering Combustion Explored via Numerical Modelling: Sensitivity to Key Parameters" is a manuscript that explains the interplay between chemical reactions and heat transfer processes taking place in space and time in smouldering of organic liquid fuels via a model sensitivity analysis. Moreover, local and global extinction criteria, robustness of smouldering scenarios, and optimization of smouldering applications were explored. This chapter will be submitted to a peer-reviewed journal.

Chapter 7 summarizes the major conclusions of the thesis and presents a series of recommendations for future work.

Appendix A presents a Supplementary Material for "Determination of the interfacial heat transfer coefficient between forced air and sand at Reynold's numbers relevant to smouldering combustion", showing sand thermal properties and permeability measurements.

Appendix B provides Supplementary Material for "The Role of Local Thermal Non-Equilibrium in Modelling Smouldering Combustion of Organic Liquids", describing the Kissinger method and showing Thermogravimetry (TG) and Differential Scanning Calorimetry (DSC) data for an organic liquid fuel.

Appendix C presents supplementary analysis of the performance of the developed numerical model, including a mesh analysis along with proof of conservation of energy and mass.

Appendix D presents data on smouldering experiments that were not presented in the main chapters, including under weak and extinction conditions. It also shows a modelling sensitivity analysis of heat losses and heat of oxidation for such conditions.

1.4   References

[1] T.J. Ohlemiller, Modeling of smoldering combustion propagation, Progress in Energy and Combustion Science, 11(4) (1985) 277-310.

[2] P. Pironi, C. Switzer, G. Rein, A. Fuentes, J.I. Gerhard, J.L. Torero, Small-scale forward smouldering experiments for remediation of coal tar in inert media, Proceedings of the Combustion Institute, 32(2) (2009) 1957-1964.

[3] P. Pironi, C. Switzer, J.I. Gerhard, G. Rein, J.L. Torero, Self-Sustaining Smoldering Combustion for NAPL Remediation: Laboratory Evaluation of Process Sensitivity to Key Parameters, Environmental Science and Technology, 45(7) (2011) 2980-2986.

[4] G. Rein, Smouldering combustion phenomena in science and technology, International Review of Chemical Engineering, 1 (2009) 3-18.

[5] D. Drysdale, An Introduction to Fire Dynamics, Wiley, 2011.

[6] G. Rein, S. Cohen, A. Simeoni, Carbon emissions from smouldering peat in shallow and strong fronts, Proceedings of the Combustion Institute, 32 II (2009) 2489-2496.

[7] J.G. Quintiere, M. Birky, F. Macdonald, G. Smith, An analysis of smoldering fires in closed compartments and their hazard due to carbon monoxide, Fire and Materials, 6(3-4) (1982) 99-110.

[8] A.B. Dodd, C. Lautenberger, C. Fernandez-Pello, Computational modeling of smolder combustion and spontaneous transition to flaming, Combustion and Flame, 159(1) (2012) 448-461.

[9] A. Bar-Ilan, G. Rein, D.C. Walther, A.C. Fernandez-Pello, J.L. Torero, D.L. Urban, The effect of buoyancy on opposed smoldering, Combustion Science and Technology, 176(12) (2004) 2027-2055.

[10] G. Rein, Smoldering combustion, in: SFPE Handbook of Fire Protection Engineering, Fifth Edition, 2016, pp. 581-603.

[11] M.F. Martins, S. Salvador, J.F. Thovert, G. Debenest, Co-current combustion of oil shale - Part 2: Structure of the combustion front, Fuel, 89(1) (2010) 133-143.

[12] L. Yermán, R.M. Hadden, J. Carrascal, I. Fabris, D. Cormier, J.L. Torero, J.I. Gerhard, M. Krajcovic, P. Pironi, Y.-L. Cheng, Smouldering combustion as a treatment technology for faeces: Exploring the parameter space, Fuel, 147 (2015) 108-116.

[13] J.-P. Vantelon, B. Lodeho, S. Pignoux, J.L. Ellzey, J.L. Torero, Experimental observations on the thermal degradation of a porous bed of tires, Proceedings of the Combustion Institute, 30(2) (2005) 2239-2246.

[14] T.L. Rashwan, J.I. Gerhard, G.P. Grant, Application of self-sustaining smouldering combustion for the destruction of wastewater biosolids, Waste Management, 50 (2016) 201-212.

[15] S.V. Leach, J.L. Ellzey, O.A. Ezekoye, A numerical study of reverse smoldering, Combustion Science and Technology, 130(1-6) (1997) 247-267.

[16] S.V. Leach, J.L. Ellzey, O.A. Ezekoye, Convection, pyrolysis, and Damköhler number effects on extinction of reverse smoldering combustion, Proceedings of the Combustion Institute, 27(2) (1998) 2873-2880.

[17] S.V. Leach, G. Rein, J.L. Ellzey, O.A. Ezekoye, J.L. Torero, Kinetic and fuel property effects on forward smoldering, Combustion and Flame, 120(3) (2000) 346-358.

[18] G. Rein, A. Carlos Fernandez-Pello, D.L. Urban, Computational model of forward and opposed smoldering combustion in microgravity, Proceedings of the Combustion Institute, 31(2) (2007) 2677-2684.

[19] J. Yang, H. Chen, N. Liu, Heat Loss and Kinetic Effects on Extinction and Critical Self-Sustained Propagation of Forced Forward Smoldering, in: K. Harada, K. Matsuyama, K. Himoto, Y. Nakamura, K. Wakatsuki (Eds.) Fire Science and Technology 2015: The Proceedings of 10th Asia-Oceania Symposium on Fire Science and Technology, Springer Singapore, Singapore, 2017, pp. 831-840.

[20] G. Rein, A. Bar-Ilan, C. Fernandez-Pello, J.L. Ellzey, J.L. Torero, D.L. Urban, Modeling of One-Dimensional Smoldering of Polyurethane in Microgravity Conditions, Proceedings of the Combustion Institute, 30(2) (2005) 2327-2334.

[21] M. Fatehi, M. Kaviany, Adiabatic reverse combustion in a packed bed, Combustion and Flame, 99(1) (1994) 1-17.

[22] N. Wakao, S. Kaguei, T. Funazkri, Effect of fluid dispersion coefficients on particle-to-fluid heat transfer coefficients in packed beds: Correlation of nusselt numbers, Chemical Engineering Science, 34(3) (1979) 325-336.

Chapter 2

2 Smouldering Combustion: From Hazard to Engineering Applications

2.1 Introduction

Smouldering combustion is defined as a surface (exothermic) oxidation reaction applicable to porous materials, either organic solids [1] or liquids embedded in an inert porous matrix [2, 3]. A permeable porous medium is necessary to efficiently transport oxygen by diffusion and convection to the reaction zone. Familiar examples of smouldering combustion include charcoal barbeques and cigarettes (Figure 2.1). The energy released by the exothermic reaction is partially stored in the porous medium, partially transferred ahead by heat transfer mechanisms (conduction, convection, and radiation), and partially lost to the surroundings [1, 4-6]. Thus, smouldering has the potential to become self-sustaining (Figure 2.2), i.e., the front propagates with a constant velocity and repeating peak temperatures as long as oxygen is provided and a positive energy balance (energy released surpasses energy lost) is maintained [7].

(a)   (b)

Figure 2.1: Smouldering of (a) charcoal barbecue [8] and (b) cigarettes [9].
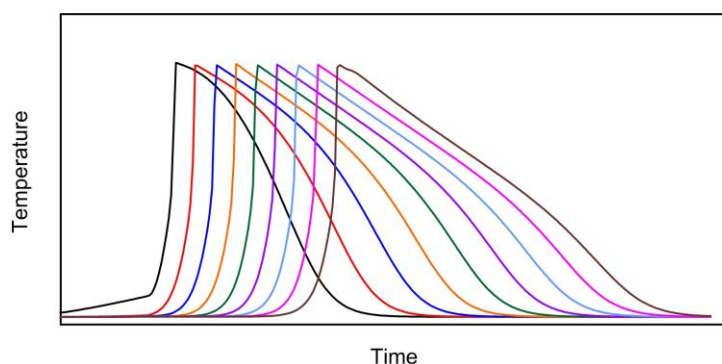
Figure 2.2: Schematic of a one-dimensional self-sustaining smouldering experiment. Colours show the temperature evolution with time along different positions in the system.

Smouldering is different from flaming combustion. Flaming is governed by gas phase homogenous reactions that result in higher temperatures (1500-1800°C), heat of combustion, and propagation velocities, when compared to smouldering [1, 4, 10]. Smoldering is classified as a flameless heterogeneous (solid and gas) reaction. Moreover, its lower temperature produces more incomplete reactions, i.e., releases more carbon monoxide (CO) (toxic gas) [4, 11-13]. Although smouldering and flaming are distinct processes, smouldering can lead to flaming [4, 14-18], creating dangerous fires.

Self-sustaining smouldering propagation is classified into natural and forced air smouldering. The former is governed by natural convection, i.e., air naturally enters the porous fuel induced by a density difference (between hot gases inside and cold gases outside) and boundary layer flows [5, 19-22]. The latter is controlled by forced convection due to an external source [2, 3, 23-29].

One-dimensional smouldering propagation is defined according to two configurations: forward and opposed (Figure 2.3). The direction of the reaction front relative to the air flux defines in which configuration smouldering is travelling [4, 19, 23, 30]. Forward smouldering (Figure 2.3a,b) is identified when both reaction front and air flux travel in the same direction [30]. Cold air flows through the burnt region that is still hot. Convective heat transfer from the solid to the gas phase heats up the air, and once it reaches the reaction zone, oxygen is depleted (feeding the oxidation reaction). The remaining gases flow

towards the unreacted (virgin) fuel, where convective heat transfer between the hot gas and the cold virgin fuel activates pyrolysis reactions, creating a solid porous material (char) available for subsequent oxidation.

In opposed smouldering (Figure 2.3c,d), the direction of the reaction front is opposed to air flux [30]. Opposed smouldering typically occurs naturally (e.g., coal pile smouldering). Air travels through the cold virgin fuel and reaches the reaction front, at which oxygen is consumed. Since the air is cold, the smouldering front is cooled down to heat up the gas [25]. Once the air is heated and passed through the front, convective heat transfer is towards the burnt region, resulting in inefficient heat transfer. Note that in a multi-dimensional scenario, smouldering is a combination of both forward and opposed propagation [19, 23].
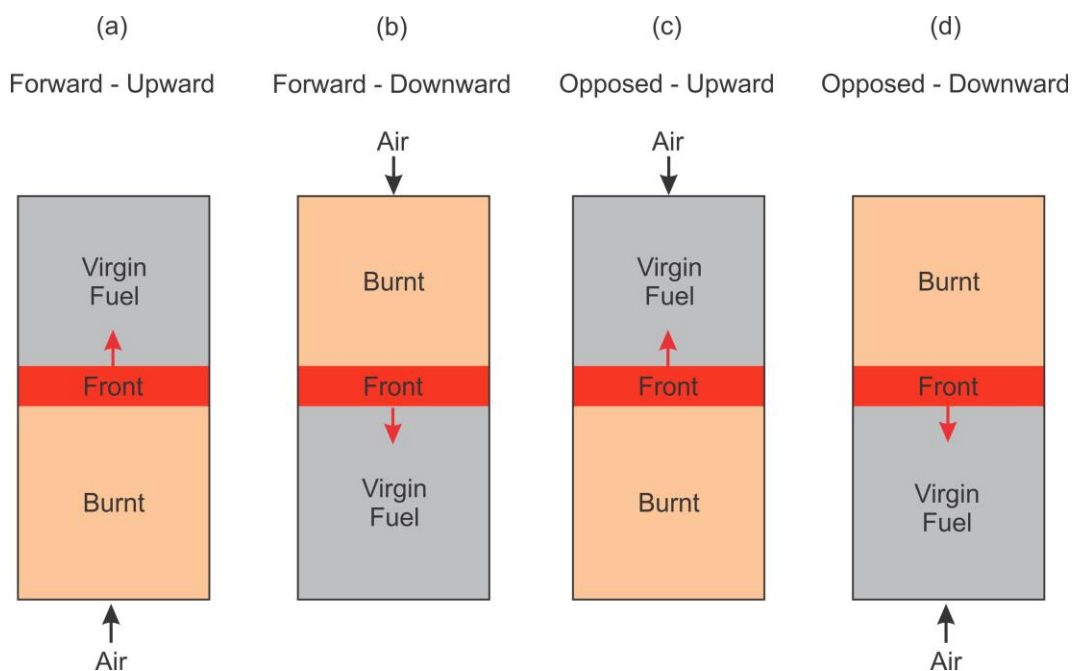
Figure 2.3: Smouldering front configurations.

Smouldering propagation can also be classified into: upward (Figure 2.3a,c) and downward (Figure 2.3b,d). In downward propagation, the reaction propagates in the direction of the gravitational acceleration, whereas in the upward propagation, the reaction travels in the opposite direction [19, 31]. Upwards forward smouldering is the most typical scenario for applied smouldering to treat organic liquids in inert media, and therefore this configuration will be the focus of the work in this thesis.

Smouldering is a complex phenomenon, involving heat and mass transfer along with chemical reactions. However, the main measurable parameter of smouldering systems is temperature. Thus, it is useful to identify different regions and processes according to their spatial distribution and with respect to temperature. Figure 2.4 represents a conceptual model (Figure 2.4a) and a corresponding plot of the vertical spatial distribution of temperature and oxygen concentrations (Figure 2.4b) for an upward, forward smouldering combustion reaction, depicted at a particular moment in time. The schematic presented in Figure 2.4 is referent to an organic fuel (solid or liquid) embedded in an inert porous matrix (e.g., sand).
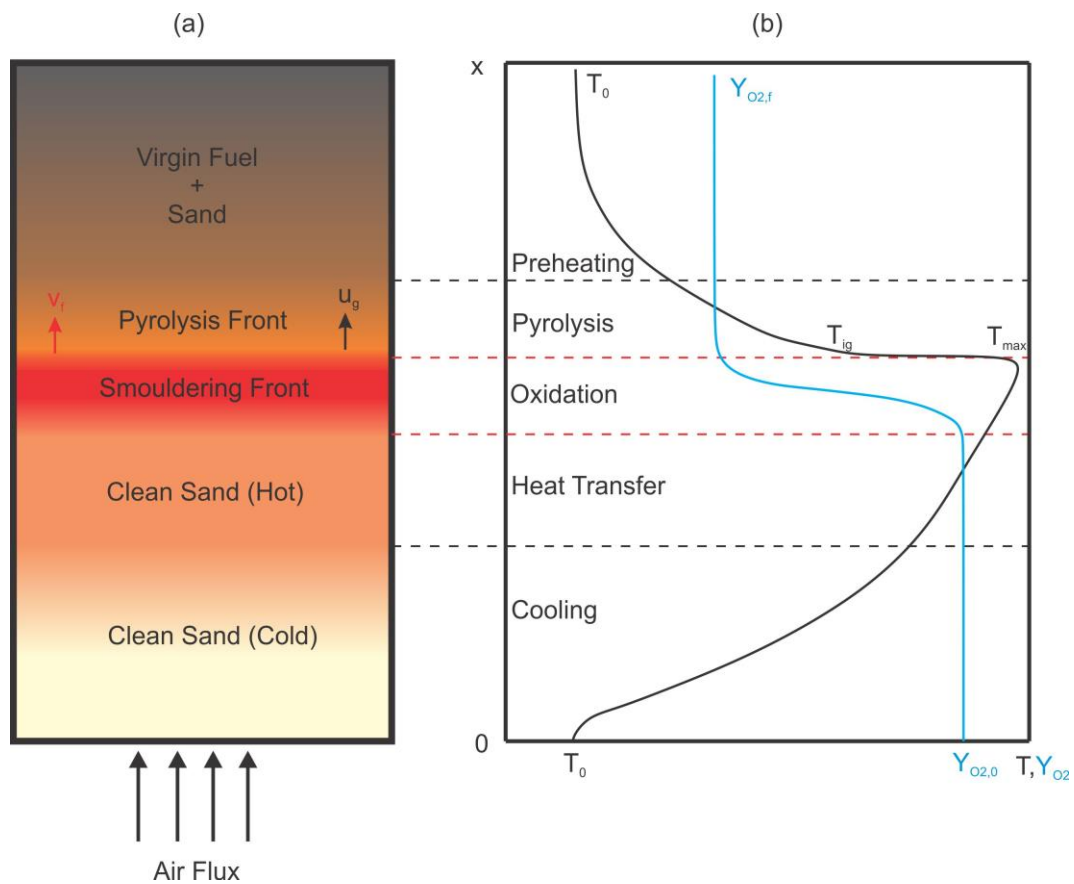
Figure 2.4: (a) Conceptual model of an upward, forward smouldering front. (b) Temperature distribution and oxygen concentration depicted at a particular moment in time (adapted from [32]).

In the uppermost region, sand and virgin fuel are unaffected by the smouldering reaction, staying at ambient temperature (T_0). In the preheating zone, the fuel is exposed to elevated temperatures due to the proximity to the exothermic oxidation zone. These elevated temperatures are a result of heat transfer via conduction, convection and radiation from the regions below to the fuel-plus-sand mixture above. The air flowing through the preheating zone exhibits a reduced oxygen fraction ($Y_{O2,f}$) due to partial consumption in the oxidation zone. Note that at high fuel concentrations, oxygen can be entirely consumed by oxidation reactions.

The elevated temperatures produce the conditions necessary for fuel to undergo pyrolysis, creating a solid porous char. As the temperature in the pyrolysis zone approaches the smouldering ignition temperature (T_{ig}), exothermic oxidation reactions between char and oxygen occur, resulting in a decrease in oxygen concentrations and an increase in temperature until the characteristic peak temperature (T_{max}) is reached. The smouldering front in the case analyzed in Figure 2.4 is typically thin, on the order of a few mm [29]. The end of the smouldering front marks the heat transfer zone, with slight decrease in temperature due radial heat losses and heat transfer. This region is characterized by hot clean sand, with no fuel remaining.

The cooling zone is characterized by a rapid slope change of the temperature curve below the heat losses zone. No reactions occur in this region and therefore the oxygen remains constant at initial concentrations ($Y_{O2,0}$). The temperatures in the cooling region are decreasing mainly due to convection from the forced air flow below and since there is no fuel source in this region, no additional heat is being produced. Overall, it is clear that a non-trivial temperature signals arises from the complex interactions of heat and mass transfer processes and chemistry. Moreover, this signal propagates and evolves in space and in time, linked to the evolving distribution of energy in the smouldering system.

For decades, smouldering of porous solid fuels has been related to economic damages, fire risk, and death, due to the release of toxic gases and slow propagation rates [1, 4, 33, 34]. The majority of smouldering research is for these kinds of scenarios. Only recently, smouldering has been applied as an intentional, engineering technology that ranges from enhanced oil recovery to waste and contaminant destruction [2, 3, 27, 29, 35-42]. Note that

engineering smouldering applications are mainly in fuels embedded in inert matrixes. Both types of smouldering research have important knowledge of relevance to this thesis. Therefore, this chapter will provide a critical review on smouldering combustion from hazard to engineering application, discussing the key contributions as well as identifying some gaps in the literature that need further research.

2.2   Smouldering as a Hazard

Properties and environmental damages created by smouldering include ignition of upholstered furniture (e.g., couches, chairs, mattresses, etc.) [10, 12, 43-45], smouldering wildfires [11, 46-52]), subsurface fires in coal seams and landfills [53-55], self-heating of organic porous media [56-60], and hidden smouldering fires in commercial and space vehicles [6, 61-63].

Ignition of upholstered furniture typically starts from an external source such as cigarettes [10, 12, 43, 64]. Then, smouldering initiates, and can burn for a long period of time (hours) without being noticed (e.g., when people are asleep) [64]. Toxic gases such as CO are produced, creating conditions that can lead to death. Typically, when smouldering encounters a free surface where fuel can vapourize and combust homogeneously, flaming can occur. Flaming is even more dangerous due to higher temperatures, large destruction power, and large amount of smoke (especially CO), reaching critical levels in seconds [12]. Smouldering fires from upholstered furniture represent one of the largest causes of fire death [43].

Smouldering wildfires can cause property damage, severe consequences in the ecosystem, and death [65]. One of the possible ways to ignite such fires is by hot metal particles from powerlines, equipment, and railroads [50]. Smouldering wildfires release large amounts of carbon emissions, which contribute to increasing global CO_2 concentrations [11, 46].

Subsurface fires in coal seams (Figure 2.5a) are the oldest, largest, most prevalent, and environmentally catastrophic fires in the world. They can be ignited by natural causes (e.g., lightning strike and self-heating) or human factors (e.g., mining activities) and are responsible for toxic emissions, acid rain, property damage, destruction of the ecosystem, heath issues, and death [53, 54].

Smouldering in landfills typically initiates due to anaerobic or aerobic biodegradation that increases the waste temperature beyond the ignition temperature of smouldering. Figure 2.5b shows a schematic of a smouldering front in landfills [55].

(a)

(b)
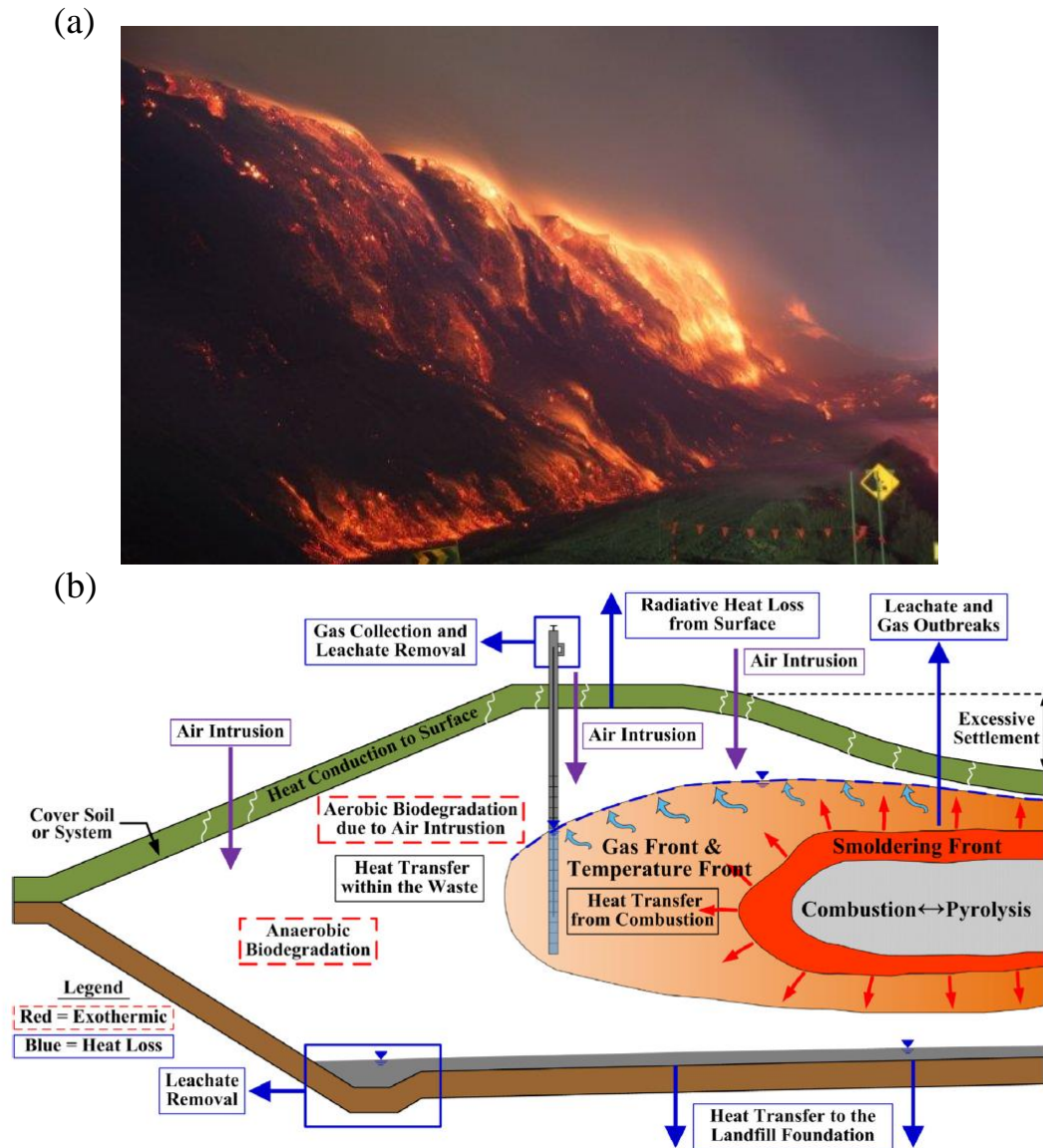
Figure 2.5: (a) The coal seam fire at Hazelwell Mine in Australia [66] (b) Schematic of a smouldering front propagating in landfills [55].

Self-heating of organic porous media can occur due to spontaneous exothermic reactions in oxidative atmospheres at low temperatures. This process can lead to self-sustained smouldering combustion depending on the balance between energy released and energy lost [13]. Consequently, if all conditions are met, it can lead to flaming near the surface, causing uncontrolled fire. Literature reports self-heating in shale rock, peat, coal, organic waste, oil-soaked lagging, etc. [13, 56-60].

Smouldering fires in space shuttles [61, 62] are feared due to the closed environment of a spacecraft and an atmosphere rich in oxygen [61]. Smouldering can originate from electrical cable insulation [63], ignition of polyurethane foams [6], among many others. Such fear has motivated NASA (National Aeronautics and Space Administration) to create the Microgravity Smoldering Combustion (MSC) research program, with the purpose of studying several smoldering characteristics of porous combustible materials [6]. Many aspects of smouldering were investigated such as smouldering in normal and microgravity, transition to flaming, and role of polyurethane foam.

A review of the main scientific conclusions associated with smouldering as a hazard will be discussed in this chapter. Several fuels such as cigarettes, peat, biomass, cellulosic materials, and polyurethane foams were studied and the main findings and gaps in the literature will be presented next.

2.2.1 Key Contributions

Literature shows a variety of smouldering combustion research in opposed [25, 30, 31, 33, 67-70] and forward [5, 14, 16, 17, 23, 25, 30, 69, 71-74] configurations under natural [5, 25, 30, 67-69, 75] and forced [14, 16, 17, 23, 31, 33, 70, 74] convection. The primary studies on smouldering were focused on solid porous fuels such as cigarettes [72, 73], polyurethane foams [5, 14, 16, 17, 23, 31, 33, 67-69, 74], cellulosic materials [25, 30, 75], peat [65, 70, 76, 77], wood [71], and coal [59, 78].

2.2.1.1 Opposed Smouldering

In the past, fire hazard was mostly linked to opposed smouldering [68], although not leading to flaming under normal conditions [25, 68]. Note that an increase in the oxygen concentration might lead to transition to flaming [70]. In opposed smouldering, heat

transfer is dominated mainly by conduction and radiation [30], with a negative (cooling) effect of convection [67] because the reaction front and air are travelling in opposite directions. Thus, smouldering is controlled by a competition between oxygen supply to the reaction zone and heat transfer from the reaction zone to the surroundings [25, 69].

Thermal degradation of solid fuels (e.g., polyurethane foams) indicated that fuel decomposition mainly occurs by (endothermic) pyrolysis, (exothermic) fuel oxidation, and (exothermic) char oxidation (see Figure 2.13 for details):

$$Fuel + Heat \ \rightarrow Char + Gases$$
$$Fuel + \ O_2 \ \rightarrow Char + Gases + Heat \qquad\qquad (2.1)$$
$$Char + \ O_2 \ \rightarrow Gases + Heat$$
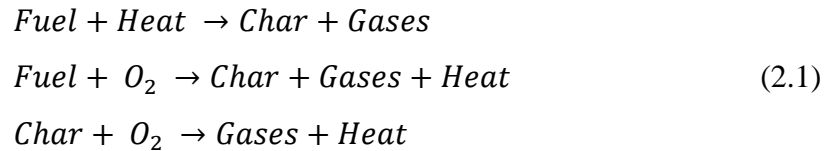
In opposed smouldering, fuel oxidation drives the process with negligible influence of char oxidation, whereas in forward smouldering, most of the energy release comes from char oxidation [25, 30, 70, 75] (see Section 2.2.1.2).

The front velocity and peak temperature increase when air flux or oxygen concentration increase [25, 30, 67, 70]. Low air flux results in a weak smouldering reaction due to low oxygen mass flux. An increase in air flux, accelerates the rate of oxygen transfer to the fuel surface, enhancing the local heat release rate, local temperature, and front velocity [71]. Further increase in the air flux causes extinction by convective cooling [25, 31]. When either air flux or oxygen concentration increases, the air-to-fuel ratio shifts towards stoichiometric burning, resulting in more complete combustion, less time to ignition [68], and thinner reaction front [30, 67]. Ignition needs a minimal char thickness to insulate the front against heat losses. If the char thickness is too small, ignition is weak and as soon as the igniter is turned off, extinction occurs by large heat losses [68].

Small accidents in space shuttles and space stations have motivated research under normal gravity and microgravity. Under microgravity, buoyancy at low air fluxes becomes important [33], changing heat and mass transfer processes [69]. Char oxidation is not activated, but smouldering propagated through the whole sample due to fuel oxidation with negligible radial heat losses, i.e., temperature at the front is almost planar [33].

Under normal gravity, char oxidation is activated and buoyancy enhances heat losses at the center, leading to a conical shape front [33]. Torero et al. [31] investigated the effects of buoyancy in opposed smouldering under downward and upward configurations. In downward opposed smouldering, air flows along the column's cold walls towards the reaction zone, reaching the virgin fuel region (Figure 2.6: Schematic of the mixed flow inside the polyurethane foam for opposed smouldering (adapted from [31]).Figure 2.6). Since the virgin fuel has relatively low permeability, air returns and moves upward along the center-line with the forced air. This excess of air enhances the reaction front providing more oxygen mass flux, but also can cool it, leading to extinction, if the reaction is already weak. The effects of buoyancy decrease as air flux increases. Moreover, Torero et al. [31] suggested that the onset of buoyancy depends on fuel permeability. For example, char has high permeability. Thus, buoyancy within the char is enhanced by natural convection due to differences in the temperature. In upwards opposed smouldering, extinction occurs due to buoyant flows that oppose and partially cancel the air flux. After extinction, residual char is still oxidized by the remaining oxygen in the system, especially near the igniter where temperatures are high.
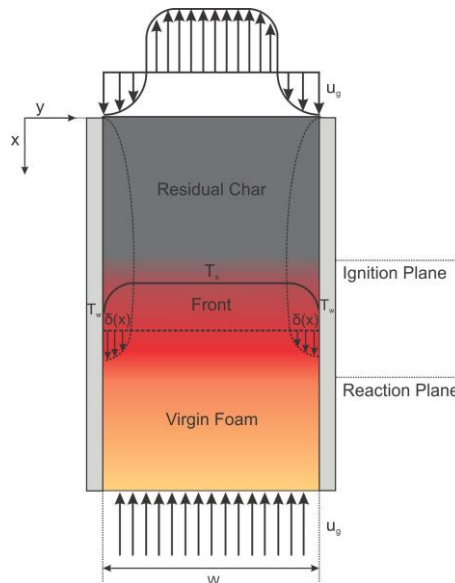
Figure 2.6: Schematic of the mixed flow inside the polyurethane foam for opposed smouldering (adapted from [31]).

Under microgravity (buoyancy is not present), the smouldering front needs less oxygen mass flux to propagate [33, 69]. This was a key finding that improved the fire safety in a space-based environment. In addition, the front velocity increases with air flux either under normal or microgravity. However, the rate of increase is different with larger front velocities under microgravity than normal gravity [33, 69].

2.2.1.2 Forward Smouldering

Research on forward smouldering of porous organic solids started with cigarettes [72, 73] and the related risk of fire [1, 7, 30]. Potential missions to Mars and the Moon motivated forward smouldering studies [1, 5, 7, 14, 16, 17, 23, 25, 30, 69, 71-74] in polyurethane foams, which is a material commonly used on both earth and spacecraft-based facilities, with well-known properties [74].

Forward smouldering is governed by char oxidation, Equation (2.1), and heat is transferred by conduction, convection, and radiation. Heat generation is carried forward by the air flux [30]. In solid fuels such as polyurethane foams, the fuel is not entirely consumed, leaving unburnt char behind the front. Thus, heat losses in the char region is an important controlling mechanism [30, 74]. Note that at high air fluxes, fuel might be entirely consumed, becoming the limiting factor [23]. Since convection heat transfer is in the same direction as the reaction front, a pyrolysis front is created and moves faster than oxidation [5, 23, 30]. The smouldering front velocity increases when air flux is increased [25], but it is lower than the one in opposed configuration [25, 30].

Forward smouldering was also studied under microgravity and normal gravity, showing similar conclusions as in opposed configuration. Under microgravity, reduced heat losses (no buoyancy) lead to the oxidation of the remaining char (second char oxidation) [16, 74]. Under normal gravity, buoyancy-induced heat losses cause the char to cool rapidly, preventing its second oxidation and causing extinction at low air fluxes. Smouldering under normal gravity presented front velocities smaller than in microgravity [69, 74].

Forward smouldering in reactive porous media such as polyurethane foam was considered a precursor of transition to flaming. Literature shows three possible causes of transition to flaming under either natural or forced air forward smouldering: *i*) strong secondary char

oxidation behind the front, *ii*) acceleration of the smouldering front velocity, and *iii*) increase of oxygen concentration. Smouldering of reactive porous matrixes typically leaves unburnt char (permeable matrix with large pore diameters) behind the front due to oxygen-limited conditions and heat losses. Residual char remains as an insulating material [25, 30, 67]. Under specific conditions, smouldering of this remaining char can be energetic enough to ignite flammable gases from pyrolysis and oxidation reactions (since flammability limits and sufficient heat are achieved [16]) that might be circulating in convective currents inside the pores, causing the transition to flaming [5, 14, 16, 17, 23, 25, 30, 74]. Note that formation of large pores is required, but it is not a sufficient condition for transition to flaming, since large pores were found in flaming and non-flaming conditions [14].

Bar-Ilan et al. [74] suggested that high front velocities might cause transition to flaming. On the other hand, Tse et al. [17] and Putzeys et al. [14] showed that the front velocity increases and sometimes decreases, as transition to flaming is approaching, indicating that an increase in the front velocity is not the primary cause of transition to flaming. Finally, large oxygen concentrations (>30%) are pointed as a cause of transition to flaming [14, 16, 75]. Note that high air fluxes may also cause the same effect. However, although it enhance the oxygen mass flux, high air fluxes may decrease the front temperature by convective cooling [16].

2.3 Engineering Smouldering Applications

Recently, the high energy released in forward smouldering processes and its potential of being self-sustaining have been recognized in several proposed or emerging industrial applications: iron ore sintering [79, 80], enhanced oil recovery [29, 81-87], underground coal gasification [37], landmine detection [88], and waste and contaminants destruction [2, 3, 32, 36, 38, 40-42, 89-97].

Iron ore sintering is a pre-treatment technology to convert ore fines into porous and permeable sinters [80]. This process requires the smouldering combustion of a solid fuel (e.g., coke breeze, charcoal, etc.) blended into the ore fines (Figure 2.7). The high combustion temperature (> 1100 ºC) creates a melting phase that results in high strength sinter [79, 80].
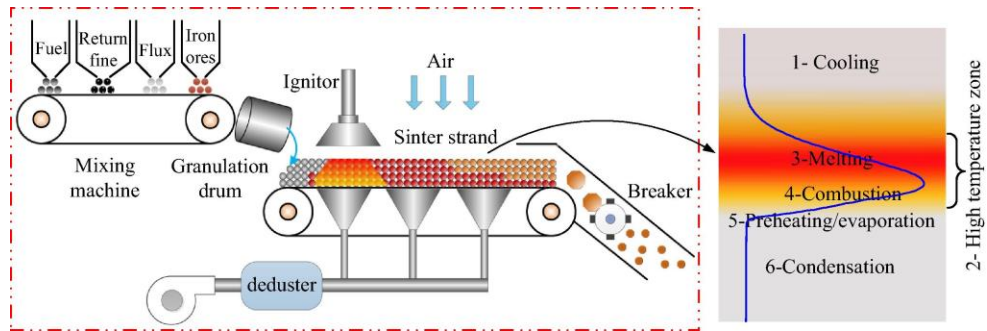
Figure 2.7: Schematic diagram of iron ore sintering process [80].

In-situ combustion also known as fire-flooding [29, 81-87] is an enhanced oil recovery technique applied in unconventional oils (i.e., challenge to be recovered by standard techniques) such as heavy oil, oil shale, and oil sands. Figure 2.8 illustrates the process. Injection of hot air (or enriched oxygen air) into the reservoir creates a smouldering combustion front that burns a fraction of oil (typically heavy fractions such as asphaltenes). Heat generated by the combustion front is carried out by the air, increasing the temperature of the region ahead of the front, and consequently, decreasing the viscosity of the virgin oil. This highly mobile oil moves to the bottom of the reservoir, where it is recovered. Although a fraction of fuel is burnt in the process, most of the oil (>80% [87]) can be technically recovered [83], with quality improvements (less viscous).
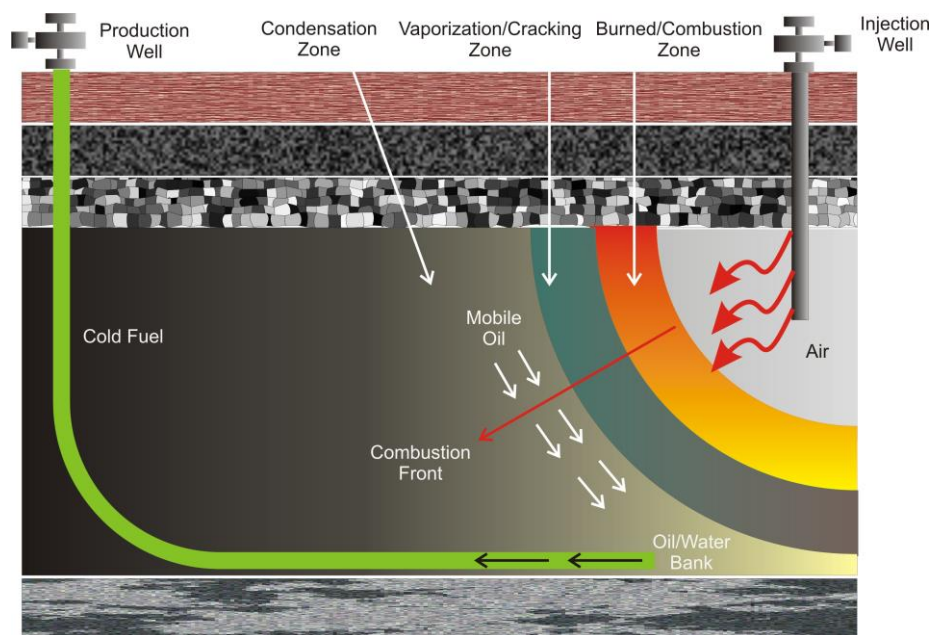
Figure 2.8: Schematic of the THAI (Toe to Heel Air Injection) in-situ combustion process (Modified from [86]).

Underground coal gasification is considered a "clean" coal technology that converts coal directly into gas via partial or complete combustion under air, oxygen, or steam. Coal gasification is considered clean because it removes sulfur, nitrogen compounds and particulates before the fuel is burnt. The gasification produces a syngas (mixture of high calorific value gases such as hydrogen, carbon monoxide, methane, etc.) as clean as natural gas and at the same time eliminates mining [37].

Proper waste management is one of the challenges of the new century. The number and type of contaminants are very extensive and range from petroleum by-products to human excreta. Semi-coke is a primary by-product of oil shale combustion (mostly from combustion in ex-situ reactors) for oil recovery. It is typically disposed in open dumps, and can potentially cause groundwater contamination (heavy metals, polycyclic aromatic hydrocarbons, etc.) due to rain and snow. Thus, semi-coke is a waste that needs effective treatment. Smouldering combustion of semi-coke has been proven to be a good alternative to eliminate the residue and also recover its energetic value under laboratory conditions.

However, a drawback is the decomposition of carbonates, which can produce large amount of carbon dioxide (CO_2) [89].

Tire waste is another residue that needs proper disposal. Typically, tires can be recycled in incinerators due to their high energetic value, replacing charcoal or oil. However, incineration by flaming combustion is costly since it requires a continuous input of energy. Thus, smouldering combustion was tested in laboratory as a promising technology for recycling tire waste [38].

Poor sanitation is one of the main causes of public health problems, due to wrong disposal of faecal matter and human waste [93]. Other organic wastes such as biosolids (i.e., separated solids with 88-99.75% moisture content) from wastewater treatment plants are also a concern [42]. Incineration by flaming is not efficient. Thus, smouldering combustion has been tested in laboratory as a new approach to destroy contaminants ex-situ in an efficient and self-sustaining process [36, 41, 94, 95, 97].

Finally, inappropriate disposal practices of organic liquid wastes from industrial activities known as Non-Aqueous Phase Liquids (NAPLs) has created extensive soil and consequently groundwater contamination [2]. A wide range of NAPLs were found as a source of contamination: coal tar, crude oil, oil sludge, creosote, and chlorinated volatile organic compounds (CVOCs) such as trichloroethylene (TCE) and tetrachloroethylene (PCE). Conventional remediation technologies (e.g., excavation, pump and treat, incineration, etc.) are costly [2, 40] and have been proven largely inefficient [3]. A relatively new remediation technology called Self-sustaining Treatment for Active Remediation (STAR) has been tested in-situ and ex-situ and it is showing promising results [2, 3, 32, 40, 90-92, 96].

STAR is based on the principle of smouldering combustion in which a smouldering front completely destroys the contaminant (i.e., different from oil recovery techniques), just leaving clean sand behind (Figure 2.9). A localized section of contaminated material (brown region in Figure 2.9) is heated by a forced hot air supply. Contaminant is thermally decomposed (pyrolysis) until the ignition of a smouldering combustion reaction, which propagates away from the ignition source. For self-sustained smouldering to be viable in

any context, a minimum air flux and contaminant concentration must be present. Note that such conditions are dependent on the scale, contaminant, and porous medium. Once the reaction is deemed self-sustaining (i.e., no longer needs an external heat supply), the igniter is turned off while the air (cold) is maintained. The reaction is typically tracked by temperature measurements via thermocouples or gas analysis. The process is terminated when there is no more fuel to react, i.e., when all contaminant has been destroyed. The reaction can also be externally quenched by removing the air supply, consequently removing the oxygen from the reaction, making it a controllable, safe process.
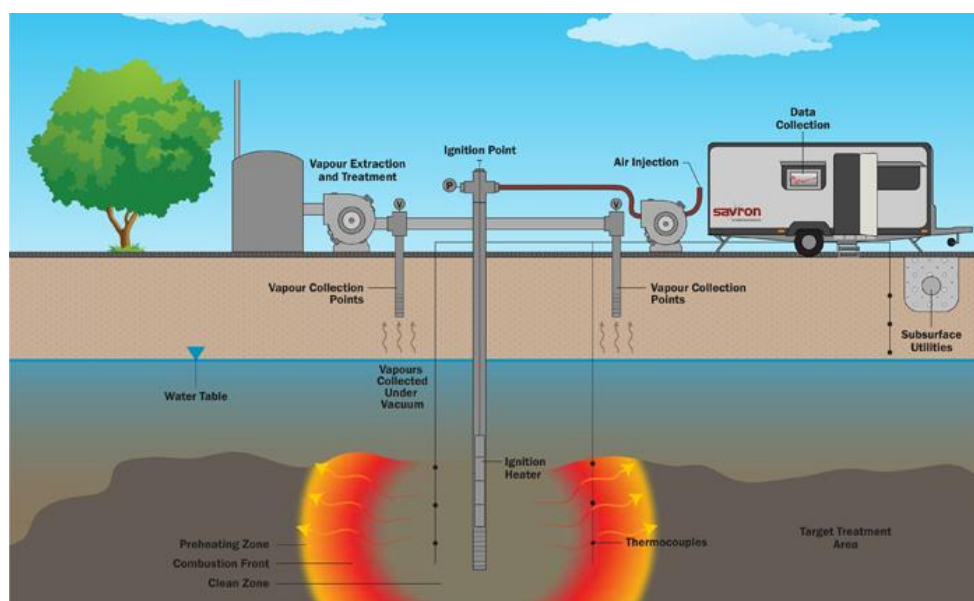
Figure 2.9: Schematic of STAR technology in the field [98].

All these applications take advantage of the self-sustaining nature of smouldering combustion to propose an engineering technique that has relatively low cost and low energy footprint. They all consider the full or partial destruction of an organic fuel (solid, sludge, or liquid) embedded in an inert porous medium; this is a key difference from the natural fire hazards posed by solid porous fuels discussed above. Most of these approaches (tires, semi-coke, biosolids) are still the subject of research and not yet commercialized. A few have been tested in the field. Oil recovery has been applied in pilot and full-scale but have had technical issues in the field [86] (see next section). STAR has been proven successful in several pilot-scale field tests [91], and a full-scale commercial application is ongoing

[99]. Ex situ treatment of oil sludge mixed with sand and contaminated soils has also advanced to the stage of commercial applications.

2.3.1   Key Contributions

Industrial application of smouldering is new and challenging. Thus, the scientific contributions are still modest, mostly focused on operational and design conditions, with limited published information on a fundamental understanding of the process or how it differs from fire hazard and natural/uncontrolled smouldering conditions.

Although petroleum engineering has applied smouldering combustion (commonly named in-situ combustion or fire-flooding) since the 80's, literature showed evidence of poor understanding of the process and the conditions that lead to high oil recovery. Garon et al. [85], conducting laboratorial experiments with oil saturation between 65 and 77%, showed that 30% of the oil was burnt at the end of the process. Only twenty years later, Xia et al. [87], using a new horizontal well technique (THAI process [86], Figure 2.8) was able to improve oil recovery up to 80% (under laboratory conditions) [85].

In many attempts of improving oil recovery, a new method called "wet combustion" was developed [100], where a mixture of air and steam was injected in the reservoir. In forward smouldering, a considerable amount of energy is stored in the sand behind the front. When water is injected with air, the high heat capacity of water can absorb and transport heat many times more efficiently than air. The heat absorbed vaporizes the water into steam that passes through the combustion front, releasing the heat via condensation in the virgin fuel region. Thus, energy stored behind the front can be recovered and transported forward, resulting in faster heat movement, decreasing the oil viscosity and increasing oil recovery up to 90% [81, 84, 85, 100]. This results in less fuel consumption, due to a decrease in the overall peak temperature [81]. Note that extinction of the combustion front may happen at high water content [84]. One of the main advantages of wet combustion is to reduce air requirements and improve oil recovery [84].

In-situ combustion for heavy oil recovery had not been very successful in the field due to poor understanding of smouldering. Most significant operational problems come from differences between gas and oil densities, channeling due to rock heterogeneity, gas/oil

mobility ratio, difficulty in minimizing fuel consumption (impacting the amount of oil recovered), and failure to supply sufficient air flux to sustain the reaction [86].

Although several failures, smouldering is still applied (under laboratory conditions) in oil shale combustion for oil recovery. Recently, Martins et al. [29] showed that oil shale can smoulder and oil can be recovered via smouldering. The high amount of inert material present in the oil shale creates a porous medium that favours the propagation of a smouldering front. However, at high temperatures, carbonates ($CaCO_3$) can decompose, releasing large amounts of CO_2. Moreover, laboratory experiments showed large radial heat losses (42% of the total energy released by combustion). A new micro-sampling system was used to measure the smouldering front thickness, and indicated a thin front (~10 mm), with an inclined curved surface.

The exploration of oil shale created new residues such as semi-coke that need to be eliminated. Thus, Sennoune et al. [89] conducted several experiments to identify the smouldering burning capacity of semi-coke as well as the influence of carbonates. Semi-coke (3.48% fixed carbon and 22.4% $CaCO_3$) was mixed with sand and ignited to form a self-sustaining front, with all the oxygen consumed. Only 0.25% of fixed carbon was left behind. The amount of $CaCO_3$ was increased from 22.4 to 72.4%, which resulted in a decrease in the peak temperature due to the high endothermicity of $CaCO_3$. Higher $CaCO_3$ (>72.4%) resulted in no change in the peak temperature. Decarbonation typically occurs around 800 ºC, and the lower temperatures created by high $CaCO_3$ could not activate the reaction. Thus, $CaCO_3$ worked mostly as an inert material. A decrease in the fixed carbon content from 3.48 to 1.74% decreased peak temperature from 1000 ºC to 562 ºC and prevented decarbonation (less CO_2 emission). Extinction occurred at 1.39% fixed carbon. At 1.74%, only half of the oxygen was consumed. Front velocity increased from 3.9 mm min^{-1} up to a maximum 5.5 mm min^{-1} when fixed carbon content was increased from 1.74% to 2.71% and then decreased to 4.0 mm min^{-1} when fixed carbon further increased to 3.48%. Heat losses were also important. Center-line and near the wall temperatures differed by 150 ºC. In two other studies, Sennoune et al. [28, 101] used air enriched with CO_2 in the smouldering process, and identified that decarbonation was reduced in 30% [101]. Moreover, an increase in the oxygen concentration from 3.5% to 6.5% increased peak

temperature and front velocity from 660 ℃ to 820 ℃ and from 2.40 mm min^{-1} to 4.26 mm min^{-1}. Note that extinction occurred at 3.5% O_2 [28].

Vantelon et al. [38] applied smouldering combustion to eliminate tire waste. Shredded tires were mixed with inert material (briquettes of refractory clay) to form a porous medium and a self-sustaining smouldering front was achieved. Water was produced, evaporated when the reaction front approached, and condensed again in the cold regions. A competition between pyrolysis and oxidation reactions was recognized. Condensation of hydrocarbons with high calorific value occurred, which could be potentially used as a fuel.

Smouldering of surrogate faeces and biosolids both mixed with sand were tested in [36, 42, 93-95, 97]. Biosolids were able to smoulder with moisture content as high as 80%. An increase in the mass destruction rate was found by lowering moisture content or sand/biosolids ratio, and increasing the air flux [42]. A parameter space based on moisture content and sand-to-biosolids ratio was created and showed the conditions the led to self-sustaining smouldering and smouldering extinction. For the self-sustaining cases, smouldering was able to destroy all the contaminants.

Yerman et al. [36, 97] identified that in the smouldering of surrogate faeces mixed with sand, moisture content within the range 64-73% had negligible impact of peak temperature and front velocity, whereas an increase in the sand content from 4 to 28 g g^{-1} decreased peak temperature and front velocity from 850 ℃ to 450 ℃ and from 0.65 cm min^{-1} to 0.35 cm min^{-1}, respectively. An increase in the air flux from 3 to 38 cm s^{-1} resulted in a linear increase in the front velocity from 0.25 to 3.5 cm min^{-1}, and peak temperature increased from 423 to 612 ℃. A further increase in the air flux to 47 cm s^{-1} decreased the peak temperature to 498 ℃ due to convective cooling. Moreover, an analysis on the sand particle diameters (d_p) was conducted, where d_p varied from 0.31 mm to 5.5 mm. Extinction occurred for $d_p \leq 0.5$ and $d_p \geq 3$ mm. Increasing d_p from 0.9 mm to 2.22 mm decreased peak temperature and front velocity from 500 ℃ to 450 ℃ and from 0.45 cm min^{-1} to 0.3 cm min^{-1}. In another study, Yerman et al. [95] confirmed that fuel consumption rates are independent of moisture content, but show a linear relationship with fuel concentration and air flux. Moreover, a general expression for front velocity changing with fuel consumption rates was developed. Smouldering and water evaporation fronts moved at similar rates, but

10-15 cm separated. At high moisture contents (56%), the smouldering reaction could not overcome the water heat sink, and both smouldering and water evaporation fronts collapsed into one, resulting in extinction. The difference between critical moisture content for biosolids and faeces is likely related to the fuel characteristics and operational conditions employed. In all the cases, fuel was entirely destroyed leaving only clean sand and ash behind.

The destruction of liquid contaminants embedded in sand was analyzed by [2, 3, 32, 90-92] in the context of developing the STAR technology (Figure 2.9). Pironi et al. [2, 3] first studied the conditions that lead to ignition and propagation of a smouldering front for coal tar destruction. The front velocity increased linearly from 0.4 cm min^{-1} to 1.5 cm min^{-1} with an increase in the air flux from 2.29 cm s^{-1} to 16.2 cm s^{-1}, whereas the peak temperature increased and decreased [2]. Moreover, peak temperature increased from 750 ºC to 1100 ºC when coal tar saturation increased from 10% to 35%, and then decreased to 850 ºC when saturation further increased to 50% [3]. The decrease in peak temperature at high saturations was hypothesized as a result of an increase in the volumetric fuel heat capacity. Increasing fuel saturation from 10% to 25% increased the energy release rate, causing an acceleration of the front velocity from 0.50 cm min^{-1} to 0.69 cm min^{-1}, despite having more fuel to consume. In this regime, the smouldering front is controlled by the amount of fuel available to react (fuel-limited). Above 25% saturation, oxygen-limited conditions likely take place and front velocity decreased to 0.50 cm min^{-1} with a further increase in fuel saturation to 50%. In addition, increasing the water content from 0 to 75% increased the time to ignition, reducing the peak temperature from 1050 ºC to 850 ºC, but resulted in negligible effects on the front velocity. Coarse (d_p=1.34 mm) and medium (d_p=0.75 mm) sand demonstrated to be the most favourable to self-sustaining conditions. Large particle diameters resulted in a decrease in peak temperature and front velocity (increased role of the porous medium as a heat sink). All the cases resulted in an average mass removal at the column center-line of 99.9% [2, 3].

STAR was also conducted in different scales, and an increase in scale (increase in the diameter of the column decreases the surface area per unit volume) led to reduced heat losses [90]. Pilot scale field tests were also conducted [91]. Smouldering was applied

beneath the water table in a soil containing coal tar, sand, brick, and other construction materials (i.e., high heterogeneity). A smouldering front was successfully ignited and propagated through the medium, with a drying front moving ahead of the smouldering front. Thus, although beneath the water table, water was not a limiting factor in the self-sustaining process.

The robustness of STAR was also tested for other contaminants such as trichloroethylene (TCE) mixed with vegetable oil and sand [92]. Vegetable oil was used to provide the energy necessary to eliminate TCE (highly volatile). Self-sustaining propagation was achieved for all the cases where TCE saturation did not exceed 20% with oil saturation in the range of 5-15%. On average, 75% of TCE was removed due to volatilization. For TCE saturation $\geq$ 30% and oil saturation equal to 15%, extinction of the smouldering front occurred due to an unfavourable energy balance created by the volatilization of TCE (absorbing energy), insufficient energy released by oxidation, and heat losses.

Vegetable oil was again used in STAR to understand mobility effects. Kinsman et al. [32] showed that downward organic mobility was found, and resulted in atypical (rapid cooling, re-ignition events, and increase in the front thickness) temperature profiles, leading to elevated peak temperatures (quasi-super-adiabatic conditions). Three conditions must simultaneous exist for downward mobility takes place: *i*) forced air flux must be sufficiently low to permit a downward hydraulic gradient, *ii*) viscosity of the liquid ahead of the front must be low to enable migration, and *iii*) pre-heating zone height must be sufficiently large (large column size). Thus, it was shown that downward mobility can be minimized by increasing the upwards air flux.

2.4 Solid versus Liquid Smouldering

2.4.1 Porous Matrix

Traditionally, smouldering combustion has been studied in solid fuels (foams, peat, wood, etc.). The porous matrix of such materials is composed of a reactive, immobile fuel that contains large pores (high porosity: 92-97% [102-104]) with high pore connectivity, low thermal conductivity (O[10^{-2} W m^{-1} K^{-1}] [102, 105, 106]) and low volumetric heat capacity (O[10^4 J m^{-3} K^{-1}] [102, 103, 106]), constant fuel concentration (if homogeneous), and a

large surface area for reaction [95, 107]. Figure 2.10a shows an example for polyester urethane foam. Since the matrix is reactive, fuel shrinkage is common, which might damage the integrity of the smouldering front. Smouldering of solid fuels typically leaves unburnt fuel behind that insulates the front against heat losses.

In contrast, liquid smouldering is only possible when the organic liquid fuel (e.g., NAPL) is embedded in an inert matrix (typically sand or sandstone), Figure 2.10b. Sand has a lower porosity (38-50% [2, 27, 32]), with relatively small pores partially or totally filled with a liquid hydrocarbon [108], higher thermal conductivity ($O[10^{-1}$ W m^{-1} K^{-1}]) and higher volumetric heat capacity ($O[10^{6}$ J m^{-3} K^{-1}] [109]) when compared to solid fuels. The presence of fuel in the matrix porosity means reduced effective permeability to air, and relatively less fuel surface area exposed to the gas phase, compared to solid fuels. The long chain liquid hydrocarbons with high energy content (e.g., crude oil, coal tar, etc.) exhibit a complex composition mixing liquid and solid particulates [110, 111]. In addition, the potential mobility of liquids, due to liquid phase gradients and influenced by gas phase gradients and temperature induced viscosity reductions, is an important difference in relation to solid smouldering. Another important difference is related to heat transfer mechanisms and heat accumulation in the matrix. In liquid smouldering, the inert matrix accumulates more energy than the reactive matrix in solid smouldering. This is important because the accumulated heat can be recovered and provide extra energy to sustain the smouldering front.

<div align="center">(a)   (b)</div>
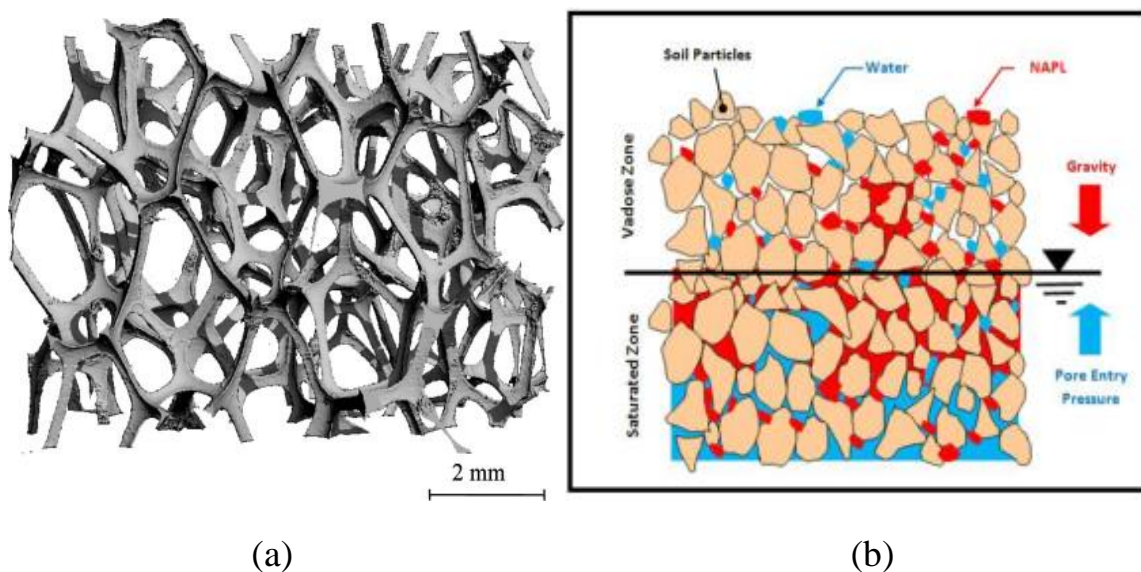
Figure 2.10: (a) Computed tomography image of a polyester urethane foam [107]. (b) NAPL-water distribution in porous media [112].

2.4.2   Flow, Heat, and Mass Transfer Processes

Smouldering combustion takes place in a porous matrix either organic reactive (e.g., foam) or inorganic inert (e.g., sand) embedded with organic fuel. The porous structure contains a large number of microscopic pores and throats through which the fluids pass. Understanding flow, mass, and heat transfer processes in smouldering is challenging because of the complexity of the medium. Figure 2.11 shows a schematic of smouldering of a liquid hydrocarbon embedded in an inert porous medium (sand) and will be used along this section to illustrate the different processes present in smouldering.
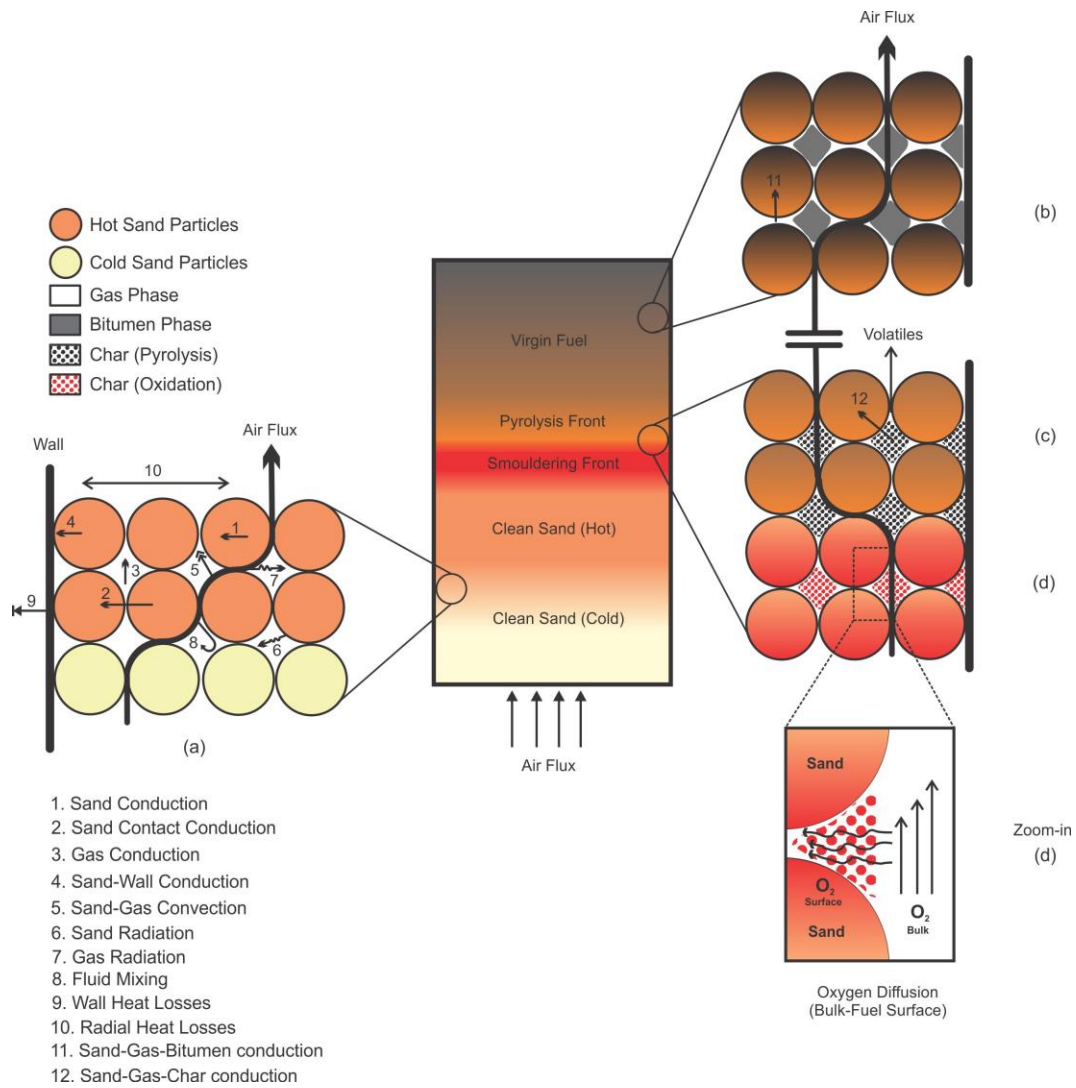
Figure 2.11: (a) Heat transfer processes between solid and gas phases, (b) liquid fuel embedded in the sand, (c) bitumen pyrolysis, (d) char oxidation, and (e) bulk and surface oxygen diffusion (adapted from Hobbs et al. [113]).

For fundamental understanding of such complex phenomenon, robust numerical models are needed. Typically, these models are not described at the pore scale (microscale), but at the scale of a Representative Elementary Volume or REV (macroscale) over which average properties (e.g., from tens to hundreds of pores) can be defined. One of the key differences is that microscale models use the full conservation of momentum to investigate the pore velocity distribution, whereas macroscale models approximate it via Darcy's Law [114-116].

A mathematical description of the relevant processes in one-dimensional liquid smouldering at macroscale is presented below. For simplicity, only two phases are considered, i.e., liquid/solid (assumed to have effective properties of a single solid phase) and gas phases (Figure 2.11b). When liquid mobility is not considered, the conservation of mass [117] for the gas phase is defined:

$$\frac{\partial(\rho_g \phi_g)}{\partial t} + \frac{\partial(\rho_g u_g)}{\partial x} = Q_g \tag{2.2}$$

Equation (2.2) solves air pressures and velocities adopting Darcy's Law [118] without gravity effects:

$$u_g = -\frac{k_p}{\mu_g}\left(\frac{\partial P_g}{\partial x}\right) \tag{2.3}$$

with gas density (ρ_g):

$$\rho_g = \frac{P_g}{R_s T_g} \tag{2.4}$$

following the ideal gas law [119]. The term Q_g in Equation (2.2) represents the generation (source) or removal (sink) of mass per unit volume per unit time for gas phase. It may include consumption or production of chemical species as well as evaporation and condensation. The bulk transport of oxygen and other species in the gas phase [120] is described by:

$$\phi_g \frac{\partial(\rho_g Y_{O_2})}{\partial t} + \frac{\partial(\rho_g u_g Y_{O_2})}{\partial x} = \phi_g \frac{\partial}{\partial x}\left(\rho_g D_g \frac{\partial Y_{O_2}}{\partial x}\right) + Q_{O_2} \tag{2.5}$$

where Q_{O_2} represents the mass per unit volume per unit time for oxygen consumption. The conservation of energy follows one of two different approaches: Local Thermal Equilibrium (LTE) and Local Thermal Non-Equilibrium (LTNE). In the LTE, the temperatures of the fluid (liquid or gas) and solid phases in the porous media are locally

the same, and only one energy equation is required. On the other hand, in the LTNE, the solid/liquid temperature (T_s) differs from the gas temperature (T_g) [116, 121]:

$$(\rho C_p)_{eff} \frac{\partial T_s}{\partial t} = \frac{\partial}{\partial x}\left(k_{eff}\frac{\partial T_s}{\partial x}\right) + h_{sg}\left(\frac{A_{s,sp}}{V_{sp}}\right)(T_g - T_s) + Q_{gen} - Q_{loss} \qquad (2.6)$$

$$\phi_g\left(\rho_g C_{p_g}\right)\frac{\partial T_g}{\partial t} + \rho_g C_{p_g}u_g\frac{\partial T_g}{\partial x} = \phi_g\frac{\partial}{\partial x}\left(k_g\frac{\partial T_g}{\partial x}\right) + h_{sg}\left(\frac{A_{s,sp}}{V_{sp}}\right)(T_s - T_g) \qquad (2.7)$$

Source/sink terms (Q) in Equation (2.6) represent the net energy per unit volume per unit time for pyrolysis (Figure 2.11c) and oxidation (Figure 2.11d) reactions (Q_{gen}), and radial heat losses (Q_{loss}). Effective thermal properties for the solid/liquid phases are considered:

$$\begin{aligned}
(\rho C_p)_{eff} &= (1 - \phi)(\rho_s C_{p_s}) + (\phi_l)(\rho_l C_{p_l}) \\
k_{eff} &= (1 - \phi)(k_s + k_{rad}) + (\phi_l)(k_l) \\
\phi &= \phi_g + \phi_l
\end{aligned} \qquad (2.8)$$

When LTNE is assumed, heat transfer among phases (Figure 2.11a) is simulated via a interfacial heat transfer coefficient (h_{sg}), which is typically employed as an empirical Nusselt (Nu) versus Reynolds (Re) and Prandtl (Pr) correlation. The most widely employed heat transfer correlation was developed by Wakao et al. [122]:

$$Nu = \frac{h_{sg}d_p}{k_g} = 2 + 1.1\left(Re^{0.6}Pr^{1/3}\right) \qquad (2.9)$$

valid for 15≤Re≤8500. If within the REV the difference between the solid and gas temperature is negligible ($T_g = T_s = T$), the hypothesis of LTE can be assumed. Thus, Equations (2.6) and (2.7) are combined into one [116, 121], resulting in:

$$(\rho C_p)_{eff}\frac{\partial T}{\partial t} + \rho_g C_{p_g}u_g\frac{\partial T}{\partial x} = \frac{\partial}{\partial x}\left(k_{eff}\frac{\partial T}{\partial x}\right) + Q_{gen} - Q_{loss} \qquad (2.10)$$

where:

$$(\rho C_p)_{eff} = (1 - \phi)(\rho_s C_{p_s}) + (\phi_l)(\rho_l C_{p_l}) + (\phi_g)\left(\rho_g C_{p_g}\right) \qquad (2.11)$$

$$k_{eff} = (1 - \phi)(k_s + k_{rad}) + (\phi_l)(k_l) + (\phi_g)(k_g)$$
$$\phi = \phi_g + \phi_l$$

Equation (2.5) considers that all of the bulk oxygen is available for the oxidation reaction. Leach et al. [106] suggested that diffusion of oxygen into the surface of the fuel (here, fuel is the porous solid) might limit the reaction rate:

$$
\begin{aligned}
\phi_{bk} \frac{\partial}{\partial t}\left(\rho_{g,bk} Y_{O_2,bk}\right) &+ \frac{\partial}{\partial x}\left(\rho_{g,bk} u_{g,bk} Y_{O_2,bk}\right) \\
&= \phi_{bk} \frac{\partial}{\partial x}\left(\rho_{g,bk} Y_{O_2,bk} D_{g,bk} \frac{\partial Y_{O_2,bk}}{\partial x}\right) \\
&+ h_m \left(\frac{A_{s,sp}}{V_{sp}}\right)\left(Y_{O_2,sf} - Y_{O_2,bk}\right)
\end{aligned}
\tag{2.12}
$$

$$
\begin{aligned}
\phi_{sf} \frac{\partial}{\partial t}\left(\rho_{g,sf} Y_{O_2,sf}\right) &\\
&= \phi_{sf} \frac{\partial}{\partial x}\left(\rho_{g,sf} Y_{O_2,sf} D_{g,sf} \frac{\partial Y_{O_2,sf}}{\partial x}\right) \\
&+ h_m \left(\frac{A_{s,sp}}{V_{sp}}\right)\left(Y_{O_2,bk} - Y_{O_2,sf}\right) + Q_{O_2}
\end{aligned}
\tag{2.13}
$$

where $\phi_g = \phi_{bk} + \phi_{sf}$ and $u_{g,sf} = 0$. Equation (2.12) describes the transport of O_2 in the bulk gas ($Y_{O2,bk}$), and Equation (2.13) shows the transport of O_2 at the surface of the solid ($Y_{O2,sf}$); both phenomena are illustrated in Figure 2.11d. The sink term (Q_{O2}) indicates the depletion of oxygen by oxidation reactions on the fuel surface. The transport of mass in two separated continuums (e.g., bulk and surface, fracture and matrix) is widely known in the porous media literature as dual-porosity models [123-125], in which these two continuums are superimposed over the same volume [126]. Equations (2.12) and (2.13) are also linked by a mass transfer coefficient (h_m) [127].

When certain assumptions are made (e.g., one-dimensional configuration, simple reaction models, LTE, etc. [7, 128, 129]), the above equations can be solved analytically. Approximate analytical expressions are used for determining the structure of the

smouldering front, the front propagation velocity, and the maximum (adiabatic) temperature at the combustion front [7, 23, 128-134].

Smouldering has been analyzed analytically by [20, 128-130, 132, 133, 135, 136], where three distinct structures were described: reaction leading, reaction trailing, and super-adiabatic (Figure 2.12). The definition of each structure is based on simple analytical assumptions, and the conditions that lead to structure change are still not well understood. However, since it is present in the smouldering literature, a brief summary will be described here for completeness. In the reaction leading structure (Figure 2.12a), the chemical reaction front propagates faster than the heat transfer front, whereas in the reaction trailing structure (Figure 2.12b), the opposite occurs. In the super-adiabatic structure (Figure 2.12c), the velocity of the reaction front overlaps the velocity of the heat transfer front, causing a steep increase in the combustion temperature (T_b); in theory, it approaches infinity. In practice, virtually of the experimental research on smouldering of organic liquids in inert porous media has exhibited the reaction leading structure; this appears to be the dominant structure for the practical conditions of interest to these systems.
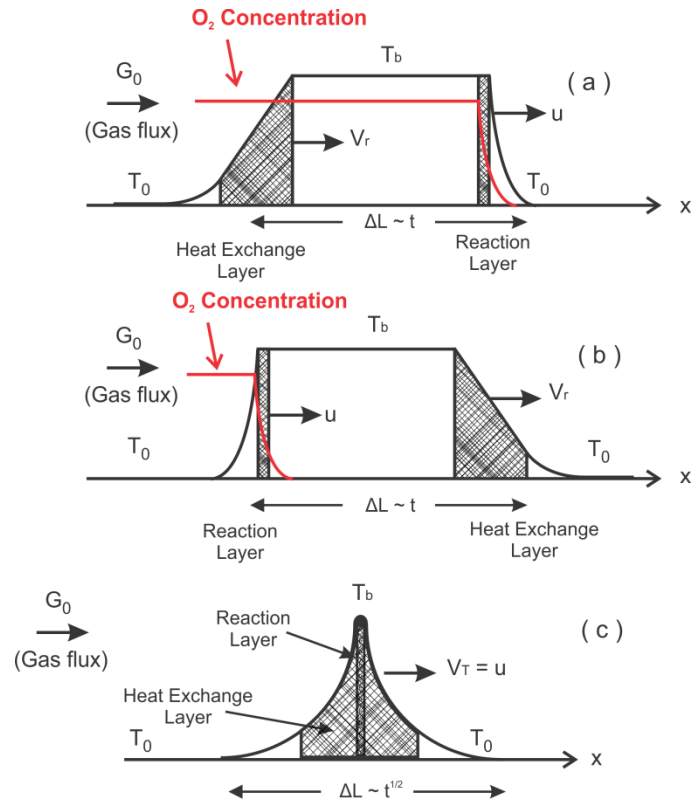
Figure 2.12: Forward smouldering front: (a) reaction leading; (b) reaction trailing; (c) super-adiabatic (Modified from [129, 130]).

Analytically, the smouldering front structure can be described as a function of a Δ factor [7, 128-131, 134]:

$$\Delta = \frac{\phi_g \rho_g u_g}{\left(\phi_g \rho_g C_{p_g} + (1 - \phi_g)\rho_s C_{p_s}\right) v_f}$$

$$= \frac{(1 - \phi_g)\rho_g C_{p_g}}{\phi_g \rho_g C_{p_g} + (1 - \phi_g)\rho_s C_{p_s}} \frac{([Fuel]_{in} - [Fuel]_{out})}{([O_2]_{in} - [O_2]_{out})} \tag{2.14}$$

where $[O_2]_{in}$ and $[O_2]_{out}$, $[Fuel]_{in}$ and $[Fuel]_{out}$, are the oxygen and fuel concentrations upstream and downstream from the combustion front, respectively. The value of Δ determines whether the smouldering front structure is reaction leading (Δ < 1), reaction trailing (Δ > 1), and super-adiabatic (Δ = 1). Thus, following the assumptions above, an

analytical expression for the smouldering front velocity (v_f) and the adiabatic temperature (T_b) were developed:

$$v_f = \frac{\phi_g}{1 - \phi_g} \frac{([O_2]_{in} - [O_2]_{out})}{([Fuel]_{in} - [Fuel]_{out})} u_g \tag{2.15}$$

$$T_b = \frac{(1 - \phi_g)([Fuel]_{in} - [Fuel]_{out})\Delta H_{oxid}}{\phi_g \rho_g C_{p_g} + (1 - \phi_g)\rho_s C_{p_s}} \tag{2.16}$$

Equation (2.15) can be reformulated based on a single carbon oxidation reaction [28] and become:

$$v_f = \frac{u_g \rho_g Y_{O_2} fr_{oxid} M_{cb}}{M_g \rho_{bed} x_{FC} fr_{oxid}(1 - fr_{CO}/2)} \tag{2.17}$$

Torero et al. [5, 23, 31, 33] developed another analytical expression for the front velocity based on an energy balance at the oxygen-limited reaction front, local thermal equilibrium, and two-step reactions (pyrolysis and oxidation):

$$v_f = \frac{Y_{O_2} \rho_g u_g \Delta H_{oxid} + (\dot{Q}_{ig}^{"} - \dot{Q}_{loss}^{"})(A_s/V)}{\left[(1 - \phi_g)\rho_s C_{p_s} + \phi_g \rho_g C_{p_g}\right](T - T_0) - (1 - \phi_g)\rho_s \Delta H_{pyr} + Y_{O_2} \rho_g \Delta H_{oxid}} \tag{2.18}$$

Although analytical expressions are useful for general understanding of the process, in complex cases in which many chemical reactions take place, local thermal equilibrium is not valid, or fundamental understanding is necessary, evaluating smouldering with simple analytical expressions is challenging, and numerical models are therefore valuable.

2.4.3   Chemical Reactions

Smouldering kinetic mechanisms generally describe competing exothermic and endothermic reactions, that combined, can result in net consumption or generation of heat [1, 70, 106, 137-142]. There are many chemical reactions that can possibly occur within pyrolysis and oxidation of fuels [143]. Oxidative reactions tend to be much faster than pyrolysis reactions, so simplifications are possible and the literature provides kinetic models of different levels of complexity [49, 139-141, 144]. These models range from single one-step global reactions to multiple steps. Table 2.1 shows a compilation of several kinetic mechanisms from one to nine steps available in the literature for a variety of solid and liquid hydrocarbons (peat, polyurethane foam, biomass, cellulose, cardboard, wood, tire waste, crude oil, heavy oil, bitumen, tar sands, oil shale, and asphalt).

Thermogravimetry (TG), Differential Thermogravimetry (DTG), and Differential Scanning Calorimetry (DSC) (under air, N_2, and O_2 atmospheres, heating rates from 1 to 80 ℃/min, and sample mass between 2 and 50 mg [138, 140, 145-166]) along with SARA (Saturated, Aromatics, Resins, and Asphaltenes [167-169]) analysis (i.e., a technique that separate liquid compounds into fractions according to their solubility in solvents of different polarity), were used to develop such mechanisms. TG is an analytical technique that measures mass changes of a sample that was submitted to a heating procedure under an inert atmosphere (e.g., N_2) or oxidative (e.g., air) atmosphere. DTG is the derivative of the TG and is used to identify the temperature range at which global reactions are taking place. In the DSC, a heat flux (endothermic or exothermic) is measured, and compared with a reference at the same temperature [170]. Figure 2.13 shows an example of TG and DSC for cellulosic insulation heated in air. DSC captured one endothermic peak before 100 ℃ (likely water evaporation) and two exothermic peaks after 300 ℃, which suggests two oxidation reactions. Thus, TG, DTG, and DSC can identify the different chemical regions presented in Figure 2.11 and are typically used to characterize and develop chemical reaction mechanisms of materials.
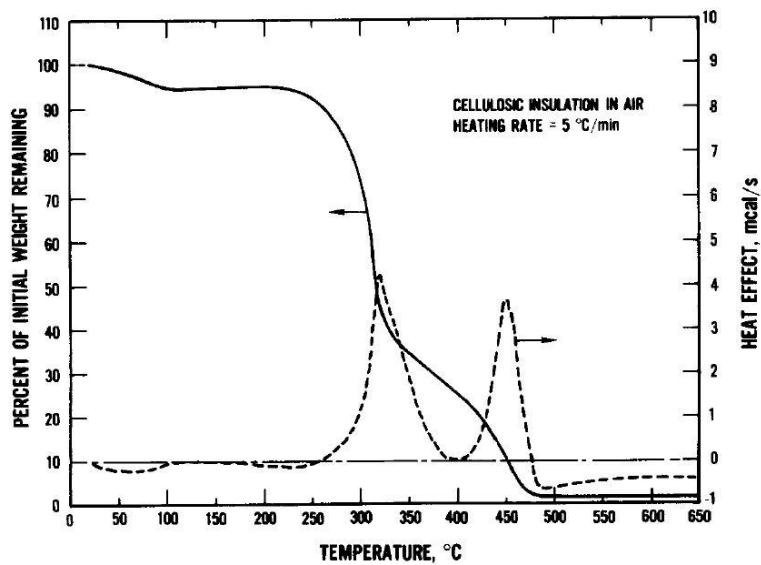
Figure 2.13: TG (solid line) and DSC (dashed line) results for cellulosic insulation heated in air at 5 °C/min [30].

Table 2.1: Compilation of Generic Kinetic Mechanism from Literature

Ref.	Eq.	Steps	Rection Type	Generic Mechanism	Fuel	Liquid	Solid	Highlights
[20, 128-130, 132, 133, 135, 136, 142, 171-175]	(2.19)	1-step	1 oxidation	$Fuel + O_2 \rightarrow Ash + H_2O + Gases + Heat$	Carbon [132, 142, 171-173, 175], Hydrocarbon mixture [133, 174], Diesel Particulate Filters [135], Wood [136], Cellulosic material [20], Porous solid fuel [128-130]	-	Ash	Simple global mechanisms, mostly employed in analytical smouldering models. Kinetic parameters are typically estimated through analytical methods.
[7, 27, 75, 176-179]	(2.20)	2-step	1 pyrolysis; 1 oxidation	$Fuel + Heat \rightarrow Char + Gases$ $Fuel + O_2 \rightarrow Char + Gases + Heat$	Oil shale [27], Polyurethane foam [176-179], Cellulosic materials [7, 75]	-	$CaCO_3$, CaO, Char, Ash	Fuel pyrolysis is included in Eqs. (2.19) and (2.20). Eq. (2.19) implies that char oxidation can be neglected and Eq. (20) indicates that fuel oxidation is not relevant. Eq. (2.21) shows decarbonation of oil shale. Eq. (2.22) neglects pyrolysis reactions and takes into account fuel and char oxidation.
	(2.21)			$Fuel + Heat \rightarrow Char + Gases$ $Char + O_2 \rightarrow Ash + Gases + Heat$				
	(2.22)		1 oxidation; 1 decarbonation	$Fuel + O_2 \rightarrow Char + Gases$ $CaCO_3 + Heat \rightarrow CaO + CO_2$				
	(2.23)		2 oxidation	$Fuel + O_2 \rightarrow Char + Gases + Heat$ $Char + O_2 \rightarrow Ash + Char + Gases + Heat$				
[1, 70, 103, 106, 137, 140, 180-184]	(2.24)	3-step	1 pyrolysis; 2 oxidation	$Fuel + Heat \rightarrow Char + Gases$ $Fuel + O_2 \rightarrow Char + H_2O + Gases + Heat$ $Char + O_2 \rightarrow Ash + Gases + Heat$	Polyurethane foam [106, 180, 184], Cellulosic materials [1, 103, 137], Wood [181], Biomass [140, 183], Peat [70], Porous solid fuel [182]	-	Char, Ash	Eq. (2.23) shows competition between fuel pyrolysis and fuel oxidation, whereas drying is included in Eq. (2.24) neglecting fuel oxidation.
	(2.25)		1 drying; 1 pyrolysis; 1 oxidation	$Fuel_{(wet)} + Heat \rightarrow Fuel_{(dry)} + H_2O$ $Fuel + Heat \rightarrow Char + Gases$ $Char + O_2 \rightarrow Ash + H_2O + Gases + Heat$				
[165, 185]	(2.26)	4-step	1 pyrolysis; 3 oxidation	$Fuel + Heat \rightarrow Tar + Char + Gases$ $Fuel + O_2 \rightarrow H_2O + Gases + Heat$ $Tar + O_2 \rightarrow H_2O + Gases + Heat$ $Char + O_2 \rightarrow H_2O + Gases + Heat$	Heavy oil [185], Oil shale [165]	Tar (Organic matter, light oil, oil)	$CaCO_3$, CaO, char (coke, fixed carbon), ash (inert material)	Three oxidation reactions are introduced in Eq. (2.25). Eq. (26) shows drying and decarbonations for oil shale.
	(2.27)		1 drying, 1 pyrolysis, 1 oxidation; 1 decarbonation	$Fuel_{(wet)} + Heat \rightarrow Fuel_{(dry)} + H_2O$ $Fuel + Heat \rightarrow Tar + Char + Gases$ $Char + O_2 \rightarrow Gases + Heat$ $CaCO_3 + Heat \rightarrow CaO + CO_2$				

Table 2.1: Continue.

Ref.	Eq.	Steps	Rection Type	Generic Mechanism	Fuel	Liquid	Solid	Highlights
[49, 102, 138-141, 186, 187]	(2.28)	5-step	2 pyrolysis; 3 oxidation	$Fuel + Heat \rightarrow \beta - Fuel + Gases$ $\beta - Fuel + Heat \rightarrow Char + Gases$ $Fuel + O_2 \rightarrow Char + Gases + Heat$ $\beta - Fuel + O_2 \rightarrow Char + Gases + Heat$ $Char + O_2 \rightarrow Ash + Gases + Heat$	Peat [49, 139, 141, 186], Polyurethane foam [102, 138], Biomass [140]	-	char, α–char, β-char, β-fuel, ash	The concept of α-, β-, and γ-fuel (or char) is introduced in Eqs. (2.27)-(2.29), and applied hereafter.
	(2.29)		1 drying; 1 pyrolysis; 3 oxidation	$Fuel_{(wet)} + Heat \rightarrow Fuel_{(dry)} + H_2O$ $Fuel + Heat \rightarrow \alpha - Char + Gases$ $Fuel + O_2 \rightarrow \beta - Char + Gases + Heat$ $\beta - Char + O_2 \rightarrow Ash + Gases + Heat$ $\alpha - Char + O_2 \rightarrow Ash + Gases + Heat$				
	(2.30)		3 pyrolysis; 2 oxidation	$\alpha - Fuel + Heat \rightarrow \beta - Fuel$ $\beta - Fuel + Heat \rightarrow Char$ $\beta - Fuel + Heat \rightarrow Gases$ $\alpha - Fuel + O_2 \rightarrow \beta - Fuel + Heat$ $\beta - Fuel + O_2 \rightarrow Char + Heat$	Oil sands [187]	α–Fuel (maltene)	α–Fuel (asphaltene), char (coke)	
[188]	(2.31)	6-step	3 pyrolysis; 3 oxidation	$\alpha - Fuel + Heat \rightarrow Char + Gases$ $Tar + Heat \rightarrow Char + Gases$ $\alpha - Tar + Heat \rightarrow \alpha - Char + Gases$ $Tar + O_2 \rightarrow \alpha - Tar + Heat$ $Char + O_2 \rightarrow H_2O + Gases + Heat$ $\alpha - Char + O_2 \rightarrow H_2O + Gases + Heat$	Heavy oil	-	α–Fuel (Asphaltene), char (coke$_1$), Tar (heavy fractions), α–Tar (oxidized heavy fractions), α–char (coke$_2$)	The mechanism showed in [188] was reformulated and presented in a generic format in Eq. (2.30).
[189]	(2.32)	7-step	3 pyrolysis; 4 oxidation	$Fuel + Heat \rightarrow \beta - Fuel + Gases$ $\beta - Fuel + Heat \rightarrow \gamma - Char + Gases$ $\gamma - Char + Heat \rightarrow Gases$ $Fuel + O_2 \rightarrow Char + Gases + Heat$ $\beta - Fuel + O_2 \rightarrow Char + Gases + Heat$ $Char + O_2 \rightarrow \alpha - Char + Gases + Heat$ $\alpha - Char + O_2 \rightarrow Gases + Heat$	Polyurethane foam	-	β–Foam, γ-char (Thermal char), char, α–char	The processes that lead the transition from smouldering to flaming might be analyzed by the incorporation of char and α-char oxidation reactions in Eq. (2.31).
[18]	(2.33)	8-step	3 pyrolysis; 4 oxidation; 1 gas oxidation	$Fuel + Heat \rightarrow \beta - Fuel + Gases$ $\beta - Fuel + Heat \rightarrow \gamma - Char + Gases$ $\gamma - Char + Heat \rightarrow Gases$ $Fuel + O_2 \rightarrow Char + Gases + Heat$ $\beta - Fuel + O_2 \rightarrow Char + Gases + Heat$ $Char + O_2 \rightarrow \alpha - Char + Gases + Heat$ $\alpha - Char + O_2 \rightarrow Gases + Heat$ $Gases + O_2 \rightarrow Final\ Gases + Heat$	Polyurethane foam	-	β–Foam, γ-char (thermal char), char, α–char	Same mechanism as Eq. (2.31) with the addition of gas-phase oxidation to simulate the transition from smouldering to flaming.

Table 2.1: Continue.

Ref.	Eq.	Steps	Rection Type	Generic Mechanism	Fuel	Liquid	Solid	Highlights
[140]	(2.34)	9-step	1 drying; 3 pyrolysis; 5 oxidation	$Fuel_{(wet)} + Heat \rightarrow Fuel_{(dry)} + H_2O$ $\alpha - Fuel + Heat \rightarrow \alpha - Char + Gases$ $\beta - Fuel + Heat \rightarrow \alpha - Char + Gases$ $\gamma - Fuel + Heat \rightarrow \alpha - Char + Gases$ $\alpha - Fuel + O_2 \rightarrow \beta - Char + Gases + Heat$ $\beta - Fuel + O_2 \rightarrow \beta - Char + Gases + Heat$ $\gamma - Fuel + O_2 \rightarrow \beta - Char + Gases + Heat$ $\beta - Char + O_2 \rightarrow Ash + Gases + Heat$ $\alpha - Char + O_2 \rightarrow Ash + Gases + Heat$	Biomass	-	α –Fuel (Hemicellulose), β – Fuel (cellulose), γ –Fuel (lignin), α – char, β – char, ash	Multiple competition between pyrolysis and oxidation reactions

The kinetic mechanisms presented in Table 2.1, standing alone, are not sufficient for simulating combustion reactions; they provide only the stoichiometry. Chemistry theory additionally describes such mechanisms in terms of reaction rates (R):

$$R[s^{-1}] = k_a [Y_f]^n [Y_{O_2}]^m \tag{2.35}$$

where n and m are the reaction orders, Y_f and Y_{O2} are the mass fractions of fuel and oxygen, respectively, and k_a is the Arrhenius equation:

$$k_a = A exp\left(-\frac{E}{R_g T}\right) \tag{2.36}$$

where A is the pre-exponential factor (s^{-1}), E is the activation energy (J mol^{-1}), R_g is the ideal gas constant (J K^{-1} mol^{-1}), and T is the temperature (K). Pyrolysis reaction rates are represented by Equation (2.35), ignoring Y_{O2}, i.e., $[Y_{O2}]^m=1$.

The application of such kinetic mechanisms into smouldering numerical models requires the estimation of the kinetic parameters, i.e., activation energy (E), pre-exponential factor (A), and reaction orders (n,m), described in the Arrhenius equation. These expressions are continuous functions. Therefore, a unique temperature for the onset of these reactions is difficult to establish. Characteristic temperature values obtained from TG/DTG/DSC data generally describe the temperature at which each process occurs, although strongly depending on heating rates and sample size employed.

Thus, several methods when coupled with TG/DTG/DSC data may be used to calculate/estimate the Arrhenius parameters: Kissinger, Ozawa, Freeman-Carroll, Coats-Redfern, Genetic Algorithms (GA), Levenberg-Marquart (LM) algorithm, etc. [140, 145-149, 165, 190-198]. Limitations can be found in almost all of them. For example, graphical methods (e.g., Kissinger, Ozawa, etc.) are only suitable for reactions that are simple, non-noisy and non-overlapping. LM algorithm converges quickly but it is very sensitive to the initial guess. GA algorithm can be used for a large number of unknown kinetic parameters; however, it is time consuming and stochastic, i.e., uniqueness of the solution is not guaranteed [148, 165, 190, 196].

Since chemical mechanisms and kinetic parameters depend on the type of fuel, TG/DTG/DSC heating rates, and methods of estimation, it is currently unknown the minimal number of reactions necessary to proper simulate smouldering combustion.

2.4.4 Key Contributions

Analytical and numerical models in smouldering combustion mostly focused on the understanding of smouldering as a fire hazard [1, 18, 20, 102, 103, 106, 136, 137, 141, 177-180, 184, 186, 189, 199-202], with a few studies in smouldering applications [27, 133, 171-173]. The fuels analyzed were: polyurethane foams [1, 18, 20, 102, 106, 177-180, 184, 189, 199, 202], peat [141, 186], cellulosic materials [1, 103], wood [136, 137], cigarette [200, 201], oil shale [27, 114, 172], crude oil [133], and carbon (pyrolized sugar) [171];

Heat transfer in the porous medium employed one of two approaches: Local Thermal Equilibrium (LTE) [20, 27, 133, 136, 137, 177, 180, 186, 189, 202] or Local Thermal Non-Equilibrium (LTNE) [18, 102, 103, 106, 141, 171, 178, 179, 184, 199-201]. LTE is widely used due to its simplicity, requiring only a single temperature model. However, Oliveira and Kaviany [203] noted that highly exothermic reactions (typical of smouldering combustion) may cause LTNE. In addition, heat transfer controls pyrolysis ahead of the smouldering front and cooling behind the front, with both affecting the energy balance at the reaction zone. Moreover, at high air fluxes smouldering can be extinguished by heat transfer processes [1, 31]. Thus, it is hypothesized here that a LTNE model is likely required for forced air smouldering of fuel embedded in an inert porous medium.

Smouldering numerical models in LTNE [103, 106, 141, 179, 184, 199-201] generally assumed heat transfer between phases based on Wakao et al. [122], Equation (2.9). Leach et al. [106] tested Wakao's correlation and concluded that Equation (2.9) incorrectly predicted LTE. Several other studies that applied LTNE based on other empirical correlations and sensitivity analysis on h_{sg} [102, 171, 178, 199, 200] showed small temperature difference between solid and gas phases, concluding that LTE can be assumed. To date, there is no h_{sg} correlation that correctly predicts LTNE in smouldering combustion.

The effect of heat losses on smouldering propagation were studied by [1, 27, 29, 102, 133, 137, 141, 171, 180, 184, 199, 202, 204]. Heat losses may have a substantial impact on the smouldering front. Model solution of a smouldering front in the absence of heat losses (or pyrolysis) could lead to peak temperatures that tend to increase indefinitely [1]. Two-dimensional models typically treat heat losses as boundary conditions [141, 171, 199], whereas one-dimensional models employ a global heat loss coefficient (U) [27, 102, 137, 180, 184]. Experimental and numerical work estimated that 42-50% of the energy released by oxidation is lost at the cell walls [29, 171]. This creates a curvature in the shape of the smouldering front, as shown in Figure 2.14. Martins et al. [29] experimentally measured the front curvature for forward (downward) smouldering, resulting in a concave shape (Figure 2.14a). Numerically, the front shape is identified by changing the heat loss coefficient (U), as shown in Figure 2.14b. Figure 2.14b shows a case of forward (downward) smouldering with and without heat losses. The convex shape in the front with heat losses indicates that near the wall, the smouldering front is quenched, whereas at the center-line, the front is mostly flat (similar to the shape without heat losses, Figure 2.14b – right) and propagates faster insulated from the surroundings [137, 171, 189, 199]. Note that, although both cases showed forward (downward) smouldering, the experimental shape of the smouldering front is different than the numerical. This is likely because in the experiment, channeling (not considered in the model) can favour the passage of air at the walls, or lower wall temperatures that results in higher gas density and faster front velocity [29]. In one-dimensional models, the global heat loss coefficient is typically adjusted to match the slope of the experimental temperature curve behind the front [27], Figure 2.15.
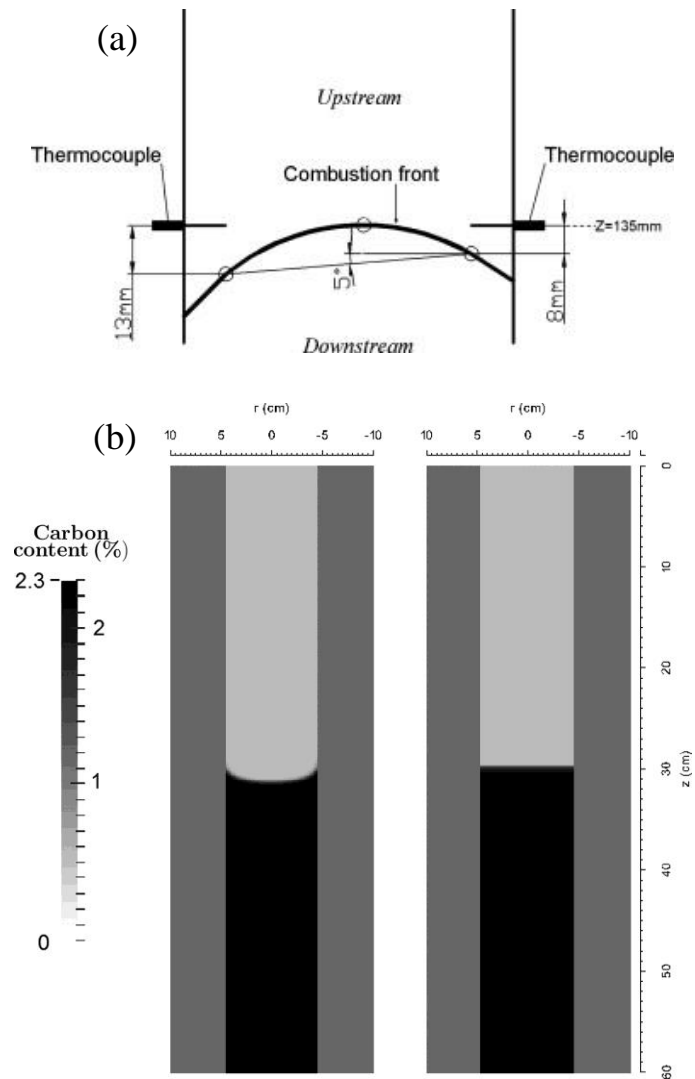
Figure 2.14: (a) Experimental curvature of the reaction front [29] for forward (downward) smouldering and (b) Numerical front curvature of the forward (downward) smouldering of carbon: (left) with heat losses and (right) without heat losses [171].
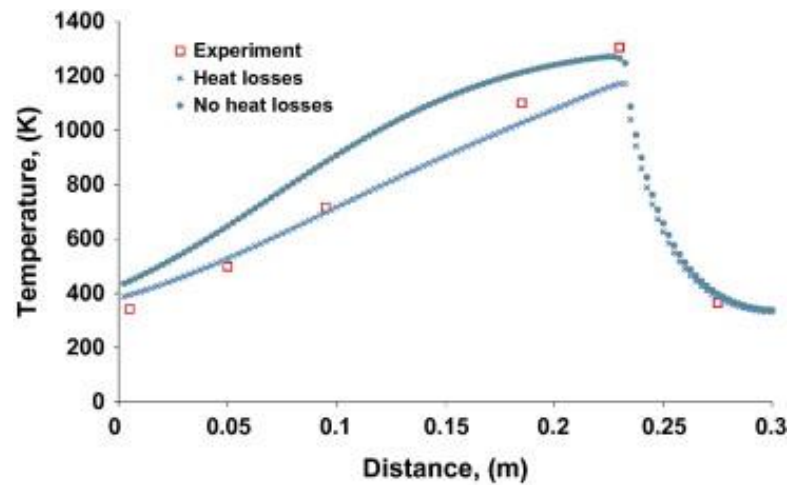
Figure 2.15: Temperature profile versus distance: (□) experimental and numerical results (x) with and (●) without heat losses [27].

Literature on numerical forward smouldering showed a linear relationship between peak temperature and front velocity with air flux [27, 106, 180]. Figure 2.16a describes numerical front velocities from Leach et al. [106] compared with experiments from Torero and Fernandez-Pello [23], and Figure 2.16b describes numerical predictions of the front velocity [180] compared with the analytical front velocity developed by Torero et al. [31], Equation (2.18). The numerical results in [180] agree well with the analytical model [31], except for extinction and high air fluxes.
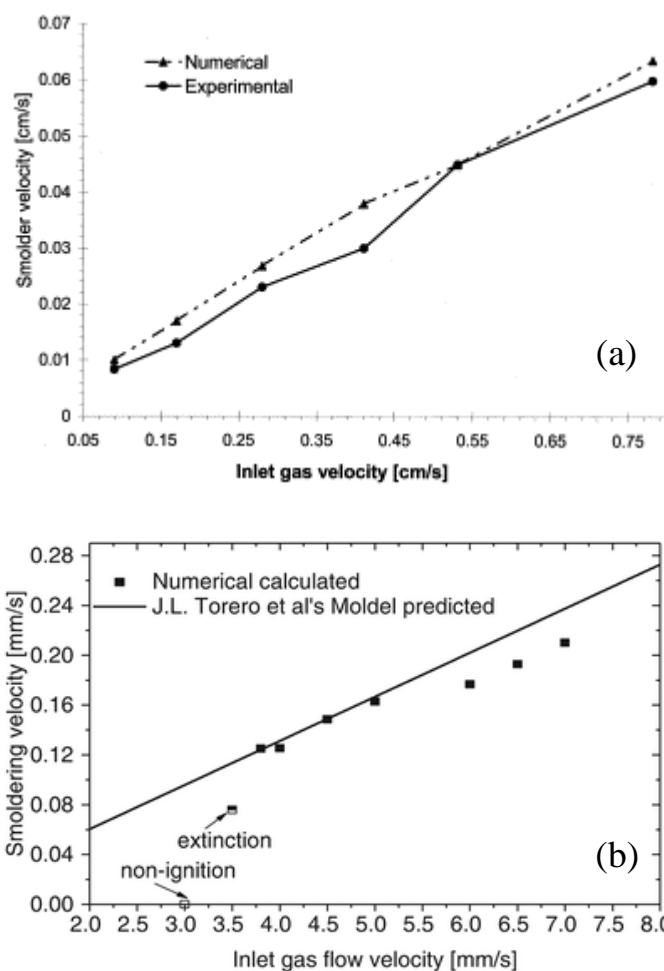
Figure 2.16: Front velocity versus air flux (a) [106] and (b) [180].

In opposed smouldering of solid porous fuels, numerical extinction by convective cooling at high air fluxes was found by [102, 136, 177-179, 202], agreeing with the experiments from Torero et al. [31]. Under oxygen-limited conditions (Figure 2.17), additional oxygen supply by the high air flux creates additional heat generation, which offsets the heat removed as the gas passes through the reaction front; smouldering velocity and peak temperature increase when air flux is increased. Under fuel-limited conditions, cold air passes through the hot sample, absorbing heat from the solid, decreasing the peak temperature and front velocity when air flux is further increased, causing extinction [106, 136, 177, 179, 184].
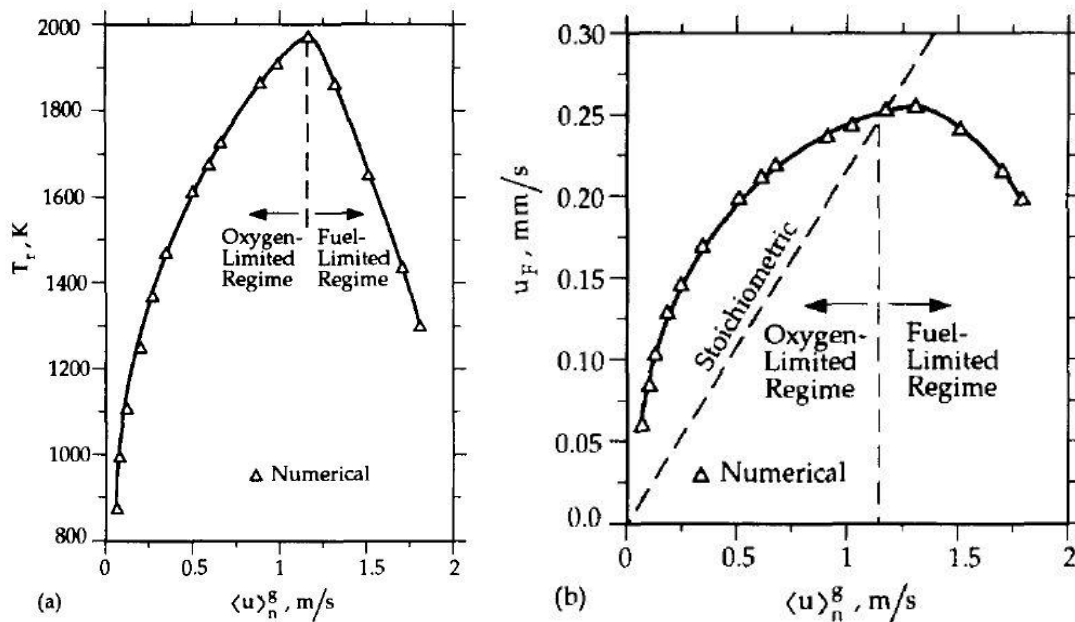
Figure 2.17: Predicted (a) adiabatic temperature and (b) the front velocity versus air flux for the oxygen- and fuel-limited regimes [136].

Literature also shows that extinction of the smouldering front occurs due to heat losses [133, 141, 180, 186] and low (oxygen-limited) air fluxes [102, 136, 177-180, 184]. Leach et al. [179] suggested that extinction was not linked to the dominance of pyrolysis reactions, whereas Lozinski and Buckmaster [202] indicated that pyrolysis needed to be introduced to proper simulate extinction.

Local chemical non-equilibrium between gas and solid phases, i.e., oxygen concentration in the bulk gas phase differs from that at the solid surface, was numerically studied [106, 136, 179, 184, 199] by employing Equations (2.12) and (2.13). Reaction rates are controlled by the rate at which oxygen can diffuse to the surface of the solid fuel by a solid-gas mass transfer coefficient (h_m) [136]. However, literature lacks in presenting the effects of h_m and bulk and surface oxygen concentrations on the smouldering front.

Most of the kinetic mechanisms proposed in Table 2.1 had the end goal of simply fitting kinetic reaction parameters against TG/DTG data without any application into numerical

models [205]. One-step oxidation reaction mechanism, Equation (2.19), is widely used in the smouldering literature [20, 128-130, 132, 133, 135, 136, 142, 171-175] due to its simplicity. Such global reactions assume that pyrolysis is negligible and only oxidation governs the process [20, 136]. It is very popular in analytical smouldering models [20, 128-130, 132, 133, 135, 136] and in models that investigate factors affecting the smouldering self-sustaining behaviour [174].

The absence of pyrolysis reactions in analytical models is understandable since more reactions introduce non-linearity in the governing equations. However, it is known that pyrolysis is an important energy sink near extinction, since large amount of fuel undergoes pyrolysis and its reaction rate is much higher than the oxidation one [1, 106, 178, 179, 182, 186, 202]. In addition, the understanding of pyrolysis is crucial to simulate ignition, propagation, and extinction of smouldering combustion [106, 140, 148, 179, 202, 206, 207].

Model solutions of a smouldering front in the absence of pyrolysis and heat losses show that the peak temperature tends to increase indefinitely as a result of a typically large heat of oxidation (ΔH_{oxid}). Thus, such one-step oxidation models [20, 128-130, 132, 133, 135, 136, 142, 171-175] may need to adjust ΔH_{oxid} to avoid extremely high temperatures. Moreover, numerical models usually neglect pyrolysis reactions based on the assumption that the heat of pyrolysis (ΔH_{pyr}) is relatively small when compared with the heat of oxidation (ΔH_{oxid}) [1, 20, 27, 128-130, 132, 133, 135, 136, 142, 171-177].

Moussa et al. [75] proposed a two-step mechanism with one pyrolysis and one oxidation for cellulosic materials. Other two-step mechanisms can be found in Table 2.1, Equations (2.20-2.23). Ohlemiller [1], and a few others later on, based on two exothermic peaks in DSC experiments (Figure 2.13), proposed a three-step mechanism defining smouldering as a competition between (endothermic) pyrolysis and fuel oxidation, Equation (2.23). Both reactions form char, which is completely or partially oxidized, resulting in self-sustained smouldering [1, 70, 137, 156, 167, 176, 178, 179, 187, 188, 196, 205, 208, 209]. Opposed smouldering research revealed that the smouldering front is governed mostly by the competition between pyrolysis and fuel oxidation (both reactions overlap to form a single front [102]) with negligible contribution of the char oxidation [1, 103, 136, 176, 178, 179].

In forward smouldering, oxidation and pyrolysis reactions form two distinct propagation fronts, with pyrolysis faster than oxidation. Moreover, char oxidation drives the front propagation [1, 184]. Forward smouldering is typically faster than opposed smouldering [102].

After Ohlemiller [1], Rein et al. [138] were the precursors of proposing more complex (realistic) kinetic mechanisms for polyurethane foams. Based on TG experiments, they concluded that a five-step mechanism (two pyrolysis and three oxidations, Equation (2.28)) would be more appropriate to simulate smouldering of polyurethane foam, since the inclusion of only one pyrolysis reaction to simulate two consecutive reactions paths would significantly under-estimate the production of char [184].

One of the reasons for disparities between experimental and numerical results in the smouldering of wet fuels (e.g., biomass, peat, etc.) was attributed to the lack of water evaporation in the kinetic mechanisms [102]. However, water evaporation is typically assumed as a chemical reaction [140, 141, 146, 165, 186, 200] rather than a phase-change process. Thus, most of the kinetic mechanisms including water evaporation when applied into smouldering combustion models are not able to capture the temperature plateau around 100 ºC. It is important to note that some fuels (e.g., peat) have a significant fraction of water and its movement by condensation and evaporation can alter the energy balance in the ignition, propagation, and extinction of the smouldering front [1, 186]. Another important parameter is the inorganic content in fuels such as peat and oil shale [27, 186].

Complex kinetic mechanisms with seven (Equation (2.32)) and eight (Equation (2.33)) reactions were used with the intention of predicting the transition to flaming [18, 182, 189], incorporating a secondary char oxidation [189] and one gas-phase oxidation [18]. More reactions have the tendency of fitting TG data with more precision. However, when employed into smouldering combustion models, these extra reactions produced negligible effects in the smouldering process. For example, Rein et al. [138] concluded that the oxidation of the virgin foam may be virtually neglected since all of it was converted to β-foam. In addition, β-foam was consumed by the oxidation reaction instead of its competing pyrolysis reaction. Another example can be found in [189], in which the model was very

sensitive to the first char oxidation but not sensitive to the final step of pyrolysis and final char oxidation.

It is important to note that, although the literature on kinetic parameters estimation is very extensive and well established, TG/DTG/DSC experiments use low and constant heating rates, whereas smouldering typically occurs at high heating rates (O[10^1-10^3 C/min)]) [140]. Such low heating rates favour some minor, low temperature reactions that most of the time disappear at high heating rates, causing some discrepancy in the calculation of the Arrhenius parameters. Moreover, the compensation effect (i.e., ln (A) has a linear relationship with E) may occur, especially in complex mechanisms, in which several reactions may have similar decomposition temperature intervals. The compensation effect may arise as a result of either the influence of experimental factors (e.g., heating rates) or the mathematical nature of the Arrhenius equation [27, 137, 148, 171, 196, 210-213]. Thus, some studies [106, 179] suggested that kinetic parameters associated with a specific reaction mechanism might have no fundamental physical meaning, and even if carefully estimated, they may have to be significantly changed in order to produce the best possible description of reality.

2.5   Conclusion

In this chapter we have presented the many advances in the fundamental understanding of forward and opposed smouldering combustion in the past 35 years. Smouldering, for most of the time, has been treated as a fire hazard, leading to property and environmental damages and death. Only recently, smouldering has been employed as an engineering technology in a wide range of applications from oil recovery to waste and contaminant destruction.

A large amount of fundamental research on smouldering was first devoted to solid porous reactive matrixes. Recently, liquid and solid fuels embedded in an inert porous matrix have also been objective of study. Together, they have successfully elucidated a number of heat and mass transfer processes in porous media. The main contributions are related to column-scale experiments coupled with numerical models. Experiments and numerical models were able to identify and understand important operational conditions such as peak

temperature and smouldering front velocity varying with air flux, fuel and oxygen concentrations. Moreover, there have also been significant advances in the understanding of heat losses, chemical reaction mechanisms (from simple to complex), smouldering extinction, smouldering in microgravity, and transition to flaming.

Despite the large number of advances and successes, there remain many gaps in the current fundamental understanding of smouldering. Although extensive research was devoted to chemical reaction mechanisms, it is still unclear the minimum number of pyrolysis and oxidation reactions necessary to properly simulate smouldering. The number of reactions will depend on the fuel and conditions analyzed (e.g., simple or complex hydrocarbons, heating rates, etc.). Moreover, literature does not well articulate how reactions are distributed in time and space. Numerical models still struggle to correctly simulate water evaporation, with most of the studies employing water evaporation as a chemical reaction instead of a phase-change process.

Literature also lacks in providing a satisfactory correlation to correctly predict heat transfer between solid and gas phases, i.e., local thermal non-equilibrium. Existing correlations were developed for conditions that are not applicable to smouldering combustion. Proper models for non-equilibrium are likely particularly important for simulating smouldering of liquid or solid fuels embedded in inert porous media. Likewise, numerical models have not yet performed a detailed analysis on the mass transfer between bulk and surface oxygen concentrations.

Smouldering propagation depends on a positive net energy balance in which energy added into the system needs to be higher than energy removed from the system. Thus, while literature provides some local energy balance methods, a global energy balance is also required to understand smouldering propagation and extinction. Furthermore, the understanding of heat losses under different experimental scales or multi-dimensional numerical models needs further investigation.

Finally, liquid fuel mobility has been proven to be challenge to understand with possible negative impact on waste and contaminant destruction. Thus, further experimental and numerical studies are necessary. Together, the above listed challenges represent a

significant opportunity for advances that will undoubtedly lead to more understanding of smouldering combustion. That, in turn, should assist bringing more smouldering applications from research to practice and optimization of engineered smouldering technologies.

2.6   References

[1] T.J. Ohlemiller, Modeling of smoldering combustion propagation, Progress in Energy and Combustion Science, 11(4) (1985) 277-310.

[2] P. Pironi, C. Switzer, G. Rein, A. Fuentes, J.I. Gerhard, J.L. Torero, Small-scale forward smouldering experiments for remediation of coal tar in inert media, Proceedings of the Combustion Institute, 32(2) (2009) 1957-1964.

[3] P. Pironi, C. Switzer, J.I. Gerhard, G. Rein, J.L. Torero, Self-Sustaining Smoldering Combustion for NAPL Remediation: Laboratory Evaluation of Process Sensitivity to Key Parameters, Environmental Science and Technology, 45(7) (2011) 2980-2986.

[4] G. Rein, Smouldering combustion phenomena in science and technology, International Review of Chemical Engineering, 1 (2009) 3-18.

[5] J.L. Torero, A.C. Fernandez-Pello, Natural convection smolder of polyurethane foam, upward propagation, Fire Safety Journal, 24(1) (1995) 35-52.

[6] D.C. Walther, A.C. Fernandez-Pello, D.L. Urban, Space shuttle based microgravity smoldering combustion experiments, Combustion and Flame, 116(3) (1999) 398-414.

[7] S.S. Dosanjh, P.J. Pagni, A.C. Fernandez-Pello, Forced cocurrent smoldering combustion, Combustion and Flame, 68(2) (1987) 131-142.

[8] J.B. Nielsen, Glowing Embers, (2006).

[9] S. Arya, Wife Draws On Cigarettes To Help Husband Stop Smoking, Morning News USA, Available in https://www.morningnewsusa.com/wife-draws-cigarettes-help-husband-stop-smoking-2381168.html [Accessed April 4, 2018], (2016).

[10] T.J. Ohlemiller, Smoldering Combustion, in: P.J. DiNenno, D. Drysdale, C.L. Beyler, W.D. Walton (Eds.) SFPE Handbook of Fire Protection Engineering, National Fire Protection Association, Quincy, MA, USA, 2002, pp. 200-210.

[11] G. Rein, S. Cohen, A. Simeoni, Carbon emissions from smouldering peat in shallow and strong fronts, Proceedings of the Combustion Institute, 32 II (2009) 2489-2496.

[12] J.G. Quintiere, M. Birky, F. Macdonald, G. Smith, An analysis of smoldering fires in closed compartments and their hazard due to carbon monoxide, Fire and Materials, 6(3-4) (1982) 99-110.

[13] D. Drysdale, Spontaneous Ignition within Solids and Smouldering Combustion, in: An Introduction to Fire Dynamics, John Wiley & Sons, Ltd, 2011, pp. 317-348.

[14] O. Putzeys, A. Bar-Ilan, G. Rein, A.C. Fernandez-Pello, D.L. Urban, The role of secondary char oxidation in the transition from smoldering to flaming, Proceedings of the Combustion Institute, 31(2) (2007) 2669-2676.

[15] O.M. Putzeys, A.C. Fernandez-Pello, G. Rein, D.L. Urban, The piloted transition to flaming in smoldering fire retarded and non-fire retarded polyurethane foam, Fire and Materials, 32(8) (2008) 485-499.

[16] A. Bar-Ilan, O.M. Putzeys, G. Rein, A.C. Fernandez-Pello, D.L. Urban, Transition from forward smoldering to flaming in small polyurethane foam samples, Proceedings of the Combustion Institute, 30(2) (2005) 2295-2302.

[17] S.D. Tse, A.C. Fernandez-Pello, K. Miyasaka, Controlling mechanisms in the transition from smoldering to flaming of flexible polyurethane foam, Symposium (International) on Combustion, 26(1) (1996) 1505-1513.

[18] A.B. Dodd, C. Lautenberger, C. Fernandez-Pello, Computational modeling of smolder combustion and spontaneous transition to flaming, Combustion and Flame, 159(1) (2012) 448-461.

[19] J.L. Torero, Buoyancy Effects on Smoldering of Polyurethane Foam, PhD, University of California at Berkeley, Mechanical Engineering, 1992.

[20] S. Dosanjh, J. Peterson, A.C. Fernandez-Pello, P.J. Pagni, Buoyancy effects on smoldering combustion, Acta Astronautica, 13(11) (1986) 689-696.

[21] F. He, F. Behrendt, Experimental investigation of natural smoldering of char granules in a packed bed, Fire Safety Journal, 46(7) (2011) 406-413.

[22] F. He, W. Yi, Y. Li, J. Zha, B. Luo, Effects of fuel properties on the natural downward smoldering of piled biomass powder: Experimental investigation, Biomass and Bioenergy, 67(0) (2014) 288-296.

[23] J.L. Torero, A.C. Fernandez-Pello, Forward smolder of polyurethane foam in a forced air flow, Combustion and Flame, 106(1–2) (1996) 89-109.

[24] A. Bar-Ilan, G. Rein, A.C. Fernandez-Pello, J.L. Torero, D.L. Urban, Forced forward smoldering experiments in microgravity, Experimental Thermal and Fluid Science, 28(7) (2004) 743-751.

[25] T.J. Ohlemiller, Forced smolder propagation and the transition to flaming in cellulosic insulation, Combustion and Flame, 81(3–4) (1990) 354-365.

[26] C. Switzer, J.I. Gerhard, P. Pironi, G. Rein, J.L. Torero, Self-sustaining smouldering combustion: A novel remediation process for non-aqueous phase liquids in porous media, Environmental Science and Technology, 43 (2009) 5871-5877.

[27] H. Fadaei, M. Sennoune, S. Salvador, A. Lapene, G. Debenest, Modelling of non-consolidated oil shale semi-coke forward combustion: Influence of carbon and calcium carbonate contents, Fuel, 95(0) (2012) 197-205.

[28] M. Sennoune, S. Salvador, M. Quintard, Toward the Control of the Smoldering Front in the Reaction-Trailing Mode in Oil Shale Semicoke Porous Media, Energy & Fuels, 26(6) (2012) 3357-3367.

[29] M.F. Martins, S. Salvador, J.F. Thovert, G. Debenest, Co-current combustion of oil shale - Part 2: Structure of the combustion front, Fuel, 89(1) (2010) 133-143.

[30] T.J. Ohlemiller, D.A. Lucca, An experimental comparison of forward and reverse smolder propagation in permeable fuel beds, Combustion and Flame, 54(1–3) (1983) 131-147.

[31] J.L. Torero, A.C. Fernandez-Pello, M. Kitano, Opposed Forced Flow Smoldering of Polyurethane Foam, Combustion Science and Technology, 91(1-3) (1993) 95-117.

[32] L. Kinsman, J.L. Torero, J.I. Gerhard, Organic liquid mobility induced by smoldering remediation, Journal of Hazardous materials, 325 (2017) 101-112.

[33] A. Bar-Ilan, G. Rein, D.C. Walther, A.C. Fernandez-Pello, J.L. Torero, D.L. Urban, The effect of buoyancy on opposed smoldering, Combustion Science and Technology, 176(12) (2004) 2027-2055.

[34] G. Rein, Smoldering combustion, in: SFPE Handbook of Fire Protection Engineering, Fifth Edition, 2016, pp. 581-603.

[35] G. Debenest, V. Mourzenko, J. Thovert, Smouldering in fixed beds of oil shale grains. A three-dimensional microscale numerical model, Combustion Theory and Modelling, 9(1) (2005) 113-135.

[36] L. Yermán, R.M. Hadden, J. Carrascal, I. Fabris, D. Cormier, J.L. Torero, J.I. Gerhard, M. Krajcovic, P. Pironi, Y.-L. Cheng, Smouldering combustion as a treatment technology for faeces: Exploring the parameter space, Fuel, 147 (2015) 108-116.

[37] A.W. Bhutto, A.A. Bazmi, G. Zahedi, Underground coal gasification: From fundamentals to applications, Progress in Energy and Combustion Science, 39(1) (2013) 189-214.

[38] J.-P. Vantelon, B. Lodeho, S. Pignoux, J.L. Ellzey, J.L. Torero, Experimental observations on the thermal degradation of a porous bed of tires, Proceedings of the Combustion Institute, 30(2) (2005) 2239-2246.

[39] P. Pironi, Smouldering combustion of liquids in porous media for remediating NAPL-contaminated soils, PhD Thesis, University of Edinburgh, Edinburgh, Scotland, UK, 2009.

[40] C. Switzer, P. Pironi, J.I. Gerhard, G. Rein, J.L. Torero, Self-sustaining smoldering combustion: A novel remediation process for non-aqueous-phase liquids in porous media, Environmental Science and Technology, 43(15) (2009) 5871-5877.

[41] F.A.F. Monhol, M.F. Martins, Cocurrent Combustion of Human Feces and Polyethylene Waste, Waste and Biomass Valorization, 6(3) (2015) 425-432.

[42] T.L. Rashwan, J.I. Gerhard, G.P. Grant, Application of self-sustaining smouldering combustion for the destruction of wastewater biosolids, Waste Management, 50 (2016) 201-212.

[43] F. Clarke, J. Ottoson, Fire death scenarios and fire safety planning, Fire Journal, 70(3) (1976) 20–22, 117–118.

[44] H. Hotta, Y. Oka, O. Sugawa, Interaction between hot layer and updraft from a smoldering fire source-Part I An experimental approach, Fire Science and Technology, 7(2) (1987) 17-25.

[45] J.-I. Watanabe, T. Tanaka, Experimental Investigation into Penetration of a Weak Fire Plume into a Hot Upper Layer, Journal of Fire Sciences, 22(5) (2004) 405-420.

[46] S.E. Page, F. Siegert, J.O. Rieley, H.-D.V. Boehm, A. Jaya, S. Limin, The amount of carbon released from peat and forest fires in Indonesia during 1997, Nature, 420 (2002) 61.

[47] I. Bertschi, Trace gas and particle emissions from fires in large diameter and belowground biomass fuels, Journal of Geophysical Research, 108 (2003) 8472.

[48] G. Rein, N. Cleaver, C. Ashton, P. Pironi, J.L. Torero, The severity of smouldering peat fires and damage to the forest soil, CATENA, 74 (2008) 304-309.

[49] X. Huang, G. Rein, Interactions of Earth's atmospheric oxygen and fuel moisture in smouldering wildfires, Science of the Total Environment, 572 (2016) 1440-1446.

[50] J.L. Urban, C.D. Zak, J. Song, C. Fernandez-Pello, Smoldering spot ignition of natural fuels by a hot metal particle, Proceedings of the Combustion Institute, 36(2) (2017) 3211-3218.

[51] G. Rein, Chapter 17 - Smoldering Combustion Phenomena and Coal Fires, in: G.B. Stracher, A. Prakash, E.V. Sokol (Eds.) Coal and Peat Fires: A Global Perspective, Elsevier, Amsterdam, 2011, pp. 307-315.

[52] C. Zaccone, G. Rein, V. D'Orazio, R.M. Hadden, C.M. Belcher, T.M. Miano, Smouldering fire signatures in peat and their implications for palaeoenvironmental reconstructions, Geochimica et Cosmochimica Acta, 137 (2014) 134-146.

[53] M.A. Nolter, D.H. Vice, Looking back at the Centralia coal fire: a synopsis of its present status, International Journal of Coal Geology, 59(1) (2004) 99-106.

[54] G.B. Stracher, T.P. Taylor, Coal fires burning out of control around the world: thermodynamic recipe for environmental catastrophe, International Journal of Coal Geology, 59(1) (2004) 7-17.

[55] N.H. Jafari, T.D. Stark, T. Thalhamer, Spatial and temporal characteristics of elevated temperatures in municipal solid waste landfills, Waste Management, 59 (2017) 286-301.

[56] F. Restuccia, N. Ptak, G. Rein, Self-heating behavior and ignition of shale rock, Combustion and Flame, 176 (2017) 213-219.

[57] F. Restuccia, X. Huang, G. Rein, Self-ignition of natural fuels: Can wildfires of carbon-rich soil start by self-heating?, Fire Safety Journal, 91 (2017) 828-834.

[58] N. Dräger, A. Brauer, B. Brademann, R. Tjallingii, M. Słowiński, M. Błaszkiewicz, N. Schlaak, Spontaneous self-combustion of organic-rich lateglacial lake sediments after freeze-drying, Journal of Paleolimnology, (2016) 1-10.

[59] D. Wu, X. Huang, F. Norman, F. Verplaetsen, J. Berghmans, E. Van den Bulck, Experimental investigation on the self-ignition behaviour of coal dust accumulations in oxy-fuel combustion system, Fuel, 160 (2015) 245-254.

[60] M. Della Zassa, A. Biasin, M. Zerlottin, D. Refosco, P. Canu, Self-heating of dried industrial wastewater sludge: Lab-scale investigation of supporting conditions, Waste Management, 33(6) (2013) 1469-1477.

[61] R. Friedman, Fire Safety in Extraterrestrial Environments, in: Space 98, ASCE, 1998.

[62] F. Fiorino, Lessons From Swissair Crash, Aviation Week & Space Technology, 158 (2003) 62.

[63] D. Walther, A. Fernandez-Pello, D. Urban, Smoldering combustion experiments in microgravity, in: 36th AIAA Aerospace Sciences Meeting and Exhibit, American Institute of Aeronautics and Astronautics, 1998.

[64] J.L. Torero, Smoldering: The Fire Scenario, University of Maryland, USA, 1999.

[65] G. Rein, N. Cleaver, C. Ashton, P. Pironi, J.L. Torero, The severity of smouldering peat fires and damage to the forest soil, CATENA, 74(3) (2008) 304-309.

[66] S. Zhang, The World's Oldest Underground Fire Has Been Burning For 6,000 Years, GIZMODO, Available in https://gizmodo.com/the-worlds-oldest-underground-fire-has-been-burning-fo-1539049759 [Accessed in April 6 2018], (2014).

[67] R.E. Rogers, T.J. Ohlemiller, Smolder Characteristics of Flexible Polyurethane Foams, The Journal of fire & flammability, 11(1) (1980) 32-44.

[68] M.K. Anderson, R.T. Sleight, J.L. Torero, Ignition signatures of a downward smolder reaction, Experimental Thermal and Fluid Science, 21(1–3) (2000) 33-40.

[69] J.L. Torero, A.C. Fernandez-Pello, D. Urban, Experimental observations of the effect of gravity changes on smoldering combustion, AIAA Journal, 32(5) (1994) 991-996.

[70] R.M. Hadden, G. Rein, C.M. Belcher, Study of the competing chemical reactions in the initiation and spread of smouldering combustion in peat, Proceedings of the Combustion Institute, 34(2) (2013) 2547-2553.

[71] T.J. Ohlemiller, Smoldering combustion propagation on solid wood, Fire Safety Science, 3 (1991) 565-574.

[72] A. Egerton, K. Gugan, F.J. Weinberg, The mechanism of smouldering in cigarettes, Combustion and Flame, 7(0) (1963) 63-78.

[73] M. Summerfield, T.J. Ohlemiller, H.W. Sandusky, A thermophysical mathematical model of steady-draw smoking and predictions of overall cigarette behavior, Combustion and Flame, 33 (1978) 263-279.

[74] A. Bar-Ilan, G. Rein, A.C. Fernandez-Pello, J.L. Torero, D.L. Urban, Forced forward smoldering experiments in microgravity, Experimental Thermal and Fluid Science, 28 (2004) 743-751.

[75] N.A. Moussa, T.Y. Toong, C.A. Garris, Mechanism of smoldering of cellulosic materials, Symposium (International) on Combustion, 16(1) (1977) 1447-1457.

[76] W.H. Frandsen, The influence of moisture and mineral soil on the combustion limits of smoldering forest duff, Canadian Journal of Forest Research, 17(12) (1987) 1540-1544.

[77] X. Huang, F. Restuccia, M. Gramola, G. Rein, Experimental study of the formation and collapse of an overhang in the lateral spread of smouldering peat fires, Combustion and Flame, (2016).

[78] R. Hadden, G. Rein, Ignition and suppression of smouldering coal fires in small-scale experiments, in: 6th Mediterranean Combustion Symposium, Ajaccio, Corsica, France, 2009.

[79] T.C. Ooi, D. Thompson, D.R. Anderson, R. Fisher, T. Fray, M. Zandi, The effect of charcoal combustion on iron-ore sintering performance and emission of persistent organic pollutants, Combustion and Flame, 158(5) (2011) 979-987.

[80] Z. Cheng, J. Yang, L. Zhou, Y. Liu, Q. Wang, Characteristics of charcoal combustion and its effects on iron-ore sintering performance, Applied Energy, 161 (2016) 364-374.

[81] S. Bagci, Estimation of Combustion Zone Thickness during In Situ Combustion Processes, Energy & Fuels, 12(6) (1998) 1153-1160.

[82] M. Kumar, A.M. Garon, An experimental investigation of the fireflooding combustion zone, Journal Name: SPE (Society of Petroleum Engineers) Reservoir Engineering; (United States); Journal Volume: 6:1, (1991) Medium: X; Size: Pages: 55-61.

[83] L.M. Castanier, W.E. Brigham, Upgrading of crude oil via in situ combustion, Journal of Petroleum Science and Engineering, 39(1-2) (2003) 125-136.

[84] A.S. Bagci, Wet Forward Combustion for Heavy Oil Recovery, Energy Sources, Part A: Recovery, Utilization, and Environmental Effects, 28(3) (2006) 221-232.

[85] A.M. Garon, M. Kumar, K.K. Lau, M.D. Sherman, A laboratory investigation of sweep during oxygen and air fireflooding, SPE Reservoir Engineering, 1(6) (1986) 565-574.

[86] T.X. Xia, M. Greaves, A.T. Turta, C. Ayasse, THAI—A 'short-distance displacement' in situ combustion process for the recovery and upgrading of heavy oil, Chemical Engineering Research and Design, 81(3) (2003) 295-304.

[87] T.X. Xia, M. Greaves, In Situ Upgrading of Athabasca Tar Sand Bitumen Using Thai, Chemical Engineering Research and Design, 84(9) (2006) 856-864.

[88] G. Rein, X. Huang, F. Restuccia, T. McArdle, Detection of landmines in peat soils by controlled smouldering combustion: Experimental proof of concept of O-Revealer, Experimental Thermal and Fluid Science, 88 (2017) 632-638.

[89] M. Sennoune, S. Salvador, M. Quintard, Reducing CO2 emissions from oil shale semicoke smoldering combustion by varying the carbonate and fixed carbon contents, Combustion and Flame, 158(11) (2011) 2272-2282.

[90] C. Switzer, P. Pironi, J.I. Gerhard, G. Rein, J.L. Torero, Volumetric scale-up of smouldering remediation of contaminated materials, Journal of Hazardous materials, 268 (2014) 51-60.

[91] G.C. Scholes, J.I. Gerhard, G.P. Grant, D.W. Major, J.E. Vidumsky, C. Switzer, J.L. Torero, Smoldering Remediation of Coal-Tar-Contaminated Soil: Pilot Field Tests of STAR, Environmental Science & Technology, 49(24) (2015) 14334-14342.

[92] M. Salman, J.I. Gerhard, D.W. Major, P. Pironi, R. Hadden, Remediation of trichloroethylene-contaminated soils by star technology using vegetable oil smoldering, Journal of Hazardous materials, 285 (2015) 346-355.

[93] L. Yermán, D. Cormier, I. Fabris, J. Carrascal, J.L. Torero, J.I. Gerhard, Y.L. Cheng, Potential Bio-oil Production from Smouldering Combustion of Faeces, Waste and Biomass Valorization, (2016) 1-10.

[94] I. Fabris, D. Cormier, J.I. Gerhard, T. Bartczak, M. Kortschot, J.L. Torero, Y.-L. Cheng, Continuous, self-sustaining smouldering destruction of simulated faeces, Fuel, 190 (2017) 58-66.

[95] L. Yermán, H. Wall, J.L. Torero, Experimental investigation on the destruction rates of organic waste with high moisture content by means of self-sustained smoldering combustion, Proceedings of the Combustion Institute, 36(3) (2017) 4419-4426.

[96] J.L. Torero, J.I. Gerhard, L.L. Kinsman, L. Yermán, 18 - Using fire to remediate contaminated soils, in: M.S. Blinderman, A.Y. Klimenko (Eds.) Underground Coal Gasification and Combustion, Woodhead Publishing, 2018, pp. 601-625.

[97] L. Yermán, H. Wall, J. Torero, J.I. Gerhard, Y.L. Cheng, Smoldering Combustion as a Treatment Technology for Feces: Sensitivity to Key Parameters, Combustion Science and Technology, 188(6) (2016) 968-981.

[98] STAR, Self-Sustaining Smoldering Treatment for Active Remediation. Available in http://www.savronsolutions.com [Accessed March 21, 2018].

[99] G.P. Grant, D. Major, G.C. Scholes, J. Horst, S. Hill, M.R. Klemmer, J.N. Couch, Smoldering Combustion (STAR) for the Treatment of Contaminated Soils: Examining Limitations and Defining Success, Remediation Journal, 26(3) (2016) 27-51.

[100] P.S. Sarathi, In-situ combustion handbook: Principles and practices, National Petroleum Technology Office, 1999.

[101] M. Sennoune, S. Salvador, G. Debenest, Impact of a CO2-Enriched Gas on the Decarbonation of CaCO3 and the Oxidation of Carbon in the Smoldering Process of Oil Shale Semicoke, Energy & Fuels, 26 (2011) 391-399.

[102] G. Rein, A. Carlos Fernandez-Pello, D.L. Urban, Computational model of forward and opposed smoldering combustion in microgravity, Proceedings of the Combustion Institute, 31(2) (2007) 2677-2684.

[103] B.-s. Jia, M.-z. Xie, H. Liu, Numerical study on the propagation characteristics of forward smoldering in a cellulosic packed bed, Journal of Shanghai University (English Edition), 12(2) (2008) 171-179.

[104] X. Huang, G. Rein, H. Chen, Computational smoldering combustion: Predicting the roles of moisture and inert contents in peat wildfires, Proceedings of the Combustion Institute, (2014).

[105] H. Zhang, W.-Z. Fang, Y.-M. Li, W.-Q. Tao, Experimental study of the thermal conductivity of polyurethane foams, Applied Thermal Engineering, 115 (2017) 528-538.

[106] S.V. Leach, G. Rein, J.L. Ellzey, O.A. Ezekoye, J.L. Torero, Kinetic and fuel property effects on forward smoldering, Combustion and Flame, 120(3) (2000) 346-358.

[107] W.-Y. Jang, A.M. Kraynik, S. Kyriakides, On the microstructure of open-cell foams and its effect on elastic properties, International Journal of Solids and Structures, 45(7–8) (2008) 1845-1875.

[108] Zeiss, Oil Sand Microstructure in, Accessed August 27, 2014.

[109] R.H. Perry, D.W. Green, Perry's Chemical Engineers' Handbook, 7th ed., McGraw-Hill, New York, USA, 1999.

[110] P. Chambrion, R. Bertau, P. Ehrburger, Effect of polar components on the physico-chemical properties of coal tar, Fuel, 74(9) (1995) 1284-1290.

[111] L.-n. Han, R. Zhang, J.-c. Bi, Upgrading of coal-tar pitch in supercritical water, Journal of Fuel Chemistry and Technology, 36(1) (2008) 1-5.

[112] K. Brill, MassDEP Releases Long-Awaited LNAPL Guidance, Law & The Environment, Available in http://www.lawandenvironment.com/2016/02/24/massdep-releases-long-awaited-lnapl-guidance/ [Accessed April 24, 2018], (2016).

[113] M.L. Hobbs, P.T. Radulovic, L.D. Smoot, Combustion and gasification of coals in fixed-beds, Progress in Energy and Combustion Science, 19(6) (1993) 505-586.

[114] G. Debenest, V.V. Mourzenko, J.F. Thovert, Smouldering in fixed beds of oil shale grains: governing parameters and global regimes, TCTM, 9(2) (2005) 301-321.

[115] S. Whitaker, Improved constraints for the principle of local thermal equilibrium, Industrial & Engineering Chemistry Research, 30(5) (1991) 983-997.

[116] M. Kaviany, Principles of Heat Transfer in Porous Media, Springer, 1995.

[117] A. Bejan, Mass Transfer, Convection heat transfer: John Wiley & Sons, Incorporated, 1995.

[118] H. Darcy, Les fontaines publiques de la ville de Dijon: Exposition et application des principes a suivre et des formules a employer dans les questions de distribution d'eau; ouvrage terminé par un appendice relatif aux fournitures d'eau de plusieurs villes au filtrage des eaux et a la fabrication des tuyaux de fonte, de plomb, de tole et de bitume. Atlas, Victor Dalmont, Libraire des Corps imperiaux des ponts et chaussées et des mines, 1856.

[119] É. Clapeyron, Mémoire sur la puissance motrice de la chaleur, Jacques Gabay, 1834.

[120] J. Bear, Dynamics of Fluids in Porous Media, Dover, 1988.

[121] D.A.A. Nield, A.A. Bejan, Heat Transfer through a Porous Medium, 2nd ed., Convection in Porous Media: Springer Verlag, 1999.

[122] N. Wakao, S. Kaguei, T. Funazkri, Effect of fluid dispersion coefficients on particle-to-fluid heat transfer coefficients in packed beds: Correlation of nusselt numbers, Chemical Engineering Science, 34(3) (1979) 325-336.

[123] K.H. Coats, B.D. Smith, Dead-End Pore Volume and Dispersion in Porous Media, Society of Petroleum Engineers Journal, 4(1) (1964) 73-84.

[124] M.T. Van Genuchten, P. Wierenga, Mass transfer studies in sorbing porous media I. Analytical solutions, Soil Science Society of America Journal, 40(4) (1976) 473-480.

[125] L. Li, D.A. Barry, P.J. Cuiligan-Hensley, K. Bajracharya, Mass transfer in soils with local stratification of hydraulic conductivity, Water Resources Research, 30(11) (1994) 2891-2900.

[126] T. Samardzioska, V. Popov, Numerical comparison of the equivalent continuum, non-homogeneous and dual porosity models for flow and transport in fractured porous media, Advances in Water Resources, 28(3) (2005) 235-255.

[127] F.P. Incropera, Fundamentals of heat and mass transfer, John Wiley, 2007.

[128] D.A. Schult, B.J. Matkowsky, V.A. Volpert, A.C. Fernandez-Pello, Propagation and extinction of forced opposed flow smolder waves, Combustion and Flame, 101(4) (1995) 471-490.

[129] D.A. Schult, B.J. Matkowsky, V.A. Volpert, A.C. Fernandez-Pello, Forced forward smolder combustion, Combustion and Flame, 104(1–2) (1996) 1-26.

[130] A.P. Aldushin, I.E. Rumanov, B.J. Matkowsky, Maximal energy accumulation in a superadiabatic filtration combustion wave, Combustion and Flame, 118(1–2) (1999) 76-90.

[131] G. Debenest, Simulation numérique 3D, à la microéchelle, de la combustion en lit fixe de schistes bitumineux, Tese de doutorado da Universidade de Poitiers, (2003).

[132] A.A. Mailybaev, J. Bruining, D. Marchesin, Analysis of in situ combustion of oil with pyrolysis and vaporization, Combustion and Flame, 158(6) (2011) 1097-1108.

[133] I.Y. Akkutlu, Y.C. Yortsos, The dynamics of in-situ combustion fronts in porous media, Combustion and Flame, 134(3) (2003) 229-247.

[134] M.F. Martins, The structure of a combustion front propagating in a fixed bed of crushed oil shale: co-current configuration, PhD Thesis, Université de Toulouse, 2008.

[135] N.C. Roy, Y. Nakamura, Investigation of unsteady behaviors of forward and opposed flow combustion of solid fuel, Combustion and Flame, 163 (2016) 517-531.

[136] M. Fatehi, M. Kaviany, Adiabatic reverse combustion in a packed bed, Combustion and Flame, 99(1) (1994) 1-17.

[137] C. Di Blasi, Mechanisms of two-dimensional smoldering propagation through packed fuel beds, Combustion Science and Technology, 106(1-3) (1995) 103-124.

[138] G. Rein, C. Lautenberger, A.C. Fernandez-Pello, J.L. Torero, D.L. Urban, Application of genetic algorithms and thermogravimetry to determine the kinetics of polyurethane foam in smoldering combustion, Combustion and Flame, 146(1-2) (2006) 95-108.

[139] X. Huang, G. Rein, Smouldering combustion of peat in wildfires: Inverse modelling of the drying and the thermal and oxidative decomposition kinetics, Combustion and Flame, 161(6) (2014) 1633-1644.

[140] X. Huang, G. Rein, Thermochemical conversion of biomass in smouldering combustion across scales: The roles of heterogeneous kinetics, oxygen and transport phenomena, Bioresource Technology, 207 (2016) 409-421.

[141] J. Yang, H. Chen, N. Liu, Modeling of Two-Dimensional Natural Downward Smoldering of Peat, Energy & Fuels, 30(10) (2016) 8765-8775.

[142] C. Yang, J.F. Thovert, G. Debenest, Upscaling of mass and thermal transports in porous media with heterogeneous combustion reactions, International Journal of Heat and Mass Transfer, 84 (2015) 862-875.

[143] J.S. Tumuluru, S. Sokhansanj, J.R. Hess, C.T. Wright, R.D. Boardman, A review of biomass torrefaction process and product properties for energy applications, Industrial biotechnology, 7(5) (2011) 384-401.

[144] X. Huang, G. Rein, Computational smoldering combustion: Interactions of atmospheric oxygen and fuel moisture in peat fires, in: 2016 Spring Technical Meeting of the Western States Section of the Combustion Institute, WSSCI 2016, 2016.

[145] C. Lautenberger, C. Fernandez-Pello, Generalized pyrolysis model for combustible solids, Fire Safety Journal, 44(6) (2009) 819-839.

[146] J. Yang, H. Chen, W. Zhao, J. Zhou, Combustion kinetics and emission characteristics of peat by using TG-FTIR technique, Journal of Thermal Analysis and Calorimetry, 124(1) (2016) 519-528.

[147] W. Zhao, H. Chen, N. Liu, J. Zhou, Thermogravimetric analysis of peat decomposition under different oxygen concentrations, Journal of Thermal Analysis and Calorimetry, 117(1) (2014) 489-497.

[148] K.-Y. Li, X. Huang, C. Fleischmann, G. Rein, J. Ji, Pyrolysis of Medium-Density Fiberboard: Optimized Search for Kinetics Scheme and Parameters via a Genetic Algorithm Driven by Kissinger's Method, Energy & Fuels, 28(9) (2014) 6130-6139.

[149] J.-L. Dirion, C. Reverte, M. Cabassud, Kinetic parameter estimation from TGA: Optimal design of TGA experiments, Chemical Engineering Research and Design, 86(6) (2008) 618-625.

[150] C. Branca, A. Albano, C. Di Blasi, Critical evaluation of global mechanisms of wood devolatilization, Thermochimica Acta, 429(2) (2005) 133-141.

[151] M. Cardona, D.C. Boffito, G.S. Patience, Thermogravimetric heat and mass transfer: Modeling of bitumen pyrolysis, Fuel, 143 (2015) 253-261.

[152] J. Zhao, X. Huang, T. Xu, Combustion mechanism of asphalt binder with TG–MS technique based on components separation, Construction and Building Materials, 80 (2015) 125-131.

[153] P. Liu, M. Zhu, Z. Zhang, W. Wan, S. Yani, D. Zhang, Thermogravimetric Studies of Characteristics and Kinetics of Pyrolysis of Buton Oil Sand, Energy Procedia, 61 (2014) 2741-2744.

[154] A.N. Pereira, O.V. Trevisan, Thermoanalysis and reaction kinetics of heavy oil combustion, Journal of the Brazilian Society of Mechanical Sciences and Engineering, 36(2) (2014) 393-401.

[155] A.S. Gundogar, M.V. Kok, Thermal characterization, combustion and kinetics of different origin crude oils, Fuel, 123 (2014) 59-65.

[156] C. Fan, C. Zan, Q. Zhang, D. Ma, Y. Chu, H. Jiang, L. Shi, F. Wei, The oxidation of heavy oil: Thermogravimetric analysis and non-isothermal kinetics using the distributed activation energy model, Fuel Processing Technology, 119 (2014) 146-150.

[157] J. Yan, X. Jiang, X. Han, J. Liu, A TG–FTIR investigation to the catalytic effect of mineral matrix in oil shale on the pyrolysis and combustion of kerogen, Fuel, 104 (2013) 307-317.

[158] M. Al-Harahsheh, O. Al-Ayed, J. Robinson, S. Kingman, A. Al-Harahsheh, K. Tarawneh, A. Saeid, R. Barranco, Effect of demineralization and heating rate on the pyrolysis kinetics of Jordanian oil shales, Fuel Processing Technology, 92(9) (2011) 1805-1811.

[159] F. Trejo, M.S. Rana, J. Ancheyta, Thermogravimetric determination of coke from asphaltenes, resins and sediments and coking kinetics of heavy crude asphaltenes, Catalysis Today, 150(3–4) (2010) 272-278.

[160] T. Xu, X. Huang, Study on combustion mechanism of asphalt binder by using TG–FTIR technique, Fuel, 89(9) (2010) 2185-2190.

[161] O.O. Sonibare, R. Egashira, T.A. Adedosu, Thermo-oxidative reactions of Nigerian oil sand bitumen, Thermochimica Acta, 405(2) (2003) 195-205.

[162] A.G. Barneto, J.A. Carmona, M.J.F. Garrido, Thermogravimetric assessment of thermal degradation in asphaltenes, Thermochimica Acta, 627–629 (2016) 1-8.

[163] M.C. Merola, C. Carotenuto, V. Gargiulo, F. Stanzione, A. Ciajolo, M. Minale, Chemical–physical analysis of rheologically different samples of a heavy crude oil, Fuel Processing Technology, 148 (2016) 236-247.

[164] A. Al-Otoom, M. Al-Harahsheh, M. Allawzi, S. Kingman, J. Robinson, A. Al-Harahsheh, A. Saeid, Physical and thermal properties of Jordanian tar sand, Fuel Processing Technology, 106 (2013) 174-180.

[165] M.A. Bazelatto Zanoni, H. Massard, M. Ferreira Martins, Formulating and optimizing a combustion pathways for oil shale and its semi-coke, Combustion and Flame, 159(10) (2012) 3224-3234.

[166] L. Jiang, H.-H. Xiao, J.-J. He, Q. Sun, L. Gong, J.-H. Sun, Application of genetic algorithm to pyrolysis of typical polymers, Fuel Processing Technology, 138 (2015) 48-55.

[167] M.A. Varfolomeev, A. Galukhin, D.K. Nurgaliev, M.V. Kok, Thermal decomposition of Tatarstan Ashal'cha heavy crude oil and its SARA fractions, Fuel, 186 (2016) 122-127.

[168] K.K. Bissada, J. Tan, E. Szymczyk, M. Darnell, M. Mei, Group-type characterization of crude oil and bitumen. Part I: Enhanced separation and quantification of saturates, aromatics, resins and asphaltenes (SARA), Organic Geochemistry, 95 (2016) 21-28.

[169] M. Mouazen, A. Poulesquen, F. Bart, J. Masson, M. Charlot, B. Vergnes, Rheological, structural and chemical evolution of bitumen under gamma irradiation, Fuel Processing Technology, 114 (2013) 144-153.

[170] J. Leifeld, Thermal stability of black carbon characterised by oxidative differential scanning calorimetry, Organic Geochemistry, 38(1) (2007) 112-127.

[171] V. Pozzobon, G. Baud, S. Salvador, G. Debenest, Darcy Scale Modeling of Smoldering: Impact of Heat Loss, Combustion Science and Technology, 189(2) (2017) 340-365.

[172] G. Debenest, V.V. Mourzenko, J.F. Thovert, Three-dimensional microscale numerical simulation of smoldering process in heterogeneous porous media, Combustion Science and Technology, 180(12) (2008) 2170-2185.

[173] G. Debenest, V.V. Mourzenko, J.F. Thovert, Smouldering in fixed beds of oil shale grains. A three-dimensional microscale numerical model, Combustion Theory and Modelling, 9(1) (2005) 113-135.

[174] H. Chen, G. Rein, N. Liu, Numerical investigation of downward smoldering combustion in an organic soil column, International Journal of Heat and Mass Transfer, 84(0) (2015) 253-261.

[175] H. van Kuijk, J. van Oijen, R. Bastiaans, P. de Goey, Reverse combustion: Kinetically controlled and mass transfer controlled conversion front structures, Combustion and Flame, 153(3) (2008) 417-433.

[176] T.J. Ohlemiller, J. Bellan, F. Rogers, A model of smoldering combustion applied to flexible polyurethane foams, Combustion and Flame, 36(C) (1979) 197-215.

[177] M.L. Kelley, D.A. Schult, Modeling extinction in forced opposed-flow smolder, Combustion Theory and Modelling, 10(1) (2006) 133-143.

[178] S.V. Leach, J.L. Ellzey, O.A. Ezekoye, A numerical study of reverse smoldering, Combustion Science and Technology, 130(1-6) (1997) 247-267.

[179] S.V. Leach, J.L. Ellzey, O.A. Ezekoye, Convection, pyrolysis, and Damköhler number effects on extinction of reverse smoldering combustion, Proceedings of the Combustion Institute, 27(2) (1998) 2873-2880.

[180] J. Yang, H. Chen, N. Liu, Heat Loss and Kinetic Effects on Extinction and Critical Self-Sustained Propagation of Forced Forward Smoldering, in: K. Harada, K. Matsuyama, K. Himoto, Y. Nakamura, K. Wakatsuki (Eds.) Fire Science and Technology 2015: The Proceedings of 10th Asia-Oceania Symposium on Fire Science and Technology, Springer Singapore, Singapore, 2017, pp. 831-840.

[181] E.A. Salganskii, E.V. Polianchik, G.B. Manelis, Modeling filtration combustion of a pyrolyzing solid fuel, Combustion, Explosion, and Shock Waves, 49(1) (2013) 38-52.

[182] A.P. Aldushin, A. Bayliss, B.J. Matkowsky, Is there a transition to flaming in reverse smolder waves?, Combustion and Flame, 156(12) (2009) 2231-2251.

[183] N. Fernandez-Anez, K. Christensen, G. Rein, Two-dimensional model of smouldering combustion using multi-layer cellular automaton: The role of ignition location and direction of airflow, Fire Safety Journal, (2017).

[184] G. Rein, A. Bar-Ilan, C. Fernandez-Pello, J.L. Ellzey, J.L. Torero, D.L. Urban, Modeling of One-Dimensional Smoldering of Polyurethane in Microgravity Conditions, Proceedings of the Combustion Institute, 30(2) (2005) 2327-2334.

[185] M.S.K. Youtsos, E. Mastorakos, Numerical simulation of thermal and reaction waves for in situ combustion in hydrocarbon reservoirs, Fuel, 108(0) (2013) 780-792.

[186] X. Huang, G. Rein, H. Chen, Computational smoldering combustion: Predicting the roles of moisture and inert contents in peat wildfires, Proceedings of the Combustion Institute, 35(3) (2015) 2673-2681.

[187] J. Belgrave, R. Moore, M. Ursenbach, D. Bennion, A comprehensive approach to in-situ combustion modeling, SPE Advanced Technology Series, 1(01) (1993) 98-107.

[188] S. Lovett, F. Monmont, N. Nikiforakis, An experimentally-based in-situ combustion model with adaptive meshing, Combustion and Flame, 162(4) (2015) 960-977.

[189] A.B. Dodd, C. Lautenberger, A.C. Fernandez-Pello, Numerical examination of two-dimensional smolder structure in polyurethane foam, Proceedings of the Combustion Institute, 32(2) (2009) 2497-2504.

[190] A. Matala, C. Lautenberger, S. Hostikka, Generalized direct method for pyrolysis kinetic parameter estimation and comparison to existing methods, Journal of Fire Sciences, 30(4) (2012) 339-356.

[191] H.E. Kissinger, Reaction kinetics in differential thermal analysis, Analytical Chemistry, 29(11) (1957) 1702-1706.

[192] T. Ozawa, A new method of analyzing thermogravimetric data, Bulletin of the Chemical Society of Japan, v. 38(n.11) (1965) p. 1881-1886.

[193] K. Levenberg, A method for the solution of certain non-linear problems in least square, Quarterly of Applied Mathematics, 2(2) (1944) 164–168.

[194] D.W. Marquardt, An algorithm for least square estimation of nonlinear parameters, Journal of the Society for Industrial and Applied Mathematics, 11(2) (1963) 431–441.

[195] D.E. Goldberg, Genetic Algorithms in Search, Optimization, and Machine Learning, Addison-Wesley, 1989.

[196] G. Rein, C. Lautenberger, A.C. Fernandez-Pello, J.L. Torero, D.L. Urban, Application of genetic algorithms and thermogravimetry to determine the kinetics of polyurethane foam in smoldering combustion, Combustion and Flame, 146(1–2) (2006) 95-108.

[197] E.S. Freeman, B. Carroll, The Application of Thermoanalytical Techniques to Reaction Kinetics: The Thermogravimetric Evaluation of the Kinetics of the Decomposition of Calcium Oxalate Monohydrate, The Journal of Physical Chemistry, 62(4) (1958) 394-397.

[198] A.W. Coats, J.P. Redfern, Kinetic Parameters from Thermogravimetric Data, Nature, 201(4914) (1964) 68-69.

[199] C. Ghabi, H. Benticha, M. Sassi, Parametric study of the heat transfer coefficient in bi-dimensional smoldering simulation, Thermal Science, 11(4) (2007) 95-112.

[200] A. Rostami, J. Murthy, M. Hajaligol, Modeling of a smoldering cigarette, Journal of Analytical and Applied Pyrolysis, 66(1–2) (2003) 281-301.

[201] A. Rostami, J. Murthy, M. Hajaligol, Modeling of smoldering process in a porous biomass fuel rod, Fuel, 83(11–12) (2004) 1527-1536.

[202] D. Lozinski, J. Buckmaster, Quenching of reverse smolder, Combustion and Flame, 102(1–2) (1995) 87-100.

[203] A.A.M. Oliveira, M. Kaviany, Nonequilibrium in the transport of heat and reactants in combustion in porous media, Progress in Energy and Combustion Science, 27(5) (2001) 523-545.

[204] G. Baud, S. Salvador, G. Debenest, J.-F. Thovert, New Granular Model Medium To Investigate Smoldering Fronts Propagation—Experiments, Energy & Fuels, 29(10) (2015) 6780-6792.

[205] P.R. Kapadia, M.S. Kallos, I.D. Gates, A review of pyrolysis, aquathermolysis, and oxidation of Athabasca bitumen, Fuel Processing Technology, 131 (2015) 270-289.

[206] Q. Chen, R. Yang, B. Zhao, Y. Li, S. Wang, H. Wu, Y. Zhuo, C. Chen, Investigation of heat of biomass pyrolysis and secondary reactions by simultaneous thermogravimetry and differential scanning calorimetry, Fuel, 134 (2014) 467-476.

[207] A. Liñán, The asymptotic structure of counterflow diffusion flames for large activation energies, Acta Astronautica, 1(7) (1974) 1007-1039.

[208] W. Pu, S. Pang, H. Jia, Using DSC/TG/DTA techniques to re-evaluate the effect of clays on crude oil oxidation kinetics, Journal of Petroleum Science and Engineering, 134 (2015) 123-130.

[209] Y. Chu, C. Fan, Q. Zhang, C. Zan, D. Ma, H. Jiang, Y. Wang, F. Wei, The oxidation of heavy oil to enhance oil recovery: The numerical model and the criteria to describe the low and high temperature oxidation, Chemical Engineering Journal, 248 (2014) 422-429.

[210] B.V. L'vov, Thermochemical approach to solid-state decomposition reactions against the background of traditional theories, Journal of Thermal Analysis and Calorimetry, 96(2) (2009) 487-493.

[211] B.V. L'vov, The physical approach to the interpretation of the kinetics and mechanisms of thermal decomposition of solids: the state of the art, Thermochimica Acta, 373(2) (2001) 97-124.

[212] A.K. Galwey, M.E. Brown, Application of the Arrhenius equation to solid state kinetics: can this be justified?, Thermochimica Acta, 386(1) (2002) 91-98.

[213] A.K. Galwey, M.E. Brown, Arrhenius parameters and compensation behaviour in solid-state decompositions, Thermochimica Acta, 300(1) (1997) 107-115.

Chapter 3

3 Determination of the interfacial heat transfer coefficient between forced air and sand at Reynold's numbers relevant to smouldering combustion[1]

3.1 Introduction

Smouldering is defined as an oxygen-limited, flameless form of combustion with low temperatures and slow propagation rates relative to flaming [1]. It is a heterogeneous, exothermic chemical reaction between the (solid or liquid) reactive fuel and oxygen, using the heat released during the exothermic process to sustain the combustion front [1-4]. Traditionally, research on smouldering focused on porous organic solids, such as polyurethane foam and peat in the context of fire safety [5]. Examples include smouldering involved in residential, industrial, and forest fires and subsurface fires in coal seams.

Recently, smouldering has been developed as an engineering technology. Applications include liberating oil from shale [6-8], treating human feces [9], underground coal gasification [10], tire recycling [11], treating wastewater biosolids [12], and remediating contaminated soil [13-16]. In each case, smouldering is enabled by the fact that the organic fuels are embedded in an inert porous matrix (e.g., rock, soil, sand). This matrix plays important roles, including: (*i*) its permeability permits oxygen transfer to the reaction zone by convection and diffusion [1, 4, 15, 17], and (*ii*) its high heat capacity acts as a thermal reservoir, which recycles the released energy into the reaction. This energy efficiency enables the smouldering of fuels with low calorific values [18-20].

Generally, predictions of smouldering must take into account the transport of momentum, mass, and energy in the solid and fluid phases [21, 22]. The transport of energy is dependent on the ability of the porous medium to store, conduct, and radiate heat, as well as

---

convective transfer between phases. Modelling of energy generally follows one of two approaches: Local Thermal Equilibrium (LTE) or Local Thermal Non-Equilibrium (LTNE) [23-28]. In LTE, the local temperature of the solid and gas phases is assumed to be the same so only one energy equation is employed. In LTNE, this is not assumed, so the energy equation for each phase is solved:

$$
\begin{aligned}
(1-\phi)\left(\rho_s C_{p_s}\right)\frac{\partial T_s}{\partial t} \\
= (1-\phi)\frac{\partial}{\partial x}\left((k_s + k_{rad})\frac{\partial T_s}{\partial x}\right) - U\left(\frac{A_{s,cl}}{V_{cl}}\right)(T_s - T_\infty) \\
+ h_{sg}\left(\frac{A_{s,sp}}{V_{sp}}\right)(T_g - T_s)
\end{aligned}
\tag{3.1}
$$

$$
\phi\left(\rho_g C_{p_g}\right)\frac{\partial T_g}{\partial t} + \rho_g C_{p_g} u_g \frac{\partial T_g}{\partial x} = \phi\frac{\partial}{\partial x}\left(k_g \frac{\partial T_g}{\partial x}\right) + h_{sg}\left(\frac{A_{s,sp}}{V_{sp}}\right)(T_s - T_g)
\tag{3.2}
$$

The two equations are linked by the interfacial heat transfer coefficient (h_{sg}), which dictates transfer between solid and gas phases. h_{sg} is multiplied by the surface area per unit volume assumed as perfect spheres ($A_{s,sp}/V_{sp}=6(1-\phi)/d_p$) [29]. The global heat loss coefficient (U) is multiplied by the surface area per unit volume of cylindrical column ($A_{s,cl}/V_{cl}=2/r$). Note that source/sink terms would appear in Equations (3.1) and (3.2) if chemical reactions were taking place.

Analytical and numerical models of smouldering assuming LTE [7, 18, 20, 29-37] and LTNE [21, 22, 38-45] have been extensively applied. It is suspected that LTNE is necessary to predict scenarios with forced air flow through hot sand. For example, high inlet gas velocities can decrease the solid temperature until smouldering quenches [1, 38, 46-52]. LTNE predictions require quantifying the thermophysical properties of both phases and h_{sg}.

The thermophysical properties of sand are important for a wide range of heat transfer applications beyond only applied smouldering. Sand's specific heat capacity (C_{ps}) and thermal conductivity (k_s) vary with temperature (T), porosity (ϕ), and particle diameter (d_p). Literature thermophysical properties for quartz sand are compiled in Table 3.1. The range

of values reveal that these measurements need to be conducted with care and under relevant experimental conditions.

Table 3.1: Literature Values for Thermophysical Properties of Sand

Ref.	d_p [mm]	C_{ps} [J kg^{-1} K^{-1}]	k_s [W m^{-1} K^{-1}]	k_p [m^2]	ϕ [-]	ρ_{bk} [kg m^{-3}]	T [ºC]
[53]	0.76-0.91	776	4.2	-	-	2632	20-70
[54]	0.50-1.00	-	0.27-0.40	-	-	-	20-200
[55]	-	-	0.52	-	-	1730	-
[56]	0.38-1.70	840	-	-	0.31-038	1600-1800	-
[57]	-	-	0.23	1.8×10^{-9}	0.39-0.41	-	-
[58]	-	726	0.53-0.59	-	-	1630-1740	-
[59]	0.15-0.60	796	0.32-0.34	-	-	1400	-
[60]	-	-	0.3	-	-	-	-
[61]	-	800	0.27	-	-	1520	27
[62]	-	950	0.45	-	-	1700	-

h_{sg} has been examined to predict heat transfer processes in a range of porous media including sand beds [62, 63], sintered particles [64-66], spherical glass particles [67-69], ceramic foam [70-73], metal foam [74], and porous carbon foam [75]. h_{sg} is independent of the surface area per unit volume of the porous medium ($a_v=A_s/V$) (see Equation 3.1). When a_v is unknown, the results are reported in terms of a volumetric heat transfer coefficient ($h_v=a_vh_{sg}$) [70, 71]. Analytical equations [23-26, 42, 66], inverse modeling [70, 71], and experiments [66, 70, 71, 76-83] have been used to derive empirical correlations for h_{sg} or h_v as a function of the parameters on which it depends, such as Reynolds number

$(Re=\rho_g u_g d_p/\phi\mu_g)$, Nusselt number $(Nu=h_{sg}d_p/k_g)$, Prandtl number $(Pr=\mu_g C_{pg}/k_g)$, ϕ, and d_p. Wakao et al. [78, 84], conducting an extensive review of experiments in packed beds (Figure 3.1), provided:

$$Nu = \frac{h_{sg}d_p}{k_g} = 2 + 1.1\left(Re^{0.6}Pr^{1/3}\right) \tag{3.3}$$

which has become the correlation most widely employed.
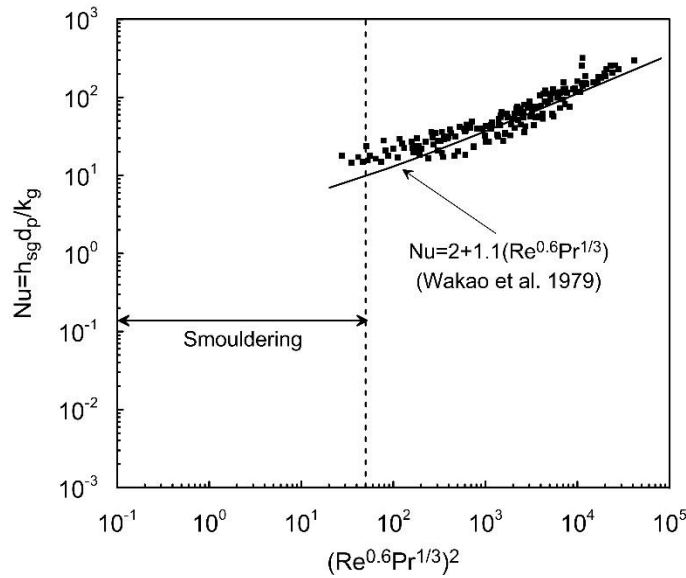
Figure 3.1: Log-log plot of the experimental data (■) compiled by [78] along with Eq. (3) (solid black line). The data from [78] were reproduced with permission.

A compilation of other empirical correlations is provided in Table 3.2. Many aspects of these correlations are inconsistent. For example, several studies found that h_{sg} increases [85, 86] or decreases [65, 66, 69-71, 87] with d_p, while others indicate the h_{sg} (d_p) relationship is affected by the solid and fluid thermal conductivities, Darcy air fluxes, and porosities [88, 89]. In general, they agree that an increase in the Darcy air flux (u_g) (i.e., increase in Re) results in an increase in h_{sg} [65-67, 69, 74, 87, 90] up to a maximum beyond which it is independent of u_g [67, 87, 90].

Table 3.2: Literature Correlation Equations for Predicting the Heat Transfer Coefficient in Porous Beds

Ref.	Eq.	Correlation	Material	d_p (mm)	ϕ	Fluid	Re	Pr	Description
[41]	(3.4)	$Nu_v = \dfrac{h_v d_p^2}{k_g} = a + bRe^c$	Polyurethane foam	-	0.97-0.99	Air	-	-	Values of a, b, and c are empirical constants.
[66]	(3.5)	$Nu = \dfrac{h_{sg} d_p}{k_g} = 0.198\phi^{0.07} Re^{0.66} Pr^{1/3}$	Sinter particles	12-32	0.49-0.54	Air	537-2233	0.67-0.70	-
[69]	(3.6)	$Nu = CRe^a Pr^b$	Spherical glass particles	11-22	-	Air	1000-5000	-	Values of a, b, and c are empirical constants.
[70]	(3.7)	$Nu = 0.819\left[1 - 7.33\left(\dfrac{d}{L}\right)\right] Re^{0.36\left[1+15.5\left(\frac{d}{L}\right)\right]}$	Ceramic Foam	-	0.83-0.87	Air	5.1-564	-	The ratio d/L varies from 0.005 to 0.136, where d is the pore diameter and L is the thickness of the porous ceramic.
[71]	(3.8)	$Nu_v = \dfrac{h_v d_p^2}{k_g} = CRe^m$	Cellular Ceramics	-	-	Air	0.02-1594	-	Values of C and m vary depending on the porous medium properties.
[73]	(3.9)	$Nu_v = aRe^b$	Ceramic foams	-	-	Air	100-2000	-	Values of a and b are empirical constants.
[74]	(3.10)	$Nu_v = b_1 Re^{b_2}$	Aluminum foams	-	0.70-0.95	Air	1900-7800	-	Values of b_1 and b_2 vary with porosity.
[80]	(3.11)	$Nu = \left\{(1.18Re^{0.58})^4 + \left[\left(0.23\left(\dfrac{Re}{1-\phi}\right)^{075}\right)^4\right]\right\}^{1/4}$	Pebble beds	-	0.26-0.94	Air Helium	$10\text{-}10^5$	0.71	-
[81]	(3.12)	$Nu_v = 0.124(RePr)^{0.791}$	Open-cellular materials	-	0.74-0.95	Air	-	-	-
[82]	(3.13)	$Nu = 0.015 + 0.11(Pe)^{0.73}$	Shredded materials	-	0.80	Air	-	-	Valid for $Pe=RePr<25$.
[83]	(3.14)	$Nu_v = 0.07\left(\dfrac{\phi}{1-\phi}\right)^{2/3}(RePr)$	Spherical particles	-	0.70-0.95	Air	3-1000	0.72	-
[91]	(3.15)	$Nu = 2.4x10^{-5} + 285.6\left(Re^{2.7}Pr^{1/3}\right)$	Sand	0.3-1	0.30	Water	0.001-0.01	-	Based on h_{sg} calculated from [92]

Smouldering studies have extensively used Equation (3.3) [78] to predict h_{sg} or h_v [22, 38-40, 44, 93]. However, Leach et al. [22] concluded that Equation (3.3) overestimates the heat transfer coefficient, resulting in an incorrect assumption of LTE for smouldering. A key issue is that Equation (3.3) was developed for systems very different from smouldering. The packed bed systems considered for Equation (3.3) exhibit $15 \leq Re \leq 8500$ and $30 \leq d_p \leq 171$ mm, which leads to Nu in the range 10^1-10^2. In contrast, natural convection (i.e., accidental) smouldering typically exhibits $0.01 < Re < 0.1$ [50] and forced air (i.e., engineered) smouldering typically employs $1 < Re < 40$ [6, 8, 12, 14-16, 94-101] and $0.1 < d_p < 2$ mm [9, 12, 15, 16, 102], which corresponds to Nu in the range 10^{-4}-10^1. Therefore, smouldering combustion is outside the range of applicability of Equation (3.3), as illustrated in Figure 3.1. No h_{sg} correlation exists for the specific conditions of applied smouldering, namely hot gases flowing through sand at relevant Re.

The main objective of this study is to develop an empirical correlation for h_{sg} between forced air and sand at the low Reynolds' numbers relevant to smouldering. Twelve column experiments were conducted to evaluate heat transfer in sand for different air fluxes and sand particle diameters. All of the necessary parameters were obtained independently except h_{sg}, which was optimized through inverse modelling of the experimental results. The developed correlation was validated against two additional experiments. A numerical model, equipped with the validated correlation, was then employed to explore the system's sensitivity to key parameters. In addition, the model allowed exploration of the validity of assuming local thermal equilibrium and this was compared to an analytical LTE criterion developed for these systems. The outcome is a new empirical Nu vs Re and Pr correlation that is valid for air flow through sand in conditions relevant to smouldering, namely $0.125 < d_p < 2.000$ mm, Pr=0.72, and $0.5 < Re < 31$. This correlation is valuable for improving our understanding of thermal non-equilibrium in such systems and predicting h_{sg} in a variety of similar heat transfer scenarios.

3.2   Methodology

3.2.1   Experimental Setup

Heat propagation and transfer experiments were carried out in a stainless-steel cylindrical column with 0.160 m inner diameter and 0.505 m in height (Figure 3.2). The column was placed over a stainless-steel base (0.14 m inner diameter, 0.20 m in height), containing a flat, spiral-coiled heater (0.14 m outer diameter, 450 W, 120V, Watlow Ltd) connected to a 120 V AC, single-phase variable power supply (STACO Energy Products), and an air diffuser made of perforated tubes connected to laboratory compressed air supply via a mass flow controller (FMA5400/5500 Series, 0-500 L min^{-1}, Omega Ltd). The air diffuser was covered with commercially available quartz sand (number 1240, Bell & MacKenzie Co., mean $d_p = 0.5$ mm, coefficient of uniformity < 1.5) to ensure uniform airflow. The column was filled with clean quartz sand with one of three distinct particle diameters (Table 3.3). The particle diameters were obtained by sieving sands number 12ST, 1240, and 505 (Bell & MacKenzie Co.) and retaining only what remained on sieves number 16, 40, and 120, respectively, for the hereafter named "*coarse*", "*medium*", and "*fine*" sands. The sieved sands were carefully packed in 0.05 m lifts, each tamped, for maximum uniformity. Twelve thermocouples (3.2 mm diameter, 150 mm length, Type K, Inconel, Omega) were horizontally positioned at intervals of 0.035 m to measure the variation in temperature at the column centerline. The thermocouples were connected to a computer through a data logger (Multifunction Switch/Measure Unit 34980A, Agilent) that acquired temperatures every 2 seconds. The column was wrapped in insulation (high-temperature mineral wool, McMaster-Carr) to minimize heat losses.

Table 3.3 summarizes the fourteen experiments that were performed. All experiments followed a heating procedure similar to that established for igniting a smouldering experiment [15, 16]; however, no fuel was used in this study. Exps. 1 – 12 were used to develop the heat transfer correlation while Exps. *A* and *B* were used for model validation. In each experiment, the heat wave was initiated by providing power to the heater (90% capacity, 4.4A) for 1800 s. Then, air injection just below the heater was initiated and maintained at a constant Darcy air flux (volume per unit cross-sectional area per unit time). Darcy air fluxes ranged from 0.016 to 0.113 m s^{-1}, which correspond to volumetric flow

rates from 20 to 140 L min^{-1}; this spans the range typically employed in applied smouldering studies [15, 16, 103]. After 600 s of air injection (i.e., 2400 s of heating) the heater was turned off while the air flow was maintained. Exp. *B* tripled the "*pre-air*" heating time to 5400 s, at which time the air flow was initiated and the heater was turned off at 6000 s. The base case experiment ($1.18 < d_p < 2.00$ mm, 0.065 m s^{-1}) was repeated five times to provide a measurement of the experimental uncertainty. Only three Darcy air fluxes (0.016, 0.040, and 0.065 m s^{-1}) were used for the fine sand because the sand fluidized at higher air fluxes.
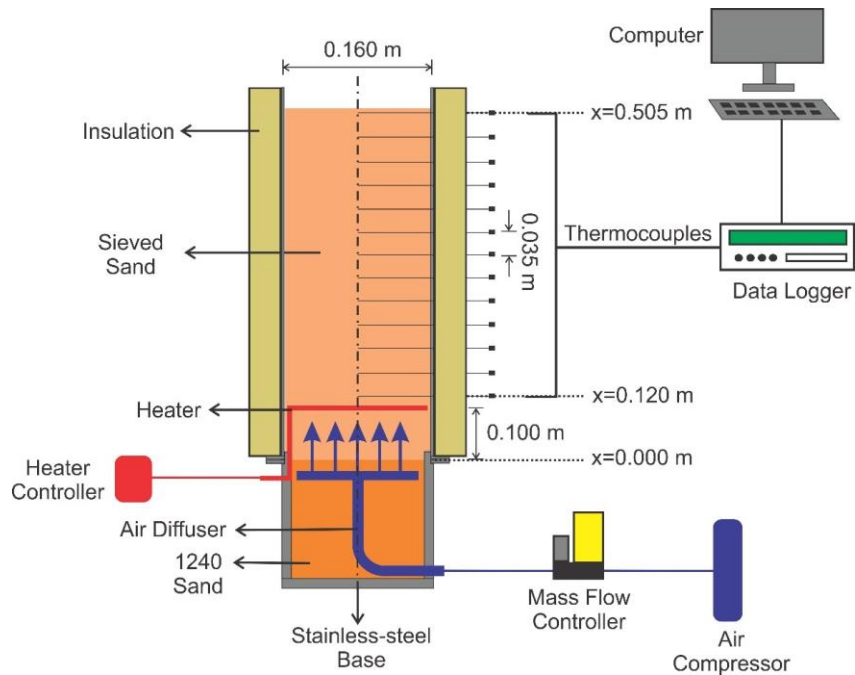
Figure 3.2: Schematic of the experimental apparatus.

Table 3.3: Heat Transfer Experiments

Exp. [#]	d_p [mm]	Q_g [L min^{-1}]	u_g [m s^{-1}]	*Heating Period* [s]	*n* [#]
1		20	0.016	2400	1
2		50	0.040	2400	1
3	$1.180<d_p<2.000$	80	0.065	2400	5
4		140	0.113	2400	1
5		20	0.016	2400	1
6		50	0.040	2400	1
7	$0.425<d_p<0.600$	80	0.065	2400	1
8		110	0.089	2400	1
9		140	0.113	2400	1
10		20	0.016	2400	1
11	$0.125<d_p<0.250$	50	0.040	2400	1
12		80	0.065	2400	1
A		110	0.089	2400	1
B	$1.180<d_p<2.000$	110	0.089	6000	1

3.2.2 Global Energy Balance

Heat losses play an important role in heat transfer systems. Although a rigorous analysis of heat loss effects requires multi-dimensional modeling [7, 21, 36], radial heat losses in these experiments may be quantified by the use of a global heat loss coefficient (*U*) and assuming a one-dimensional system. *U* was calculated through an energy balance:

$$\dot{E}_{in} - \dot{E}_{out} + \dot{E}_{gen} - \dot{E}_{loss} = \frac{dE_s}{dt} \qquad (3.16)$$

The energy entering $(\dot{E}_{in})$ the column comes from the heater (Figure 3.2). Energy can leave the column vertically out the top $(\dot{E}_{out})$ or through radial heat losses $(\dot{E}_{loss})$. Since no chemical reactions occur, the energy generation term $(\dot{E}_{gen})$ is zero, and the result is the rate at which energy stored in the system (dE_s/dt) changes. $\dot{E}_{in}$ and $\dot{E}_{out}$ are difficult to estimate since the gas enthalpy and heater energy are unknown. Therefore, the approach here was to isolate a time interval during which approximately zero energy is entering and leaving the system $(\dot{E}_{in} = \dot{E}_{out} = 0)$; in other words, when both the inlet and outlet temperatures were approximately ambient (25-35 °C). This allows E_s in the time interval (i) to be calculated:

$$E_{s,j} = \sum_{j=1}^{12} \left[m_{s,j} C_{p_s} \left(T_{s,j}(x) - T_\infty \right) \right] \tag{3.17}$$

where the mass of sand in each control volume of the column ($m_{s,j}$) is calculated from the total mass of sand ($m_{s,T}$) divided by the number of thermocouples (j), which here is 12. The sand temperature in each control volume ($T_{s,j}$) was taken from the thermocouple at the axis of symmetry. The thermocouple was assumed to best represent the sand since the thermocouple's characteristic heating time is likely most consistent with the solid phase. If heat losses are occurring, Equation (3.17) would show E_s decreasing with time during this interval (while adiabatic conditions would result in constant E_s). Since the control volume is small enough that the Biot number (Bi) is also small and radial heat losses $(\dot{E}_{loss})$ are assumed, Equation (3.16) becomes:

$$\dot{E}_{loss} = -UA_{s,cl}\left(T_{avg(t)} - T_\infty \right) = m_{s,T} C_{p_s} \frac{dT_{avg(t)}}{dt} \tag{3.18}$$

which can be integrated over time to obtain U:

$$U = -ln\left(\frac{\left(T_{avg(t_2)} - T_\infty \right)}{\left(T_{avg(t_1)} - T_\infty \right)} \right) \frac{m_{s,T} C_{p_s}}{A_{s,cl}(t_2 - t_1)} \tag{3.19}$$

The surface area of the cylinder is $A_{s,cl}=2\pi Hr$, C_{ps} was measured (see Section 3.2.3), T_∞ is the ambient temperature, t_2 and t_1 represent the time period over which Equation (3.18) was integrated, and the mass-weighted average temperature was calculated:

$$T_{avg(t)} = \frac{\sum_{j=1}^{12}\left[m_{s,j}C_{p_s}\left(T_{s,j}(x) - T_\infty\right)\right]}{m_{s,T}C_{p_s}} \tag{3.20}$$

As the temperature of the system varies with time and distance, the purpose of Equation (3.20) was to obtain an average temperature of the entire domain varying just with time. Overall, this approach uses the centerline thermocouple data from a particular interval in each experiment to estimate the fraction of energy decline at the centerline due to radial heat loss throughout the experiment.

3.2.3   Sand Properties

The porosity (ϕ) and bulk density (ρ_{bk}) of each sand pack was calculated using the mass of sand, the particle density (ρ_s) and the cell volume. The intrinsic permeability (k_p) of each sand was determined in a custom-built permeameter (following ASTM D6539-00 [104]). A Hot Disk Thermal Constants Analyzer [105] was used to measure k_s as a function of temperature for each sand. C_{ps} as a function of temperature was measured by Differential Scanning Calorimetry (DSC Q2000, TA Instruments) following ASTM-E1269 [106]. Further details are provided in the Appendix A and supplied references [104, 105, 107, 108].

Table 3.4 presents the measured properties for all three sand sizes. As expected, ϕ and ρ_{bk} varied little with d_p, and k_p increased two orders of magnitude from the smallest to the largest sand. As expected, k_s linearly increased with temperature for all three sands, as shown in Figure 3.3. Note that the experimental uncertainty was $\pm 5\%$, and the maximum difference in k_s for all three sands was only 7%; it can therefore be concluded that k_s exhibits negligible dependence on d_p. Figure 3.4 presents C_{ps} measurements for the medium ($0.425 < d_p < 0.600$ mm) and coarse ($1.180 < d_p < 2.000$ mm) sands. The DSC method did not provide reliable C_{ps} results for the fine sand ($0.125 < d_p < 0.250$ mm). As expected, C_{ps} linearly increased with temperature, with a maximum value of 1886 J kg^{-1} K^{-1} (medium sand) and 1653 J kg^{-1} K^{-1} (coarse sand) at 760 K (486.85 °C). The experimental

uncertainty for C_{ps} was found to be 5% and the maximum C_{ps} difference from coarse to medium sand was only 8%. Therefore, it is concluded that d_p has a negligible influence on C_{ps}. Moreover, the high C_{ps} values measured in this work confirm the widely held (but seldom tested) assumption that sand has a relatively high specific heat capacity.

Table 3.4: Measurements of the Sand Properties.

d_p [mm]	T [°C]	k_s [W m^{-1} K^{-1}]	ϕ [-]	ρ_{bk} [kg m^{-3}]	k_p [m^2]
	19.0	0.247			
0.125<d_p<0.250	86.0	0.278	0.36	1691	2.07x10^{-11}
	175.0	0.325			
	269.0	0.359			
	22.0	0.256			
0.425<d_p<0.600	85.0	0.308	0.37	1660	1.84x10^{-10}
	172.0	0.348			
	264.0	0.391			
	22.0	0.276			
1.180<d_p<2.000	85.0	0.322	0.37	1672	1.03x10^{-9}
	173.0	0.382			
	267.0	0.432			

Figure 3.3: Thermal conductivity of sand versus temperature increase for three particle diameters: +: 1.180 < d_p < 2.000 mm; ■: 0.425 < d_p < 0.600 mm; ●: 0.125 < d_p < 0.250 mm. Solid and dashed lines represent the linear regression for each particle diameter. The accuracy and reproducibility of each measurement were within ± 5% and ± 2%, respectively [109].
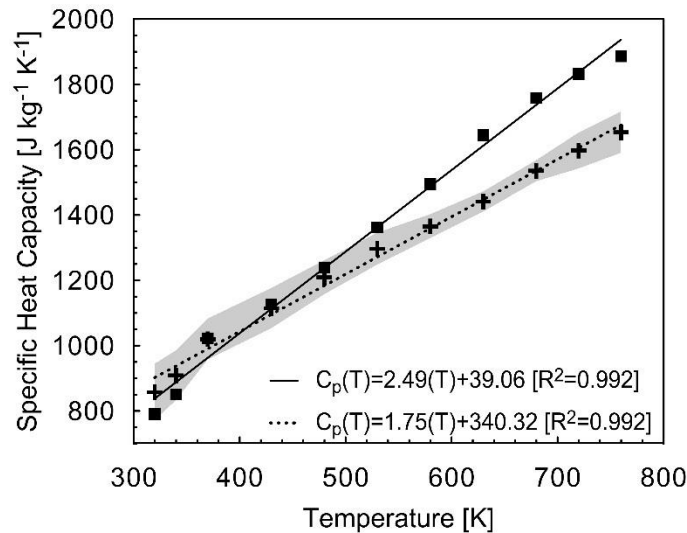
Figure 3.4: C_p of sand versus temperature increase for two particle diameters (dashed line: linear regression for (+) 1.180 < d_p < 2.000 mm; solid line: linear regression for (■) 0.450 < d_p < 0.600 mm). Confidence intervals (shaded region) were evaluated based on three distinct experiments for 1.180 < d_p < 2.000 mm calculating the area under the standard normal curve that equals 95%.

3.3 Modelling

3.3.1   Governing Equations

A one-dimensional numerical model was developed in COMSOL Multiphysics (*Version 5.0*), which uses the finite-element method. The domain simulated the 0.505 m column, with the lower boundary coincident with the air diffuser and the upper boundary at the sand's upper surface (Figure 3.2). Air pressures and velocities were solved via the gas-phase continuity equation [110]:

$$\frac{\partial(\rho_g \phi)}{\partial t} + \frac{\partial(\rho_g u_g)}{\partial x} = 0 \tag{3.21}$$

which employed Darcy flow without gravity effects [111]. The gas density followed the ideal gas law [112]. The model solves the transient energy equation for both solid and gas phases, Equations (3.1) and (3.2), respectively; therefore, LTNE was considered. Heat transfer in the porous medium included conduction, convection, and radiation. Radiation heat transfer follows the Rosseland approximation [113] and was expressed as a radiative conductivity ($k_{rad}=16\sigma d_p T_s^3/3$). An average global heat loss coefficient (U_{avg}) was included (see Sections 3.2.2 and 3.4.1), and used the surface area per unit volume ($A_{s,cl}/V_{cl}=2/r$) of the column.

Sand particles were taken as spheres with a surface area per unit volume ($A_{s,sp}/V_{sp}$) equal to $6(1-\phi)/d_p$ [29]. Sand properties, as described in Section 3.2.3, were employed and a homogeneous porous medium was assumed. As described above, direct measurements revealed no significant dependence on d_p for either k_s (Figure 3.3) or C_{ps} (Figure 3.4). Therefore, the determined k_s and C_{ps} for $0.425 < d_p < 0.600$ mm were used in the simulations for all grain sizes. The properties of air – C_{pg}, k_g, and μ_g – were fitted from thermodynamic tables within 1% from 300 to 1500 K.

The initial and boundary conditions are provided in Table 3.5. Both heater and air diffuser were simulated by piecewise functions without smoothing effects. The air diffuser was described by a mass flux located at $x=0$ m and the heater was described by a constant heat flux applied at $x=0.100$ m. The piecewise functions followed the experimental procedure described in Section 3.2.1. The upper boundary was simulated by a convective heat flux at

x=0.505 m and fixed atmospheric pressure. Table 3.6 presents the model input parameters for the base case, revealing that the majority were measured directly and the rest were obtained from the literature. The only exception was the interfacial heat transfer coefficient (h_{sg}), which needed to be determined independently (Section 3.3.2).

Table 3.5: Initial and Boundary Conditions for Numerical Model

Eq.	Initial Condition	Boundary Condition
(3.1-3.2)	$t = 0 \Rightarrow \begin{cases} T_s = T_0 \\ T_g = T_0 \end{cases}$	$x = 0.100\ m \Rightarrow \begin{cases} -(k_s + k_{rad})\dfrac{\partial T_s}{\partial x} = \dot{q}'' \to 0 \le t \le t_h \\ -(k_s + k_{rad})\dfrac{\partial T_s}{\partial x} = 0 \to t_h < t \le t_f \\ T_g = T_0 \end{cases}$ $x = 0.505\ m \Rightarrow \begin{cases} -(k_s + k_{rad})\dfrac{\partial T_s}{\partial x} = U(T_s - T_\infty) \\ -(k_g)\dfrac{\partial T_g}{\partial x} = U(T_g - T_\infty) \end{cases}$
(3.21)	$t = 0 \Rightarrow P_g = P_0$	$x = 0.000\ m \Rightarrow \rho_g u_g = \rho_g u_g(t) \to \begin{cases} u_g = 0 \to 0 \le t \le t_g \\ u_g = u_g \to t_g < t \le t_f \end{cases}$ $x = 0.505\ m \Rightarrow P_g = P_0$

Table 3.6: Model Input Parameters Common to All Simulations

Parameters	Value	Unit	Reference
C_{ps}	$2.49(T_s)+39.06$	J kg^{-1} K^{-1}	Measured
C_{pg}	$-3\text{x}10^{-5}(T_g{}^2)+0.2261(T_g)+940.35$	J kg^{-1} K^{-1}	[114]
k_s	$0.000541(T_s)+0.1044$	W m^{-1} K^{-1}	Measured
k_g	$-1\text{x}10^{-8}(T_g{}^2)+8\text{x}10^{-5}(T_g)+4.3\text{x}10^{-3}$	W m^{-1} K^{-1}	[114]
$m_{s,T}$	14.1	kg	This work
μ_g	$-9\text{x}10^{-12}(T_g{}^2)+4\text{x}10^{-8}(T_g)+6\text{x}10^{-6}$	Pa s	[114]
P_0	101375	Pa	This work
$\dot{q}''$	25000	W m^{-2}	Calculated
r	0.08	m	This work
ρ_s	2650	kg m^{-3}	[114]
T_0	293	K	This work
T_∞	293	K	This work
U	1.7	W m^{-2} K^{-1}	Calculated

3.3.2 Inverse Modelling

The only unknown parameter in the governing equations, h_{sg}, was obtained via inverse modelling of the experiments (Table 3.3). The objective function (S) minimized was:

$$S = \sum_{i=1}^{11} \sum_{j=1}^{t_f} \left(T_{s(exp)}^{i,j} - T_{s(num)}^{i,j} \right)^2 \tag{3.22}$$

where $T_{s(exp)}$ is the experimental sand temperature and $T_{s(num)}$ is the simulated sand temperature at each thermocouple (i) and time step (j). The temperature curve for the first thermocouple above the heater ($x=0.120$ m) was not used in the h_{sg} optimization due to

experimental variability in the heater position and the heat flux delivered at the inlet boundary. The rest of the thermocouples were used at all times. A unique h_{sg}, was obtained for each experiment by varying h_{sg} only and minimizing S to best-fit the observed evolution of the heat wave. The Levenberg-Marquardt (LM) algorithm was used to minimize Equation (3.22), which is a gradient-based optimization method available in the COMSOL Optimization Module. Further information on Levenberg-Marquardt algorithm can be found in [115-119].

3.3.3   LTE Criterion

Kaviany [25] and Oliveira and Kaviany [27] present a framework for developing case-specific LTE criteria. They indicate that LTE can be assumed when the characteristic time (τ) associated with heat transfer at the scale of a representative elementary volume (REV) is much greater than that at the scale of a single particle:

$$\tau_{REV} \gg \tau_p \tag{3.23}$$

In this work, this is evaluated by considering the energy balance between a sand particle and the air flowing past it. The developed LTE criterion for heat transfer associated with flowing air in hot sand is:

$$\frac{6h_{sg}}{u_g \rho_s C_{p_s}} \gg 1 \tag{3.24}$$

The full derivation of Equation (3.24) is presented in the Appendix A. This LTE criterion was evaluated by employing (*i*) C_{ps} provided by the measurement (see Section 3.2.3) taken at the average temperature given in Equation (3.20), and (*ii*) h_{sg} provided by the optimized value from the inverse modelling.

3.4   Results and Discussion

Figure 3.5*a*, showing temperature evolution in the base case experiment, demonstrates that conduction from the heater (*x*=0.100 m) extends only as far as the second thermocouple (*x*=0.155 m) just before the air was turned on (*t*=1800 s). The heating of the sand below the heater could not be shown due to the lack of thermocouples. Assuming symmetry of

conduction suggests a heated zone 0.11 m thick centered on the heater. When air injection was initiated, convective heat transfer of this stored energy along the column was observed, starting with a rapid rise in the temperature of the first thermocouple above the heater (x=0.120 m). The heater was then turned off (t=2400 s) and the stored energy in the sand was transferred upwards and spread longitudinally, corresponding to a steady decrease in the peak temperature. This is clearly shown in Figure 3.5b, which presents temperature profiles as a function of time. Figure 3.5 also reveals the excellent repeatability of the experiment for temperatures in both space and time.
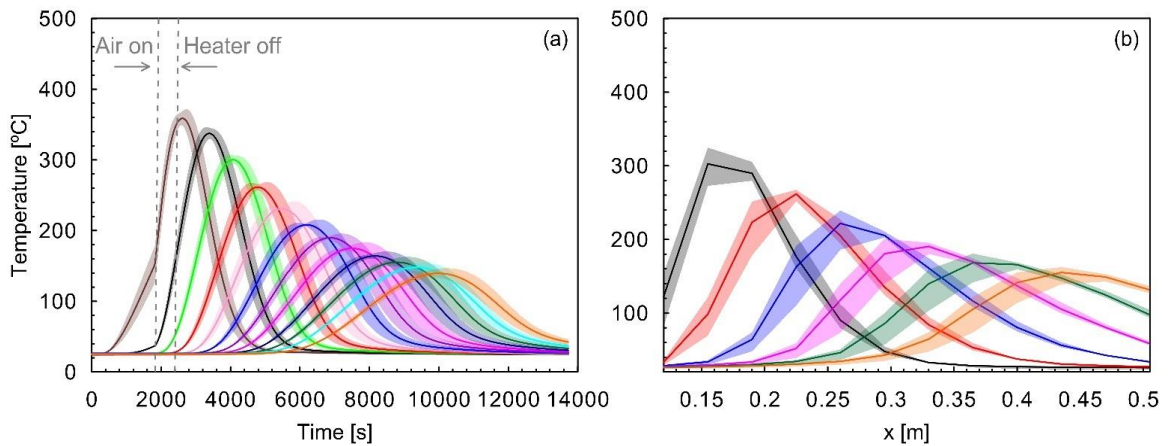
Figure 3.5: (*a*) Experimental temperature evolution versus time and (*b*) temperature profile versus height of the column (*x*) for base case experiment (1.18 < d_p < 2.00 mm, 0.065 m s^{-1}). Solid lines represent the mean value of the temperatures (T_M) for five independent repeats (*n*). The colours in the figure (*a*) represent thermocouple positions (*x*) from 0.120 to 0.505 m with 0.035 m intervals, and (*b*) experimental times (*t*) from 3840 to 9240 s with intervals of 1080 s. The shading represents 95% confidence intervals.

The other experiments listed in Table 3.3 (except Exp. *B*) provide results that are similar to the base case, so the main trends are summarized in Figure 3.6 and Figure 3.7. Figure 3.6 presents the peak temperature as a function of height for all experiments. First, it reveals a consistent decrease in the peak temperature as the heat wave proceeds through the column due to cooling processes. In addition, it shows that an increase in the Darcy air flux leads to an increase in the peak temperature. The velocity of the heat wave (Figure 3.7) was

calculated from the time interval necessary for two consecutive thermocouples reach their peak temperature and their known separation distance. Figure 3.7 indicates that the speed of the heat wave is driven by convection. Taken together, the figures indicate that d_p has a negligible effect on both peak temperature and heat wave velocity (except for a minor effect for the cases of high Darcy air fluxes and fine sand).
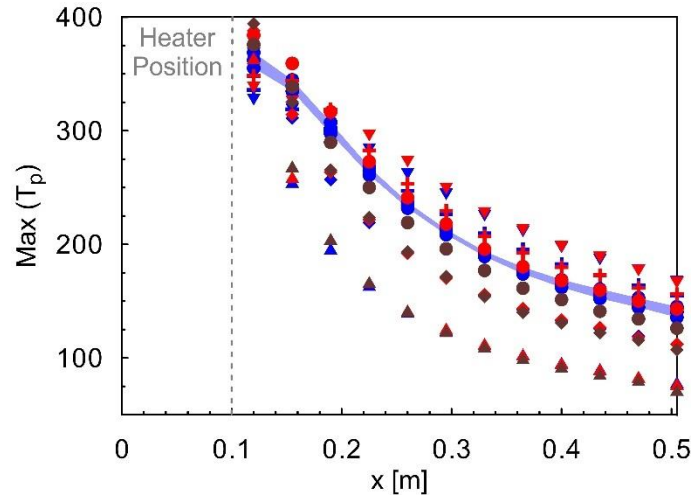
Figure 3.6: Experimental peak temperature as a function of column height. The colours describe three sand particle diameters: blue (1.180 < d_p < 2.000 mm), red (0.425 < d_p < 0.600 mm), and brown (0.125 < d_p < 0.250 mm) and the symbols show five Darcy air fluxes: (▲) 0.016 m s⁻¹, (♦) 0.040 m s⁻¹, (●) 0.065 m s⁻¹, (+) 0.089 m s⁻¹, and (▼) 0.113 m s⁻¹. The shaded region corresponds to the 95% confidence interval for base case (0.065 m s⁻¹, 1.180 < d_p < 2.000 mm).
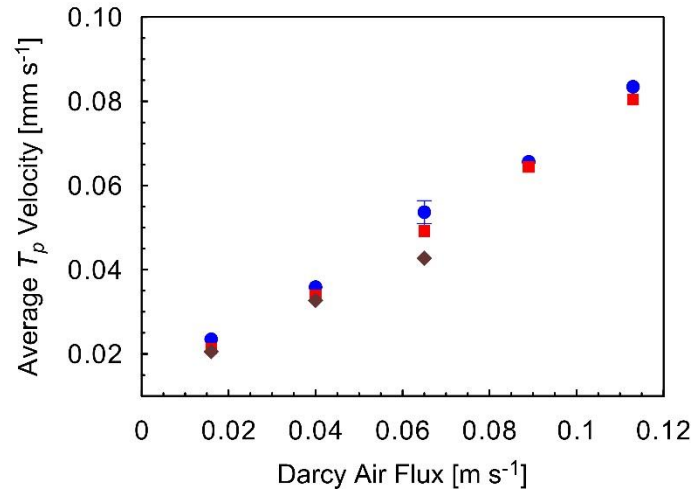
Figure 3.7: Average peak temperature velocity as a function of Darcy air flux. The colours and symbols describe three sand particle diameters: (●) 1.180 < d_p < 2.000 mm, (■) 0.425 < d_p < 0.600 mm, and (♦) 0.125 < d_p < 0.250 mm. The error bar shows the 95% confidence interval on the average velocity (0.065 m s^{-1}, (●) 1.180 < d_p < 2.000 mm).

Conduction versus convection dominance was analyzed via Equation (A.14) – Appendix A – and the results are presented in Figure 3.8. The figure plots the ratio of the characteristic time for conduction to the characteristic time for convection for all of the experiments conducted and includes how the ratio changes as the heat wave propagates the length of the column. Convection is dominant when $\tau_{cond}/\tau_{conv} >> 1$, thus Figure 3.8 shows that heat transfer in all of the experiments are dominated by convection at all times. It also reveals that conduction is less important as the heat wave propagates away from the heater. Note that Figure 3.8 shows negligible influence of d_p on this ratio. Appendix A also shows an analysis of mixed convection (buoyancy in forced convection) investigated via a Darcy-modified Rayleigh number (Ra) [120], Equation (A.15). The results indicate negligible Ra ($10^{-3} < Ra < 10^{-1}$); therefore, buoyancy in forced convection may be disregarded in this scenario.
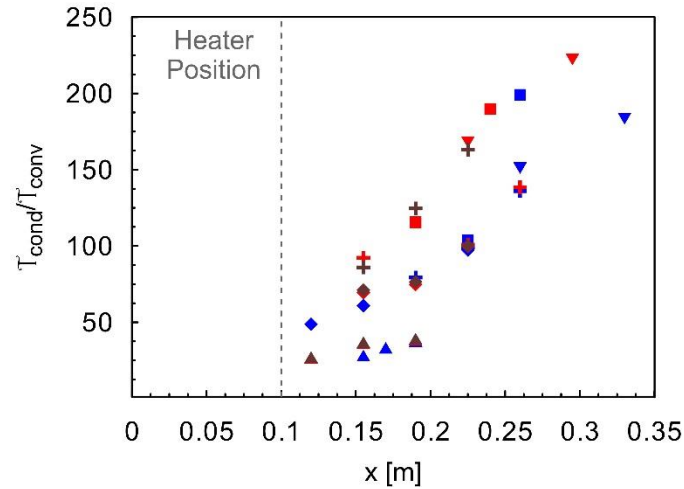
Figure 3.8: The ratio between the characteristic time for conduction and the characteristic time for convection (τ_{cond}/τ_{conv}) as a function of heat wave position (x). The colours describe three sand particle diameters: blue ($1.180 < d_p < 2.000$ mm), red ($0.425 < d_p < 0.600$ mm), and brown ($0.125 < d_p < 0.250$ mm) and the symbols shows five Darcy air fluxes: ($\blacktriangle$) 0.016 m s^{-1}, ($\blacklozenge$) 0.040 m s^{-1}, ($\bullet$) 0.065 m s^{-1}, (+) 0.089 m s^{-1}, and ($\blacktriangledown$) 0.113 m s^{-1}.

3.4.1   Global Heat Loss Coefficient (*U*)

Figure 3.9a describes the energy in the system calculated from Equation (3.18) for the base case experiment. The mass of sand and the adopted C_{ps} (measured in Section 3.2.3) are provided in Table 3.6. Note that C_{ps} for $0.425 < d_p < 0.600$ mm (retrieved at the average temperature) was used as the basis for the energy and all U values calculations. The figure identifies four distinct regions, of which Region (*III*) is of primary importance in this context because it represents the interval during which no energy was entering or leaving through the ends of the column (i.e., $\dot{E}_{in} = \dot{E}_{out} = 0$).
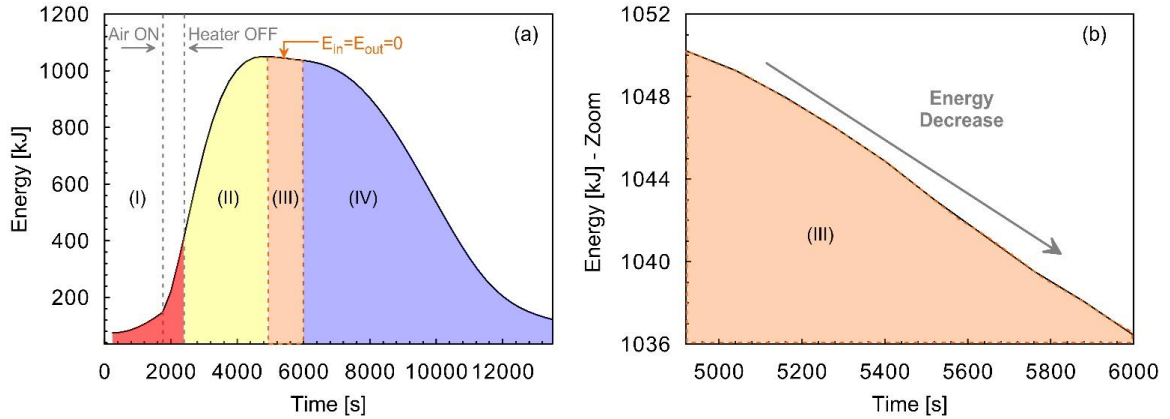
Figure 3.9: (*a*) **Energy evolution with time in the system and** (*b*) **zoomed in to focus on Region** (*III*) **for the base case experiment (1.18 < d_p < 2.00 mm, and 0.065 m s⁻¹). Region** (*I*) **describes the period that the heater is powered; Region** (*II*) **shows the period of energy recovery after the heater has been shut off; Region** (*III*) **corresponds to the time-period between 4920 and 6000 s in which $\dot{E}_{in} = \dot{E}_{out} = 0$; Region** (*IV*) **defines the period in which energy is leaving the system via the outlet.**

Under adiabatic conditions, Region (*III*) would be characterized by a constant amount of energy in the system. However, Figure 3.9b reveals a decrease in stored energy with time, which means that heat losses are taking place. *U* was then calculated through Equation (3.19) by applying $\dot{E}_{in} = \dot{E}_{out} = 0$ on Region (*III*). This was repeated for all experiments in which Region (*III*) could be isolated, namely all experiments but three (Table 3.7). Figure 3.10 and Table 3.7, presenting the results of these calculations, illustrate that *U* varied from 1.0 to 2.0 W m⁻² K⁻¹ between experiments, which was smaller than the random error from five repeats. No clear relationship between *U*, d_p, and *Re* was observed. Therefore, the average *U* (U_{avg}=1.7 W m⁻² K⁻¹) was employed as a constant heat loss coefficient in all model simulations. It should be noted that U_{avg} does not only represent heat losses across the column wall but also includes energy lost radially from the centerline of the column, a fraction of which is stored in sand between the centerline and the wall.
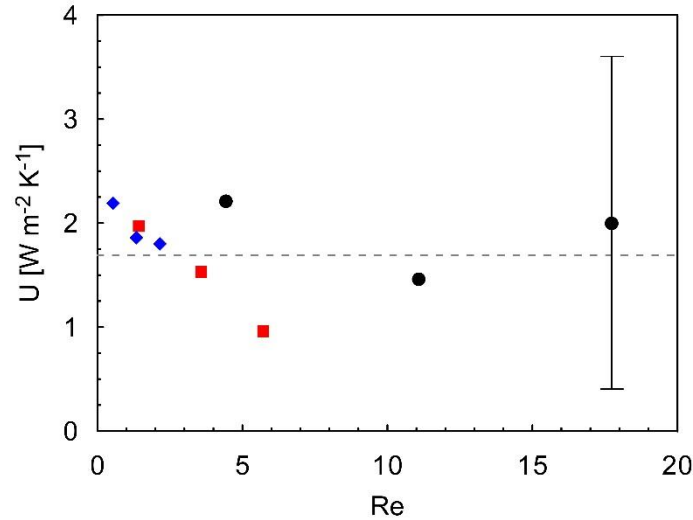
Figure 3.10: Global heat loss coefficient calculated from Equation (3.20) varying with *Re* number: (●) 1.180 < *d_p* < 2.000 mm; (■) 0.425 < *d_p* < 0.600 mm; (♦) 0.125 < *d_p* < 0.250 mm. The error bar encompasses the calculated range of values obtained for five repeat experiments at 0.065 m s⁻¹ and the dashed line corresponds to an average of all measured *U* values (*U_{avg}*=1.7 W m⁻² K⁻¹).

3.4.2 Interfacial Heat Transfer Coefficient (h_{sg})

A value of h_{sg} was obtained for each experiment by inverse modelling (Section 3.3.2). For the base case, h_{sg} was 5.34 W m⁻² K⁻¹ and, in general, h_{sg} increased with increased Darcy air flux and with increased grain size up to a maximum of 10.43 W m⁻² K⁻¹ (Table 3.7). Figure 3.11 shows that when the base case h_{sg} was input into the model, the simulated heat wave propagation was in excellent agreement with the experiment in both space and time.

This comparison between simulation and experiment was completed for all 12 cases. The fit was quantified in each case with the Normalized Root-Mean-Square Deviation (NRMSD) between experimental sand temperature ($T_{s,exp}$) and numerical sand temperature ($T_{s,num}$):

$$NRMSD = \frac{\sqrt{\sum_{i=1}^{z}\left(T_{s,exp} - T_{s,num}\right)^2/z}}{\left(T_{s,max} - T_{s,min}\right)} \tag{3.25}$$

The NRMSD with respect to time evaluates inaccuracy associated with h_{sg} (e.g., Figure 3.11a) while the NRMSD with respect to distance evaluated inaccuracy with respect to U (e.g., Figure 3.11b). The NMRSD-h_{sg} and NRMSD-U values are listed for each experiment in Table 3.7. It reveals that, for the base case, the NRMSD values for both h_{sg} and U are 6%, which are within the 95% confidence interval for temperature versus time (9%) and temperature versus distance (9%) (see Figure 3.5). Moreover, they reveal that the optimized h_{sg} values do reasonably well in providing simulations that match the observations. The lowest air flow rate shows up to 23% error, which might be associated with uncertainty associated with assuming uniform values of sand thermal conductivity and specific heat capacity, since low air flow experiments experience a larger influence from conduction near the heater (see Figure 3.8).

Table 3.7: Summarized Results for all Experiments and Simulations

d_p [mm]	u_g [m s^{-1}]	$\dot{E}_{in} = \dot{E}_{out} = 0$ [-]	U [W m^{-2} K^{-1}]	h_{sg} [W m^{-2} K^{-1}]	NRMSD-h_{sg} [%]	NRMSD-U [%]
1.180<d_p<2.000	0.016	✓	2.0	0.23	23	50
	0.040	✓	1.5	1.601	7	13
	0.065	✓	1.6±1.1*	5.34±0.2*	6±0.1*	6±0.1*
	0.113	✗	-	10.43	6	10
0.425<d_p<0.600	0.016	✓	2.0	0.09	21	32
	0.040	✓	1.5	0.62	7	12
	0.065	✓	1.0	1.62	9	18
	0.089	✗	-	3.00	17	32
	0.113	✗	-	5.50	15	35
0.125<d_p<0.250	0.016	✓	2.0	0.04	17	35
	0.040	✓	1.9	0.30	19	29
	0.065	✓	1.8	0.35	10	16

*Based on 95% confidence interval
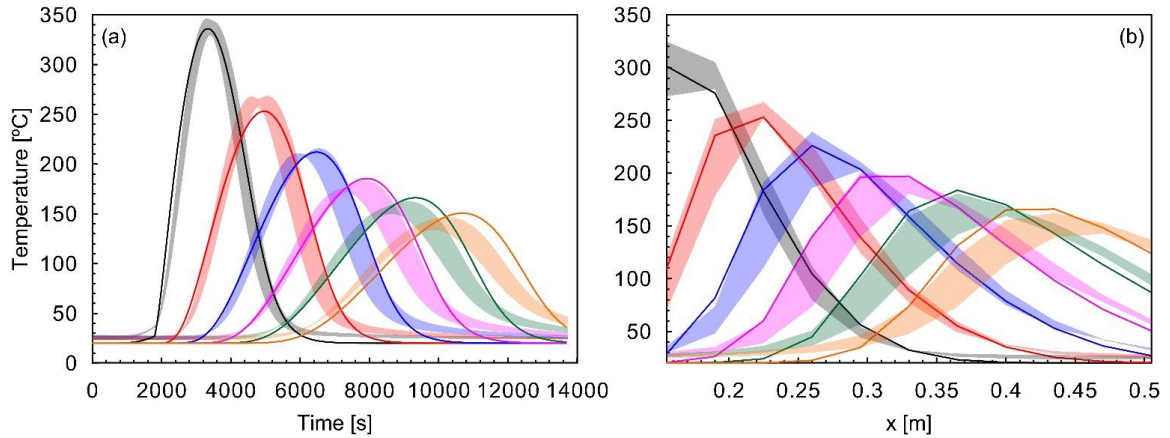
Figure 3.11: (*a*) Temperature versus time and (*b*) temperature versus *x* showing a comparison between experimental (shaded region: 95% confidence interval) and numerical (solid line) data for base case (1.180 < *d~p~* < 2.000 mm, 0.065 m s⁻¹). The colours show (*a*) thermocouple positions from 0.155 to 0.505 m with 0.07 m intervals, and (*b*) experimental times from 3840 to 9240 s with intervals of 1080 s. The numerical data shows the sand temperature for *U~avg~*=1.7 W m⁻² K⁻¹ and optimized *h~sg~*=5.34 W m⁻² K⁻¹.

The NRMSD values in Table 3.7 reveal that the uncertainty associated with energy loss (U) is larger than associated with the heat transfer coefficient (h_{sg}) in all cases. A sensitivity analysis of the temperature curves to U (Figure 3.12) for base case revealed that small variations in U ($0 < U < 3.6$ W m⁻² K⁻¹; i.e., the range associated with experimental repeatability) caused significant changes in the predicted peak temperatures. Assuming $U=0$ W m⁻² K⁻¹ (adiabatic conditions) increased peak temperatures, as expected (see upper limit of grey shading on Figure 3.12) resulting in an increase in the *NRMSD-U* from 6% to 12%. Assuming $U=3.6$ W m⁻² K⁻¹ slightly overestimated the heat losses (see lower limit of orange shading on Figure 3.12), increasing *NRMSD-U* from 6% to 7%. This illuminates the role of radial heat loss on the centerline temperatures and provides support for the independent method provided (Section 3.2.2) for determining its magnitude.
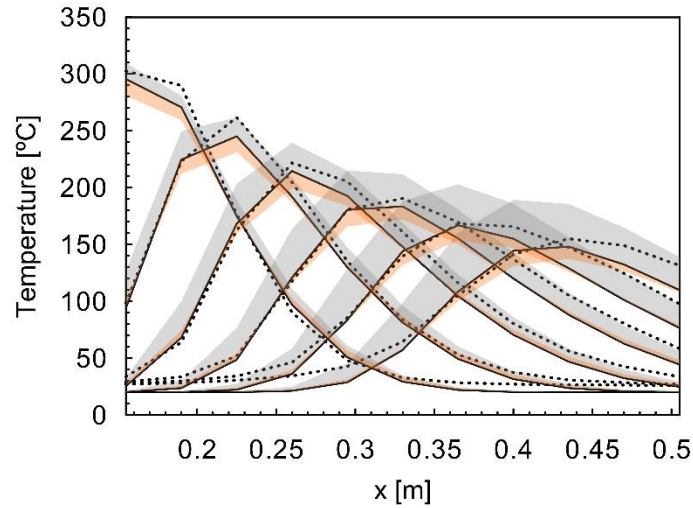
Figure 3.12: Sensitivity of the temperature profiles to the heat loss coefficient (*U*).
The dashed line shows the average experimental data for base case (0.065 m s^{-1},
1.180 < d_p < 2.000 mm) and the solid line represents the simulated sand temperature
employing *U*=1.7 W m^{-2} K^{-1} and optimized h_{sg}=5.34 W m^{-2} K^{-1} for times from 3840 to
9240 s with intervals of 1080 s. The upper limit of the grey region is the predicted
temperature profiles for *U*=0 W m^{-2} K^{-1} (adiabatic) and the lower limit of the orange
region represents *U*=3.6 W m^{-2} K^{-1}.

3.4.3   Evaluating the LTE Criterion

Table 3.8 shows the results for the LTE evaluations against the criterion presented in
Equation (3.24), using the optimized h_{sg} values for each experiment (Table 3.7). First, the
table reveals that *Bi*<<1 for all experiments therefore, the bulk heating approximation
assumed in Equation (3.24) is valid. Moreover, it demonstrates that τ_{REV}/τ_p is much less
than 1 for all cases. This means that LTNE is important in this scenario and the LTE
assumption is invalid. Equation (3.24) suggests that h_{sg} in excess of 10^5 W m^{-2} K^{-1} is
required to assume LTE (compared to the maximum order of 10^1 W m^{-2} K^{-1} found in this
work); however it is noted that the *Bi<<1* assumption is violated when h_{sg} exceeds 180 W
m^{-2} K^{-1}.

Table 3.8: Evaluation of LTE Criterion

d_p [mm]	u_g [m s^{-1}]	τ_p [s]	τ_{REV} [s]	τ_{REV}/τ_p [-]	Bi [-]	$\Delta T_{sg}/T_p$ [%]
	0.016	2.6×10^3	3.7×10^{-2}	1.4×10^{-5}	1.3×10^{-3}	22
	0.040	3.9×10^2	1.5×10^{-2}	3.8×10^{-5}	8.9×10^{-3}	10
$1.180<d_p<2.000$	0.065	7.4×10^1	9.0×10^{-3}	1.2×10^{-4}	4.7×10^{-2}	6
	0.113	5.9×10^1	5.2×10^{-3}	8.8×10^{-5}	5.6×10^{-2}	6
	0.016	2.2×10^3	1.2×10^{-2}	5.4×10^{-6}	1.6×10^{-4}	20
	0.040	3.2×10^2	4.7×10^{-3}	1.5×10^{-5}	1.1×10^{-3}	9
$0.425<d_p<0.600$	0.065	1.2×10^2	3.0×10^{-3}	2.4×10^{-5}	2.9×10^{-3}	7
	0.089	6.6×10^1	2.0×10^{-3}	3.2×10^{-5}	5.4×10^{-3}	7
	0.113	3.5×10^1	1.7×10^{-3}	4.8×10^{-5}	1.0×10^{-2}	6
	0.016	1.8×10^3	4.2×10^{-3}	2.3×10^{-6}	2.6×10^{-5}	19
$0.125<d_p<0.250$	0.040	2.4×10^2	1.7×10^{-3}	7.0×10^{-6}	2.0×10^{-4}	9
	0.065	2.0×10^2	1.0×10^{-3}	5.1×10^{-6}	2.3×10^{-4}	7

3.4.4 New Empirical Correlation for the Heat Transfer Coefficient

Figure 3.13 plots the h_{sg} values from this work (Table 3.7) as a function of *Nu*, *Re*, and *Pr*. A power-law regression was employed that provides a new empirical correlation for the heat transfer between sand and air:

$$Nu = 0.001\left(Re^{1.97}Pr^{1/3}\right) \tag{3.26}$$

that is valid for *Pr*=0.72, $0.5 < Re < 31$, and $0.125 < d_p < 2.000$ mm. The Prandtl number was added into Equation (3.26) based on the boundary layer theory ($Pr^{1/3}$) [114].
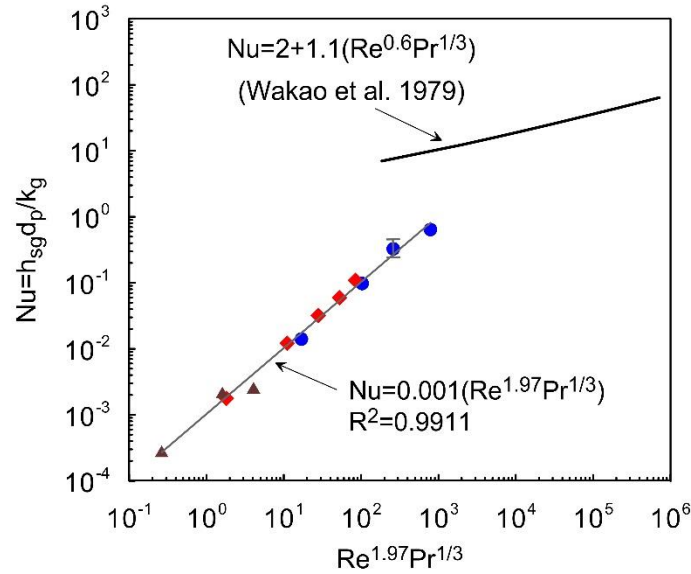
Figure 3.13: Log-log plot describing h_{sg} as a function of Nu versus Re and Pr for three sand particle diameters (●: $1.180 < d_p < 2.000$ mm; ♦: $0.425 < d_p < 0.600$ mm; ▲: $0.125 < d_p < 0.250$ mm). The solid gray line shows the power law regression corresponding to Equation (3.26). The solid black line shows the most commonly used correlation from the literature, Equation (3.3).

Figure 3.13 contrasts this new correlation, Equation (3.26), with that most commonly used from the literature, Equation (3.3). Note that the presented correlation captures low Re and Nu, which are outside the range of applicability of Equation (3.3). Equation (3.26) exhibits a higher slope than Equation (3.3), which suggests an increased sensitivity of h_{sg} to Re in this region. Previous work has projected Equation (3.3) to a Re~0, predicting Nu~2 for smouldering by natural convection [39]. This work reveals that such extrapolations of Equation (3.3) would overestimate Nu by at least three orders of magnitude.

3.4.5   Validation

The developed correlation, Equation (3.26), was input into the model as a function of h_{sg} and used to simulate two additional, distinct experiments (Exp. *A* and *B,* Table 3.3); these simulations employed no fitting or optimization. The predicted sand temperatures are compared to the experimental data in Figure 3.14. The model predicted Exp. *A* (2400 s of heating) extremely well, with a NRMSD-h_{sg} = 6% (Figure 3.14a) and NRMSD-U = 7% (Figure 3.14b). The model prediction of Exp. *B* (6000 s of heating) was reasonable with a

NRMSD-h_{sg} = 13% (Figure 3.14c) and NRMSD-U = 21% (Figure 3.14d). It is not surprising that this simulation was less accurate than for Exp. *A* since the heat losses in Exp. *B* would have been higher due to the higher peak temperatures (see Figure 3.14). The U_{avg} value used for all simulations was developed from experiments with lower peak temperatures like Exp. *A* (see Section 3.4.1). The figure further shows that using the model equipped with the commonly used correlation, Equation (3.3), is less able to reproduce validation Exp. *A*; in this case NRMSD-h_{sg} = 14% (Figure 3.14e) and NRMSD-U = 22% (Figure 3.14f).

3.4.6   Temperature Difference between Sand and Air

The simulation of each experiment provides the temperatures of both phases, which are unattainable from the experiments themselves. Figure 3.15 plots the difference between the sand and gas temperatures along the length of the column normalized to the maximum (experimental) peak temperature ($\Delta T_{sg}/T_p$). LTE is approached as this ratio approaches zero. The figure illustrates that the Exp. *A* validation simulation shows $\Delta T_{sg}/T_p$ = 12% near the heater and decreasing with distance to less than 5% due to reduced heater influence and increased convective cooling of the sand. The figure shows that the extended heating of Exp. *B* results in $\Delta T_{sg}/T_p$ = 23% near the heater, decreasing along the column to less than 6%. Note that the model generally predicts the gas phase temperature is higher at the peak of the heat wave, but at certain distance and times the sand temperature is higher. When these experiments are simulated using Equation (3.3) to dictate h_{sg}, $\Delta T_{sg}/T_p$ never exceeds 2%; nearly identical results are found when using an arbitrarily high, constant value of h_{sg}=500 W m^{-2} K^{-1} (Figure 3.15). The average $\Delta T_{sg}/T_p$ for Exp. *A* is 6% and for Exp. *B* is 9%, while for the latter two simulations in Figure 3.15 are 1% and 0.3%. The average $\Delta T_{sg}/T_p$ for all of the simulated experiments are shown in Table 3.8; these metrics provide additional evidence that LTE is not achieved in this system.
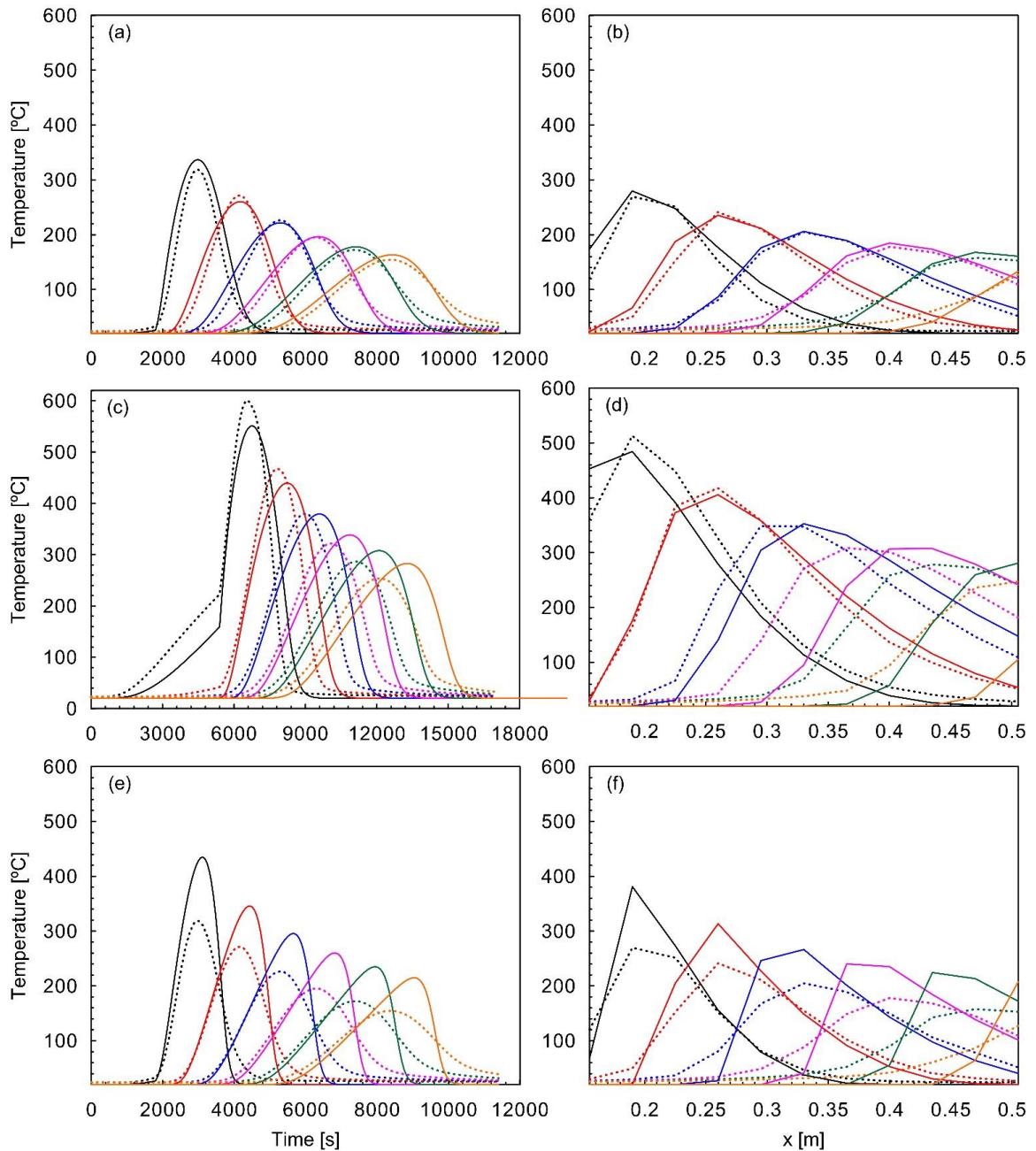
Figure 3.14: Comparison of simulations (solid lines) to experiments (dashed lines). (*a,b*) Simulation using Equation (3.26) for validation Exp. *A* (2400 s of heating) and (*c,d*) for validation Exp. *B* (6000 s of heating). (*e,f*) Simulation using Equation (3.3) for validation Exp. *A*. The left column shows temperature-time with colours indicating thermocouple positions from 0.155 to 0.505 m at 0.07 m intervals. The right column shows temperature-height with experimental times from (*b,f*) 3840 to 9240 s with 1080 s intervals or (*d*) experimental times from 7500 to 15000 s with intervals of 1500 s.
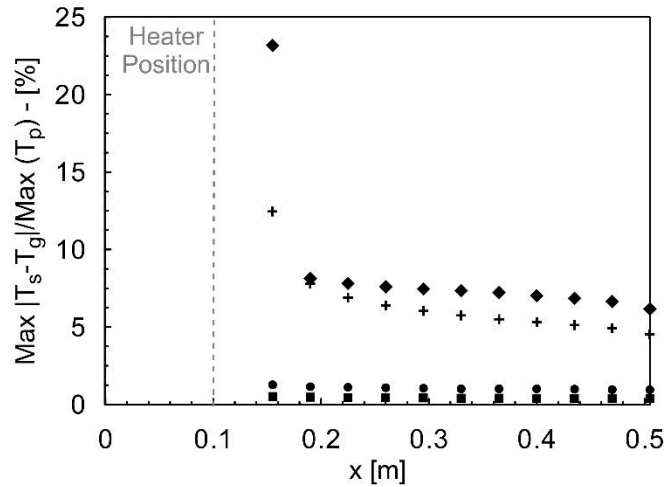
Figure 3.15: Normalized maximum simulated solid (T_s) and gas (T_g) temperature varying with column height (x) for: (+) validation of Exp. A; ($\blacklozenge$) validation of Exp. B; ($\bullet$) Exp. A using Equation (3.3); ($\blacksquare$) Exp. A using h_{sg}=500 W m^{-2} K^{-1}.

3.5 Conclusion and Summary

Many systems of interest involve a heat wave travelling via flowing air through a fixed bed of fine to coarse sand at low Reynold's numbers (Re<30). Such systems are typically assumed to be at local thermal equilibrium. When local thermal non-equilibrium is assumed, the heat transfer coefficient (h_{sg}) is typically calculated using the correlation of Wakao et al. [78, 84]. This work identified that Wakao et al. [78, 84] correlation was developed from high Reynold's numbers experiments ($15 \leq Re \leq 8500$) and can over-predict Nu by up to three orders of magnitude when extrapolated to low Re. It also demonstrated that the h_{sg} values produced by that correlation for these systems ($180 < h_{sg} < 420$ W m^{-2} K^{-1}) effectively generate local thermal equilibrium, which is not appropriate for these systems.

Twelve column experiments were conducted with a variety of sand sizes and air flow rates, providing a novel data set for heat wave propagation relevant to these systems. These were simulated with a one-dimensional numerical model that assumed local thermal non-equilibrium. All of the material properties and system parameters were obtained independently except h_{sg}, which was optimized via inverse modelling. A methodology for

estimating heat losses based on a global energy balance in the experimental system demonstrated that radial heat losses were significant and needed to be included. The determined values of h_{sg}, which varied from 0.04 to 10.43 W m^{-2} K^{-1}, were used to develop a new correlation: $Nu=0.001(Re^{1.97}Pr^{1/3})$, which is valid for $0.5 < Re < 31$ and $0.125 < d_p < 2.000$ mm. The numerical model employing this correlation was validated against two distinct experiments, producing excellent predictions of the measured temperatures even for significantly higher peak temperatures than considered in the development (e.g., characteristic of smouldering).

A new criterion for assuming local thermal equilibrium was developed based on characteristic time scales. Its application to these experiments demonstrated that the local thermal equilibrium assumption is incorrect for these low Reynold's number systems. Indeed, the validated model predicts temperatures differences between the air and sand of up to 23% in certain locations and up to 6% on average. When the model employed the Wakao et al. [78, 84] correlation, negligible non-equilibrium was predicted locally and the model could not accurately reproduce the experiments. The high heat capacity of the sand combined with the dominance of convection in these systems acts to ensure that non-equilibrium must be considered in all of these cases, with increasing error in assuming equilibrium at lower air flow rates, smaller grain sizes, and increased proximity to the heater.

Overall, the new correlation was demonstrated to be reliable for simulating heat transfer between flowing air and a fixed sand bed. The fact that the model was able to predict low and high temperature processes with such low deviation indicates its robustness and wide applicability. This work is expected to be useful for understanding local thermal non-equilibrium in a variety of processes characterized by low Reynolds' numbers. Future work is exploring the value of this correlation in predicting the performance of ambient and applied smouldering systems.

3.6   References

[1] T.J. Ohlemiller, Modeling of smoldering combustion propagation, Progress in Energy and Combustion Science, 11(4) (1985) 277-310.

[2] K.N. Palmer, Smouldering combustion in dusts and fibrous materials, Combustion and Flame, 1(2) (1957) 129-154.

[3] J.L. Torero, A.C. Fernandez-Pello, Forward smolder of polyurethane foam in a forced air flow, Combustion and Flame, 106(1–2) (1996) 89-109.

[4] G. Rein, Smouldering combustion phenomena in science and technology, International Review of Chemical Engineering, 1 (2009) 3-18.

[5] A. Bar-Ilan, G. Rein, D.C. Walther, A.C. Fernandez-Pello, J.L. Torero, D.L. Urban, The effect of buoyancy on opposed smoldering, Combustion Science and Technology, 176(12) (2004) 2027-2055.

[6] M.F. Martins, S. Salvador, J.F. Thovert, G. Debenest, Co-current combustion of oil shale - Part 2: Structure of the combustion front, Fuel, 89(1) (2010) 133-143.

[7] H. Fadaei, M. Sennoune, S. Salvador, A. Lapene, G. Debenest, Modelling of non-consolidated oil shale semi-coke forward combustion: Influence of carbon and calcium carbonate contents, Fuel, 95(0) (2012) 197-205.

[8] G. Debenest, V. Mourzenko, J. Thovert, Smouldering in fixed beds of oil shale grains. A three-dimensional microscale numerical model, Combustion Theory and Modelling, 9(1) (2005) 113-135.

[9] L. Yermán, R.M. Hadden, J. Carrascal, I. Fabris, D. Cormier, J.L. Torero, J.I. Gerhard, M. Krajcovic, P. Pironi, Y.-L. Cheng, Smouldering combustion as a treatment technology for faeces: Exploring the parameter space, Fuel, 147 (2015) 108-116.

[10] A.W. Bhutto, A.A. Bazmi, G. Zahedi, Underground coal gasification: From fundamentals to applications, Progress in Energy and Combustion Science, 39(1) (2013) 189-214.

[11] J.-P. Vantelon, B. Lodeho, S. Pignoux, J.L. Ellzey, J.L. Torero, Experimental observations on the thermal degradation of a porous bed of tires, Proceedings of the Combustion Institute, 30(2) (2005) 2239-2246.

[12] T.L. Rashwan, J.I. Gerhard, G.P. Grant, Application of self-sustaining smouldering combustion for the destruction of wastewater biosolids, Waste Management, 50 (2016) 201-212.

[13] P. Pironi, Smouldering combustion of liquids in porous media for remediating NAPL-contaminated soils, PhD Thesis, University of Edinburgh, Edinburgh, Scotland, UK, 2009.

[14] P. Pironi, C. Switzer, J.I. Gerhard, G. Rein, J.L. Torero, Self-Sustaining Smoldering Combustion for NAPL Remediation: Laboratory Evaluation of Process Sensitivity to Key Parameters, Environmental Science and Technology, 45(7) (2011) 2980-2986.

[15] P. Pironi, C. Switzer, G. Rein, A. Fuentes, J.I. Gerhard, J.L. Torero, Small-scale forward smouldering experiments for remediation of coal tar in inert media, Proceedings of the Combustion Institute, 32(2) (2009) 1957-1964.

[16] C. Switzer, P. Pironi, J.I. Gerhard, G. Rein, J.L. Torero, Self-sustaining smoldering combustion: A novel remediation process for non-aqueous-phase liquids in porous media, Environmental Science and Technology, 43(15) (2009) 5871-5877.

[17] T.J. Ohlemiller, Smoldering Combustion, in: P.J. DiNenno, D. Drysdale, C.L. Beyler, W.D. Walton (Eds.) SFPE Handbook of Fire Protection Engineering, National Fire Protection Association, Quincy, MA, USA, 2002, pp. 200-210.

[18] A.P. Aldushin, I.E. Rumanov, B.J. Matkowsky, Maximal energy accumulation in a superadiabatic filtration combustion wave, Combustion and Flame, 118(1–2) (1999) 76-90.

[19] M.R. Henneke, J.L. Ellzey, Modeling of filtration combustion in a packed bed, Combustion and Flame, 117(4) (1999) 832-840.

[20] D.A. Schult, B.J. Matkowsky, V.A. Volpert, A.C. Fernandez-Pello, Forced forward smolder combustion, Combustion and Flame, 104(1–2) (1996) 1-26.

[21] G. Rein, A. Carlos Fernandez-Pello, D.L. Urban, Computational model of forward and opposed smoldering combustion in microgravity, Proceedings of the Combustion Institute, 31(2) (2007) 2677-2684.

[22] S.V. Leach, G. Rein, J.L. Ellzey, O.A. Ezekoye, J.L. Torero, Kinetic and fuel property effects on forward smoldering, Combustion and Flame, 120(3) (2000) 346-358.

[23] M. Quintard, S. Whitaker, One- and two-equation models for transient diffusion processes in two-phase systems, in: Advances in Heat Transfer, 1993, pp. 369-464.

[24] M. Quintard, S. Whitaker, Local thermal equilibrium for transient heat conduction: theory and comparison with numerical experiments, International Journal of Heat and Mass Transfer, 38(15) (1995) 2779-2796.

[25] M. Kaviany, Principles of Heat Transfer in Porous Media, Springer, 1995.

[26] S. Whitaker, Improved constraints for the principle of local thermal equilibrium, Industrial & Engineering Chemistry Research, 30(5) (1991) 983-997.

[27] A.A.M. Oliveira, M. Kaviany, Nonequilibrium in the transport of heat and reactants in combustion in porous media, Progress in Energy and Combustion Science, 27(5) (2001) 523-545.

[28] D.A.A. Nield, A.A. Bejan, Heat transfer through a porous medium, 2nd ed., Springer Verlag, 1999.

[29] M. Fatehi, M. Kaviany, Adiabatic reverse combustion in a packed bed, Combustion and Flame, 99(1) (1994) 1-17.

[30] H. Chen, G. Rein, N. Liu, Numerical investigation of downward smoldering combustion in an organic soil column, International Journal of Heat and Mass Transfer, 84(0) (2015) 253-261.

[31] F. He, N. Zobel, W. Zha, F. Behrendt, Effects of physical properties on one-dimensional downward smoldering of char: Numerical analysis, Biomass and Bioenergy, 33(8) (2009) 1019-1029.

[32] D.A. Schult, B.J. Matkowsky, V.A. Volpert, A.C. Fernandez-Pello, Propagation and extinction of forced opposed flow smolder waves, Combustion and Flame, 101(4) (1995) 471-490.

[33] C. Di Blasi, Mechanisms of two-dimensional smoldering propagation through packed fuel beds, Combustion Science and Technology, 106(1-3) (1995) 103-124.

[34] S.S. Dosanjh, P.J. Pagni, A.C. Fernandez-Pello, Forced cocurrent smoldering combustion, Combustion and Flame, 68(2) (1987) 131-142.

[35] M.S.K. Youtsos, E. Mastorakos, Numerical simulation of thermal and reaction waves for in situ combustion in hydrocarbon reservoirs, Fuel, 108(0) (2013) 780-792.

[36] I.Y. Akkutlu, Y.C. Yortsos, The Dynamics of In-situ Combustion Fronts in Porous Media, Combustion and Flame, 134(3) (2003) 229-247.

[37] X. Huang, G. Rein, H. Chen, Computational smoldering combustion: Predicting the roles of moisture and inert contents in peat wildfires, Proceedings of the Combustion Institute, 35(3) (2015) 2673-2681.

[38] S.V. Leach, J.L. Ellzey, O.A. Ezekoye, A numerical study of reverse smoldering, Combustion Science and Technology, 130(1-6) (1997) 247-267.

[39] A. Rostami, J. Murthy, M. Hajaligol, Modeling of a smoldering cigarette, Journal of Analytical and Applied Pyrolysis, 66(1–2) (2003) 281-301.

[40] B.-s. Jia, M.-z. Xie, H. Liu, Numerical study on the propagation characteristics of forward smoldering in a cellulosic packed bed, Journal of Shanghai University (English Edition), 12(2) (2008) 171-179.

[41] A.B. Dodd, C. Lautenberger, C. Fernandez-Pello, Computational modeling of smolder combustion and spontaneous transition to flaming, Combustion and Flame, 159(1) (2012) 448-461.

[42] C. Yang, J.F. Thovert, G. Debenest, Upscaling of mass and thermal transports in porous media with heterogeneous combustion reactions, International Journal of Heat and Mass Transfer, 84 (2015) 862-875.

[43] C. Yang, G. Debenest, Numerical simulations for smoldering in a horizontal channel: Comparisons between variable density-based formulation and incompressible one, Combustion Science and Technology, 186(12) (2014) 1954-1974.

[44] N.C. Roy, Y. Nakamura, Investigation of unsteady behaviors of forward and opposed flow combustion of solid fuel, Combustion and Flame, 163 (2016) 517-531.

[45] G. Debenest, V.V. Mourzenko, J.F. Thovert, Smouldering in fixed beds of oil shale grains: Governing parameters and global regimes, Combustion Theory and Modelling, 9(2) (2005) 301-321.

[46] S.D. Tse, A.C. Fernandez-Pello, K. Miyasaka, Controlling mechanisms in the transition from smoldering to flaming of flexible polyurethane foam, Symposium (International) on Combustion, 26(1) (1996) 1505-1513.

[47] R. Hadden, A. Alkatib, G. Rein, J.L. Torero, Radiant Ignition of Polyurethane Foam: The Effect of Sample Size, Fire Technology, 50(3) (2014) 673-691.

[48] J.L. Torero, A.C. Fernandez-Pello, D. Urban, Experimental observations of the effect of gravity changes on smoldering combustion, AIAA Journal, 32(5) (1994) 991-996.

[49] M.K. Anderson, R.T. Sleight, J.L. Torero, Downward smolder of polyurethane foam: ignition signatures, Fire Safety Journal, 35(2) (2000) 131-147.

[50] J.L. Torero, A.C. Fernandez-Pello, Natural convection smolder of polyurethane foam, upward propagation, Fire Safety Journal, 24(1) (1995) 35-52.

[51] A.P. Aldushin, A. Bayliss, B.J. Matkowsky, Is there a transition to flaming in reverse smolder waves?, Combustion and Flame, 156(12) (2009) 2231-2251.

[52] J.L. Torero, A.C. Fernandez-Pello, M. Kitano, Opposed Forced Flow Smoldering of Polyurethane Foam, Combustion Science and Technology, 91(1-3) (1993) 95-117.

[53] M.A. Izquierdo-Barrientos, C. Sobrino, J.A. Almendros-Ibáñez, Experimental heat transfer coefficients between a surface and fixed and fluidized beds with PCM, Applied Thermal Engineering, 78(0) (2015) 373-379.

[54] M.F. Martins, The structure of a combustion front propagating in a fixed bed of crushed oil shale: co-current configuration, PhD Thesis, Université de Toulouse, 2008.

[55] K. Manohar, D.W. Yarbrough, J.R. Booth, Measurement of apparent thermal conductivity by the thermal probe method, Journal of Testing and Evaluation (JOTE), 28(5) (2000) 345-351.

[56] S. Peng, N. Wang, J. Chen, Steam and air co-injection in removing residual TCE in unsaturated layered sandy porous media, Journal of Contaminant Hydrology, 153(0) (2013) 24-36.

[57] J. Gudbjerg, T.O. Sonnenborg, K.H. Jensen, Remediation of NAPL below the water table by steam-induced heat conduction, Journal of Contaminant Hydrology, 72(1–4) (2004) 207-225.

[58] S.M. Farouq Ali, Steam injection, secondary and tertiary oil recovery process, Interstate Oil Compact Commission, Oklahoma City, 1974.

[59] K. Manohar, R. Shirish, Apparent thermal conductivity of sand, International Journal of Heat Exchangers, 6 (1) (2005) 125-134.

[60] G. Papadakis, P. Giaglaras, S. Kyritsis, A numerical method for determining thermal conductivity of porous media from in-situ measurements using a cylindrical heat source, Journal of Agricultural Engineering Research, 45(0) (1990) 281-293.

[61] M.J. Moran, H.N. Shapiro, D.D. Boettner, M.B. Bailey, Fundamentals of engineering thermodynamics, Wiley, 2010.

[62] L. Chen, Y. Wang, L. Peng, P. Fu, H. Jiang, Study on the interfacial heat transfer coefficient between AZ91D magnesium alloy and silica sand, Experimental Thermal and Fluid Science, 54(0) (2014) 196-203.

[63] G. Palumbo, V. Piglionico, A. Piccininni, P. Guglielmi, D. Sorgente, L. Tricarico, Determination of interfacial heat transfer coefficients in a sand mould casting process using an optimised inverse analysis, Applied Thermal Engineering, 78(0) (2015) 682-694.

[64] P.X. Jiang, R.N. Xu, W. Gong, Particle-to-fluid heat transfer coefficients in miniporous media, Chemical Engineering Science, 61(22) (2006) 7213-7222.

[65] P.-X. Jiang, X.-C. Lu, Numerical simulation of fluid flow and convection heat transfer in sintered porous plate channels, International Journal of Heat and Mass Transfer, 49(9–10) (2006) 1685-1695.

[66] J. Feng, H. Dong, J. Gao, J. Liu, K. Liang, Experimental study of gas–solid overall heat transfer coefficient in vertical tank for sinter waste heat recovery, Applied Thermal Engineering, 95 (2016) 136-142.

[67] R. Pešić, T. Kaluđerović Radoičić, N. Bošković-Vragolović, Z. Arsenijević, Ž. Grbavčić, Heat transfer between a packed bed and a larger immersed spherical particle, International Journal of Heat and Mass Transfer, 78(0) (2014) 130-136.

[68] J. Shent, S. Kaguei, N. Wakao, Measurements of particle-to-gas heat transfer coefficients from one-shot thermal responses in packed beds, Chemical Engineering Science, 36(8) (1981) 1283-1286.

[69] M. Al-Hasan, M.Q. Al-Odat, M. Al-Busoul, An experimental investigation of forced convection heat transfer from a coiled heat exchanger embedded in a packed bed, Experimental Heat Transfer, 25(4) (2012) 363-376.

[70] L.B. Younis, R. Viskanta, Experimental determination of the volumetric heat transfer coefficient between stream of air and ceramic foam, International Journal of Heat and Mass Transfer, 36(6) (1993) 1425-1434.

[71] X. Fu, R. Viskanta, J.P. Gore, Measurement and correlation of volumetric heat transfer coefficients of cellular ceramics, Experimental Thermal and Fluid Science, 17(4) (1998) 285-293.

[72] Z. Wu, C. Caliot, G. Flamant, Z. Wang, Numerical simulation of convective heat transfer between air flow and ceramic foams to optimise volumetric solar air receiver performances, International Journal of Heat and Mass Transfer, 54(7–8) (2011) 1527-1537.

[73] K. Ando, H. Hirai, Y. Sano, An accurate experimental determination of interstitial heat transfer coefficients of ceramic foams using the single blow method, Open Transport Phenomena Journal, 5(1) (2013) 7-12.

[74] J.J. Hwang, G.J. Hwang, R.H. Yeh, C.H. Chao, Measurement of interstitial convective heat transfer and frictional drag for flow across metal foams, Journal of Heat Transfer, 124(1) (2001) 120-129.

[75] A.G. Straatman, N.C. Gallego, B.E. Thompson, H. Hangan, Thermal characterization of porous carbon foam—convection in parallel flow, International Journal of Heat and Mass Transfer, 49(11–12) (2006) 1991-1998.

[76] D. Bhattacharyya, D.C.T. Pei, Heat transfer in fixed bed gas—solid systems, Chemical Engineering Science, 30(3) (1975) 293-300.

[77] C.-H. Li, B.A. Finlayson, Heat transfer in packed beds—a reevaluation, Chemical Engineering Science, 32(9) (1977) 1055-1066.

[78] N. Wakao, S. Kaguei, T. Funazkri, Effect of fluid dispersion coefficients on particle-to-fluid heat transfer coefficients in packed beds: Correlation of nusselt numbers, Chemical Engineering Science, 34(3) (1979) 325-336.

[79] A.G. Dixon, D.L. Cresswell, Theoretical prediction of effective heat transfer parameters in packed beds, AIChE Journal, 25(4) (1979) 663-676.

[80] E. Achenbach, Heat and flow characteristics of packed beds, Experimental Thermal and Fluid Science, 10(1) (1995) 17-27.

[81] K. Kamiuto, S.S. Yee, Heat transfer correlations for open-cellular porous materials, International Communications in Heat and Mass Transfer, 32(7) (2005) 947-953.

[82] M.S. Saidi, F. Rasouli, M.R. Hajaligol, Heat transfer coefficient for a packed bed of shredded materials at low peclet numbers, Heat Transfer Engineering, 27(7) (2006) 41-49.

[83] A. Nakayama, K. Ando, C. Yang, Y. Sano, F. Kuwahara, J. Liu, A study on interstitial heat transfer in consolidated and unconsolidated porous media, Heat and Mass Transfer, 45(11) (2009) 1365-1372.

[84] N. Wakao, S. Kagei, Heat and Mass Transfer in Packed Beds, Gordon and Breach Science Publishers, 1982.

[85] S.E. Mahgoub, Forced convection heat transfer over a flat plate in a porous medium, Ain Shams Engineering Journal, 4(4) (2013) 605-613.

[86] P.-X. Jiang, B.-X. Wang, D.-A. Luo, Z.-P. Ren, Fluid flow and convective heat transfer in a vertical porous annulus, Numerical Heat Transfer, Part A: Applications, 30(3) (1996) 305-320.

[87] J. Chao, J. Lu, H. Yang, M. Zhang, Q. Liu, Experimental study on the heat transfer coefficient between a freely moving sphere and a fluidized bed of small particles, International Journal of Heat and Mass Transfer, 80(0) (2015) 115-125.

[88] P.-X. Jiang, Z.-P. Ren, B.-X. Wang, Z. Wang, Forced convective heat transfer in a plate channel filled with solid particles, Journal of Thermal Science, 5(1) (1996) 43-53.

[89] G.F. Al-Sumaily, A. Nakayama, J. Sheridan, M.C. Thompson, The effect of porous media particle size on forced convection from a circular cylinder without assuming local thermal equilibrium between phases, International Journal of Heat and Mass Transfer, 55(13–14) (2012) 3366-3378.

[90] Z.Y. Zhou, A.B. Yu, P. Zulli, Particle scale study of heat transfer in packed and bubbling fluidized beds, AIChE Journal, 55(4) (2009) 868-884.

[91] H. Roshan, M.O. Cuthbert, M.S. Andersen, R.I. Acworth, Local thermal non-equilibrium in sediments: Implications for temperature dynamics and the use of heat as a tracer, Advances in Water Resources, 73 (2014) 176-184.

[92] D. Kunii, J.M. Smith, Heat transfer characteristics of porous rocks: II. Thermal conductivities of unconsolidated particles with flowing fluids, AIChE Journal, 7(1) (1961) 29-34.

[93] M.S. Saidi, M.R. Hajaligol, A. Mhaisekar, M. Subbiah, A 3D modeling of static and forward smoldering combustion in a packed bed of materials, Applied Mathematical Modelling, 31(9) (2007) 1970-1996.

[94] G. Debenest, V.V. Mourzenko, J.F. Thovert, Three-dimensional microscale numerical simulation of smoldering process in heterogeneous porous media, Combustion Science and Technology, 180(12) (2008) 2170-2185.

[95] I. Fabris, D. Cormier, J.I. Gerhard, T. Bartczak, M. Kortschot, J.L. Torero, Y.-L. Cheng, Continuous, self-sustaining smoldering destruction of simulated faeces, Fuel, 190 (2017) 58-66.

[96] L. Yermán, D. Cormier, I. Fabris, J. Carrascal, J.L. Torero, J.I. Gerhard, Y.L. Cheng, Potential Bio-oil Production from Smouldering Combustion of Faeces, Waste and Biomass Valorization, (2016) 1-10.

[97] G. Baud, S. Salvador, G. Debenest, J.-F. Thovert, New Granular Model Medium To Investigate Smoldering Fronts Propagation—Experiments, Energy & Fuels, 29(10) (2015) 6780-6792.

[98] M. Sennoune, S. Salvador, M. Quintard, Toward the Control of the Smoldering Front in the Reaction-Trailing Mode in Oil Shale Semicoke Porous Media, Energy & Fuels, 26(6) (2012) 3357-3367.

[99] M. Sennoune, S. Salvador, G. Debenest, Impact of a CO2-Enriched Gas on the Decarbonation of CaCO3 and the Oxidation of Carbon in the Smoldering Process of Oil Shale Semicoke, Energy & Fuels, 26(1) (2012) 391-399.

[100] M. Salman, J.I. Gerhard, D.W. Major, P. Pironi, R. Hadden, Remediation of trichloroethylene-contaminated soils by star technology using vegetable oil smoldering, Journal of Hazardous materials, 285 (2015) 346-355.

[101] L. Yermán, H. Wall, J. Torero, J.I. Gerhard, Y.L. Cheng, Smoldering Combustion as a Treatment Technology for Feces: Sensitivity to Key Parameters, Combustion Science and Technology, 188(6) (2016) 968-981.

[102] P. Pironi, C. Switzer, J.I. Gerhard, G. Rein, J.L. Torero, Self-Sustaining Smoldering Combustion for NAPL Remediation: Laboratory Evaluation of Process Sensitivity to Key Parameters, Environmental Science & Technology, 45(7) (2011) 2980-2986.

[103] L. Kinsman, J.L. Torero, J.I. Gerhard, Organic liquid mobility induced by smoldering remediation, Journal of Hazardous materials, 325 (2017) 101-112.

[104] A. D6539, Standard test method for measurement of pneumatic permeability of partially saturated porous materials by flowing air, in, ASTM International, West Conshohocken, PA, 2000 (2006).

[105] S.E. Gustafsson, Transient plane source techniques for thermal conductivity and thermal diffusivity measurements of solid materials, Review of Scientific Instruments, 62(3) (1991) 797-804.

[106] ASTM-E1269-11, Standard test method for determining specific heat capacity by differential scanning calorimetry, in, ASTM International, West Conshohocken, PA, 2011.

[107] S. Lagüela, P. Bison, F. Peron, P. Romagnoni, Thermal conductivity measurements on wood materials with transient plane source technique, Thermochimica Acta, 600 (2015) 45-51.

[108] Y. Yang, T.G. Voskuilen, T.L. Pourpoint, D.R. Guildenbecher, J.P. Gore, Determination of the thermal transport properties of ammonia borane and its thermolysis

product (polyiminoborane) using the transient plane source technique, International Journal of Hydrogen Energy, 37(6) (2012) 5128-5136.

[109] T. Log, S.E. Gustafsson, Transient plane source (TPS) technique for measuring thermal transport properties of building materials, Fire and Materials, 19(1) (1995) 43-49.

[110] A. Bejan, Mass Transfer, Convection heat transfer: John Wiley & Sons, Incorporated, 1995.

[111] H. Darcy, Les fontaines publiques de la ville de Dijon: Exposition et application des principes a suivre et des formules a employer dans les questions de distribution d'eau; ouvrage terminé par un appendice relatif aux fournitures d'eau de plusieurs villes au filtrage des eaux et a la fabrication des tuyaux de fonte, de plomb, de tole et de bitume. Atlas, Victor Dalmont, Libraire des Corps imperiaux des ponts et chaussées et des mines, 1856.

[112] É. Clapeyron, Mémoire sur la puissance motrice de la chaleur, Jacques Gabay, 1834.

[113] S. Rosseland, Astrophysik aud Atom-Theoretische Grundlagen, Springer, Berlin, 1931.

[114] F.P. Incropera, Fundamentals of heat and mass transfer, John Wiley, 2007.

[115] D.W. Marquardt, An algorithm for least square estimation of nonlinear parameters, Journal of the Society for Industrial and Applied Mathematics, 11(2) (1963) 431–441.

[116] K. Levenberg, A method for the solution of certain non-linear problems in least square, Quarterly of Applied Mathematics, 2(2) (1944) 164–168.

[117] M.N. Özisik, H.R.B. Orlande, Inverse heat transfer, (2000) 35 - 114.

[118] M.A. Bazelatto Zanoni, H. Massard, M. Ferreira Martins, Formulating and optimizing a combustion pathways for oil shale and its semi-coke, Combustion and Flame, 159(10) (2012) 3224-3234.

[119] M.A.B. Zanoni, H. Massard, M.F. Martins, S. Salvador, Application of inverse problem and thermogravimetry to determine the kinetics of oil shale pyrolysis, High Temperatures - High Pressures, 41(3) (2012) 197-213.

[120] A. Bejan, K.R. Khair, Heat and mass transfer by natural convection in a porous medium, International Journal of Heat and Mass Transfer, 28(5) (1985) 909-918.

Chapter 4

4 The Role of Local Thermal Non-Equilibrium in Modelling Smouldering Combustion of Organic Liquids[2]

4.1 Introduction

Smouldering combustion is a surface oxidation reaction common to porous organic solids [1]. Organic liquids embedded in an inert porous matrix can also smoulder due to the production of char during pyrolysis [2, 3]. Soil is frequently contaminated by liquid hydrocarbons, such as bitumen, coal tar, and crude oil, and intentional smouldering is gaining acceptance as a soil remediation technology [4-6]. Numerical modelling of these smouldering processes is essential to determine operating conditions but simulating the intentional smouldering of liquids for remediation is challenging and novel. Models to date have either focused on porous organic solids [7, 8] or have been heuristic engineering tools that significantly simplified chemical reactions and mass transfer processes [9, 10].

Smouldering numerical models require appropriate chemistry. Smouldering kinetic mechanisms have received significant attention and been described with varying degrees of detail, from simple [11] to complex [8] and are typically presented as Arrhenius-type equations. The Arrhenius parameters – pre-exponential factor (A), activation energy (E), and heat of reaction (ΔH) – are obtained by analyzing Thermogravimetry (TG), Differential Thermogravimetry (DTG), and Differential Scanning Calorimetry (DSC) experiments on the fuel [1, 7, 12]. An analytical analysis [13] is useful for simple chemical schemes while complex schemes require stochastic methods such as Genetic Algorithms [7].

Smouldering numerical models also require appropriate heat transfer processes. In contrast to chemistry, heat transfer in smouldering has received little attention. Smouldering models treat heat transfer with one of two approaches [14]: Local Thermal Equilibrium (LTE) [11,

15] and Local Thermal Non-Equilibrium (LTNE) [8, 16]; the former assumes that the gas and the solid are in thermal equilibrium while the latter allows for heat exchange between them. There are numerous reasons to hypothesize that LTNE is important for simulating smouldering. Oliveira and Kaviany [14] note that highly exothermic reactions may cause LTNE. In addition, heat transfer (via convection and conduction) controls pyrolysis of the fuel ahead of the smouldering front and controls cooling of the hot, clean sand behind the front (heat is transferred to the cold air and is lost radially), with both affecting the energy balance at the reaction zone. Moreover, at high gas velocities smouldering can be extinguished by heat transfer processes [1, 17].

LTNE models require an interfacial heat transfer coefficient (h_{sg}). This has been quantified via empirical Nusselt (Nu) versus Reynolds (Re) and Prandtl (Pr) numbers correlations [18] that are not related to smouldering. For example, Wakao et al. [18]:

$$Nu = \frac{h_{sg}d_p}{k_g} = 2 + 1.1\left(Re^{0.6}Pr^{1/3}\right) \tag{4.1}$$

is valid for $15 \leq Re \leq 8500$, whereas natural and intentional smouldering typically exhibits $Re<15$. Nevertheless, Equation (4.1) has been widely employed in smouldering numerical models, predicting large h_{sg} values [8], which may lead to the untested conclusion that the gas and solid are in thermal equilibrium in smouldering [16].

Chapter 3 used the convective propagation of a heat wave through sand (no smouldering) to develop a new correlation for h_{sg}:

$$Nu = \frac{h_{sg}d_p}{k_g} = 0.001\left(Re^{1.97}Pr^{1/3}\right) \tag{4.2}$$

valid for $Pr=0.72$, $0.5 \leq Re \leq 31$, and $0.125 < d_p < 2.000$ mm; these ranges are typical for smouldering remediation of liquids [6]. A recently developed criterion (Chapter 3) for the validity of assuming local thermal equilibrium was demonstrated to be violated within these parameter ranges, indicating that LTNE is appropriate and essential for heat transfer in these scenarios. Heat generation and heat transfer parameters have the potential to compensate for errors when models are calibrated to experiments. Therefore, the minimum

kinetic mechanisms necessary to simulate smouldering and the appropriate approach for heat transfer remain open questions.

The objective of this study was to develop and build confidence in a one-dimensional numerical model that simulates smouldering with explicitly quantified heat transfer. The target scenario was the intentional (forced), self-sustaining smouldering remediation of bitumen-contaminated sand. Simple smouldering chemistry (one pyrolysis and one oxidation reaction) was employed as a baseline scenario. The kinetic constants were populated from TG/DTG/DSC experiments. Only four independent parameters that minimize the potential for error compensation were calibrated to a base case smouldering experiment (conducted in triplicate). Confidence in the model was obtained by comparing predictions to observations of independent experiments. The role of heat transfer was analyzed by considering various LTE/LTNE models and comparing them to the experimental observations. This comparison provides unique conclusions about the importance and magnitude of LTNE in smouldering processes.

4.2 Methodology

4.2.1 Experiments

The smouldering experiments were carried out in a stainless-steel column (Figure 4.1) following an established methodology [19]. A base case experiment (Exp. #1) was conducted in triplicate and another three experiments (Exp. #2-4) varied the injected Darcy air flux (u_g), Table 4.1.

Table 4.1: Smouldering Experiments.

Exp. # [-]	$u_g{}^a$ [m s^{-1}]	Saturation (S_b) [-]	Repeats [-]	Air on (t_g) [s]	Heater off (t_h) [s]
1	0.058	0.15	3	4532 ± 378 [b]	4865 ± 300 [b]
2	0.025	0.15	1	4926	5357
3	0.050	0.15	1	5287	5670
4	0.083	0.15	1	5077	5329

[a] Volume per unit cross-sectional area per unit time; [b] 95% confidence interval

The column contained 0.10 m of clean sand (d_p=0.88 mm, particle density (ρ_s)=2650 kg m^{-3}) below the heater and a 0.35 m layer (L) of a mixture (bulk density of 1726 kg m^{-3}) of sand and bitumen (density (ρ_b)=1030 kg m^{-3}, PG 58-28, McAsphalt Industry Limited) above it. Eleven thermocouples spaced 0.035 m apart were assumed to measure the solid (sand/bitumen) temperature (Chapter 3) along the column center-line every 2 seconds. Evaluating combustion only by thermocouple data is appropriated here, since the primary goal is to predict smouldering front propagation rates, peak temperatures, and temperature distributions. The apparatus was insulated with 5 cm of insulation (high-temperature mineral wool, McMaster-Carr) to minimize heat losses; under such conditions it is usually observed that approximately a 150 °C temperature drop occurs from the center-line to the wall, although radial temperatures were not measured in this case. Each experiment was initiated by powering the resistive heater until the temperature of the second thermocouple (the first in the bitumen, x=0.12 m) reached 400 ºC. Then, air injection at a fixed rate was supplied, which initiated smoldering. The heater was then switched off while the air was maintained. A self-sustained smouldering front propagated upwards until all the bitumen was consumed, leaving clean sand.
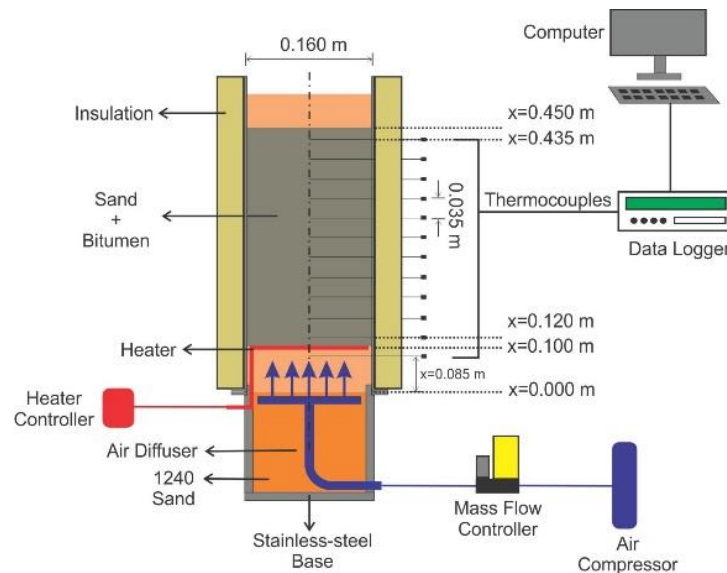
Figure 4.1: Schematic of the experimental apparatus.

TG, DTG, and DSC experiments on the bitumen were conducted at heating rates (β) of 10, 20, 30, and 40 K min^{-1} under N_2 and air atmospheres (see Appendix B). Since the DTG and DSC results suggested two main decomposition peaks, one endothermic and one exothermic, a 2-step kinetic mechanism was proposed:

$$Bitumen \xrightarrow{R_b} v_c Char + (1 - v_c) Gas$$
$$Char + v_{O_2} O_2 \xrightarrow{R_c} Gas$$

(4.3)
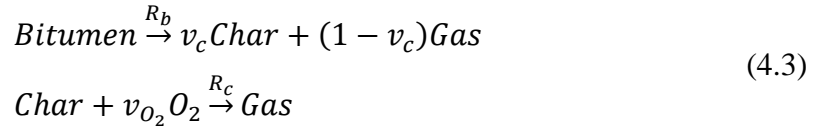
Competing reactions are not considered since their influence on the observed smouldering behaviour is expected to be minor. Table 4.2 provides all determined values, including the reaction rates (R_i) described as first-order Arrhenius reactions, and the Arrhenius parameters (A_i and E_i) for each reaction (i) obtained by the use of the Kissinger method [13, 20] (see Appendix B). Heat of reactions (ΔH_i) for pyrolysis and oxidation were determined from DSC experiments by the time integration of the heat flow over mass loss (mW mg^{-1}) under N_2 and air, respectively.

Table 4.2: Kinetic Parameters Calculated by Kissinger Method from TG and DSC Experiments under N_2 and Air at four Heating Rates (10, 20, 30, 40 K min^{-1}).

	N₂ (Pyrolysis)				Air (Oxidation)			
B [K min^{-1}]	T_p [K]	$log (A_p)$ [log(s^{-1})]	E_p [kJ mol^{-1}]	ΔH_p [MJ kg^{-1}]	T_p [K]	$log (A_c)$ [log(s^{-1})]	E_c [kJ mol^{-1}]	ΔH_c [MJ kg^{-1}]
10	725				848			
20	746				885			
		7.5	135	1.62		3.0	90	-38.73
30	758				921			
40	769				930			

$$R_b = A_b exp\left(-\frac{E_b}{R_g T_s}\right)(Y_b) \qquad R_c = A_c exp\left(-\frac{E_c}{R_g T_s}\right)(Y_c)(Y_{O_2})$$

4.2.2   Modelling

A new, one-dimensional numerical model was developed in COMSOL Multiphysics (*Version 5.0*). The computational domain represents the 0.45 m sand/bitumen pack (Figure 4.1). The model considers the conservation of mass for solid:

$$\frac{\partial (Y_b)}{\partial t} = -R_b$$

$$\frac{\partial (Y_c)}{\partial t} = v_c R_b - R_c$$

(4.4)

and gas:

$$\frac{\partial \left(\rho_g \phi_g\right)}{\partial t} + \frac{\partial \left(\rho_g u_g\right)}{\partial x} = (\phi_b \rho_b)\left((1-v_c)R_b + \left(1-v_{O_2}\right)R_c\right)$$

(4.5)

phases, where v_c is the char yield coefficient and v_{O2} is the oxygen stoichiometric coefficient. Equation (4.5) adopts Darcy's Law without gravity effects and the gas density (ρ_g) follows the ideal gas law. A homogeneous porous medium was assumed with intrinsic permeability $k_p=1\times10^{-9}$ m^2 (Chapter 3 and Appendix A) and sand particles were taken as spheres ($A_{s,sp}/V_{sp}=6(1-\phi)/d_p$). The bulk transport of oxygen is described by:

$$\phi_g \frac{\partial \left(\rho_g Y_{O_2}\right)}{\partial t} + \frac{\partial \left(\rho_g u_g Y_{O_2}\right)}{\partial x} = \phi_g \frac{\partial}{\partial x}\left(\rho_g D_g \frac{\partial Y_{O_2}}{\partial x}\right) - (\phi_b \rho_b)v_{O_2}R_c$$

(4.6)

where the diffusion coefficient $D_g=4.53\times10^{-5}$ m^2 s^{-1} [17]. The model solves the transient energy equation for both solid (representing the combined, effective properties of bitumen plus sand) (T_s) and gas (T_g) phases, respectively:

$$\left(\rho C_p\right)_{eff} \frac{\partial T_s}{\partial t} = \frac{\partial}{\partial x}\left(k_{eff}\frac{\partial T_s}{\partial x}\right) - U\left(\frac{A_{s,cl}}{V_{cl}}\right)(T_s - T_0) + h_{sg}\left(\frac{A_{s,sp}}{V_{sp}}\right)(T_g - T_s) - Q$$

(4.7)

$$\phi_g \left(\rho_g C_{p_g}\right)\frac{\partial T_g}{\partial t} + \rho_g C_{p_g}u_g \frac{\partial T_g}{\partial x} = \phi_g \frac{\partial}{\partial x}\left(k_g \frac{\partial T_g}{\partial x}\right) + h_{sg}\left(\frac{A_{s,sp}}{V_{sp}}\right)(T_s - T_g)$$

(4.8)

with h_{sg} specified by Equation (4.2) unless otherwise indicated. Effective thermal properties for the solid/liquid phases were considered: $(\rho C_p)_{eff}=(1-\phi)(\rho_s C_{ps})+(\phi_b)(\rho_b C_{pb})$, $k_{eff}=(1-\phi)(k_s+k_{rad})+(\phi_b)(k_b)$, and $\phi=\phi_g+\phi_b$, where total porosity $\phi=0.37$, liquid-filled porosity $\phi_b=\phi S_b=0.055$, and gas-filled porosity $\phi_g=0.315$.

Conduction, convection, and radiation are included with the latter using the Rosseland approximation and expressed as a radiative conductivity ($k_{rad}=16\sigma d_p T_s^3/3$), with the Stefan–Boltzmann constant $\sigma= 5.67\text{x}10^{-8}$ W m^{-2} K^{-4} (Chapter 3). Since temperature data are measured at the column center-line, radial heat losses are taken into account via a global heat loss coefficient, U [8], which used the surface area per unit volume ($A_{s,cl}/V_{cl}=2/r$) of the column, with radius $r=0.08$ m. The thermal properties of air and sand vary with temperature (see Chapter 3 and Appendix A for measurements and details) whereas bitumen specific heat capacity ($C_{pb}=921$ J kg^{-1} K^{-1} [21]) and thermal conductivity ($k_b=0.15$ W m^{-1} K^{-1} [22]) are assumed constant. The fuel is considered immobile. The source/sink term (Q) in Equation (4.7) is defined as:

$$Q = (\phi_b \rho_b)(\Delta H_c R_c + \Delta H_b R_b) \tag{4.9}$$

where ΔH_b and ΔH_c can be found in Table 4.2. The initial and boundary conditions are defined in Table 4.3. Note that the inlet boundary specifies a constant, positive air mass flux after the air is turned on (time t_g) and the outlet boundary specifies free air exit and zero conduction; as a result, the only means for energy to leave the column is via the heat content of the exiting air.

Table 4.3: Initial and Boundary Conditions for Numerical Model.

Eq.	Initial Condition	Boundary Condition
(4.4)	$t = 0 \Rightarrow Y_b = 1;\ Y_c = 0$	-
(4.5)	$t = 0 \Rightarrow P_g = 101375\ Pa$	$x = 0.00\ m \Rightarrow \rho_g u_g(t) \to \begin{cases} u_g(t) = 0 \to 0 \le t \le t_g \\ u_g(t) = u_g \to t_g < t \le t_f \end{cases}$ $x = 0.45\ m \Rightarrow P_g = 101375\ Pa$
(4.6)	$t = 0 \Rightarrow Y_{O_2} = 0.204$	$x = 0.00\ m \Rightarrow Y_{O_2} = 0.204$ $x = 0.45\ m \Rightarrow -D_g \dfrac{\partial(\rho_g Y_{O_2})}{\partial x} = h_m\left(Y_{O_2,0} - Y_{O_2}\right) \to h_m = 100\ kg\ m^{-2}\ s^{-1}$
(4.7-4.8)	$t = 0 \Rightarrow T_s = T_g = T_0 = 298\ K$	$x = 0.10\ m \Rightarrow \begin{cases} -(k_{eff})\dfrac{\partial T_s}{\partial x} = 25\ kW\ m^2 \to 0 \le t \le t_h \\ -(k_{eff})\dfrac{\partial T_s}{\partial x} = 0 \to t_h < t \le t_f \\ T_g = 298\ K \end{cases}$ $x = 0.45\ m \Rightarrow \begin{cases} -(k_{eff})\dfrac{\partial T_s}{\partial x} = 0 \\ -(k_g)\dfrac{\partial T_g}{\partial x} = 0 \end{cases}$

Three parameters (v_{O2}, v_c, and U) are not independently known, and thus their values were calibrated to experimental results. Note that the U value calculated in Chapter 3 was too small for smouldering conditions, where temperatures are much higher (i.e., higher heat losses). Then, U had to be calibrated for smouldering conditions. A sensitivity analysis to all key parameters (Appendix B) revealed that the calculated A_c produced a non-self-sustaining smouldering front in all cases, which is not realistic. TG heating rates are inevitably smaller than those relevant to smouldering, privileging some minor, low temperature reactions that disappear at high heating rates [1], therefore, affecting the A_c value. Thus, A_c was corrected by treating it as a fourth fitting parameter.

The model calibration involved minimizing the error between the model prediction (*num*) and Exp. #1 (*exp*, average of three repeats) giving equal weight to four aspects of the fit: average peak temperature (T_p), smouldering front velocity (v_f), temperature versus time plots ($T(t)$), and temperature versus distance profiles ($T(x)$):

$$ERROR[\%] = \frac{1}{4}\left|\frac{T_{p,exp} - T_{p,num}}{T_{p,num}}\right| + \frac{1}{4}\left|\frac{v_{f,exp} - v_{f,num}}{v_{f,num}}\right| + \frac{1}{4}NRMSD_{T(t)}$$

$$+ \frac{1}{4}NRMSD_{T(x)}$$

(4.10)

where the average Normalized Root-Mean-Square Deviation (NRMSD) follows the approach taken in Chapter 3. v_f was calculated from the time lapse of the front arrival at two consecutive thermocouples and their known separation distance [6], and a single average value for each experiment was used. The four parameters (A_c, v_{O2}, v_c, and U) were systematically adjusted in following ranges (see Appendix B): U=5–16 W m^{-2} K^{-1}, log(A_c)=3–6 (with 3 being the value obtained from independent experiments (Table 4.2)), v_c=0.4–0.6, and v_{O2}=0.5–3 kg O$_2$ kg fuel^{-1}. The final choice of U=13 W m^{-2} K^{-1}, log(A_c)=4.9, v_c=0.55, and v_{O2}=1.7 kg O$_2$ kg fuel^{-1} resulted in the minimum ERROR=13±3%.

4.3 Results

4.3.1 Model Calibration

Figure 4.2 compares Exp. #1 (three repeats) and the calibrated simulation. The experimental time (t) was normalized, for the purpose of averaging the experiments, and is referred to as Dimensionless Time (DT=$(t-t_g)v_f/L$ [19]) where DT<0 is the pre-heating period, DT=0 is when the air is turned on and smouldering begins, and DT=1 is when no fuel remains. Excellent agreement for temperature in time and space is observed. The average v_f was 4.16 mm min^{-1} (numerical) and 4.96±0.65 mm min^{-1} (experimental) and the average T_p was 641±11 ºC (experimental) and 679 ºC (numerical). Small differences are observed at early and late time, which is not surprising since experimental observations indicate edge effects not considered in the model. Note that the abrupt slope changes in Figure 4.2b are the result of the spatial resolution (0.35 m) of the thermocouples in the experiment and the matching resolution plotted for the numerical data; when the numerical data is plotted at the mesh resolution (0.1 mm), the temperature profiles are smooth (figure not shown).
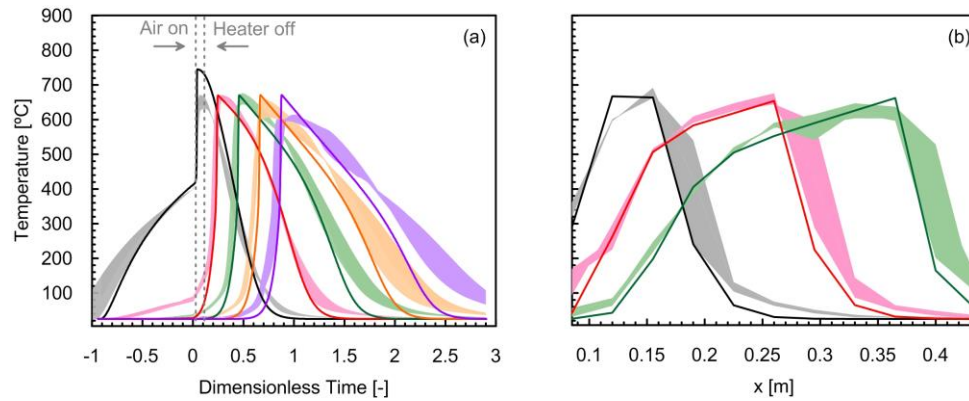
Figure 4.2: (a) Temperature evolution versus dimensionless time (DT) and (b) temperature profile versus height of the column (x). The coloured shading encompass three experimental repeats and show (a) thermocouple positions (x) from 0.12 to 0.40 m with 0.07 m intervals and (b) experimental DT = 0.2, 0.5, and 0.8. Solid lines describe the model-predicted sand/bitumen temperature (T_s), plotted at the same DTs (a) and same spatial resolution (b) for comparison purposes.

4.3.2 Developing Confidence in the Model

The calibrated model was tested against three additional smouldering experiments (Exp. #2-4, Table 4.1) without any fitting. Figure 4.3a presents the temperature-time plots for Exp. #3; this an example representative of the results of the three additional experiments. The predicted bitumen/sand temperatures show excellent agreement in time and space, with ERROR=9%. Figure 4.3b compares all four experiments in terms of T_p and v_f. Very good agreement between predicted and observed average T_p and v_f was found. Smouldering front velocity increased linearly with increased air flux, as expected [5]. Small differences in T_p at high air flux and in v_f at low air flux are noted. This is likely due to the model's simple approach to handling the global energy balance. Further work is currently investigating these additional factors, which appear to manifest in cases that approach the limits of smouldering. Nevertheless, the model testing performed provides confidence that this simple model does satisfactorily simulate smouldering front propagation under robust, self-sustaining conditions.
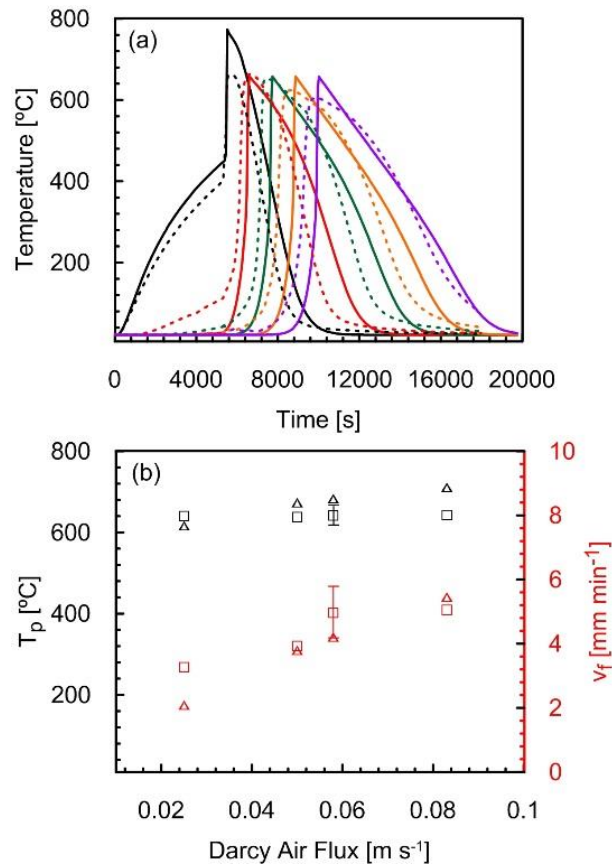
Figure 4.3: (a) Temperature vs. time for Exp. #3 (u_g=0.05 m s^{-1}). Dashed lines are experimental data and solid lines are model-predicted sand/bitumen temperature. Colours represent thermocouple positions (x) from 0.12 to 0.40 m with 0.07 m intervals. (b) Peak temperature and smouldering front velocity versus Darcy air flux for all cases: (■) experimental and (▲) numerical data. The error bars denote the variation observed in three repeats of Exp. #1; that simulation was calibrated while the other three were independent.

4.3.3   LTE vs LTNE

Since the difference between gas and solid phase temperatures cannot be easily assessed in experiments, the model is an excellent tool to evaluate the role of LTNE in smouldering scenarios. Using the calibrated model and only changing the h_{sg} correlation, Figure 4.4 compares LTE, LTNE–Eq. (4.1), and LTNE–Eq. (4.2) to Exp. #1 when the smouldering front was midway along the column. Note that the LTE model replaces Equations (4.7) and (4.8) with a single temperature equation. In the Figure, the LTE and LTNE–Eq. (4.1) results overlay each other, indicating that the Wakao et al. [18] correlation predicts h_{sg} sufficiently

large that it results in LTE; this was true for all smouldering scenarios modelled in this work (results not shown).
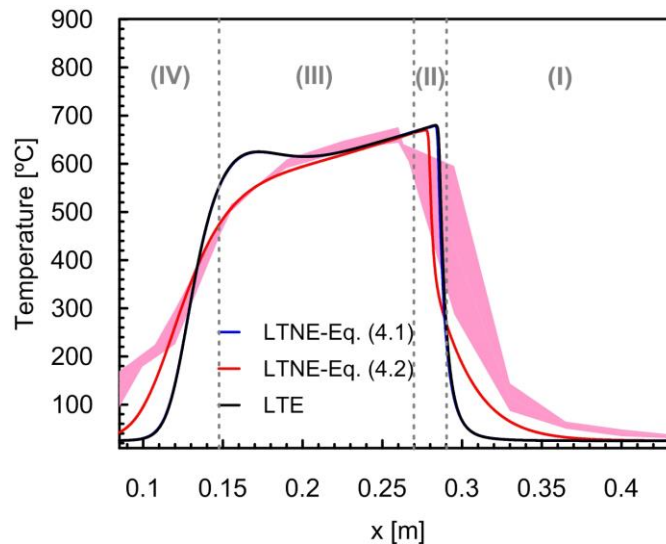
Figure 4.4: Temperature profile versus height of the column (x) at DT=0.5 for Exp. #1. The shading shows experimental data for three repeats. Note that the solid black and blue lines overlay each other. Solid lines are plotted at numerical resolution (mesh size: 0.1 mm; see mesh analysis in Appendix C). Four distinct regions are identified (see text).

Four regions can be identified in Figure 4.4. In Region (I), heat transfer mechanisms increase the temperature of the virgin fuel, but no chemical reactions occur (see Figure 4.5). Figure 4.4 reveals that the LTE and LTNE–Eq. (4.1) simulations significantly under-predicted temperatures in Region (I), whereas the LTNE–Eq. (4.2) simulation provides more satisfactory results, with a slower, more realistic spread of the heating front.

Region (II) contains the smouldering front, i.e., where pyrolysis and oxidation reactions occur. Figure 4.5 confirms that the front is thin, with all the energy absorbed by pyrolysis and released by oxidation located between 0.275 and 0.285 m (Figure 4.5c). Correspondingly, all O_2 consumption occurs in this 1 cm front, decreasing from 20.4% to 15.0% (Figure 4.5a). Detailed experiments in [3] confirm that smouldering fronts are observed to be on the order of this thickness. Figure 4.5b shows that within this narrow

front, pyrolysis is converting bitumen to char and then being rapidly oxidized; ultimately, no fuel remained behind the front, which matches all experiments conducted (data not shown). Figure 4.5c confirms that oxygen consumption is only by oxidation. The excellent prediction of the experiment in this region (Figure 4.4) suggests that one oxidation and one pyrolysis reactions are sufficient for predicting the self-sustained smouldering front under robust conditions.
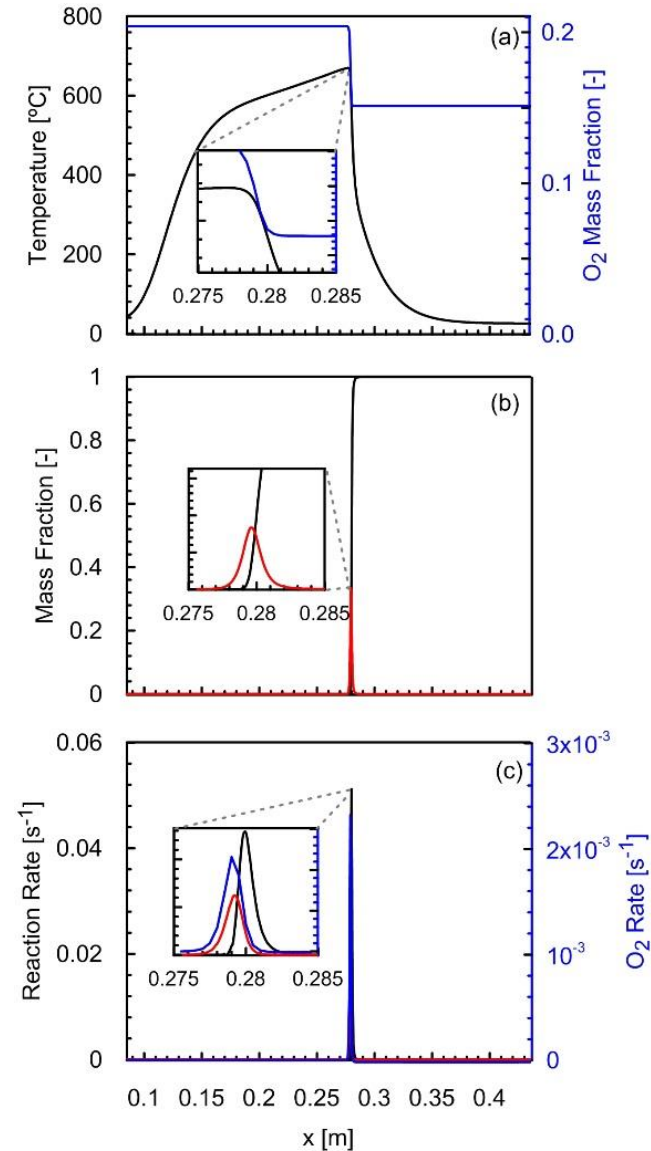
Figure 4.5: Model predictions versus height of the column (x) for Exp #1 at DT=0.5 for: (a) sand/bitumen temperature profile (black) and O_2 mass fraction (blue), (b) mass fractions of bitumen (black) and char (red) and (c) reaction rates for bitumen (black) and char (red), and O_2 consumption rate (blue). These plots correspond to Figure 4.4.

Region (III), located behind the front in Figure 4.4, is controlled by the balance between radial heat losses and heat storage by the clean sand. Despite all simulations using the same U (13 W m^{-2} K^{-1}), both LTE and LTNE–Eq. (4.1) predict the retention of too much heat while LTNE–Eq. (4.2) more accurately predicts the balance of heat retention, loss, and transfer behind the front. Region (IV) represents the heat transfer between the hot clean sand behind the smouldering front and the cold incoming air. Here too, the LTNE–Eq. (4.2) model shows the best agreement with experiment, with LTE or LTNE–Eq. (4.1) simulating extremely fast cooling due to over-predicted interphase heat transfer.

Figure 4.6 presents the predicted magnitude of LTNE for all simulations. LTNE–Eq. (4.2) used in the model to predict smouldering conditions (Table 4.1) showed maximum $\Delta T_{sg}/T_p$ near the heater and decreasing with column height, as expected. The average $\Delta T_{sg}/T_p$ was 36% for air fluxes of 0.025, 0.050, and 0.058 m s^{-1}, and 31% for 0.083 m s^{-1}. This suggests the magnitude of LTNE is significant for smouldering and relatively insensitive to air flux. In contrast, using LTNE–Eq. (4.1) resulted in predictions of $\Delta T_{sg}/T_p$ <1% for the base case (0.058 m s^{-1}), confirming the earlier conclusion that Wakao et al. [18] applied to smouldering predicts essentially LTE conditions.

Figure 4.6 also compares Exp. #4 (Table 4.1) to an identical experiment conducted in Chapter 3 except the latter contained no fuel (simply heat transfer in sand by convection). Figure 4.6 demonstrates that heat transfer in the absence of smouldering exhibits an average $\Delta T_{sg}/T_p$=6%, which is more than LTE but less than the smouldering cases. The approximately six times increase in the magnitude of LTNE is not surprising since smouldering oxidation reactions significantly increase temperatures in the fuel/solid phase. This confirms the widely held – but seldom tested – Oliveira and Kaviany [14] assumption that large gradients caused by highly exothermic reactions can create and enhance LTNE conditions.
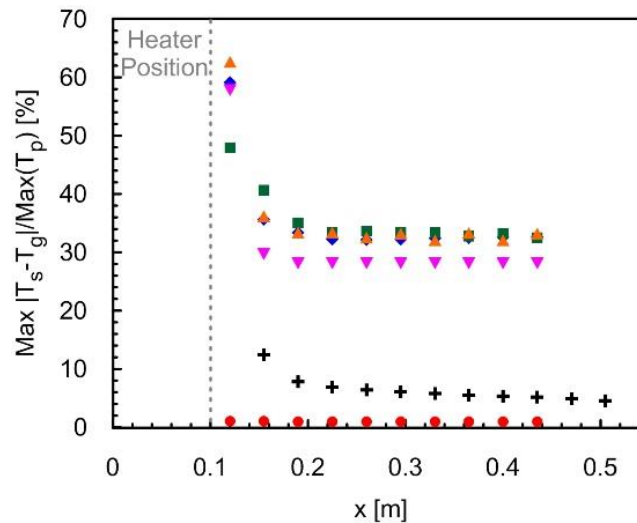
Figure 4.6: Normalized maximum difference between model-predicted solid (sand plus bitumen) temperature (T_s) and gas (T_g) temperature varying with column height (x). Smouldering: LTNE–Eq. (4.2): (■) 0.025 m s^{-1}, (▲) 0.050 m s^{-1}, (♦) 0.0580 m s^{-1}, (▼) 0.083 m s^{-1}, and (●) LTNE–Eq. (4.1), 0.058 m s^{-1}; Heat Transfer: (+) LTNE–Eq. (4.2): Exp. *A* from Chapter 3, 0.089 m s^{-1}.

4.4 Conclusions

A one-dimensional numerical model of smouldering was developed. It was primarily parameterized with independently measured parameters and, for the remaining four parameters, calibrated against a single, forced air injection, upwards smouldering column experiment containing bitumen mixed with sand. This application represents a soil remediation strategy that is gaining wide acceptance. Confidence in the model was gained by its good predictions of peak temperatures, front velocities, and temperatures in space and time for experiments with different air flow rates.

A relatively simply, two-step kinetic mechanism was found to be sufficient to reproduce the main behaviour of self-sustained smouldering under robust conditions if heat transfer between the phases is treated correctly. LTNE between air and fuel/solid was demonstrated to be significant in smouldering, and incorporating LTNE is clearly important for predicting heat transfer ahead and behind the front during smouldering propagation. Moreover, it was confirmed that the widely employed Wakao et al. [18] correlation

essentially predicts LTE and these predictions provide a less accurate match to experiments.

This work represents the first step in developing a model to confidently simulate the wide range of scenarios relevant to liquid smouldering in porous media. Ongoing work is exploring the prediction of smouldering limits and extinction. Nevertheless, it is expected the conclusions presented are widely applicable to smouldering combustion research and applications.

4.5 References

[1] T.J. Ohlemiller, Modeling of smoldering combustion propagation, Progress in Energy and Combustion Science, 11(4) (1985) 277-310.

[2] G. Debenest, V.V. Mourzenko, J.F. Thovert, Smouldering in fixed beds of oil shale grains. A three-dimensional microscale numerical model, Combustion Theory and Modelling, 9(1) (2005) 113-135.

[3] M.F. Martins, S. Salvador, J.F. Thovert, G. Debenest, Co-current combustion of oil shale - Part 2: Structure of the combustion front, Fuel, 89(1) (2010) 133-143.

[4] P. Pironi, C. Switzer, G. Rein, A. Fuentes, J.I. Gerhard, J.L. Torero, Small-scale forward smouldering experiments for remediation of coal tar in inert media, Proceedings of the Combustion Institute, 32(2) (2009) 1957-1964.

[5] P. Pironi, C. Switzer, J.I. Gerhard, G. Rein, J.L. Torero, Self-Sustaining Smoldering Combustion for NAPL Remediation: Laboratory Evaluation of Process Sensitivity to Key Parameters, Environmental Science and Technology, 45(7) (2011) 2980-2986.

[6] C. Switzer, P. Pironi, J.I. Gerhard, G. Rein, J.L. Torero, Self-sustaining smoldering combustion: A novel remediation process for non-aqueous-phase liquids in porous media, Environmental Science and Technology, 43(15) (2009) 5871-5877.

[7] G. Rein, C. Lautenberger, A.C. Fernandez-Pello, J.L. Torero, D.L. Urban, Application of genetic algorithms and thermogravimetry to determine the kinetics of polyurethane foam in smoldering combustion, Combustion and Flame, 146(1-2) (2006) 95-108.

[8] G. Rein, A. Carlos Fernandez-Pello, D.L. Urban, Computational model of forward and opposed smoldering combustion in microgravity, Proceedings of the Combustion Institute, 31(2) (2007) 2677-2684.

[9] T. Hasan, J.I. Gerhard, R. Hadden, G. Rein, Self-sustaining smouldering combustion of coal tar for the remediation of contaminated sand: Two-dimensional experiments and computational simulations, Fuel, 150 (2015) 288-297.

[10] S.L. MacPhee, J.I. Gerhard, G. Rein, A novel method for simulating smoldering propagation and its application to STAR (Self-sustaining Treatment for Active Remediation), Environmental Modelling & Software, 31(0) (2012) 84-98.

[11] H. Fadaei, M. Sennoune, S. Salvador, A. Lapene, G. Debenest, Modelling of non-consolidated oil shale semi-coke forward combustion: Influence of carbon and calcium carbonate contents, Fuel, 95(0) (2012) 197-205.

[12] M.A. Bazelatto Zanoni, H. Massard, M. Ferreira Martins, Formulating and optimizing a combustion pathways for oil shale and its semi-coke, Combustion and Flame, 159(10) (2012) 3224-3234.

[13] H.E. Kissinger, Reaction kinetics in differential thermal analysis, Analytical Chemistry, 29(11) (1957) 1702-1706.

[14] A.A.M. Oliveira, M. Kaviany, Nonequilibrium in the transport of heat and reactants in combustion in porous media, Progress in Energy and Combustion Science, 27(5) (2001) 523-545.

[15] X. Huang, G. Rein, H. Chen, Computational smoldering combustion: Predicting the roles of moisture and inert contents in peat wildfires, Proceedings of the Combustion Institute, 35(3) (2015) 2673-2681.

[16] S.V. Leach, G. Rein, J.L. Ellzey, O.A. Ezekoye, J.L. Torero, Kinetic and fuel property effects on forward smoldering, Combustion and Flame, 120(3) (2000) 346-358.

[17] J.L. Torero, A.C. Fernandez-Pello, M. Kitano, Opposed Forced Flow Smoldering of Polyurethane Foam, Combustion Science and Technology, 91(1-3) (1993) 95-117.

[18] N. Wakao, S. Kaguei, T. Funazkri, Effect of fluid dispersion coefficients on particle-to-fluid heat transfer coefficients in packed beds: Correlation of nusselt numbers, Chemical Engineering Science, 34(3) (1979) 325-336.

[19] L. Kinsman, J.L. Torero, J.I. Gerhard, Organic liquid mobility induced by smoldering remediation, Journal of Hazardous materials, 325 (2017) 101-112.

[20] K.-Y. Li, X. Huang, C. Fleischmann, G. Rein, J. Ji, Pyrolysis of Medium-Density Fiberboard: Optimized Search for Kinetics Scheme and Parameters via a Genetic Algorithm Driven by Kissinger's Method, Energy & Fuels, 28(9) (2014) 6130-6139.

[21] R.H. Perry, D.W. Green, Perry's Chemical Engineers' Handbook, 7th ed., McGraw-Hill, New York, USA, 1999.

[22] S.K. Elam, I. Tokura, K. Saito, R.A. Altenkirch, Thermal conductivity of crude oils, Experimental Thermal and Fluid Science, 2(1) (1989) 1-6.

Chapter 5

5 Determining the Conditions that Lead to Self-Sustained Smouldering Combustion by Means of Numerical Modelling[3]

5.1 Introduction

Recently, forward smouldering combustion has been intentionally applied as a remediation technique for liquid [1] and solid [2] contaminants (e.g., oils, tars, biosolids, etc.) embedded in an inert porous matrix (e.g., sand). Forward smouldering is the ideal mode of propagation because it optimizes heat transfer towards the fuel [3]. Critical to the success of smouldering remediation is maintaining the reaction as self-sustaining (SS), which enables energy released by the contaminant (i.e., fuel) to support propagation, minimizing energy (input) consumption. Extinction of the combustion reaction occurs when locally heat losses are greater or equal than heat generation. Local extinction is influenced by adjacent conditions and the heating and cooling time-scales of all the different regions (e.g., reaction zone, heat transfer zone) that can potentially contribute to the local energy balance. Unfavourable conditions that lead to local extinction can be reverted by changing operating conditions and taking advantage of the energy accumulated in the reactor. This allows re-stabilization of the reaction. For contaminant destruction, it is therefore important to conduct a global energy management to maintain operational conditions that prevent extinction.

Modelling of the smouldering front propagation is important for establishing operating conditions and contaminant destruction rates, which influence cost and thus commercial competitiveness. Numerical and analytical formulations have shown that heat losses can decrease the peak temperature, potentially leading to extinction [4, 5]. They have also suggested that, in the absence of heat losses (and pyrolysis reactions), temperatures can

---

[3] A version of this chapter has been accepted for presentation at the 37th International Symposium on Combustion in Dublin, Ireland in July, 2018: M.A.B. Zanoni, J.L. Torero, J.I. Gerhard, Determining the Conditions that Lead to Self-Sustained Smouldering Combustion by Means of Numerical Modelling, (2018).

experience unlimited growth [6]. In contrast, experimental studies suggested that, although heat losses can modify the front velocity, extinction is avoided since peak temperatures and reaction rates at the center-line are not altered [7, 8]. Thus, in general, models used different approaches to explain experimental observations near extinction. Despite the importance of heat losses in smouldering (an estimate of 42% of the energy released by oxidation [9]), models have only induced extinction by means of ad-hoc heat loss terms (global heat loss coefficients [10, 11]), which cannot determine the influence of the accumulated energy (time integral) on the smouldering reaction [4].

Heat generation is dominated by smouldering chemistry which is generally modelled either via simple [6] or complex [7] kinetic mechanisms. In the absence of an adequate quantification of all heat transfer mechanisms, it is difficult to ascertain the validity of any detailed or simplified kinetic mechanism. Heat transfer in numerical [10, 12] or analytical [4, 6] smouldering models have relied on Local Thermal Equilibrium assumptions (LTE) [4, 6, 10] or have used Local Thermal Non-Equilibrium (LTNE) empirical heat transfer correlations [13] that lead to LTE [12]. Chapter 4 showed via a new heat transfer correlation developed in Chapter 3 that LTNE must be employed to properly simulate heat transfer among phases as well as evaluate the role of the sand (acting as a heat reservoir due to its high heat capacity) on propagation and extinction.

Experimental studies have shown the importance of LTNE for opposed smouldering, in which convective cooling can decrease the temperature leading to extinction [8, 14, 15]. For forward smouldering, the process is more complex since convection transfers heat towards the fuel. Thus, the role of convective heat transfer on extinction of a forward smouldering front is unclear.

The objective of this study is to use a numerical model to investigate the operating conditions leading to self-sustained forward smouldering and those leading to extinction. The role of heat stored in the sand and exchanged among phases is explored through a range of scenarios relevant to smouldering contaminant remediation that lead to self-sustaining smouldering as well as extinction conditions. The numerical model employed and the parameters incorporated were validated against smouldering experiments in

Chapter 4. This work introduces new insights into the role of local and system energy balance on smouldering propagation and extinction.

5.2 Methodology

5.2.1 Modelling

The one-dimensional numerical model developed in Chapter 4 was used here to simulate a set of smouldering scenarios with bitumen-contaminated sand (Table 5.1). The model was developed in COMSOL Multiphysics with constant mesh size (0.1 mm) and time step variable, controlled by COMSOL to meet stability criteria. Some of the model parameters (Table 5.2) were calculated via the Kissinger method (i.e., well known method for calculating kinetic parameters for first-order pyrolysis and oxidation reactions [16]) coupled with Thermogravimetry (TG) (A_b, E_b, and E_c), and integrating Differential Scanning Calorimetric (DSC) data over time (ΔH_b and ΔH_c). The four unknown parameters (A_c, v_c, v_{O2}, and U) were calibrated via experimental fitting of a base case experiment (Run #2, Table 5.1) conducted in triplicate. Note that a sensitivity analysis to all key parameters (not shown) revealed that the calculated A_c from the Kissinger method produced a non-self-sustaining smouldering front in all cases, which is not realistic. TG heating rates are inevitably smaller than those relevant to smouldering, privileging some minor, low temperature reactions that disappear at high heating rates [3], therefore, affecting the A_c value. Thus, A_c was corrected by treating it as a fourth fitting parameter. The remaining parameters were obtained from the literature (Table 5.2). The model was validated against independent smouldering experiments (Chapter 4).

Runs #1-6 (Table 5.1) correspond to self-sustained smouldering conditions while three additional cases exhibit extinction (#7-9) at low Darcy air flux (u_g), oxygen concentration (O_2), and bitumen saturation (S_b). These were the main parameters suggested to lead to extinction [15]. The computational domain (Figure 5.1) describes the 0.10 m layer of clean sand located below the heater plus a 0.35 m layer (L) of bitumen mixed with sand above it. The heater was simulated by a constant heat flux ($\dot{q}''_{in}$=25 kW m^{-2}) boundary condition at x=0.10 m. The Darcy air flux was initiated at x=0 m by a constant u_g. Both boundary conditions were described by piece-wise functions (see Figure 5.1).
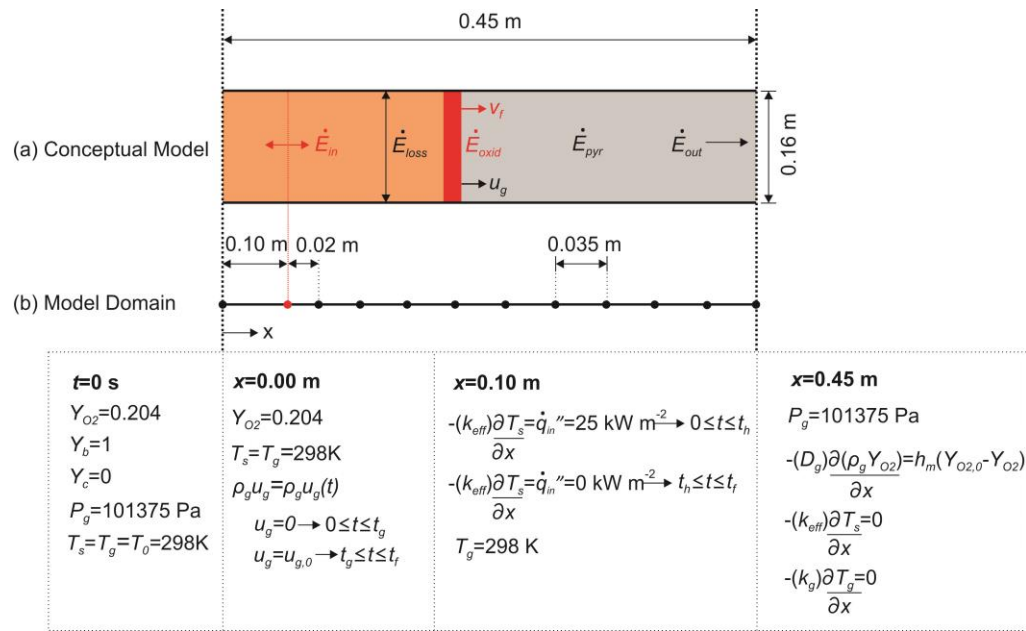
Figure 5.1: (a) Conceptual model showing: (orange) clean sand, (red) reaction front, (gray) contaminated region. Energy rate components ($\dot{E}$) describe (red) energy rate added into and (black) removed from the system. (b) Numerical model domain with initial and boundary conditions.

Table 5.1: Smouldering Numerical Simulations.

Run # [-]	u_g [m s^{-1}]	S_b [%]	O_2 [%]	t_g [s]	t_h [s]	SS [-]
1	0.025	15	20.4	4926	5357	Yes
2[a]	0.058	15	20.4	4532	4865	Yes
3	0.083	15	20.4	5077	5329	Yes
4[b]	0.058	15	20.4	4532	4865	Yes
5[b]	0.500	15	20.4	4532	4865	Yes
6	0.058	10	20.4	5486	6004	Yes
7	0.033	10	20.4	4677	5110	No
8	0.058	10	2	5486	6004	No
9	0.058	5	20.4	5890	6370	No

[a] Base case simulation; [b] Numerical domain: 3 m

The kinetics for bitumen smouldering followed a 2-step mechanism:
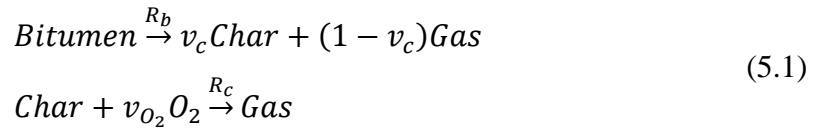
$$Bitumen \xrightarrow{R_b} v_c Char + (1 - v_c)Gas$$

$$Char + v_{O_2}O_2 \xrightarrow{R_c} Gas \tag{5.1}$$

The reaction rates for pyrolysis (R_b) and oxidation (R_c) were described as first-order Arrhenius reactions:

$$R_b = A_b exp\left(-\frac{E_b}{R_g T_s}\right)(Y_b)$$

$$R_c = A_c exp\left(-\frac{E_c}{R_g T_s}\right)(Y_c)(Y_{O_2}) \tag{5.2}$$

The conservation of mass for solid:

$$\frac{\partial(Y_b)}{\partial t} = -R_b$$

$$\frac{\partial(Y_c)}{\partial t} = v_c R_b - R_c \tag{5.3}$$

and gas:

$$\frac{\partial(\rho_g \phi_g)}{\partial t} + \frac{\partial(\rho_g u_g)}{\partial x} = (\phi_b \rho_{bT})\left((1 - v_c)R_b + \left(1 - v_{O_2}\right)R_c\right) \tag{5.4}$$

phases were included. Equation (5.4) solves air pressures and velocities adopting Darcy's Law without gravity effects and the gas density (ρ_g) follows the ideal gas law (Chapter 3). The bulk transport of oxygen is described by:

$$\phi_g \frac{\partial(\rho_g Y_{O_2})}{\partial t} + \frac{\partial(\rho_g u_g Y_{O_2})}{\partial x} = \phi_g \frac{\partial}{\partial x}\left(\rho_g D_g \frac{\partial Y_{O_2}}{\partial x}\right) - (\phi_b \rho_{bT})v_{O_2} R_c \tag{5.5}$$

The model solves the transient energy equation for both solid (T_s) and gas (T_g) phases:

$$(\rho C_p)_{eff} \frac{\partial T_s}{\partial t} = \frac{\partial}{\partial x}\left(k_{eff} \frac{\partial T_s}{\partial x}\right) - U\left(\frac{A_{s,cl}}{V_{cl}}\right)(T_s - T_0) + h_{sg}\left(\frac{A_{s,sp}}{V_{sp}}\right)(T_g - T_s) - Q \tag{5.6}$$

$$\phi_g \left(\rho_g C_{p_g} \right) \frac{\partial T_g}{\partial t} + \rho_g C_{p_g} u_g \frac{\partial T_g}{\partial x} = \phi_g \frac{\partial}{\partial x} \left(k_g \frac{\partial T_g}{\partial x} \right) + h_{sg} \left(\frac{A_{s,sp}}{V_{sp}} \right) (T_s - T_g) \qquad (5.7)$$

Therefore, LTNE was considered by applying the interfacial heat transfer coefficient (h_{sg}) according to the empirical Nusselt (Nu) versus Reynolds (Re) and Prandtl (Pr) correlation developed in Chapter 3:

$$Nu = \frac{h_{sg} d_p}{k_g} = 0.001 \left(Re^{1.97} Pr^{1/3} \right) \qquad (5.8)$$

Effective thermal properties for the solid/liquid phases were considered (Chapter 4). A homogeneous porous medium was assumed and sand particles were taken as spheres ($A_{s,sp}/V_{sp}=6(1-\phi)/d_p$). The source/sink term (Q) in Equation (5.6) is defined as:

$$Q = (\phi_b \rho_{bT})(\Delta H_c R_c + \Delta H_b R_b) \qquad (5.9)$$

Radiation heat transfer follows the Rosseland approximation and was expressed as a radiative conductivity ($k_{rad}=16\sigma d_p T_s^3/3$), Chapter 3. A global heat loss coefficient (U) was included and used the surface area per unit volume ($A_{s,cl}/V_{cl}=2/r$), where r is the radius of the column. Thermal properties of air and sand vary with temperature (Chapter 3), whereas C_{pb} and k_b are assumed constant (Table 5.2). Fuel mobility was not considered.

Table 5.2: Model Input Parameters

Par.	Value	Unit	Ref.
$log(A_b)$	7.5	$log(s^{-1})$	Chapter 4
$log(A_c)$	4.9	$log(s^{-1})$	Chapter 4
C_{pb}	921	$J\,kg^{-1}\,K^{-1}$	[17]
d_p	0.88	mm	Chapter 4
D_g	4.53×10^{-5}	$m^2\,s^{-1}$	[14]
ΔH_b	1.62	$MJ\,kg^{-1}$	Chapter 4
ΔH_c	-38.73	$MJ\,kg^{-1}$	Chapter 4
E_b	135	$kJ\,mol^{-1}$	Chapter 4
E_c	90	$kJ\,mol^{-1}$	Chapter 4
h_m	100	$kg\,m^{-2}\,s^{-1}$	-
k_b	0.15	$W\,m^{-1}\,K^{-1}$	[18]
k_p	1×10^{-9}	m^2	Chapter 3
ϕ	0.37	-	Chapter 3
ϕ_g	0.315	-	Chapter 4
ϕ_b	0.055	-	Chapter 4
ρ_{bT}	1030	$kg\,m^{-3}$	Chapter 4
r	0.08	m	Chapter 4
R_g	8.314	$J\,K^{-1}\,mol^{-1}$	Chapter 3
U	13	$W\,m^{-2}\,K^{-1}$	Chapter 4
v_c	0.55	-	Chapter 4
v_{O2}	1.70	$kg.O_2\,kg.fuel^{-1}$	Chapter 4
σ	5.67×10^{-8}	$W\,m^{-2}\,K^{-4}$	Chapter 3

5.2.2 Energy Balance

A global energy balance was developed (Figure 5.1) that accounts for the rate of energy (J s^{-1}) that is (*i*) provided by the heater:

$$\dot{E}_{in} = \dot{q}''_{in}A_{cs} \tag{5.10}$$

(*ii*) released by oxidation:

$$\dot{E}_{oxid} = \int_{0.1}^{0.45} (-\Delta H_c R_c A_{cs})dx \tag{5.11}$$

(*iii*) absorbed by pyrolysis:

$$\dot{E}_{pyr} = \int_{0.1}^{0.45} (-\Delta H_b R_b A_{cs})dx \tag{5.12}$$

(*iv*) removed by radial heat losses:

$$\dot{E}_{loss} = \int_{0}^{0.45} -U(2\pi r)(T_s - T_0)dx \tag{5.13}$$

and (*v*) removed by convective gas flow out of the system:

$$\dot{E}_{out} = -(\rho_g u_g A_{cs})C_{p_g}(T_g - T_0) \tag{5.14}$$

Therefore, the net energy rate is:

$$\dot{E}_{net} = \dot{E}_{in} + \dot{E}_{oxid} + \dot{E}_{pyr} + \dot{E}_{loss} + \dot{E}_{out} \tag{5.15}$$

Equations (5.10)-(5.15) were also integrated over time to find the net energy E_i (J) associated with each component:

$$E_i = \int_{0}^{t_f} (\dot{E}_i)dt \tag{5.16}$$

where *i* represents *net*, *in*, *oxid*, *pyr*, *loss*, and *out*. The limits of integration of Equation (5.16) will vary depending on the conditions presented in Table 5.1.

The simulation time (*t*) was normalized and is referred to as Dimensionless Time (DT=$(t-t_g)v_f/L$ [19], with v_f as the average front velocity) where DT<0 is the pre-heating period, DT=0 is when the air is turned on and smouldering begins, and DT=1 is when the reaction reaches the end of the fuel bed. The integration of Equations (5.11) and (5.12) at DT=1 for the base case (Run #2) resulted in -8.575 MJ and 0.652 MJ, respectively, matching the total energy available to be released by oxidation ($E_{av,o}=\Delta H_c m_{av} v_c$=-8.570 MJ) and absorbed by pyrolysis ($E_{av,p}=\Delta H_b m_{av}$=0.651 MJ). A global energy balance, via integration of Equation (5.15) at final DT (DT$_f$), indicated a numerical error less than 2% of the total energy added ($E_{add}=E_{in}+E_{oxid}$). Mass balance analysis on the fuel, char, and products before and after smouldering indicated a numerical error less than 1%. Therefore, both mass and energy are conserved in the model (see Appendix C).

5.3 Results

5.3.1 Self-Sustaining Smouldering

Numerical predictions reproduced all the features of experiments following the same configuration. As an example, Figure 5.2a presents experimental and numerical results for the self-sustaining smouldering propagation of Run #2 (Table 5.1) with average front velocity (v_f) and average peak temperature (T_p) equal to 4.16 mm min^{-1} and 679 ºC, respectively.

Figure 5.2d and Figure 5.2g present the energy analysis of Run #2. During the pre-heating (DT<0), energy is provided to the system by the heater $(\dot{E}_{in})$ and lost radially $(\dot{E}_{loss})$, with all other terms equal to zero (Figure 5.2d). In this period, the heat input exceeds the losses, thus $(\dot{E}_{net})$ is positive (Figure 5.2g), the temperature of the first thermocouple (x=0.12 m) increases (Figure 5.2a), and there is energy accumulation $(\dot{E}_{net} > 0)$ in the system (red line in Figure 5.2g).

When the air flux is initiated (DT=0), the temperature at x=0.12 m rapidly increases (Figure 5.2a) due to the energy released by $\dot{E}_{oxid}$ (Figure 5.2d), followed by a sharp increase in

$\dot{E}_{net}$ and the subsequent steeper increase in E_{net}. Coincident is the onset of endothermic pyrolysis ($\dot{E}_{pyr}$, Figure 5.2d). Note that upon air flux initiation, a short transient peak takes place in the heat generation $\dot{E}_{oxid}$ and $\dot{E}_{net}$ due to boundary influences on a spatially-integrated model property. The heater is turned off $\left(\dot{E}_{in} = 0\right)$ when the first thermocouple peaks following experimental protocols.

After the short transient, $\dot{E}_{oxid}$ remains constant while $\dot{E}_{loss}$ continues to increase (Figure 5.2d) as the surface area of the clean, heated sand region behind the front continues to increase; therefore, $\dot{E}_{net}$ decreases with time. Since $\dot{E}_{net}$ remains positive, E_{net} continues increasing (Figure 5.2g) and the reaction is self-sustaining. As the reaction approaches the end of the domain (DT=1), energy starts leaving the system via hot air convection $\left(\dot{E}_{out}\right)$, causing $\dot{E}_{net}$ to abruptly decrease to negative values. For DT>1, all fuel is eliminated (i.e., only clean, hot sand remains) and only $\dot{E}_{loss}$ and $\dot{E}_{out}$ are observed as the system cools (Figure 5.2d).
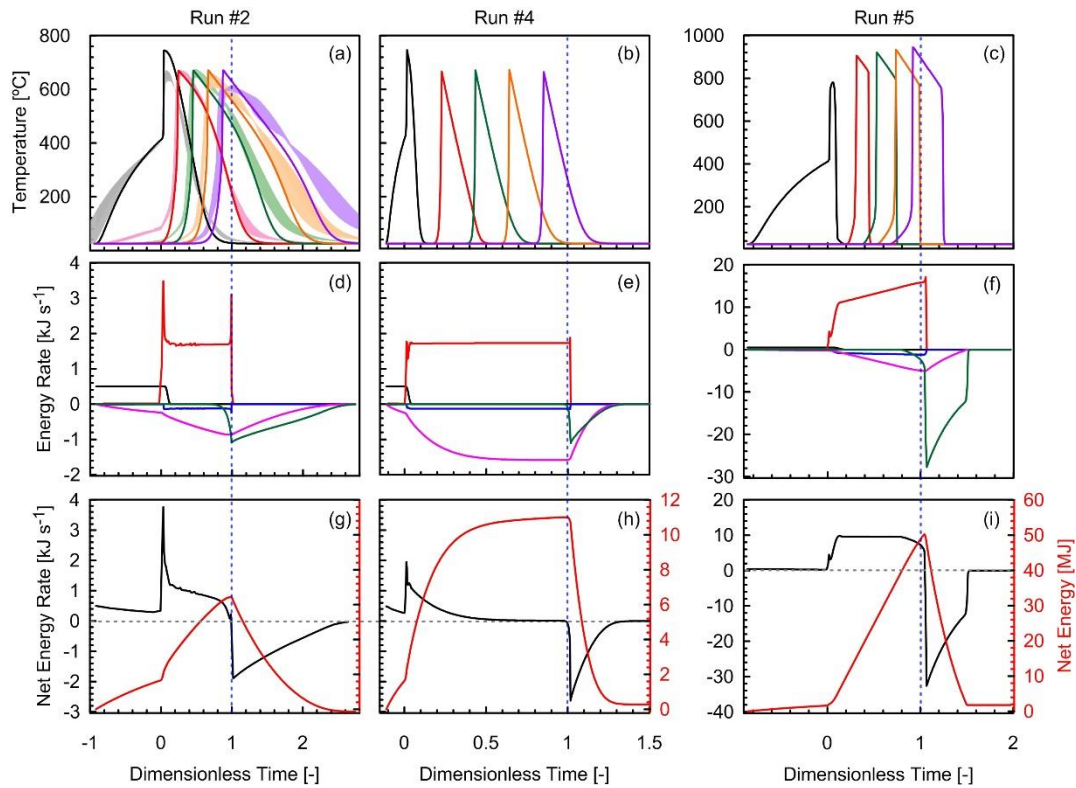
Figure 5.2: (a-c) Temperature evolution versus dimensionless time (DT). The shadings in (a) represent experimental results of three repeats (Chapter 4). Solid lines show model-predicted sand/bitumen temperature (T_s). Colours describe thermocouple positions (x) from (a) 0.12 to 0.40 m with 0.07 m intervals and (b-c) 0.12 to 2.92 m with 0.6 m intervals. (d-f) Energy rate for each component versus DT: (black) heater, (red) oxidation, (blue) pyrolysis, (magenta) radial loss, and (green) convection out. (g-i) (black) Net energy rate and (red) net energy versus DT. Dashed blue line shows the end of the column (DT=1).

Runs #4 and #5 (Figure 5.2) demonstrate how different energy balance regimes can also produce self-sustaining propagation and complete remediation. In Run #4 (Run #2 conditions in a 3 m domain), the system reaches steady-state after DT=0.5, with energy input balanced by losses; thus, $\dot{E}_{net} = 0$. In Run #5, $\dot{E}_{net}$ is constant at a positive value because the increasing $\dot{E}_{oxid}$ balances the increasing $\dot{E}_{loss}$. As a result, E_{net} and peak temperatures are continuously increasing. Such conditions might explain transition to flaming. Continuous energy accumulation is favoured by operational conditions that minimize heat losses (e.g., enhanced insulation, increased diameter) and enhance oxidation

(e.g., increased air flux). Note that the temperature curves in Figure 5.2c are atypical but consistent with a rapidly propagating front cooled quickly by incoming air.

5.3.2   Smouldering Extinction

Figure 5.3 presents the extinction cases (Run #7-9), characterized by a decrease in the peak temperature with time. $\dot{E}_{oxid}$ decreases immediately after the peak generated by the onset of the air flux. Independent of the method used to weaken the reaction, the process remains the same. Figure 5.3g-i reveals that $\dot{E}_{net}$ becomes negative when the ignition source is eliminated. Traditionally, smouldering extinction has been characterized as a local phenomenon, e.g., critical temperature or *Damköhler* number (*Da*) [4, 15]. While this remains the true extinction point, the results showed in the global energy balance indicate that the fate of the smouldering reaction, from the perspective of operating conditions, can be defined $\dot{E}_{net} < 0$, which is when E_{net} starts decreasing (Figure 5.3g-i). This is important for practical aspects since it predicts extinction when temperatures are still high, contrary to typical local criteria.

However, while the $\dot{E}_{net} < 0$ criterion identifies a reaction that is not self-sustaining, it cannot establish when the reaction will cease propagating nor the mass of contaminant remediated. Oxidation and pyrolysis reactions continue for some time after $\dot{E}_{net} < 0$, as the reaction temperatures decrease until eventually heat generation ceases (Figure 5.3d-f). This underscores that energy accumulated in the treated sand will continue to affect the energy balance, sustaining propagation for a finite period even if $\dot{E}_{net}$ is negative. Since the reaction terminates before the front reaches the end of the fuel bed in all three cases, residual contamination remains. Such scenarios are important as they represent incomplete remediation.
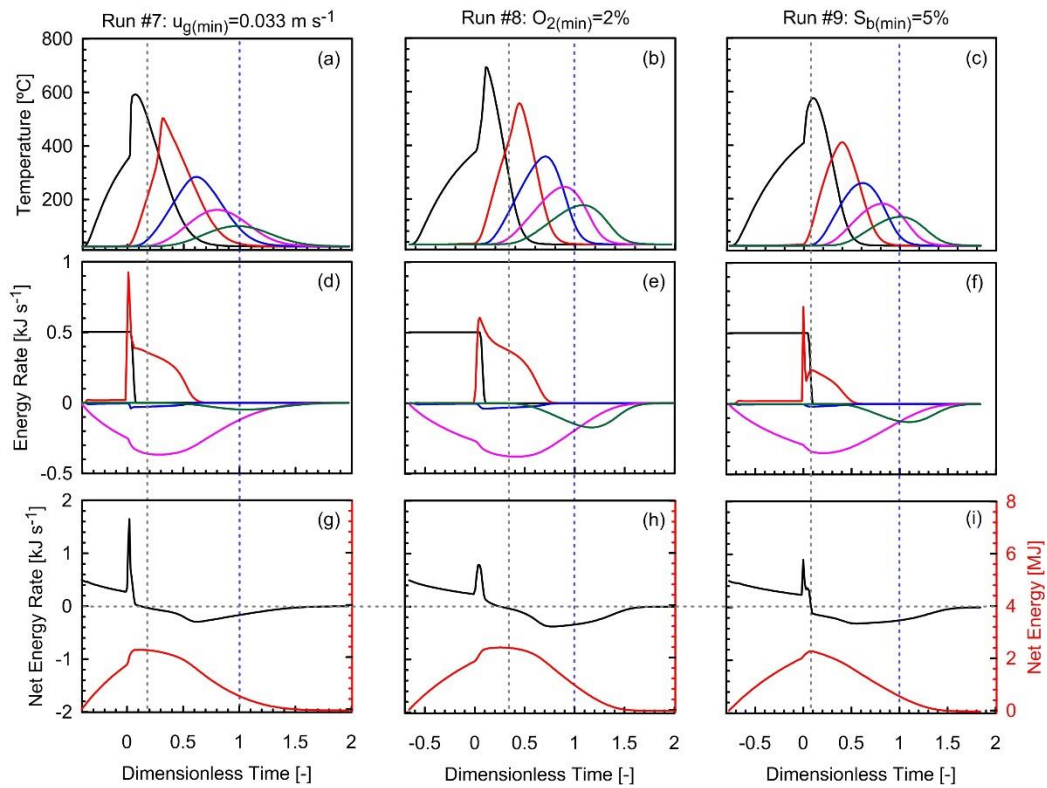
Figure 5.3: (a-c) Numerical sand/bitumen temperature versus DT. Colours describe thermocouple positions (x) from 0.12 to 0.40 m with 0.07 m intervals; (d-f) energy rate for each component versus DT: (black) heater, (red) oxidation, (blue) pyrolysis, (magenta) radial loss, and (green) convection out; and (g-i) (black) net energy rate and (red) cumulative net energy versus DT. Dashed grey line marks when $\dot{E}_{net} < 0$ while dashed blue line marks when a constant velocity front would have reached the end of the column (DT=1).

Figure 5.4 presents $\dot{E}_{net}$ at DT=0.5 for all 9 Runs. Extinction cases exhibit $\dot{E}_{net} < 0$ while self-sustaining cases exhibit $\dot{E}_{net} > 0$. For the latter, the magnitude of $\dot{E}_{net}$ reflects the robustness of the reaction, which increases with increased air flux, as expected.
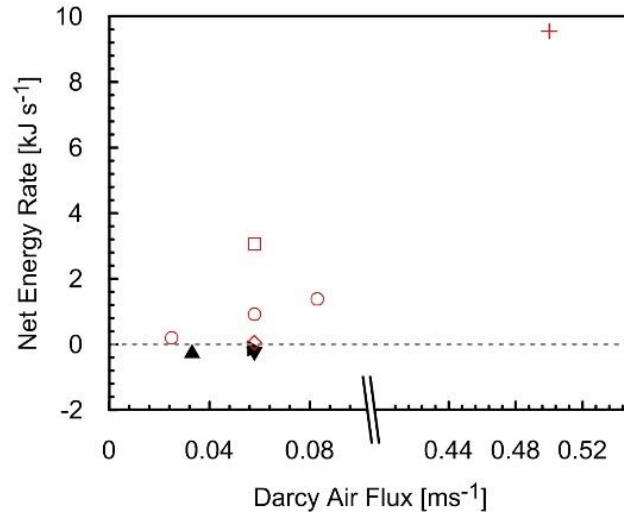
Figure 5.4: Net energy rate versus air flux at DT=0.5: (open red symbols) self-sustaining, (closed black symbols) non-self-sustaining: Run # (○) 1-3, (◊) 4, and (+) 5, (□) 6, (▲) 7, (►) 8, and (▼) 9. Dashed gray line shows transition to extinction.

5.3.3   Global Energy Balance

Table 5.3 provides all the energy components, Equation (5.15), integrated over time as per Equation (5.16); as such, it provides a global (system) analysis. The first green column, $E_{oxid}/E_{av,o}$, integrated the components in time from the start of ignition until the time $\dot{E}_{net} = 0$. Values of 100% (Runs #1-5) indicate that all the fuel was converted into energy. Values for Runs #7-9 (11-17%) reveal that the reaction started failing before all the fuel was consumed. The second green column, $E_{oxid}/E_{av,o(DTf)}$, integrated the components until oxidation terminated. Values for Runs #7-9 (28-40%) reveal that some additional fuel was converted but fuel remained when the front extinguished. Run #6 is an intermediate case: $\dot{E}_{net} < 0$ before the front reaches the end of the column ($E_{oxid}/E_{av,o}$=83%) but the front is able to continue long enough that all of the fuel is converted ($E_{oxid}/E_{av,o(DTf)}$=100%) before the reaction dies.

Table 5.3: Cumulative Energy Analysis for all Simulations.

Run # [-]	u_g [m s^{-1}]	S_b [%]	O_2 [%]	SS [-]	E_{add} [MJ]	E_{in}/E_{add} [%]	E_{oxid}/E_{add} [%]	E_{st}/E_{add} [%]	E_{pyr}/E_{add} [%]	E_{loss}/E_{add} [%]	E_{out}/E_{add} [%]	$E_{oxid}/E_{av,o}$ [%]	$E_{oxid}/E_{av,o(DTf)}$ [%]
1	0.025	15	20.4	Yes	11.44	24	76	39	6	52	3	100	100
2	0.058	15	20.4	Yes	11.07	23	77	58	6	33	3	100	100
3	0.083	15	20.4	Yes	11.26	24	76	64	6	28	2	100	100
4	0.058	15	20.4	Yes	71.48	4	96	16	7	77	0	100	100
5	0.500	15	20.4	Yes	73.00	4	96	69	7	21	3	100	100
6	0.058	10	20.4	Yes	7.80	39	61	47	5	46	2	83	100
7	0.033	10	20.4	No	3.47	76	24	66	2	32	0	17	40
8	0.058	10	2	No	4.07	75	25	59	2	39	0	12	35
9	0.058	5	20.4	No	3.52	92	8	65	1	34	0	11	28

The total energy added into the system (E_{add}) was used to normalize the integrated energy components (Table 5.3). This reveals that extinction occurred in Runs #7-9 due to higher energy lost radially (E_{loss}/E_{add}=32-39%) than energy released by oxidation (E_{oxid}/E_{add} = 8-25%). It reveals that the influence of pyrolysis on the energy balance is negligible in all cases (E_{pyr}/E_{add} ≤7%). Furthermore, the amount of energy stored in the sand at the end of smouldering is found to be significant (E_{st}/E_{add}=39-69%) in most self-sustained cases.

5.4   Conclusions

A previously validated one-dimensional model was employed to investigate the transition between self-sustained smouldering and extinction. Self-sustaining smouldering depends on a positive balance between energy added into and removed from the system. Extinction occurs when energy removed exceeds energy added, resulting in a negative energy balance. This is consistent with previous studies that point to a critical *Damköhler* number criterion for local extinction of the reaction. The global energy balance criterion presented here provides a new method to predict if a smouldering scenario will be self-sustained. Simulations using long domains reveal steady-state scenarios, including (*i*) indefinite self-sustained smouldering and (*ii*) continual energy accumulation, which could be related to transition to flaming.

The global energy balance analysis revealed that pyrolysis had a negligible role, while self-sustaining versus extinction conditions depended primarily on the competition between char oxidation and radial heat losses. Increased air flux created more robust self-sustaining scenarios because oxidation rates increased while the fraction of energy lost radially decreased. As a result, the stored energy in the post-treatment clean sand increased with increased air flux, showing increased potential for energy recovery. The possible extinction of a forward reaction by high air flux was not evaluated because the necessary air flux values exceed those of practical importance for applied smouldering.

The energy accumulated in the treated sand continues to support the reaction for a period even if the local energy balance becomes negative; thus complete treatment can be achieved in some cases where the reaction is in the process of dying. An overall energy balance is found to be a robust and valuable tool to explain the conditions under which smouldering transitions from self-sustaining towards extinction and to predict the residual mass of contaminant upon extinction. Residual contaminant mass is an important practical parameter for remediation.

5.5   References

[1] P. Pironi, C. Switzer, G. Rein, A. Fuentes, J.I. Gerhard, J.L. Torero, Small-scale forward smouldering experiments for remediation of coal tar in inert media, Proceedings of the Combustion Institute, 32(2) (2009) 1957-1964.

[2] T.L. Rashwan, J.I. Gerhard, G.P. Grant, Application of self-sustaining smouldering combustion for the destruction of wastewater biosolids, Waste Management, 50 (2016) 201-212.

[3] T.J. Ohlemiller, Modeling of smoldering combustion propagation, Progress in Energy and Combustion Science, 11(4) (1985) 277-310.

[4] S.S. Dosanjh, P.J. Pagni, A.C. Fernandez-Pello, Forced cocurrent smoldering combustion, Combustion and Flame, 68(2) (1987) 131-142.

[5] J. Yang, H. Chen, N. Liu, in: K. Harada (Ed.) Fire Sci Technol., Springer Singapore, Singapore, 2015, pp. 831-840.

[6] A.P. Aldushin, I.E. Rumanov, B.J. Matkowsky, Maximal energy accumulation in a superadiabatic filtration combustion wave, Combustion and Flame, 118(1–2) (1999) 76-90.

[7] D. Lozinski, J. Buckmaster, Quenching of reverse smolder, Combustion and Flame, 102(1–2) (1995) 87-100.

[8] A.P. Aldushin, A. Bayliss, B.J. Matkowsky, Is there a transition to flaming in reverse smolder waves?, Combustion and Flame, 156(12) (2009) 2231-2251.

[9] M.F. Martins, S. Salvador, J.F. Thovert, G. Debenest, Co-current combustion of oil shale - Part 2: Structure of the combustion front, Fuel, 89 (2010) 133-143.

[10] H. Fadaei, M. Sennoune, S. Salvador, A. Lapene, G. Debenest, Modelling of non-consolidated oil shale semi-coke forward combustion: Influence of carbon and calcium carbonate contents, Fuel, 95(0) (2012) 197-205.

[11] G. Rein, A. Carlos Fernandez-Pello, D.L. Urban, Computational model of forward and opposed smoldering combustion in microgravity, Proceedings of the Combustion Institute, 31(2) (2007) 2677-2684.

[12] S.V. Leach, G. Rein, J.L. Ellzey, O.A. Ezekoye, J.L. Torero, Kinetic and fuel property effects on forward smoldering, Combustion and Flame, 120(3) (2000) 346-358.

[13] N. Wakao, S. Kaguei, T. Funazkri, Effect of fluid dispersion coefficients on particle-to-fluid heat transfer coefficients in packed beds: Correlation of nusselt numbers, Chemical Engineering Science, 34(3) (1979) 325-336.

[14] J.L. Torero, A.C. Fernandez-Pello, M. Kitano, Opposed Forced Flow Smoldering of Polyurethane Foam, Combustion Science and Technology, 91(1-3) (1993) 95-117.

[15] S.V. Leach, J.L. Ellzey, O.A. Ezekoye, Convection, pyrolysis, and Damköhler number effects on extinction of reverse smoldering combustion, Proceedings of the Combustion Institute, 27(2) (1998) 2873-2880.

[16] T. Kashiwagi, H. Nambu, Global kinetic constants for thermal oxidative degradation of a cellulosic paper, Combustion and Flame, 88(3-4) (1992) 345-368.

[17] R.H. Perry, D.W. Green, Perry's Chemical Engineers' Handbook, 7th ed., McGraw-Hill, New York, USA, 1999.

[18] S.K. Elam, I. Tokura, K. Saito, R.A. Altenkirch, Thermal conductivity of crude oils, Experimental Thermal and Fluid Science, 2(1) (1989) 1-6.

[19] L. Kinsman, J.L. Torero, J.I. Gerhard, Organic liquid mobility induced by smoldering remediation, Journal of Hazardous materials, 325 (2017) 101-112.

Chapter 6

6 Smouldering Combustion Explored via Numerical Modelling: Sensitivity to Key Parameters[4]

6.1 Introduction

Smouldering is driven by an oxidation reaction occurring on the surface of organic materials [1]. Under certain conditions, smouldering is a self-sustaining process: following a brief ignition event, the energy released from oxidation is sufficient to support a reaction. Smouldering reactions are most commonly found propagating within porous fuel beds. For decades, smouldering of solid materials (e.g., polyurethane foam, peat, coal) has been studied as a safety hazard which threatens the loss of life and property and has the potential for significant negative environmental impact [2]. Smouldering has also been applied as a viable technology for waste and contaminant destruction, specifically for organic liquids and sludges embedded in an inert porous matrix (e.g., coal tar in sand, oil shale, biosolids in sand) [3-11].

The success of applied smouldering depends on optimizing operating conditions (e.g., air injection rates, fuel concentration, heat losses) as well as understanding operational limits (i.e., conditions that lead to extinction). Experimental, analytical, and numerical approaches have evaluated the impact on peak temperatures and front velocity versus air flux [1, 5, 7, 9, 11-26], fuel concentration [7, 9, 13, 22, 27, 28], oxygen concentration [14, 20, 21, 29-31], moisture content [5, 6, 9, 11, 29, 32-35], inorganic content [11, 27, 32, 33], kinetic parameters [12, 14, 24, 36] and heat losses [1, 12, 13, 27, 33, 36-40].

Energy storage within the porous medium has been shown to have a very significant effect on the fate and characteristics of the smouldering reaction [17, 20]. Nevertheless, most studies considered solid fuels, which typically exhibit high porosity (92-97% [21, 41, 42]),

---

[4] A version of this chapter will be submitted to a peer-reviewed journal: M.A.B. Zanoni, J.L. Torero, J.I. Gerhard, Smouldering Combustion Explored via Numerical Modelling: Sensitivity to Key Parameters, (2018).

low thermal conductivity ($O[10^{-2}$ W m^{-1} K$^{-1}]$ [14, 41, 43]), low volumetric heat capacity ($O[10^4$ J m^{-3} K$^{-1}]$ [14, 21, 41]), constant fuel concentration (if homogeneous), and a large surface area for reaction [5, 44]. Only a fraction consider organic liquids in inert matrixes, which are characterized by low porosity (38-50% [7, 27, 45]), with relatively small pores partially or totally filled with a liquid hydrocarbon [46], higher thermal conductivity ($O[10^{-1}$ W m^{-1} K$^{-1}]$) and higher volumetric heat capacity ($O[10^6$ J m^{-3} K$^{-1}]$ [47], see also Chapter 3) when compared to solid fuels. The presence of fuel in the matrix porosity means reduced effective permeability to air, and relatively less fuel surface area exposed to the gas phase, compared to solid fuels.

In forward smouldering (i.e., air flux and reaction moving in the same direction), oxidation reactions drive the propagation of the smouldering front, favouring heat transfer towards the virgin fuel [48]. Positive heat transfer makes forward smouldering ideal for waste and contaminant destruction [7]. Figure 6.1a illustrates a forward smouldering scenario in a vertical one-dimensional column; such experiments have been routinely conducted to study smouldering scenarios for decades [1, 23]. The reaction rates are affected by heat transfer, oxygen and fuel availability, which in turn dictate whether the reactions consume all the oxygen (oxygen-limited), all the fuel (fuel-limited), or quench before one or both reactants are fully consumed. When chemistry governs the process and cannot consume either reactant fully, the reaction is defined as kinetic-limited [1, 14, 15, 17, 19, 21, 24-26, 49-52].
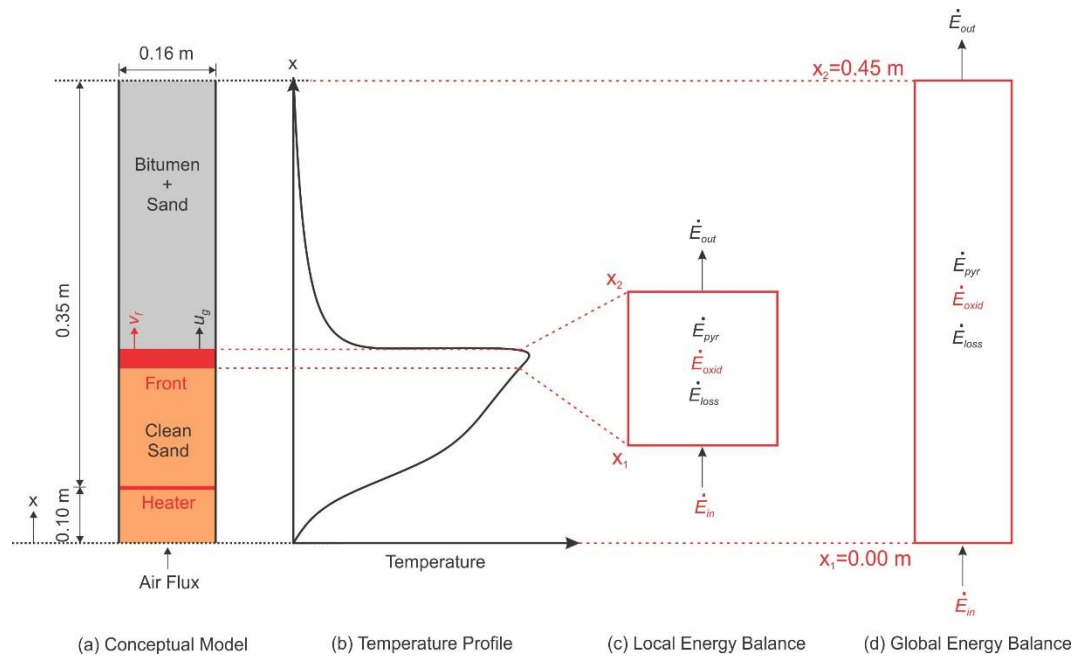
Figure 6.1: (a) Conceptual model showing a smouldering front (red) propagating through the contaminant region (gray), leaving only clean sand (orange) behind. (b) Temperature profile at a specific time. (c) Local and (d) global energy balance. Energy rate components $\left(\dot{E}\right)$ accounts for (red) energy rate added into and (black) removed from the system.

At low air fluxes (e.g., ambient or natural convection, typical for fire safety scenarios), smouldering of solid fuels was identified as oxygen-limited and fuel concentration had negligible impact on the reaction rate resulting in small fuel consumption [14, 15, 17, 21, 24, 26, 49]. At high air fluxes (e.g., injected air, typical for applied smouldering scenarios), fuel-limited conditions [15, 19] were found. Furthermore, it has been observed that fuel-limited conditions are generally characterized by more complete combustion [53]. Kinetic-limited conditions were also described analytically and numerically for solid fuels at high air fluxes due to insufficient oxygen residence time [14, 21, 24, 49]. Smouldering of these characteristics has not been observed experimentally. The introduction of the smouldering column with time and spatially dependent measurements [23] showed that as energy gets accumulated or dissipated from the reactor, the energy balance at the reaction front changes and smouldering combustion can progress from one regime to a different one. The limiting condition, and therefore the ultimate behaviour of the smouldering system, is a result of

the complex interplay of heat and mass transfer processes and chemical reactions that evolve in space and time.

Measurements within porous media are very difficult; thus, many of the components of heat and mass transfer remain experimentally unquantified. Numerical models are therefore essential to explore the spatial and temporal evolution of a smouldering front. They require assumptions about the chemical reactions and heat transfer processes that are important. Smouldering of natural and synthesized organic compounds involves dozens to hundreds of chemical reactions. Here, "complex chemistry" refers to accounting for between 3 and 9 pyrolysis and oxidation reactions (many in competition with each other), an approach regularly used in numerical models of solid fuel smouldering [32, 36, 54, 55]. Both complex and "simple chemistry" have been suggested for liquid fuels [56-58], however few have been applied in smouldering models.

Heat transfer is typically assumed to follow Local Thermal Equilibrium (LTE) between the air and fuel [15, 27, 59]. The smouldering models that assume Local Thermal Non-Equilibrium (LTNE) [14, 18, 21, 24, 33, 37, 60] widely use heat transfer correlations that originate outside of smouldering [61], and it has been found that the degree of non-equilibrium predicted is negligible [14, 60]. Models exist that neglect chemistry and heat transfer [62, 63], but they only provide heuristic engineering tools. In Chapter 3, a new heat transfer correlation specific to hot air flow in a fixed sand bed was developed, which revealed that non-equilibrium is significant and needs to be incorporated to properly simulate smouldering conditions. The new heat transfer correlation was later applied in a smouldering model that considered simple chemistry (one pyrolysis and one oxidation reaction). The model was validated against smouldering experiments of bitumen embedded in sand (Chapter 4).

Self-sustained smouldering involves a "front" (i.e., a physical region in which the reactions dominate) that propagates through space and evolves in time. Studies reveal that the smouldering front is generally narrow (thickness <1 cm) [48, 52, 64] with a few reactions dominating and the rest often negligible [1, 21, 24, 31, 54, 55, 65-68]. As a result, most analytical approaches to smouldering have either assumed that the reactions are superimposed or that they propagate at the same rate, thus maintaining a constant spacing

and front thickness [20, 49]. Therefore, they focus entirely on a local energy balance of the front, considering energy produced by (oxidation) and removed at (pyrolysis and heat losses) this narrow region. Examples of this approach for solid fuels include an analytical model to predict the front velocity [20] and a modified *Damköhler* number at the reaction front as a criterion to identify extinction [24].

It is rarely acknowledged that the energy balance at the front includes heat being driven from behind the front and from the front upstream. Therefore, the state of the porous matrix up and downstream will influence the energy balance at the front ($\dot{E}_{in}$, $\dot{E}_{out}$, Figure 6.1c), thus, requiring a global (i.e., not local) analysis of the reactor (Figure 6.1d). For example, Chapter 5 conducted liquid smouldering in inert media and indicated that 39-64% of the system's energy was stored in the clean porous media behind the front. This energy can be transferred forward to the front via heat transfer/air convection and can be lost radially. Radial heat losses behind the front have been demonstrated to be responsible for 28-52% of the total energy in the system (Chapter 5). Such losses reduce the amount of energy that can be transferred forward, leading to extinction [12, 13, 16, 32, 33, 36]. Heat transfer ahead of the front can be important in pre-heating the fuel and correspond to energy losses associated with boiling and volatilization [5]. Moreover, a numerical modelling method for considering a global (system) energy balance for smouldering systems was introduced and demonstrated in principle that it was capable of predicting the boundary between self-sustaining and extinguishing scenarios (Chapter 5).

The objective of this study is to explore the interplay between chemical reactions and heat transfer processes taking place in space and time in smouldering. A liquid fuel embedded within a porous matrix will be used to generate a low permeability, high thermal inertia (i.e., volumetric heat capacity) system that allows to rigorously study the role of energy accumulation within the porous medium. A validated numerical model was employed equipped with algorithms to compute both a local and a global energy analysis. A sensitivity analysis to the 8 main physical and chemical parameters that affect smouldering was conducted, including 20 self-sustaining cases and 8 extinguishing scenarios. The boundary between self-sustaining and extinction conditions was analyzed in the context of both local and global energy balances for all cases; this provides an in-depth understanding

of the contrasting approaches and their respective abilities to predict smouldering behaviour. This work provides unique conclusions about smouldering operational limits, optimizing applied smouldering systems, and how the net global energy balance (i.e., smouldering robustness) depends on scenario conditions and evolves in time.

6.2 Methodology

The one-dimensional numerical model developed in Chapter 4 was used here to conduct a sensitivity analysis of several smouldering scenarios with bitumen-contaminated sand. Table 6.1 shows twenty self-sustained smouldering cases (Runs #2-4, 6-9, 11-14, 17-21, 24-27) and eight additional cases exhibiting extinction (#1, 5, 10, 15, 16, 22, 23, and 28). Sensitivity to the following parameters were simulated within the maximum expected practical range for each (Table 6.1): Darcy air flux (u_g), bitumen saturation (S_b), oxygen concentration (O_2), heat of oxidation (ΔH_c), global (radial) heat loss coefficient (U), Nusselt number (Nu), and char pre-exponential factor (A_c) and activation energy (E_c). Apart from the key parameters varied, all model parameters, geometry, and boundary conditions remained the same for all simulations.

Some of the model parameters (Table 6.2) were calculated via the Kissinger method coupled with Thermogravimetry (TG) (A_b, E_b, and E_c), and integrating Differential Scanning Calorimetric (DSC) data over time (ΔH_b and ΔH_c). The four unknown parameters (A_c, v_c, v_{O2}, and U) were calibrated via experimental fitting of a base case experiment (same conditions as Run #3, Table 6.1) conducted in triplicate. Note that a sensitivity analysis to all key parameters (not shown) revealed that the calculated A_c from the Kissinger method produced a non-self-sustaining smouldering front in all cases, which is not realistic. TG heating rates are inevitably smaller than those relevant to smouldering, privileging some minor, low temperature reactions that disappear at high heating rates [1], therefore, affecting the A_c value. Thus, A_c was corrected by treating it as a fourth fitting parameter. The remaining parameters were obtained from the literature (Table 6.2). The model was validated against independent smouldering experiments (i.e., no calibration) (see Chapter 4), providing accurately simulation of peak temperature, front velocity, and heat transfer ahead and behind the front.

The computational domain includes a 0.10 m layer of clean sand located below the heater plus a 0.35 m layer (L) of bitumen mixed with sand above it (Figure 6.1a). The heater was simulated by a constant heat flux ($\dot{q}''_{in}$=25 kWm^{-2}) boundary condition at x=0.10 m and was turned off at t_h=4865 s (after ignition). Ignition coincided with the initiation of a constant air flux at t_g=4532 s (x=0 m). Both boundary conditions were defined by piece-wise functions (see Table 6.3) to best describe the experimental system. In presenting the results, the simulation time (t) was normalized and is referred to as Dimensionless Time (DT=$(t-t_g)v_f/L$ [45]) where DT<0 is the pre-heating period, DT=0 is smouldering ignition, and DT=1 is when the reaction reaches the end of the fuel bed.

Table 6.1: Smouldering Numerical Simulations.

Run # [-]	$u_g{}^a$ [m s⁻¹]	S_b [%]	O_2 [%]	U [W m⁻² K⁻¹]	ΔH_c [MJ kg⁻¹]	Nu [-]	A_c [log(s⁻¹)]	E_c [kJ mol⁻¹]	SS [-]
1	0.014	15	20.4	13	38.73	Eq. (8)	4.9	90	*No*
2	0.025	15	20.4	13	38.73	Eq. (8)	4.9	90	Yes
3[b]	0.058	15	20.4	13	38.73	Eq. (8)	4.9	90	Yes
4	0.083	15	20.4	13	38.73	Eq. (8)	4.9	90	Yes
5	0.058	7	20.4	13	38.73	Eq. (8)	4.9	90	*No*
6	0.058	10	20.4	13	38.73	Eq. (8)	4.9	90	Yes
7	0.058	20	20.4	13	38.73	Eq. (8)	4.9	90	Yes
8	0.058	40	20.4	13	38.73	Eq. (8)	4.9	90	Yes
9	0.058	50	20.4	13	38.73	Eq. (8)	4.9	90	Yes
10	0.058	15	1	13	38.73	Eq. (8)	4.9	90	*No*
11	0.058	15	10	13	38.73	Eq. (8)	4.9	90	Yes
12	0.058	15	30	13	38.73	Eq. (8)	4.9	90	Yes
13	0.058	15	20.4	9	38.73	Eq. (8)	4.9	90	Yes
14	0.058	15	20.4	17	38.73	Eq. (8)	4.9	90	Yes
15	0.058	15	20.4	60	38.73	Eq. (8)	4.9	90	*No*
16	0.058	15	20.4	13	18	Eq. (8)	4.9	90	*No*
17	0.058	15	20.4	13	30	Eq. (8)	4.9	90	Yes
18	0.058	15	20.4	13	45	Eq. (8)	4.9	90	Yes
19	0.058	15	20.4	13	38.73	0.1000[c]	4.9	90	Yes
20	0.058	15	20.4	13	38.73	0.0180[d]	4.9	90	Yes
21	0.058	15	20.4	13	38.73	0.0030[e]	4.9	90	Yes
22	0.058	15	20.4	13	38.73	0.0016[f]	4.9	90	*No*
23	0.058	15	20.4	13	38.73	Eq. (8)	3	90	*No*
24	0.058	15	20.4	13	38.73	Eq. (8)	4	90	Yes
25	0.058	15	20.4	13	38.73	Eq. (8)	6	90	Yes
26	0.058	15	20.4	13	38.73	Eq. (8)	4.9	80	Yes
27	0.058	15	20.4	13	38.73	Eq. (8)	4.9	100	Yes
28	0.058	15	20.4	13	38.73	Eq. (8)	4.9	120	*No*

[a] Volume per unit cross-sectional area per unit time; [b] Base case simulation; Gas properties (k_g, ρ_g, C_{pg}, and μ_g) at [c] 20 ℃, [d] 230 ℃, [e] 600 ℃, and [f] 800 ℃;

The kinetics for bitumen smouldering was simulated as a two-step mechanism:
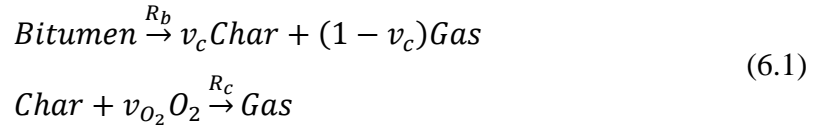
$$Bitumen \xrightarrow{R_b} v_c Char + (1 - v_c)Gas$$

$$Char + v_{O_2}O_2 \xrightarrow{R_c} Gas \tag{6.1}$$

The reaction rates for pyrolysis (R_b) and oxidation (R_c) were described as first-order Arrhenius reactions:

$$R_b = A_b exp\left(-\frac{E_b}{R_g T_s}\right)(Y_b)$$

$$R_c = A_c exp\left(-\frac{E_c}{R_g T_s}\right)(Y_c)(Y_{O_2}) \tag{6.2}$$

The conservation of mass for solid:

$$\frac{\partial(Y_b)}{\partial t} = -R_b$$

$$\frac{\partial(Y_c)}{\partial t} = v_c R_b - R_c \tag{6.3}$$

and gas:

$$\frac{\partial(\rho_g \phi_g)}{\partial t} + \frac{\partial(\rho_g u_g)}{\partial x} = (\phi_b \rho_{bT})\left((1 - v_c)R_b + (1 - v_{O_2})R_c\right) \tag{6.4}$$

phases were included. Equation (6.4) solves air pressures and velocities adopting Darcy's Law without gravity effects and the gas density (ρ_g) follows the ideal gas law (Chapter 3). The bulk transport of oxygen was described by:

$$\phi_g \frac{\partial(\rho_g Y_{O_2})}{\partial t} + \frac{\partial(\rho_g u_g Y_{O_2})}{\partial x} = \phi_g \frac{\partial}{\partial x}\left(\rho_g D_g \frac{\partial Y_{O_2}}{\partial x}\right) - (\phi_b \rho_{bT})v_{O_2}R_c \tag{6.5}$$

The model solved the transient energy equation for both solid (T_s) and gas (T_g) phases:

$$\left(\rho C_p\right)_{eff} \frac{\partial T_s}{\partial t} = \frac{\partial}{\partial x}\left(k_{eff} \frac{\partial T_s}{\partial x}\right) - U\left(\frac{A_{s,cl}}{V_{cl}}\right)(T_s - T_0) + h_{sg}\left(\frac{A_{s,sp}}{V_{sp}}\right)(T_g - T_s) - Q \quad (6.6)$$

$$\phi_g \left(\rho_g C_{p_g}\right) \frac{\partial T_g}{\partial t} + \rho_g C_{p_g} u_g \frac{\partial T_g}{\partial x} = \phi_g \frac{\partial}{\partial x}\left(k_g \frac{\partial T_g}{\partial x}\right) + h_{sg}\left(\frac{A_{s,sp}}{V_{sp}}\right)(T_s - T_g) \quad (6.7)$$

Therefore, LTNE was considered by applying the interfacial heat transfer coefficient (h_{sg}) according to the empirical Nusselt (*Nu*) versus Reynolds (*Re*) and Prandtl (*Pr*) correlation developed specifically for smouldering scenarios (Chapter 3):

$$Nu = \frac{h_{sg} d_p}{k_g} = 0.001\left(Re^{1.97} Pr^{1/3}\right) \quad (6.8)$$

Effective thermal properties for the solid/liquid phases were considered (Chapter 4). A homogeneous porous medium was assumed and sand particles were taken as spheres ($A_{s,sp}/V_{sp}=6(1-\phi)/d_p$). The source/sink term (*Q*) in Equation (6.6) was defined as:

$$Q = (\phi_b \rho_{bT})(\Delta H_c R_c + \Delta H_b R_b) \quad (6.9)$$

Radiation heat transfer follows the Rosseland approximation and was expressed as a radiative conductivity ($k_{rad}=16\sigma d_p T_s^3/3$), Chapter 3. A global heat loss coefficient (*U*) was included and used the surface area per unit volume ($A_{s,cl}/V_{cl}=2/r$), where *r* is the radius of the column (Chapter 4). The thermal properties of air and sand varied with temperature (Chapter 3), whereas C_{pb} and k_b were assumed constant (Table 6.2). The initial and boundary conditions are defined in Table 6.3. Fuel mobility was not considered.

Table 6.2: Model Input Parameters Referent to Base Case

Par.	Value	Unit	Ref.
$log(A_b)$	7.5	$log(s^{-1})$	Chapter 4
$log(A_c)$	4.9	$log(s^{-1})$	Chapter 4
C_{pb}	921	$J\,kg^{-1}\,K^{-1}$	[47]
C_{pg}	$-3x10^{-5}(T_g^2)+0.2261(T_g)+940.35$	$J\,kg^{-1}\,K^{-1}$	Chapter 3
C_{ps}	$2.49(T_s)+39.06$	$J\,kg^{-1}\,K^{-1}$	Chapter 3
d_p	0.88	mm	Chapter 4
D_g	$4.53x10^{-5}$	$m^2\,s^{-1}$	[23]
ΔH_b	1.62	$MJ\,kg^{-1}$	Chapter 4
ΔH_c	-38.73	$MJ\,kg^{-1}$	Chapter 4
E_b	135	$kJ\,mol^{-1}$	Chapter 4
E_c	90	$kJ\,mol^{-1}$	Chapter 4
k_b	0.15	$W\,m^{-1}\,K^{-1}$	[69]
k_g	$-1x10^{-8}(T_g^2)+8x10^{-5}(T_g)+4.3x10^{-3}$	$W\,m^{-2}\,K^{-1}$	Chapter 3
k_p	$1x10^{-9}$	m^2	Chapter 3
k_s	$0.000541(T_s)+0.1044$	$W\,m^{-2}\,K^{-1}$	Chapter 3
μ_g	$-9x10^{-12}(T_g^2)+4x10^{-8}\,(T_g)+6x10^{-6}$	Pa s	Chapter 3
ϕ	0.37	-	Chapter 3
ϕ_g	0.315	-	Chapter 4
ϕ_b	0.055	-	Chapter 4
ρ_{bT}	1030	$kg\,m^{-3}$	Chapter 4
r	0.08	m	Chapter 4
R_g	8.314	$J\,K^{-1}\,mol^{-1}$	Chapter 3
U	13	$W\,m^{-2}\,K^{-1}$	Chapter 4
v_c	0.55	-	Chapter 4
v_{O2}	1.70	$kg.O_2\,kg.fuel^{-1}$	Chapter 4
σ	$5.67x10^{-8}$	$W\,m^{-2}\,K^{-4}$	Chapter 3

Table 6.3: Initial and Boundary Conditions for Numerical Model.

Eq.	Initial Condition	Boundary Condition
(6.3)	$t = 0 \Longrightarrow Y_b = 1; \ Y_c = 0$	-
(6.4)	$t = 0 \Longrightarrow P_g = 101375 \ Pa$	$x = 0.00 \ m \Longrightarrow \rho_g u_g(t) \rightarrow \begin{cases} u_g(t) = 0 \rightarrow 0 \leq t \leq t_g \\ u_g(t) = u_g \rightarrow t_g < t \leq t_f \end{cases}$ $x = 0.45 \ m \Longrightarrow P_g = 101375 \ Pa$
(6.5)	$t = 0 \Longrightarrow Y_{O_2} = 0.204$	$x = 0.00 \ m \Longrightarrow Y_{O_2} = 0.204$ $x = 0.45 \ m \Longrightarrow -D_g \dfrac{\partial(\rho_g Y_{O_2})}{\partial x} = h_m\left(Y_{O_2,0} - Y_{O_2}\right) \rightarrow h_m = 100 \ kg m^{-2} s^{-1}$
(6.6-6.7)	$t = 0 \Longrightarrow T_s = T_g = T_0 = 298 \ K$	$x = 0.10 \ m \Longrightarrow \begin{cases} -(k_{eff})\dfrac{\partial T_s}{\partial x} = \dot{q}''_{in} = 25 \ kW \ m^2 \rightarrow 0 \leq t \leq t_h \\ -(k_{eff})\dfrac{\partial T_s}{\partial x} = 0 \rightarrow t_h < t \leq t_f \\ T_g = 298 \ K \end{cases}$ $x = 0.45 \ m \Longrightarrow \begin{cases} -(k_{eff})\dfrac{\partial T_s}{\partial x} = 0 \\ -(k_g)\dfrac{\partial T_g}{\partial x} = 0 \end{cases}$

For all simulations, a local energy balance (developed herein) and a global energy balance (Chapter 5) was computed for several time steps. The local energy balance integrates the energy that enters and leaves the reaction front over the front thickness (Figure 6.1b,c), whereas the global energy balance integrates the energy over the entire domain (Figure 6.1d). Table 6.4 provides the details of each method, and the differences between them reside in Equation (6.10) and Equation (6.14). In the global energy balance, Equation (6.10) calculates the energy added by the heater at x=0.1 m and Equation (6.14) calculates the energy removed at the end of the domain (x=0.45 m). In the local energy balance, energy entering and leaving the control volume encompassing the reaction front (x_1 to x_2) are due to forward convective heat transfer.

Table 6.4: Global and Local Energy Balance

Energy Rate [J s^{-1}]	Eq. #	Global Energy Balance	Local Energy Balance
In	6.10	$\dot{E}_{in} = \dot{q}''_{in} A_{cs}\big|_{x=0.1}$	$\dot{E}_{in} = (\rho_g u_g A_{cs}) C_{p_g}(T_g - T_0)\big|_{x_1}$
Oxidation	6.11	$\dot{E}_{oxid} = \int_{0.1}^{0.45} (-\Delta H_c R_c A_{cs}) dx$	$\dot{E}_{oxid} = \int_{x_1}^{x_2} (-\Delta H_c R_c A_{cs}) dx$
Pyrolysis	6.12	$\dot{E}_{pyr} = \int_{0.1}^{0.45} (-\Delta H_b R_b A_{cs}) dx$	$\dot{E}_{pyr} = \int_{x_1}^{x_2} (-\Delta H_b R_b A_{cs}) dx$
Radial Heat Loss	6.13	$\dot{E}_{loss} = \int_{0}^{0.45} -U(2\pi r)(T_s - T_0) dx$	$\dot{E}_{loss} = \int_{x_1}^{x_2} -U(2\pi r)(T_s - T_0) dx$
Out	6.14	$\dot{E}_{out} = -(\rho_g u_g A_{cs}) C_{p_g}(T_g - T_0)\big|_{x=0.45}$	$\dot{E}_{out} = -(\rho_g u_g A_{cs}) C_{p_g}(T_g - T_0)\big|_{x_2}$
Net	6.15	$\dot{E}_{net} = \dot{E}_{in} + \dot{E}_{oxid} + \dot{E}_{pyr} + \dot{E}_{loss} + \dot{E}_{out}$	$\dot{E}_{net} = \dot{E}_{in} + \dot{E}_{oxid} + \dot{E}_{pyr} + \dot{E}_{loss} + \dot{E}_{out}$
Energy [J]	**Eq. #**	**Global Energy Balance**	**Local Energy Balance**
Net	6.16	$E_{net} = \int_{0}^{t_f} (\dot{E}_{net}) dt$	$E_{net} = \int_{0}^{t_f} (\dot{E}_{net}) dt$

6.3 Results

6.3.1 Self-Sustaining Smouldering

Figure 6.2 shows a typical example of a robust self-sustaining smouldering case (Run #3, base case, Table 6.1); the panels of the figure serve to illustrate how temperature, oxygen, reaction rate, mass loss, and components of the global energy balance relate to each other over time. The beginning of the simulation is characterized by the pre-heating period (DT<0, Figure 6.2a), during which only the heater is on (no air, no reactions). Energy is input to the system by conduction and radiation at a constant rate and is lost radially at an increasing rate, due to the increasing temperature gradient and increased heated length along which losses occur (Figure 6.2b). Since the input exceeds the losses, the net energy rate is positive (black line in Figure 6.2c), the net energy increases in the system (red line

in Figure 6.2c), and a thermal wave propagates along the reactor. Correspondingly, the temperature at x=0.12 m increases (Figure 6.2a).

When the air flux is initiated (DT=0), the temperature at x=0.12 m rapidly increases (Figure 6.2a) due to the onset of smouldering, releasing substantial energy (Figure 6.2b and Figure 6.2c), and increased heat transfer from the preheated region. The heater is turned off when the first thermocouple peaks (Figure 6.2a). Numerically, it is not necessary to follow this heating protocol, nevertheless, this was conducted for consistency with experimental database. Peak temperatures are constant as the self-sustained front propagates along the column (Figure 6.2a). Note that, upon air flux initiation, a short transient peak in the oxidation energy production rate and net energy rate occurs due to boundary influences on a spatially-integrated model property. Throughout smouldering, pyrolysis consumes energy at a much smaller rate than oxidation produces it (Figure 6.2b). The oxidation and pyrolysis energy rates are constant as fuel is consumed at a constant rate by the steady velocity of the front; however, the rate of global energy losses continues to increase (Figure 6.2b) as the heated length (and surface area to volume ratio) grows. Nevertheless, until the reaction reaches the end of the fuel bed (DT=1), the net rate of energy is always positive, leading to ever increasing net energy in the system (Figure 6.2c). A positive net energy rate is characteristic of a self-sustained smouldering scenario (Chapter 5).

As the front approaches the end of the column, energy leaves the system via hot air convection and oxidation ceases (Figure 6.2b), causing the net energy rate to abruptly decrease to negative values. For DT>1, all fuel is eliminated (i.e., only clean, hot sand remains) and only radial and convective energy losses remain, causing a steady decrease in the net system energy as the column cools (Figure 6.2b and Figure 6.2c).

Note that in the smouldering of solid porous fuels (e.g., polyurethane foams), fuel is typically not entirely consumed due to heat losses and/or oxygen-limited conditions. Thus, although the smouldering front is able to propagate through the whole domain, char oxidation reactions quench and unburnt material is left behind [48, 70]. The substantial heat retention and excess oxygen in organic liquid/inert porous media scenarios means that the trailing edge of the smouldering front is typically coincident with the consumption of essentially all of the fuel.

Run #3 resulted in average smouldering front velocity (v_f) of 4.16 mm min^{-1} and constant peak temperature (T_p) of 679 °C (Figure 6.2a and Figure 6.2d); matching the base case experiment (Chapters 4 and 5). A constant peak temperature shows that the smouldering front maintains its characteristics as the reaction propagates through the reactor. A more detailed evaluation of $\dot{E}_{in}$ and $\dot{E}_{out}$ (Figure 6.1c) will be provided later. Figure 6.2d describes predicted temperature profiles at three different times. Note that the region behind the smouldering front (i.e., clean sand region) becomes thicker with time, indicating that the rate of sand cooling (due to radial heat losses plus convective heat transfer) is slower than the velocity of the reaction. Figure 6.2e and Figure 6.2f provide details of the chemical reactions at DT=0.5 (front half-way through the column), which is representative of their conditions at all times. They reveal that pyrolysis converts all of the bitumen into char, which is entirely oxidized (Figure 6.2e). The entirety of both reactions (i.e., pyrolysis and oxidation) occurs in a 0.01 m narrow region situated at the peak temperature (Figure 6.2d); this agrees with observations [71]. Since forward smouldering allows convective heat transfer ahead of the front, pyrolysis advances slightly ahead of oxidation, agreeing with [48, 52, 64]. Oxygen consumption, from 20.4% to 15.0% (Figure 6.2e), coincides with oxidation (Figure 6.2f) and occurs at the peak temperature (Figure 6.2d). Since fuel is entirely consumed and oxygen remains, the smouldering front is fuel-limited.
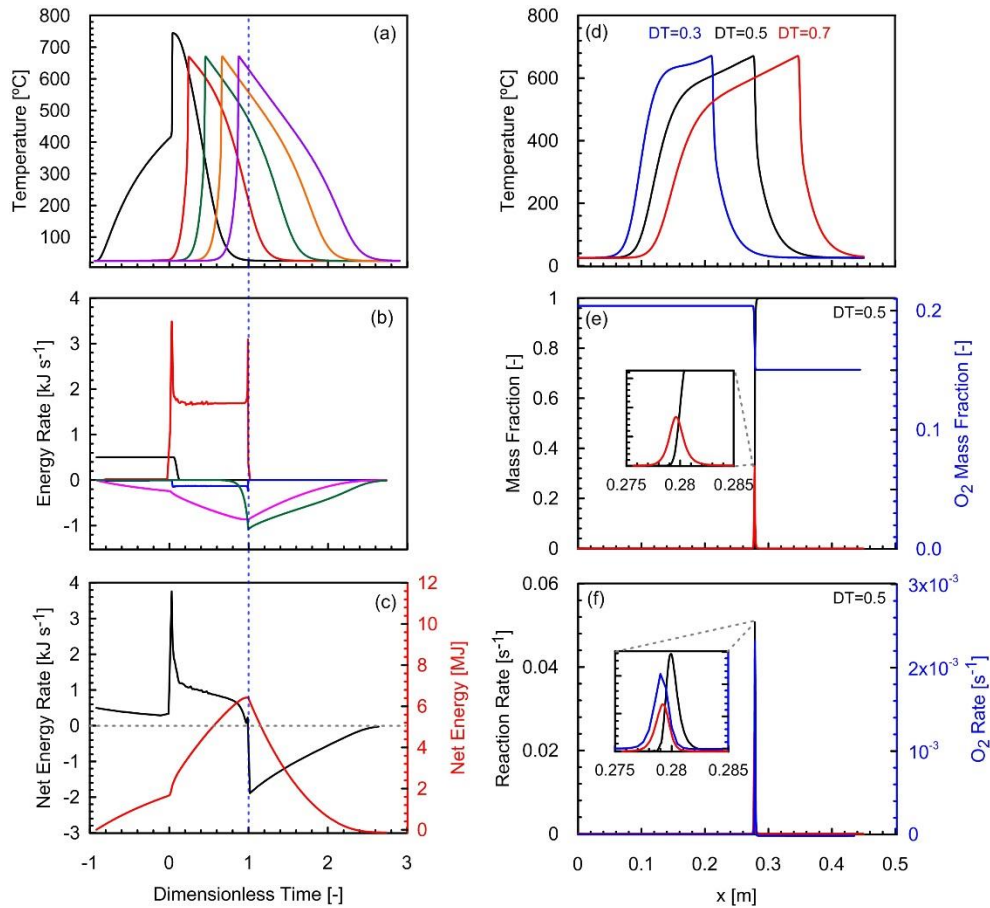
Figure 6.2: (a) Model-predicted sand/bitumen temperature (T_s) versus Dimensionless Time (DT) for Run #3 (Table 6.1). Colours describe thermocouple positions (x) from (a) 0.12 to 0.40 m with 0.07 m intervals. (b) Energy rate for each component (Table 6.4) versus DT: (black) heater, (red) oxidation, (blue) pyrolysis, (magenta) radial loss, and (green) convection out. (c) (Black) Net energy rate and (red) net energy versus DT. Dashed blue line shows the end of the column (DT=1). (d) Sand/bitumen temperature profile versus height of the column at different DTs. (e-f) (Black) Bitumen and (red) char (e) mass fractions and (f) reaction rates, (blue) (e) O_2 mass fraction and (f) O_2 consumption rate versus height of the column (x) for Run #3 (Table 6.1) at DT=0.5.

6.3.2   Smouldering Extinction

Several conditions can change a smouldering scenario from self-sustaining to extinction. Figure 6.3 shows an example of extinction due to low air flux (Run #1, Table 6.1). Compared to the base case (Figure 6.2a), it is observed that the temperature-time plot at

the first thermocouple is similar. However, after the heater is turned off, the peak temperatures rapidly decrease as the reactions extinguish. In such cases, fuel remains throughout the system wherever the reactions were not activated or were not sustained for sufficient time.

Table 6.1 shows seven additional smouldering extinction cases: *i*) low fuel content (Run #5), *ii*) low oxygen concentration (Run #10), *iii*) high heat losses (Run #15), i*v*) low heat of combustion (Run #16), *v*) low heat transfer coefficient (Run #22), *vi*) low oxidation pre-exponential factor (Run #23), and *vii*) high oxidation activation energy (Run #28). The specific values used in these simulations were obtained by additional sensitivity simulations (not shown) such that these values approximate the threshold required to achieve extinction in each case, relative to the base case. The temperuture-time curves for all of these cases looked similar to Figure 6.3. Independent of the method used to weaken the reaction, extinction is characterized by an unfavourable energy balance; this is discussed in detail below.
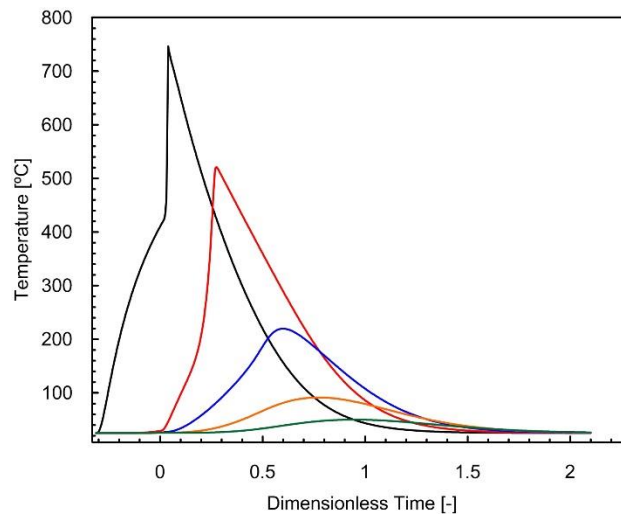
Figure 6.3: Model-predicted sand/bitumen temperature versus Dimensionless Time at u_g=0.014 m s^{-1} (Run #1, Table 6.1). Colours describe thermocouple positions (x) from 0.12 to 0.40 m with 0.07 m intervals.

6.3.3   Local vs Global Energy Balance

Figure 6.4 compares the local and global energy balances for a typical self-sustained smouldering scenario (base case, Run #3, Table 6.1); it does so by presenting the net energy rate, and all of its individual components, at three times. Note that the oxidation energy rates are the same in both measures of energy balance, and the same is true for the pyrolysis energy rates; this matches expectations since the reactions are contained entirely within the front (Section 6.3.1). In the local energy balance, the rate that energy enters from convective air flux (*In*) is approximately equal to the rate at which it leaves (*Out*) plus the pyrolysis energy rate (*Pyr*) and the energy rate of losses (*Loss*) (Figure 6.4a). Note that losses in this case can be considered negligible. As a result, the net energy rate is comprised almost entirely by the oxidation energy generation rate. Moreover, the net energy rate within the front is relatively constant with time, leading to a steady-state reaction front (Figure 6.2a and Figure 6.2d), supporting the observations of Section 6.3.1 regarding a robust, self-sustaining reaction.

In the global energy balance, there is no energy entering or leaving the system (Figure 6.4b), since the heater is off and the end of the domain is still cold at the times analyzed (see related temperature profiles in Figure 6.2d). The first key difference with the local analysis is that here the energy losses are not negligible. The heat loss occurring along the length of heated porous media behind the front exceeds by 10 to 20 times the heat loss within the front (Figure 6.4a and Figure 6.4b). Thus, in the global energy analysis, the net energy rate is considerably less than the oxidation energy rate and therefore less than the same metric in the local analysis; this is a second key difference. Moreover, those losses grow with time (although at a decaying rate) as the length of the hot zone grows (Figure 6.2d) due to slow cooling of the clean sand. Therefore, the global net energy rate necessarily decreases with time; a third key difference. The rate of this decrease, and the degree to which the net energy rate exceeds zero, will be further discussed below. However, for the moment, note that the net energy rate is substantially greater than zero for all times for both the local and global energy analysis, meaning that by both measures the smouldering scenario is self-sustaining.
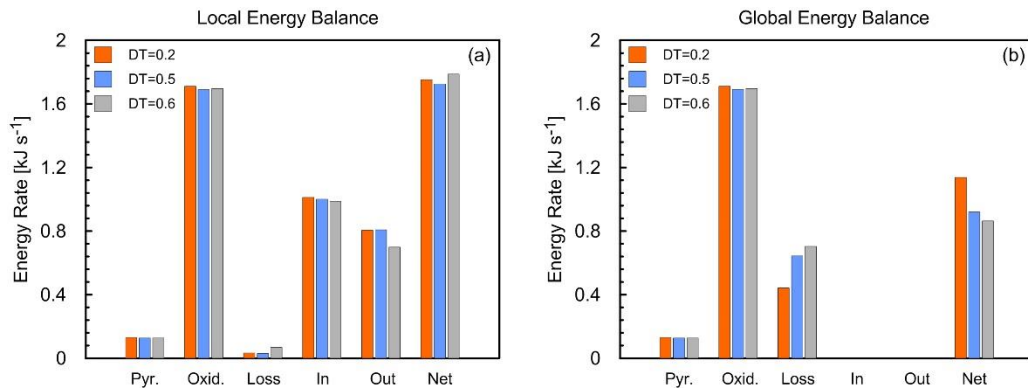
Figure 6.4: (a) Local and (b) global energy balance for base case (Run #3, Table 6.1). Energy rate depicted at DT equal to 0.2, 0.5, and 0.6.

Figure 6.5 describes the local and global energy balances for a typical smouldering extinction case (Run #1, Table 6.1). Here, pyrolysis and oxidation energy rates are much less than the self-sustaining case (note the difference in vertical axis limits between Figure 6.4 and Figure 6.5). Moreover, they decrease with time, reflecting the weakening reaction front. In the local analysis, it can be observed that while energy *In* and energy *Out* balance each other, pyrolysis and heat losses bring the net energy rate at the front into negative values only at DT=0.6. For DT=0.2, the reaction is still vigorous, nevertheless (as seen from the global energy balance) its fate is already established. The global energy balance shows a negative net energy rate as early as DT=0.2. In both local and global analyzes, the losses are not negligible. While their magnitudes are similar to the self-sustaining case (Figure 6.4), since oxidation rates are much less, they form a larger fraction of the energy balance and affect the net energy rate.

As in the self-sustaining case, the global energy loss rates are much higher than the local energy loss rates. However, as indicated above, there is a striking difference between the net energy rate, calculated by the local and global analyzes. The local energy balance becomes negative between DT = 0.5 and 0.6, whereas the global energy balance is negative as early as DT=0.2 and for all subsequent times (i.e., even when peak temperatures are still high). It has been proposed that smouldering extinction is predicted by a net energy rate less than zero (Chapter 5). Considering this criterion in this context, the local energy

analysis identifies when the reaction is indeed losing more energy than it gains; i.e., the moment of reaction extinction. However, the global energy balance predicts in advance the smouldering scenario that is not self-sustaining and will eventually extinguish. Indeed, extinction is guaranteed if no conditions change. Extinction may be averted by changing the scenario mid-run, such as increasing air flux, reducing heat losses, etc. In this way, it can be understood that both the local and the global analysis provide valuable, but different, perspectives on the system's behaviour.
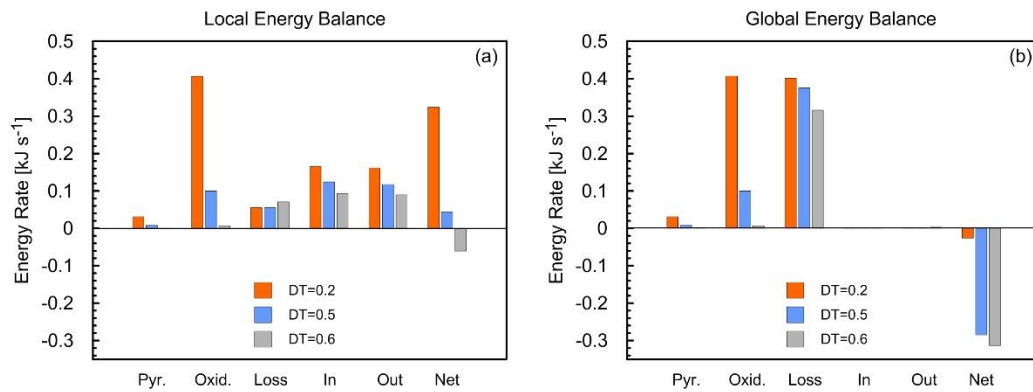
Figure 6.5: (a) Local and (b) global energy balance for smouldering extinction by low air flux (Run #1, Table 6.1). Energy rate depicted at DT equal to 0.2, 0.5, and 0.6.

6.3.4 Sensitivity Analysis of Self-sustaining Smouldering Cases

6.3.4.1 Air Flux (u_g)

Injected air flux is the easiest and most practical way to control smouldering behaviour. Figure 6.6a shows that both peak temperature (T_p) (from 616 to 707 °C) and smouldering front velocity (v_f) (from 2.12 to 5.42 mm min^{-1}) increase when u_g increased from 0.025 to 0.083 m s^{-1}. The v_f (u_g) relationship is linear (R^2=0.999), qualitatively agreeing with [5, 7, 9, 11, 12, 14, 16, 18, 21, 22, 25, 26]. Indeed, Figure 6.7 reveals that the influence of air flux on front velocity is one of the strongest parameter sensitivities found in this study. Note that u_g=0.083 m s^{-1} represents the upper end of what is practical in applied smouldering scenarios.

Figure 6.8-Figure 6.10 detail how each parameter affects the smouldering system in space and time. Figure 6.8 reveals that increasing the air flux primarily increases the peak temperature (Figure 6.8a,b) due to an increase in the oxidation reaction rate (Figure 6.8e) – with the peak reaction rate being linearly correlated to the air flux ($R^2 = 0.994$) – consequently increasing the net energy rate (Figure 6.10). Oxygen is not entirely depleted and its consumption decreases with an increase in the air flux (Figure 6.8c). Thus, the propagation of the smouldering front is limited by the fuel consumption, i.e., fuel-limited, since the fuel was entirely consumed, with remaining oxygen.

Table 6.5 summarizes the global energy balance for each case, including all the energy components integrated from the initial time until the net energy rate becomes zero. Figure 6.10 plots the global energy balance for each case at DT=0.5 (smouldering front half-way through the domain). The table and the figure underscore that increasing the air flux primarily affects the rate at which oxidation injects energy into the system, and this in turn dominates the global net rate of energy gain in the system (Figure 6.10a). The same figure illustrates that, while global heat losses do increase with an increase in peak temperature, this has a minor influence on the global energy balance.

These results also reveal how each parameter affects the temperature profiles in time and space. Figure 6.8a and Figure 6.8b show that as air flux decreases, the shape of the leading edge of the smouldering front (pyrolysis and oxidation) was relatively unchanged. However, the temperature profile along the heat transfer zone behind the front and the trailing (cooling) edge of the heated zone changed dramatically (Figure 6.8b); as air flux decreased, temperatures dropped quickly in the heat transfer zone but the cooling edge also became wider. This resulted from *i*) slower heat transfer from the solid to the gas (Chapter 3), *ii*) less energy stored behind the front (E_{st}/E_{add} was 39% for lowest air flux versus 64% for highest), and *iii*) higher heat losses (E_{loss}/E_{add} was 52% for lowest air flux versus 28% for highest). In all other respects, these cases are similar to the base case (thin reaction zone, complete oxidation of fuel, kinetically-limited regime, etc.) across the full range of practical air fluxes for applied smouldering.

Extinction was found for $u_g \leq 0.014$ m s^{-1}, which agrees qualitatively with [12, 18, 19, 25]. The details of this case were discussed in Sections 6.3.2 and 6.3.3, where it was analyzed

as a typical example for all extinction cases. Figure 6.10 and Table 6.5 further support that extinction here corresponds to a negative energy balance resulting from global heat losses exceeding the energy from oxidation.

6.3.4.2　Fuel Saturation (S_b)

Fuel saturation (volume fuel per volume pore space), comparable to fuel concentration (mass fuel per mass bulk porous medium), is a key concern in natural and applied smouldering scenarios. Figure 6.6b shows T_p increased sharply (from 600 to 1265 ℃) as S_b increased from 10 to 50%, representing a linear relationship (R^2=0.999) and agreeing qualitatively with [22, 27, 28]. This represents an even stronger sensitivity than observed for air flux and front velocity (Figure 6.7). Here, v_f exhibited more complex sensitivity, increasing from 2.9 to 5.5 mm min^{-1} with increased S_b in the range 10%$<S_b<$20%, minimal sensitivity for 20%$<S_b<$40%, and decreasing with further fuel saturation increases (Figure 6.6b).

Increasing fuel saturation in the parameter space 7%$<S_b<$40% leads to dramatic increases in the oxidation reaction rates and rate of energy added to the system (Figure 6.10b). Figure 6.8h indicates that an increased fraction of injected O_2 is consumed (from 2% to 9%) when fuel saturation increased from 10 to 20%. When oxygen is in excess, increased fuel saturation increases the heat release rate (Figure 6.8j), resulting in increased front velocity. At fuel saturations between 20 and 40%, further increased reaction rates (Figure 6.10b) are balanced by the increased time required to consume all the fuel, leading to an approximately constant front velocity. Further S_b increases to 40% resulted in O_2 being entirely consumed (figure not shown). At S_b of 50%, the reaction rate stopped increasing since no additional oxygen was available, resulting in a slight decrease in the net energy rate (Figure 6.10b) and a corresponding decrease in the front velocity (Figure 6.6b); this behaviour qualitatively agrees with experiments [9, 22, 27, 28]. At even higher fuel saturations, the propagation of the smouldering front is expected to change from a fuel-limited to an oxygen-limited regime, characterized by total O_2 consumption and potentially leading to un-oxidized fuel left behind.

Saturation has a strong effect on the distribution of energy and temperature in the system. The increase in saturation produces more char (from 29% at S_b=10% saturation to 38% at S_b=20%) during pyrolysis (Figure 6.8i) along with a 300% increase in the reaction rates at S_b=20% (Figure 6.8j). The increase in char production generates much more energy in a much more compressed space (the two reactions are less spread in space at high saturations). Thus, the increase in saturation generates more energy and increases the rate of energy generation, resulting in more energy stored behind the front. Moreover, heat losses become a lower fraction of the net system energy (from 46% down to 18%; Table 6.5). Altogether, this creates a much thicker and higher temperature heat transfer zone in the clean sand behind the front (Figure 6.8g).

Extinction was found for $S_b \leq 7\%$ (Run #5), qualitatively agreeing with [11, 13, 22, 28]. This threshold (specific to this scenario) results from oxidation energy decreasing to the point that it is insufficient to overcome heat losses (Figure 6.10b). Thus, extinction occurs right after the ignition source is eliminated.

6.3.4.3   Oxygen Mass Fraction (Y_{O2})

It could be expected that O_2 fraction of the injected air flux may be a potentially useful variable for modifying smouldering behaviour. However, T_p and v_f exhibit negligible to minor sensitivity, respectively, to O_2 in the range 10% to 30% (Figure 6.6c and Figure 6.7). It is observed that the same amount of oxygen, approximately 5%, is consumed in each case and that O_2 remains in excess for these runs (Figure 6.8m). The oxidation rates do increase with O_2 fraction, but the increases are modest relative to other parameters such as air flux and saturation (Figure 6.8o and Figure 6.10c). Overall, the influence on net energy rate is minor (Figure 6.10c). This is supported by the fact that the fraction of energy stored behind the front (54% to 64%) and fraction of energy lost (36% to 28%; Table 6.5, Runs # 11 and 12) varied little.

The only available literature considering O_2 concentration involves solid fuels. It suggests that for polyurethane foam and peat, the fraction of fuel left behind decreases with increased O_2 concentration with O_2=30% required for total fuel consumption [14]. In contrast, in no self-sustaining simulation conducted in this work was any fuel left behind

and this agrees with all available experiments in organic liquid/inert porous media systems [7-9, 45]. In general, the low sensitivity of peak temperature and front velocity observed here was also observed for solid fuels [26]. These results agree qualitatively with [31], that larger char production and thicker smouldering fronts occur at low O_2 concentrations (Figure 6.8n), which may explain the slightly higher peak temperatures. These findings explain the role of O_2 in the fuel-limited regime and complement the conclusions presented in [14, 31] for an oxygen-limited regime.

Extinction of the smouldering front due to small O_2 concentration (i.e. oxygen-limited regime) is unlikely to happen in the practical configurations analyzed in this work. It was found that only a very small O_2 concentration ($\leq$1%, Run #10) can cause extinction (Figure 6.6c and Figure 6.10c). This qualitatively agrees with smouldering of oil shale semi-coke in which extinction occurred at 3.5% O_2 [30]. Overall, this suggests that smouldering is robust, since it can be self-sustaining even at low oxygen concentrations.

6.3.4.4 Global Heat Loss (U)

Figure 6.6d and Figure 6.7 describe a negligible sensitivity of T_p and v_f with increasing U (9-17 W m^{-2} K). This is expected since the cases analyzed involve a robust reaction (far from extinction); thus, changes in the center-line temperature are expected to be less sensitive to radial heat loss changes. Figure 6.8r-t confirm that these changes in U had negligible effects on O_2 consumption, char production, reaction rates, and front thickness; thus, the system remained within the fuel-limited regime. Nevertheless, Figure 6.8p-q indicates that an increase in U causes a change in the slope of the temperature curve in the heat transfer region behind the smouldering front [27]. Thus, as U increased, more energy is lost radially (Figure 6.10d) and less energy is stored in the system, with less energy available to heat the incoming cold air (Table 6.5) and less net energy produced (Figure 6.10d).

Run #15 shows an extinction case with U=60 W m^{-2} K^{-1}; this may represent a column with no insulation. Extinction by high heat loss is well described in the literature [12, 13, 16-18, 20, 27, 33, 39, 72]. The rate of energy lost appears to be less for U=60 W m^{-2} K^{-1} than U = 17 W m^{-2} K^{-1} (Figure 6.10d). However, this is because the heat loss is so severe that the

smouldering never properly ignites. Table 5 shows that only 11% of the energy added into the system is from oxidation, with the rest provided by the heater. Moreover, energy losses accounted for 70% of the total energy added. As in previous cases, oxidation diminished to the point that it could not overcome heat losses (Figure 6.10).

6.3.4.5   Heat of Oxidation (ΔH_c)

Since pyrolysis has little influence in the global energy balance of robust self-sustaining cases (Chapter 5) (see also Table 6.5 and Figure 6.10, all cases), a sensitivity analysis to the heat of pyrolysis was not conducted. On the other hand, a sensitivity to the heat of oxidation (ΔH_c) was conducted; this can represent, for example, different fuels.

ΔH_c varied from 30 to 45 MJ kg^{-1}, increasing T_p and v_f (Figure 6.6e) from 625 to 716 ℃ and from 3.18 to 5.00 mm min^{-1}, respectively. T_p and v_f exhibit intermediate sensitivity to ΔH_c relative to all of the variables examined, with front velocity being the more sensitive of the two (Figure 6.7). Unsurprisingly, the effect of ΔH_c on the system is similar to that of fuel saturation, except the latter varies over wider range and thus has a relatively larger influence. Increasing ΔH_c causes more energy to be released by oxidation, with a corresponding increase in the global net energy rate (Figure 6.10e). Similar to the behaviour observed for saturation, the excess of energy released by the high ΔH_c is mostly stored behind the front but with some transferred ahead of the front, changing the distribution of temperature both ahead and behind the front (Figure 6.8u-v). Extinction was found for $\Delta H_c \leq 18$ MJ kg^{-1} (Run #16) due to a negative energy balance (Figure 6.10e).

6.3.4.6   Nusselt Number (Nu)

The influence of the gas properties (k_g, C_{pg}, μ_g, and ρ_g) varying with temperature in the Nu correlation (Equation 6.8) was also analyzed. Gas properties were taken from Table 6.2 according to three temperatures: 20 ℃ (low), 230 ℃ (medium), and 600 ℃ (high) and Nu was calculated as 0.100, 0.018, and 0.003, respectively. Figure 6.6f shows that a decrease in Nu results in a decrease in T_p (677-588 ℃) and v_f (4.01-1.56 mm min^{-1}), with higher sensitivity to v_f (Figure 6.7). This is expected since reduced Nu slows down the heat transfer between phases, decreasing the fraction of energy stored behind the front (from 58% to 38%) and increasing the fraction of radial heat losses (from 34% to 55%) (Table 6.5); note

the slope changes in Figure 6.6f and Figure 6.9a-b. It is noted that Leach et al. [24] found extinction at high Nu for opposed smouldering in polyurethane foam. High Nu (10^5) was also tested here, but extinction was not observed. Instead, this high Nu resulted in extremely fast heat transfer, likely generating local thermal equilibrium conditions. No further change in the temperature curves was observed, as expected (figure not shown). O_2 consumption and char production are insensitive to increased Nu (Figure 6.9c-d), whereas reaction rates decreased five times (Figure 6.9e), causing the net energy rate to decrease significantly (Figure 6.10f). Since fuel was entirely consumed and O_2 partially depleted, the smouldering front propagation is within the fuel-limited regime. Extinction took place for $Nu \leq 0.0016$ (Run #22) due to a negative energy balance (Figure 6.10f).

6.3.4.7   Char Pre-Exponential Factor (A_c) and Activation Energy (E_c)

Sensitivity to the kinetic parameters (A_c and E_c) of the Arrhenius equation for char oxidation were conducted. Figure 6.6g shows that T_p decreases (730-644 °C) and v_f increases (2.95-5.62 mm min^{-1}) when A_c increases over the range 4-6 log (s^{-1}). The results for E_c suggest opposite behaviour, with T_p increasing from 656 to 712 °C and v_f decreasing from 5.00 to 3.38 mm min^{-1} (Figure 6.6h) for E_c increasing over the range 80-100 kJ mol^{-1}. These results qualitatively agree with [12, 24, 36]. Figure 6.7 suggests that peak temperature is relatively insensitive to both parameters while front velocity is moderately and similarly sensitive to both, although in opposite directions.

High A_c values (low E_c) create temperature curves more spread out along the domain (Figure 6.9f-g), as a result of more energy stored behind the front and less radial heat losses (Table 6.5). Moreover, it consumes more O_2 (Figure 6.9h and Figure 6.9m), with less char production (Figure 6.9i and Figure 6.9n), and higher reaction rates (Figure 6.9j and Figure 6.9o). Both low A_c and high E_c result in thicker (but still very thin, i.e. < 1 cm) smouldering front due to more char production in a thicker region. All of these runs predicted a smouldering front propagation in the fuel-limited regime.

Extinction was found for $A_c \leq 3$ log (s^{-1}) (Run #23) and $E_c \geq 120$ kJ mol^{-1} (Run #28) qualitatively agreeing with [13, 14, 24, 50]. As in previous cases, under these two conditions, oxidation decreases to negligble rates and thus heat losses lead to a negative

net energy rate (Figure 6.10g and h). Table 6.5 shows that low A_c showed less fraction of energy generation by oxidation (16%) when compared to high E_c (30%), with relatively insensitive fraction of heat losses (from 30% to 34%).
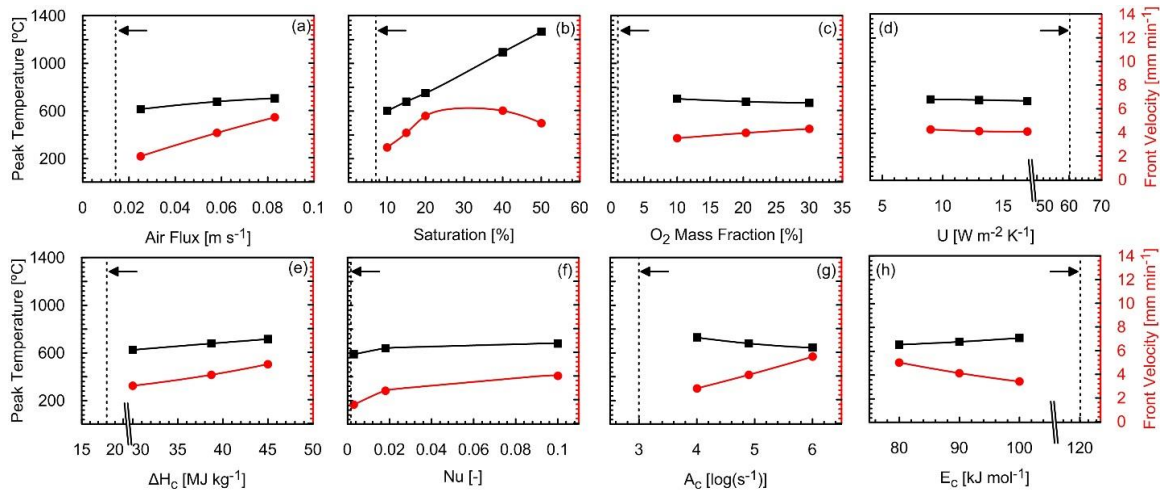
Figure 6.6: Numerical (■) peak temperature and (●) smouldering front velocity for the eight parameters analyzed in Table 6.1. The second point in each one of the graphs corresponds to the base case. Dashed vertical line shows extinction limits.
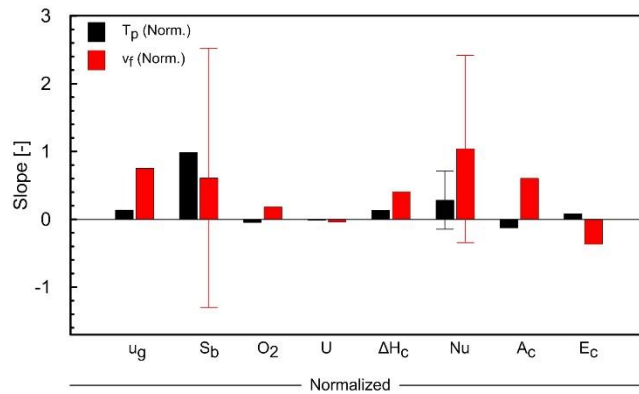
Figure 6.7: Normalized peak temperature and front velocity slopes versus normalized independent variables. Error bars shows the range from the highest positive to the highest negative slope due to non-linear increase in T_p and v_f.
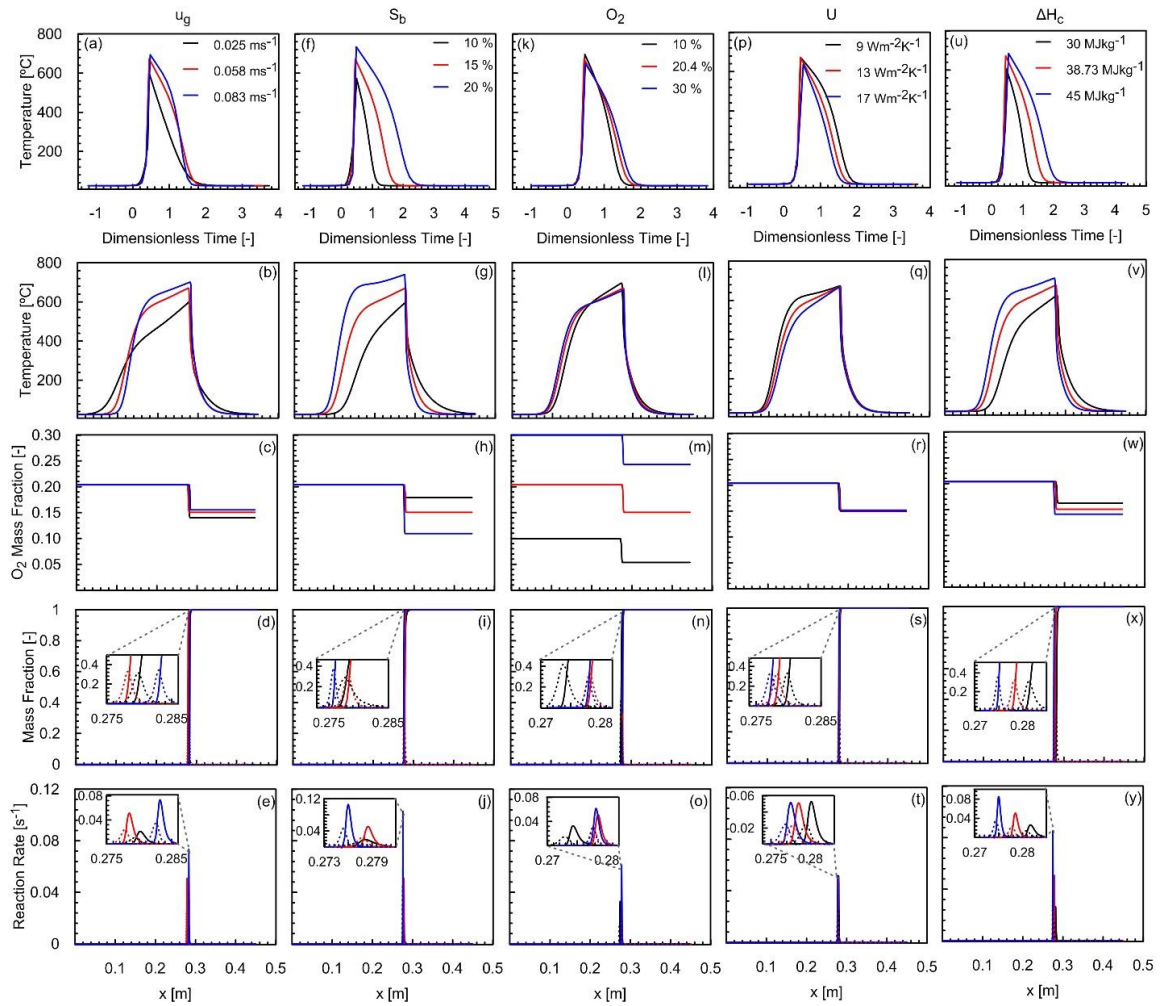
Figure 6.8: Numerical sand/bitumen temperature versus (a, f, k, p, u) Dimensionless Time (DT) at x=0.26 m and (b, g, l, q, v) height of the column (x) at DT=0.5. (c, h, m, r, w) Oxygen mass fraction, (d, i, n, s, x) fuel mass fraction, and (e, j, o, t, y) reactions rates versus height of the column. Colours show the different conditions applied according to Table 6.1 for u_g, S_b, O_2, U, and ΔH_c. Dashed lines in mass fractions and reaction rates describe char and solid lines indicates bitumen.
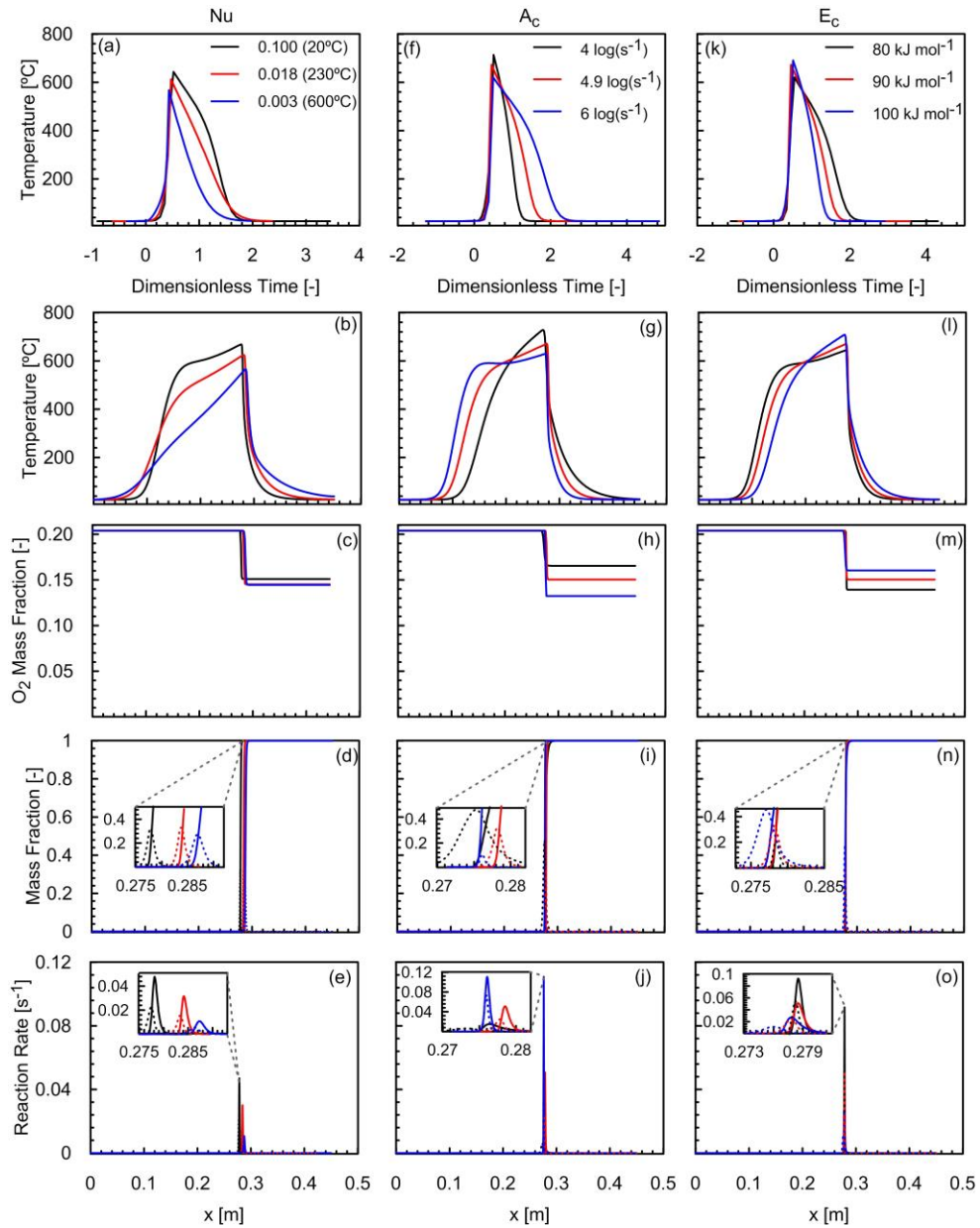
Figure 6.9: Numerical sand/bitumen temperature versus (a, f, k) Dimensionless Time (DT) at x=0.26 m and (b, g, l) height of the column (x) at DT=0.5. (c, h, m) Oxygen mass fraction, (d, i, n) fuel mass fraction, and (e, j, o) reactions rates versus height of the column. Colours show the different conditions applied according to Table 6.1 for *Nu*, *Ec*, and *Ac*. Dashed lines in mass fractions and reaction rates describe char and solid lines indicates bitumen.
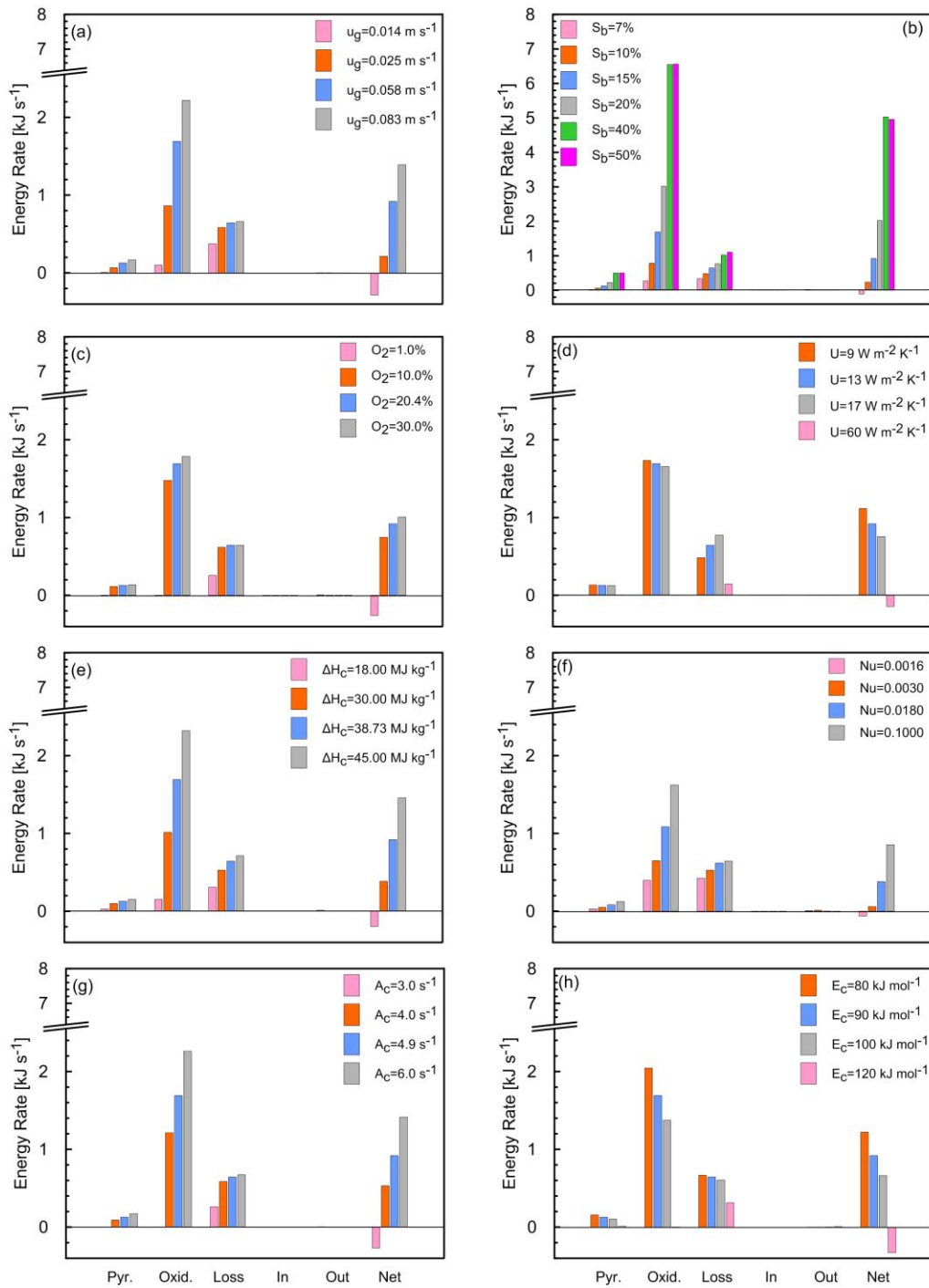
Figure 6.10: Global energy balance for all the runs presented in Table 6.1. Energy rates were depicted at DT=0.5. Pink bar describes the extinction cases.

6.3.5   Extinction Criterion

Figure 6.11 summarizes the global net energy rate calculated at DT=0.5 for all of the sensitivity runs for five out of the eight parameters analyzed in Section 6.3.4; the horizontal axis is a normalized value of the independent variable so that all cases can be compared. The figure underscores that all smouldering extinction cases exhibit a negative global net energy rate while self-sustaining cases exhibit positive values. For the latter, the magnitude of the global net energy rate reflects the robustness of the smouldering reaction (i.e., how far the scenario is from extinction in the parameter space and how rapidly energy is being generated and stored in the system). Moreover, the slope of each curve in Figure 6.11 indicates the sensitivity of smouldering behaviour to that parameter.

The figure underscores that a minimum fuel saturation is necessary, and that smouldering robustness increases strongly with further increases in fuel saturation. However, this plateaus at high fuel saturations and the results suggest a potential change from a positive to a negative slope (i.e., decreasing robustness with further increases in saturation). An increase in the air flux and heat of oxidation showed similar trends, both requiring minimum values for smouldering and both exhibiting an approximately linear increase in robustness of smouldering with increases in those variables. O_2 concentration also must exceed a minimum value (quite small, as discussed above). However, beyond that and in the case where excess oxygen will therefore be present, enriching the air flux with a higher fraction of oxygen does not make the smouldering system more robust. Finally, an increase in the heat loss coefficient results in a negative slope, decreasing the global net energy rate until the extinction point.
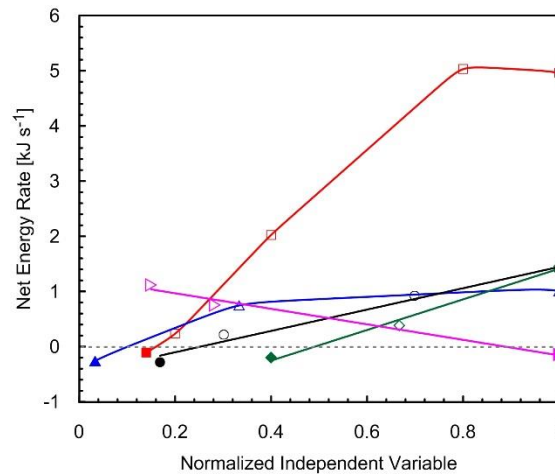
Figure 6.11: Global net energy rate at DT=0.5 versus normalized independent variable: (open symbols) self-sustaining, (closed symbols) non-self-sustaining: (●) u_g/u_{gmax}, (■) S_b/S_{bmax}, (▲) O_2/O_{2max}, (▶) U/U_{max}, and (♦) $\Delta H_c/\Delta H_{cmax}$. Dashed gray line shows transition to extinction.

Although the global energy balance can predict extinction conditions earlier than the local energy balance, it cannot establish the end of the reaction nor the total mass of contaminant remediated for some cases. The first green column in Table 6.5 shows the actual energy released by oxidation divided by the total energy available in the system that could be released by oxidation ($E_{oxid}/E_{av,o}$), calculated by integrated these energy components in time from turning the air on until the net energy rate is zero.

In self-sustained cases, values of 100% (Runs #2-4, 6- 9, 11-14, 17-21, and 24-27) indicate that all the fuel was converted into energy. In extinction cases, values for Runs #1, 5, 10, 15,16, 22, 23, and 28 range from 2 to 18%, revealing that the reaction started failing before all the fuel was consumed. At this stage, the net energy rate is negative, and the global energy balance predicts that the reaction will die. For comparison purposes, the second green column ($E_{oxid}/E_{av,o(DTf)}$) in Table 6.5 integrated the energy components until the final time (column is cold). Values of $E_{oxid}/E_{av,o(DTf)}$ for extinction cases range from 4 to 48%, revealing that some additional fuel was consumed although the reaction was destined for extinction according to the global energy balance. This agrees with the local energy balance, which indicates that oxidation is still taking place locally even after the global net

energy rate shows negative values, i.e. extinction is unavoidable (if scenario conditions remain the same) but has not happened yet.

Runs #6, 17, 21, 24, and 27 are intermediate cases, categorized as self-sustained smouldering but achieving a negative (global) net energy rate before the front reaches the end of the column ($E_{oxid}/E_{av,o}$=71-94%). However, in each case the front is able to continue long enough (i.e., exhibiting a positive local net energy rate while the global rate is negative) that all of the fuel is oxidized ($E_{oxid}/E_{av,o(DTf)}$=100%) before the reaction dies. This emphasizes that energy stored in the treated sand will continue to affect the energy balance, sustaining smouldering propagation for a finite period even if the global net energy rate is negative.

Table 6.5: Global Energy Analysis

Run # [-]	SS [-]	E_{add} [MJ]	E_{in}/E_{add} [%]	E_{oxid}/E_{add} [%]	E_{st}/E_{add} [%]	E_{pyr}/E_{add} [%]	E_{loss}/E_{add} [%]	E_{out}/E_{add} [%]	$E_{oxid}/E_{av,o}{}^{a}$ [%]	$E_{oxid}/E_{av,o(DTf)}$ [%]
1	No	4.04	63	37	63	3	34	0	17	38
2	Yes	11.44	24	76	39	6	52	3	100	100
3	Yes	11.07	23	77	58	6	33	3	100	100
4	Yes	11.26	24	76	64	6	28	2	100	100
5	No	3.21	78	22	64	2	34	0	18	48
6	Yes	7.80	39	61	47	5	46	2	83	100
7	Yes	13.90	18	82	67	6	25	2	100	100
8	Yes	25.26	10	90	75	7	18	0	100	100
9	Yes	30.80	8	92	73	7	19	1	100	100
10	No	2.66	94	6	68	2	30	0	2	22
11	Yes	11.12	22	78	54	6	36	4	100	100
12	Yes	11.09	22	78	64	6	28	2	100	100
13	Yes	11.00	23	77	67	6	25	2	100	100
14	Yes	11.21	22	78	51	6	41	2	100	100
15	No	2.77	89	11	29	1	70	0	4	4
16	No	2.98	84	16	67	3	30	0	12	38
17	Yes	8.52	29	71	50	7	41	2	91	100
18	Yes	12.46	20	80	64	5	29	2	100	100
19	Yes	10.98	23	77	58	6	34	2	100	100
20	Yes	11.07	23	77	47	6	44	3	100	100
21	Yes	8.61	29	71	38	5	55	2	71	100
22	No	4.10	62	38	62	3	35	0	18	44
23	No	2.98	84	16	67	3	30	0	6	9
24	Yes	10.28	24	76	52	6	40	2	91	100
25	Yes	11.40	22	78	65	6	27	2	100	100
26	Yes	11.06	23	77	62	6	30	2	100	100
27	Yes	10.56	24	76	54	6	38	2	94	100
28	No	3.57	70	30	63	3	34	0	13	16

[a] $E_{av,o}=\Delta H_c m_{av} v_c = -8.570$ MJ

6.4 Conclusions

The boundary between self-sustained smouldering and extinction continues to be important to understand and control smouldering. The need to use engineering approaches to extinguish hazardous smouldering scenarios remains and the use of applied engineering technologies is growing. While it is known that self-sustained smouldering requires a positive energy balance, the focus of previous work has been restricted to considering energy flow through only the thin reaction front. Such a reference frame neglects the role of energy stored and lost outside the front. Moreover, it neglects the fact that the smouldering system is dynamic, with the energy distribution evolving in space and time. This work takes a novel approach in comparing the information provided by a local energy balance to that of a global (system) energy balance. This was accomplished by employing a one-dimensional model that employs heat transfer mechanisms and chemical reactions such that it accurately simulate the smouldering of bitumen embedded in sand in both space and time. Simulations were completed across a wide range of smouldering scenarios, finding common patterns associated with robust self-sustained smouldering, propagating but slowly diminishing reactions, as well as extinguishing scenarios.

For all self-sustaining cases, the local energy balance revealed that the net energy rate is relatively constant with time, dominated by the rate at which oxidation generated energy while energy losses were negligible. However, the global energy balance for these cases revealed that energy losses in the system are not negligible; in fact, they are 10 to 20 times higher than in the local energy balance. Moreover, these losses increased with time as the length of the heated (stored energy) zone behind the front grows due to slow cooling of the clean sand, causing a decrease in the global net energy rate with time. While the net energy rate remains substantially greater than zero, the smouldering is robust, and the degree of robustness diminishes as the rate declines towards zero despite remaining self-sustaining. Robustness of smouldering is herein identified as described by the amount that the net global energy balance exceeds zero.

When the global net energy rate falls below zero, always because the energy generated by char oxidation fell below the energy lost radially throughout the domain, the system could not avoid eventual extinction. In such cases, the local energy balance may remain positive

for some time but was declining as the oxidation energy generation rate rapidly decreased. Eventually the local energy balance would also become negative if the domain was long enough. Therefore, both the local and the global analysis provide valuable, but different, perspectives on the system's behaviour. The local energy analysis identified the moment of reaction extinction, whereas the global energy balance predicted extinction of a smouldering scenario in advance, even when oxidation was still active and temperatures were high.

A sensitivity analysis of the key parameters governing self-sustaining smouldering versus smouldering extinction was conducted. It revealed that robust self-sustained smouldering can be achieved either by increasing the air flux or fuel saturation (concentration). Moreover, more energetic fuels (high heat of oxidation) favour more robust smouldering. Fuel saturation exhibited the strongest control on smouldering robustness, with peak temperature increasing with increased fuel saturation due to increased oxidation rates and the corresponding rate energy was added. Beyond fuel saturations of 50%, oxygen was fully consumed and a transition from fuel-limited to oxygen-limited regimes is expected. Peak temperature had negligible sensitivity to oxygen concentration since fuel was totally consumed at 10% O_2, resulting in excess oxygen for most cases of interest. However, 30% O_2 resulted in a slight increase in the front velocity due to faster oxidation reaction rate.

Eight different smouldering extinction conditions were identified, with five of practical application: *i*) low air flux, *ii*) low saturation, *iii*) low oxygen concentration, *iv*) low heat of oxidation, and *v*) high heat losses. All of the extinction cases presented a decrease (either slow or abrupt) in the peak temperature with time due to an unfavourable global energy balance, i.e., insufficient energy production from oxidation and dominance of heat losses as soon as the ignition source was eliminated.

Overall, this work brings new insights on the practical aspects of self-sustaining smouldering and smouldering extinction applied to organic liquid and solid fuels embedded in inert porous media. Moreover, the contributions of the local and global energy balances are novel and expected to be relevant and useful tools for furthering our fundamental understanding of smouldering combustion.

6.5 References

[1] T.J. Ohlemiller, Modeling of smoldering combustion propagation, Progress in Energy and Combustion Science, 11(4) (1985) 277-310.

[2] G. Rein, Smouldering combustion phenomena in science and technology, International Review of Chemical Engineering, 1 (2009) 3-18.

[3] J.-P. Vantelon, B. Lodeho, S. Pignoux, J.L. Ellzey, J.L. Torero, Experimental observations on the thermal degradation of a porous bed of tires, Proceedings of the Combustion Institute, 30(2) (2005) 2239-2246.

[4] L. Yermán, R.M. Hadden, J. Carrascal, I. Fabris, D. Cormier, J.L. Torero, J.I. Gerhard, M. Krajcovic, P. Pironi, Y.-L. Cheng, Smouldering combustion as a treatment technology for faeces: Exploring the parameter space, Fuel, 147 (2015) 108-116.

[5] L. Yermán, H. Wall, J.L. Torero, Experimental investigation on the destruction rates of organic waste with high moisture content by means of self-sustained smoldering combustion, Proceedings of the Combustion Institute, 36(3) (2017) 4419-4426.

[6] T.L. Rashwan, J.I. Gerhard, G.P. Grant, Application of self-sustaining smouldering combustion for the destruction of wastewater biosolids, Waste Management, 50 (2016) 201-212.

[7] P. Pironi, C. Switzer, G. Rein, A. Fuentes, J.I. Gerhard, J.L. Torero, Small-scale forward smouldering experiments for remediation of coal tar in inert media, Proceedings of the Combustion Institute, 32(2) (2009) 1957-1964.

[8] C. Switzer, P. Pironi, J.I. Gerhard, G. Rein, J.L. Torero, Self-sustaining smoldering combustion: A novel remediation process for non-aqueous-phase liquids in porous media, Environmental Science and Technology, 43(15) (2009) 5871-5877.

[9] P. Pironi, C. Switzer, J.I. Gerhard, G. Rein, J.L. Torero, Self-Sustaining Smoldering Combustion for NAPL Remediation: Laboratory Evaluation of Process Sensitivity to Key Parameters, Environmental Science and Technology, 45(7) (2011) 2980-2986.

[10] T.X. Xia, M. Greaves, A.T. Turta, C. Ayasse, THAI—A 'short-distance displacement' in situ combustion process for the recovery and upgrading of heavy oil, Chemical Engineering Research and Design, 81(3) (2003) 295-304.

[11] L. Yermán, H. Wall, J. Torero, J.I. Gerhard, Y.L. Cheng, Smoldering Combustion as a Treatment Technology for Feces: Sensitivity to Key Parameters, Combustion Science and Technology, 188(6) (2016) 968-981.

[12] J. Yang, H. Chen, N. Liu, Heat Loss and Kinetic Effects on Extinction and Critical Self-Sustained Propagation of Forced Forward Smoldering, in: K. Harada, K. Matsuyama, K. Himoto, Y. Nakamura, K. Wakatsuki (Eds.) Fire Science and Technology 2015: The

Proceedings of 10th Asia-Oceania Symposium on Fire Science and Technology, Springer Singapore, Singapore, 2017, pp. 831-840.

[13] V. Pozzobon, G. Baud, S. Salvador, G. Debenest, Darcy Scale Modeling of Smoldering: Impact of Heat Loss, Combustion Science and Technology, 189(2) (2017) 340-365.

[14] S.V. Leach, G. Rein, J.L. Ellzey, O.A. Ezekoye, J.L. Torero, Kinetic and fuel property effects on forward smoldering, Combustion and Flame, 120(3) (2000) 346-358.

[15] M. Fatehi, M. Kaviany, Adiabatic reverse combustion in a packed bed, Combustion and Flame, 99(1) (1994) 1-17.

[16] J.H. Wang, C.Y.H. Chao, W. Kong, Experimental study and asymptotic analysis of horizontally forced forward smoldering combustion, Combustion and Flame, 135(4) (2003) 405-419.

[17] D. Lozinski, J. Buckmaster, Quenching of reverse smolder, Combustion and Flame, 102(1–2) (1995) 87-100.

[18] G. Rein, A. Bar-Ilan, C. Fernandez-Pello, J.L. Ellzey, J.L. Torero, D.L. Urban, Modeling of One-Dimensional Smoldering of Polyurethane in Microgravity Conditions, Proceedings of the Combustion Institute, 30(2) (2005) 2327-2334.

[19] M.L. Kelley, D.A. Schult, Modeling extinction in forced opposed-flow smolder, Combustion Theory and Modelling, 10(1) (2006) 133-143.

[20] S.S. Dosanjh, P.J. Pagni, A.C. Fernandez-Pello, Forced cocurrent smoldering combustion, Combustion and Flame, 68(2) (1987) 131-142.

[21] B.-s. Jia, M.-z. Xie, H. Liu, Numerical study on the propagation characteristics of forward smoldering in a cellulosic packed bed, Journal of Shanghai University (English Edition), 12(2) (2008) 171-179.

[22] G. Baud, S. Salvador, G. Debenest, J.-F. Thovert, New Granular Model Medium To Investigate Smoldering Fronts Propagation—Experiments, Energy & Fuels, 29(10) (2015) 6780-6792.

[23] J.L. Torero, A.C. Fernandez-Pello, M. Kitano, Opposed Forced Flow Smoldering of Polyurethane Foam, Combustion Science and Technology, 91(1-3) (1993) 95-117.

[24] S.V. Leach, J.L. Ellzey, O.A. Ezekoye, Convection, pyrolysis, and Damköhler number effects on extinction of reverse smoldering combustion, Proceedings of the Combustion Institute, 27(2) (1998) 2873-2880.

[25] S. Dosanjh, J. Peterson, A.C. Fernandez-Pello, P.J. Pagni, Buoyancy effects on smoldering combustion, Acta Astronautica, 13(11) (1986) 689-696.

[26] T.J. Ohlemiller, J. Bellan, F. Rogers, A model of smoldering combustion applied to flexible polyurethane foams, Combustion and Flame, 36 (1979) 197-215.

[27] H. Fadaei, M. Sennoune, S. Salvador, A. Lapene, G. Debenest, Modelling of non-consolidated oil shale semi-coke forward combustion: Influence of carbon and calcium carbonate contents, Fuel, 95(0) (2012) 197-205.

[28] M. Sennoune, S. Salvador, M. Quintard, Reducing CO2 emissions from oil shale semicoke smoldering combustion by varying the carbonate and fixed carbon contents, Combustion and Flame, 158(11) (2011) 2272-2282.

[29] X. Huang, G. Rein, Interactions of Earth's atmospheric oxygen and fuel moisture in smouldering wildfires, Science of the Total Environment, 572 (2016) 1440-1446.

[30] M. Sennoune, S. Salvador, M. Quintard, Toward the Control of the Smoldering Front in the Reaction-Trailing Mode in Oil Shale Semicoke Porous Media, Energy & Fuels, 26(6) (2012) 3357-3367.

[31] R.M. Hadden, G. Rein, C.M. Belcher, Study of the competing chemical reactions in the initiation and spread of smouldering combustion in peat, Proceedings of the Combustion Institute, 34(2) (2013) 2547-2553.

[32] X. Huang, G. Rein, H. Chen, Computational smoldering combustion: Predicting the roles of moisture and inert contents in peat wildfires, Proceedings of the Combustion Institute, 35(3) (2015) 2673-2681.

[33] J. Yang, H. Chen, N. Liu, Modeling of Two-Dimensional Natural Downward Smoldering of Peat, Energy & Fuels, 30(10) (2016) 8765-8775.

[34] X. Huang, G. Rein, Thermochemical conversion of biomass in smouldering combustion across scales: The roles of heterogeneous kinetics, oxygen and transport phenomena, Bioresource Technology, 207 (2016) 409-421.

[35] J. Yang, H. Chen, W. Zhao, J. Zhou, Combustion kinetics and emission characteristics of peat by using TG-FTIR technique, Journal of Thermal Analysis and Calorimetry, 124(1) (2016) 519-528.

[36] C. Di Blasi, Mechanisms of two-dimensional smoldering propagation through packed fuel beds, Combustion Science and Technology, 106(1-3) (1995) 103-124.

[37] C. Ghabi, H. Benticha, M. Sassi, Parametric study of the heat transfer coefficient in bi-dimensional smoldering simulation, Thermal Science, 11(4) (2007) 95-112.

[38] A. Bar-Ilan, G. Rein, D.C. Walther, A.C. Fernandez-Pello, J.L. Torero, D.L. Urban, The effect of buoyancy on opposed smoldering, Combustion Science and Technology, 176(12) (2004) 2027-2055.

[39] I.Y. Akkutlu, Y.C. Yortsos, The Dynamics of In-situ Combustion Fronts in Porous Media, Combustion and Flame, 134(3) (2003) 229-247.

[40] C. Switzer, P. Pironi, J.I. Gerhard, G. Rein, J.L. Torero, Volumetric scale-up of smouldering remediation of contaminated materials, Journal of Hazardous materials, 268 (2014) 51-60.

[41] G. Rein, A. Carlos Fernandez-Pello, D.L. Urban, Computational model of forward and opposed smoldering combustion in microgravity, Proceedings of the Combustion Institute, 31(2) (2007) 2677-2684.

[42] X. Huang, G. Rein, H. Chen, Computational smoldering combustion: Predicting the roles of moisture and inert contents in peat wildfires, Proceedings of the Combustion Institute, (2014).

[43] H. Zhang, W.-Z. Fang, Y.-M. Li, W.-Q. Tao, Experimental study of the thermal conductivity of polyurethane foams, Applied Thermal Engineering, 115 (2017) 528-538.

[44] W.-Y. Jang, A.M. Kraynik, S. Kyriakides, On the microstructure of open-cell foams and its effect on elastic properties, International Journal of Solids and Structures, 45(7–8) (2008) 1845-1875.

[45] L. Kinsman, J.L. Torero, J.I. Gerhard, Organic liquid mobility induced by smoldering remediation, Journal of Hazardous materials, 325 (2017) 101-112.

[46] Zeiss, Oil Sand Microstructure in, Accessed August 27, 2014.

[47] R.H. Perry, D.W. Green, Perry's Chemical Engineers' Handbook, 7th ed., McGraw-Hill, New York, USA, 1999.

[48] T.J. Ohlemiller, D.A. Lucca, An experimental comparison of forward and reverse smolder propagation in permeable fuel beds, Combustion and Flame, 54(1–3) (1983) 131-147.

[49] D.A. Schult, B.J. Matkowsky, V.A. Volpert, A.C. Fernandez-Pello, Forced forward smolder combustion, Combustion and Flame, 104(1–2) (1996) 1-26.

[50] N.A. Moussa, T.Y. Toong, C.A. Garris, Mechanism of smoldering of cellulosic materials, Symposium (International) on Combustion, 16(1) (1977) 1447-1457.

[51] F.A. Williams, Mechanisms of fire spread, Symposium (International) on Combustion, 16(1) (1977) 1281-1294.

[52] J.L. Torero, A.C. Fernandez-Pello, Natural convection smolder of polyurethane foam, upward propagation, Fire Safety Journal, 24(1) (1995) 35-52.

[53] M.K. Anderson, R.T. Sleight, J.L. Torero, Ignition signatures of a downward smolder reaction, Experimental Thermal and Fluid Science, 21(1–3) (2000) 33-40.

[54] G. Rein, C. Lautenberger, A.C. Fernandez-Pello, J.L. Torero, D.L. Urban, Application of genetic algorithms and thermogravimetry to determine the kinetics of polyurethane foam in smoldering combustion, Combustion and Flame, 146(1-2) (2006) 95-108.

[55] A.B. Dodd, C. Lautenberger, A.C. Fernandez-Pello, Numerical examination of two-dimensional smolder structure in polyurethane foam, Proceedings of the Combustion Institute, 32(2) (2009) 2497-2504.

[56] M. Cinar, L.M. Castanier, A.R. Kovscek, Combustion Kinetics of Heavy Oils in Porous Media, Energy & Fuels, 25(10) (2011) 4438-4451.

[57] A.S. Gundogar, M.V. Kok, Thermal characterization, combustion and kinetics of different origin crude oils, Fuel, 123 (2014) 59-65.

[58] M.A. Bazelatto Zanoni, H. Massard, M. Ferreira Martins, Formulating and optimizing a combustion pathways for oil shale and its semi-coke, Combustion and Flame, 159(10) (2012) 3224-3234.

[59] H. Chen, G. Rein, N. Liu, Numerical investigation of downward smoldering combustion in an organic soil column, International Journal of Heat and Mass Transfer, 84(0) (2015) 253-261.

[60] A. Rostami, J. Murthy, M. Hajaligol, Modeling of a smoldering cigarette, Journal of Analytical and Applied Pyrolysis, 66(1–2) (2003) 281-301.

[61] N. Wakao, S. Kaguei, T. Funazkri, Effect of fluid dispersion coefficients on particle-to-fluid heat transfer coefficients in packed beds: Correlation of nusselt numbers, Chemical Engineering Science, 34(3) (1979) 325-336.

[62] T. Hasan, J.I. Gerhard, R. Hadden, G. Rein, Self-sustaining smouldering combustion of coal tar for the remediation of contaminated sand: Two-dimensional experiments and computational simulations, Fuel, 150 (2015) 288-297.

[63] S.L. MacPhee, J.I. Gerhard, G. Rein, A novel method for simulating smoldering propagation and its application to STAR (Self-sustaining Treatment for Active Remediation), Environmental Modelling & Software, 31(0) (2012) 84-98.

[64] J.L. Torero, A.C. Fernandez-Pello, Forward smolder of polyurethane foam in a forced air flow, Combustion and Flame, 106(1–2) (1996) 89-109.

[65] T.J. Ohlemiller, J. Bellan, F. Rogers, A model of smoldering combustion applied to flexible polyurethane foams, Combustion and Flame, 36(C) (1979) 197-215.

[66] S.V. Leach, J.L. Ellzey, O.A. Ezekoye, A numerical study of reverse smoldering, Combustion Science and Technology, 130(1-6) (1997) 247-267.

[67] A.P. Aldushin, A. Bayliss, B.J. Matkowsky, Is there a transition to flaming in reverse smolder waves?, Combustion and Flame, 156(12) (2009) 2231-2251.

[68] A.B. Dodd, C. Lautenberger, C. Fernandez-Pello, Computational modeling of smolder combustion and spontaneous transition to flaming, Combustion and Flame, 159(1) (2012) 448-461.

[69] S.K. Elam, I. Tokura, K. Saito, R.A. Altenkirch, Thermal conductivity of crude oils, Experimental Thermal and Fluid Science, 2(1) (1989) 1-6.

[70] A. Bar-Ilan, G. Rein, A.C. Fernandez-Pello, J.L. Torero, D.L. Urban, Forced forward smoldering experiments in microgravity, Experimental Thermal and Fluid Science, 28 (2004) 743-751.

[71] M.F. Martins, S. Salvador, J.F. Thovert, G. Debenest, Co-current combustion of oil shale - Part 2: Structure of the combustion front, Fuel, 89 (2010) 133-143.

[72] A. Rostami, J. Murthy, M. Hajaligol, Modeling of smoldering process in a porous biomass fuel rod, Fuel, 83(11–12) (2004) 1527-1536.

Chapter 7

7   Conclusions

7.1   Summary

The goal of this work was to improve our fundamental understanding of smouldering combustion of organic liquid fuels in sand. This included the sensitivity of smouldering behavior to key parameters and the cause-effect behind those behavior shifts as well as the reasons that some cases are self-sustaining while others lead to smouldering extinction. The methodology to achieve this goal revolved around developing a numerical model able to simulate the smouldering process for bitumen in sand with the minimum necessary complexity with respect to the interplay between heat and mass transfer mechanisms and chemical reactions.

Heat transfer between flowing air and a fixed sand bed at low Reynold's number (i.e., $Re < 30$) was first studied, since it is a central topic to numerous natural and applied processes, including smouldering combustion. The most widely used correlation for the heat transfer coefficient (h_{sg}), $Nu=2+1.1(Re^{0.6}Pr^{1/3})$, predicted Nusselt numbers so high, it effectively presumed local thermal equilibrium for these systems; an assumption that had never been tested. The demonstration that this widely used correlation for local thermal non-equilibrium actually predicted local thermal equilibrium conditions was a novel contribution. This work combined twelve column heat transfer experiments with numerical modelling and quantified h_{sg} across a range of relevant sand grain sizes ($0.125<d_p<2.000$ mm) and air flow rates ($0.5<Re<31$). All of the sand properties were determined independently, with only h_{sg} determined via inverse modelling. Sand properties varying with temperature and the use of inverse modelling to estimate h_{sg} is novel and represented an important step towards the development of the numerical model. A new empirical correlation for h_{sg} was obtained, $Nu=0.001(Re^{1.97} Pr^{1/3})$, which was then validated against two additional heat transfer experiments. This represents the first time that a heat transfer correlation has been validated for air flux in fixed beds relevant to smouldering conditions. A newly developed criterion for assuming local thermal equilibrium was shown to be violated in all of these convection-dominated experiments and the extent of non-

equilibrium between sand and air was quantified. The centerline temperatures were demonstrated to be sensitive not only to h_{sg} but also to a global heat loss coefficient quantified from the experiments in a novel manner.

Then, a one-dimensional numerical model was developed in order to better understand smouldering combustion and accurately predict forced, upwards, self-sustained smouldering for the purposes of treating hydrocarbon-contaminated soil. The role of local thermal non-equilibrium was explored via the previously obtained heat transfer correlation, $Nu=0.001(Re^{1.97}Pr^{1/3})$. The model was calibrated to a smouldering experiment and then confidence in the model was gained by independent simulations of additional experiments. This represents one of the first times that a smouldering model was validated against experiments so comprehensively. The smouldering chemistry was represented by a two-step kinetic mechanism (one pyrolysis and one oxidation reaction), with the results indicating that this simple framework was sufficient to reproduce the main features of self-sustained smouldering. This also represents an important contribution since much focus in the literature is on highly complex kinetic schemes that are difficult to characterize and expensive to implement. Local thermal non-equilibrium was demonstrated, for the first time, to be significant in smouldering, with an average normalized temperature difference of 36% between the air and the sand/fuel. Moreover, incorporating the new thermal non-equilibrium correlation provided accurate predictions, particularly in the heat transfer-dominated regions preceding the trailing of the front. Results further demonstrated that the most widely used correlation in the literature, $Nu=2+1.1(Re^{0.6}Pr^{1/3})$, effectively ensured local thermal equilibrium and such models could not adequately reproduce the smouldering experiments.

Self-sustained smouldering combustion is governed by a positive energy balance between the energy added into and removed from the system. In intentional smouldering applications (e.g., hydrocarbon-contaminated soil remediation), extinction is undesired and occurs when energy generation cannot compensate for heat losses. Thus, the previously validated one-dimensional numerical model was employed to explore how the energy balance controls the self-sustainability of a forward smouldering reaction. A global energy balance was developed, for the first time, and accounted for the energy provided by the

heater, absorbed by pyrolysis, released by oxidation, stored in the sand, exchanged among phases, and lost to the surroundings. The global energy balance revealed that under self-sustaining conditions char oxidation provided the major energy source to sustain smouldering, with negligible contribution from pyrolysis; this contrasts with a substantial portion of the literature which focuses on the importance of pyrolysis. Moreover, heat losses were significant but could be compensated by heat transfer from the hot sand towards the reaction. Self-sustaining conditions included, for the first time, indefinite propagation at steady-state and also continuously accumulating energy in the system. Smouldering extinction conditions were characterized by a negative rate of net energy caused by more energy lost than released by oxidation. Nevertheless, even in such cases, heat transfer from the hot sand towards the reaction delayed extinction with important implications for the extent of remediation (i.e., fuel consumption). Most work in the literature focused on a local energy balance around the smouldering front. The developed global energy balance is entirely novel and represents a new way of understanding smouldering systems. It revealed, for the first time, how to account for internal energy recycling and system heat losses, which are critical to predicting the boundary between self-sustainability and extinction.

Finally, the one-dimensional numerical model was employed to explore the interplay between heat transfer and chemical reactions in space and time for the first time in smouldering. A local energy balance was developed and compared with the previously developed global energy balance. Both energy balances were compared to develop an improved understanding of self-sustaining smouldering and smouldering extinction. In self-sustaining smouldering, the local net energy rate was generally constant with time and dominated by the oxidation energy rate, with negligible losses due to the reaction thinness. However, the global energy balance revealed an increase in heat losses with time in the system that resulted in a decreased net energy rate with time. Both net energy rates remained positive until the end of smouldering. Under extinction conditions, the local energy balance resulted in a negative net energy rate only at late time due to pyrolysis and oxidation energy rates decreasing until negligible. In the global energy balance, both the oxidation energy rate and the energy losses rate decreased with time. However, the oxidation energy rate decreased faster, resulting in a negative net energy rate at early time.

Thus, the local energy balance identified the moment of reaction extinction, whereas the global energy balance predicted smouldering extinction in advance, i.e., at earlier time, even at high temperatures when oxidation was still active. This is a key contribution of this work, leading to several practical applications.

Moreover, a sensitivity analysis of smouldering to eight key parameters was conducted. The analysis included examination of which conditions lead to self-sustaining smouldering versus smouldering extinction and why that threshold exists. In addition, detailed analysis of all simulations allowed for an explanation of the controlling mechanisms in each set of runs and thus why some parameters are more sensitive than others. The sensitivity analysis revealed novel insights into smouldering robustness by increasing either the air flux or fuel saturation, which led to higher front velocity and peak temperature as a result of more mass flux of oxygen or more available fuel to react, respectively. However, at high saturations, front velocity decreases due to total consumption of oxygen, likely changing from fuel-limited to oxygen-limited conditions. Moreover, peak temperature was insensitive to an increase in the oxygen concentration due to complete fuel consumption even at low oxygen concentrations. Altogether, this work presents several new methods for looking at smouldering as well as new insights into liquid fuel smouldering that also benefits the field of solid fuel smouldering.

7.2   Implications

The results presented in this thesis have substantial implications for improving the fundamental understanding of smouldering combustion of organic liquid hydrocarbons. Since smouldering has been recently applied as an intentional technology, understanding the interplay between chemical reactions and heat transfer mechanisms is essential for predicting and optimizing the process.

Current smouldering models fail in recognize heat transfer between phases. This work developed a new empirical correlation for simulating heat transfer between flowing air and a fixed sand bed. It is expected that this correlation will be useful for understanding local thermal non-equilibrium in a variety of processes characterized by low Reynolds' numbers, including smouldering combustion.

Moreover, this work confirmed that a two-step kinetic mechanism coupled with the new heat transfer correlation was sufficient to simulate the smouldering chemistry. Therefore, complex kinetic mechanisms were not necessary here, implying the ability to employ relatively simple numerical efforts.

The global energy balance developed here was found to be a robust and valuable tool to explain the conditions under which smouldering transitions from self-sustaining towards extinction and to predict the extent of contaminant destruction, i.e., an important practical parameter for waste and contaminant destruction. Moreover, the global energy balance can become an important tool designing and optimizing large scale smouldering applications.

The model was also able to identify important practical smouldering scenarios, involving changes in the air flux (to control the propagation of the smouldering front) and fuel saturation (when fuel is intentionally mixed with sand). It was confirmed that an increase in the air flux and saturation creates more robust self-sustaining smouldering fronts as a result of either an increase in the mass flux of oxygen or increase in the amount of fuel available to burn. However, at high fuel saturations, limitations occur due to complete oxygen consumption, needing an increase in the air flux (or oxygen concentration) to avoid unburnt fuel left behind. This is an important implication for waste and contaminant destruction.

As with all research, some limitations and assumptions exist that should be acknowledged:
- One-dimensional model;
- Bitumen as the fuel;
- Sand as the inert porous matrix;
- Bitumen and sand assumed to have the effective properties of a single solid phase;
- Water and volatiles evaporation were not included;
- Constant intrinsic permeability, i.e., relative permeability was not included;
- Constant sand particle diameter;
- Constant porosity;
- Constant bitumen thermal properties;
- Radial heat losses assumed by a global heat loss coefficient;

- Sand particles considered as perfect spheres;
- Limited oxygen mass transfer, i.e., only in the bulk phase;
- Liquid mobility not included;

Each of these assumptions and limitations represents avenues for future research and the absence of these is not expected to invalidate any of the conclusions presented, as many of these are thought to be secondary effects. However, the conclusions presented only rigorously apply to relevant scenarios within the bounds of these assumptions.

7.3 Recommendations for Future Work

Although this study has shown promising results for fundamental understanding of self-sustaining smouldering and smouldering extinction, several recommendations for further research can be proposed:

- Apply the heat transfer correlation developed in Chapter 3 to different porous media. Since the correlation was developed for air flowing through hot sand at low Reynolds number and validated against smouldering of organic liquid fuels embedded in an inert matrix, it is suggested that the robustness of the new correlation should be tested against available literature on smouldering of porous organic solids (e.g., polyurethane foam).

- To explore true ignition and/or extinction limits, instead of the conditions that lead to it, considering whether more detailed chemistry (addition of more reactions) may provide any benefit. For this purpose, it is suggested to couple thermogravimetry with genetic algorithms to estimate the kinetic parameters for the set of chemical reactions.

- Oxygen mass transfer is one of the model limitations. Thus, it is recommended to introduce oxygen diffusion to the fuel surface along with bulk oxygen diffusion. This requires a careful analysis of the mass transfer coefficient, possibly needing a new correlation that correctly simulates mass transfer from the bulk oxygen to the fuel surface.

- Chapters 5 and 6 described the role of the porous medium in storing part of the energy released during smouldering. Thus, the numerical model along with the local and global energy balance can be used to propose new strategies for energy recovery.

- Implementation of liquid mobility into the numerical model. The decrease in viscosity caused by high smouldering temperatures typically causes movement upward or downward of liquids in the porous medium, decreasing or increasing fuel concentration at specific locations.

- Use of the numerical model to simulate smouldering of fuels that contain high moisture content. This will require the implementation of water evaporation as phase-change mechanisms. Thus, the role of the evaporation front in space and time can be explored in detail. Moreover, fuel volatilization and condensation also need to be explored in details.

- A detailed study of heat losses as a function of scale would be valuable. Large scale experiments and numerical simulations can provide insight. To conduct a detailed analysis on heat losses, the one-dimensional (1D) model should be extended into two dimensions (2D) as a next step.

Appendices

Appendix A: Supplementary Material for "Determination of the interfacial heat transfer coefficient between forced air and sand at Reynold's numbers relevant to smouldering combustion"

A.1. Sand Properties

The porosity (ϕ) of the medium was measured according to Equation (A.1). The mass of sand (m_s) packed inside the experimental cell ( ) was divided by the particle density of quartz (ρ_s=2650 kg m^{-3}) to the total volume (V_T) of the cell. The bulk density (ρ_{bk}) of sand, Equation (A.2), was measured dividing the mass of sand over the total volume.

$$\phi = 1 - \left(\frac{m_s}{\rho_s}\right)\left(\frac{1}{V_T}\right) \tag{A.1}$$

$$\rho_{bk} = \frac{m_s}{\rho_s} \tag{A.2}$$

The intrinsic permeability (k_p) was determined based on ASTM D6539-00 [1]. The experiments were conducted in a stainless-steel column (5 cm inner diameter, 10 cm height) represented in , packed with three sand particle diameters (Table 3.3, Chapter 3).

The flow rate of air was regulated by a mass flow controller (FMA5400/5500 Series, 0-1000 mL min^{-1}, Omega Ltd) connected to a laboratory compressed air supply. The pressure transducers (Pressure Gage/FPG, 2 psi, Honeywell) were calibrated with water and connected to a computer through a data logger (Multifunction Switch/Measure Unit 34980A, Agilent Technologies) to measure the difference in pressure between inlet and outlet conditions. The Darcy air flux varied from 0.0017 to 0.0085 m s^{-1} (0.2 to 1.0 L min^{-1}) and the pressure drop (ΔP) for each medium was recorded.
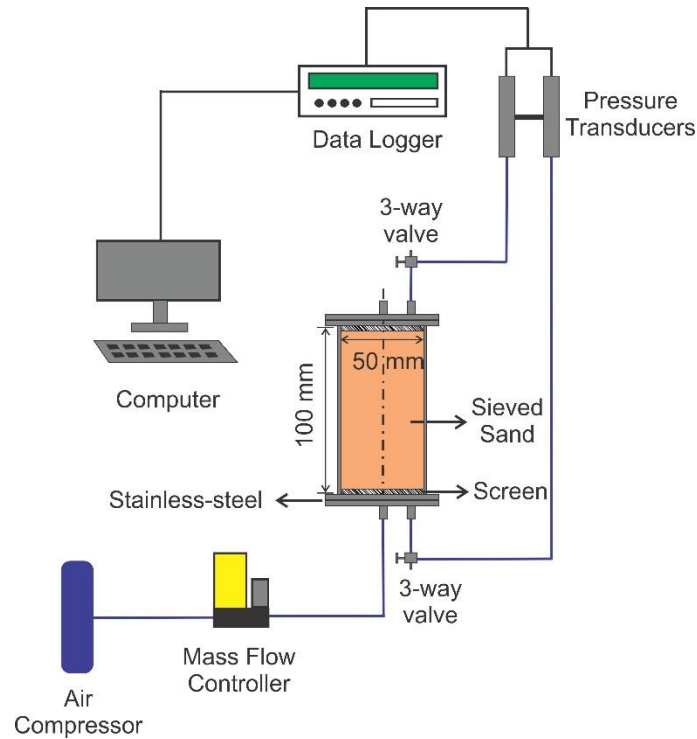
Figure A.1: Schematic of the permeameter.

The permeability of air was then determined by using Darcy's law [1]:

$$k_p = \frac{Q_g}{\Delta P}\left(\frac{L}{A}\right)\mu_g \tag{A.3}$$

where μ_g is the kinematic viscosity of air at ambient conditions, i.e., μ_g=1.846x10^{-5} Pa s.

The specific heat capacity (C_{ps}) of sand was measured based on ASTM-E1269 [2] by the use of Differential Scanning Calorimetry (DSC Q2000, TA Instruments) data. The sample heat flow (mW) was compared with the heat flow of a standard sapphire crystal of known specific heat capacity, Figure A.2. Both measurements were corrected by a baseline whereby the heat flow of an empty aluminum crucible was measured under the same experimental conditions. The mass of the standard sapphire crystal was 28.1 mg, and the mass of sand varied from 16.5 to 21.0 mg (only medium and coarse sand was considered). The DSC heating program used was: *i*) isothermal at 5 °C for 4 min; *ii*) ramp at 20 °C min^{-1} to 500 °C; and *iii*) isothermal at 500 °C for 4 min. Thus, the specific heat capacity of sand was determined by [2]:

$$C_{p_s} = C_{p_{(st)}} \frac{D_s m_{st}}{D_{st} m_s} \tag{A.4}$$

where C_{ps} is the sand specific heat capacity, $C_{p(st)}$ is the standard sapphire crystal specific heat capacity, D_s is the difference in the vertical displacement of heat flow measurements between the sand and the empty crucible, D_{st} is the difference in the vertical displacement of heat flow measurements between the sapphire standard and the empty crucible, m_s is the mass of sand, and m_{st} is the mass of sapphire standard.
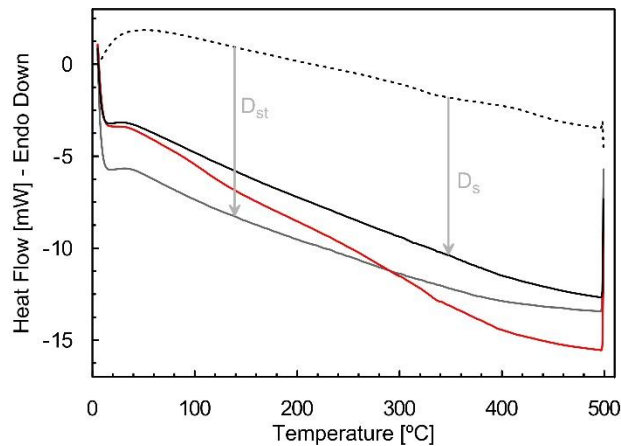
Figure A.2: DSC curves for the empty crucible baseline (dashed line), sapphire standard (gray solid line), and sand for two particle diameters (black solid line: 1.180 < d_p < 2.000 mm and red solid line: 0.425 < d_p < 0.600 mm).

The thermal conductivity of sand was measured by the Transient Plane Source (TPS) method, also known as Hot Disk Thermal Constants Analyser [3]. The TPS method can be used to characterize solid, powder, and liquid samples. The Hot Disk sensor is usually sandwiched between two solid samples or immersed in a powder or liquid medium. For porous media, the thermal conductivity is a measurement, to some extent, of the bulk thermal conductivity of the solid matrix (e.g., sand) combined with the thermal conductivity of the fluid phase (e.g., air). Note that as the sand was well packed to ensure

good contact surface between sand grains and sensor, it is expected that the Hot Disk sensor favours the measurement of the solid (quartz) rather than the air thermal conductivity.

The sensor has a double spiral shape, fabricated of 20 μm thick nickel foil covered on both sides with 100 μm thick Mica insulation, measuring thermal properties up to 1000 ℃. It acts as a heat source (current supplier) and a temperature (resistance) monitor, increasing the temperature up to few degrees (2-5 K), and recording the temperature increase as a function of time [3, 4]. The measurement time must be chosen short enough so that the assumption of infinite sample is fulfilled, i.e., the temperature increase must not be influenced by the sample outer boundaries (sample holder in the case of powder or liquid samples). It is recommended that the time between repeated experiments (relaxation time) must be equal to 36 times the measurement time to avoid effects from previous tests [3, 4].

The experimental parameters can be found in Table A.1. The tests were carried out in a stainless-steel sample holder (72 x 72 x 40 mm) without applying pressure on the sample. The sample holder was filled with sand up to 20 mm height, and the Mica sensor was positioned at the center of the sample holder and on the top of the sand layer, Figure A.3. The sensor (14.61 mm radius) was covered with another 20 mm layer of sand and a thermocouple was inserted to measure the sample temperature. The sensor was connected to TPS 1500 with an output power of 150 mW and measurement time of 320 s, and then connected to a computer. The box was placed in a temperature controlled furnace with maximum temperature of 1000 ℃. The furnace was filled with nitrogen to minimize oxidation and thermal degradation of the sensor. The temperature inside the furnace increased until reaches the temperature for the first measurement and kept constant (stabilization period) during the measurement time. Then, power was provided to the sensor, which increased the sample temperature up to 2-5 K. This increase in temperature is high enough to avoid experimental noises but low enough to neglect changes in thermal properties as a result of a temperature increase [5]. Once the measurement is completed, the furnace temperature ramps to the temperature of the next measurement. The maximum experimental temperature was kept below 300 ℃ due to nickel curie transition (300-400 ℃) and sensor degradation (above 500 ℃).
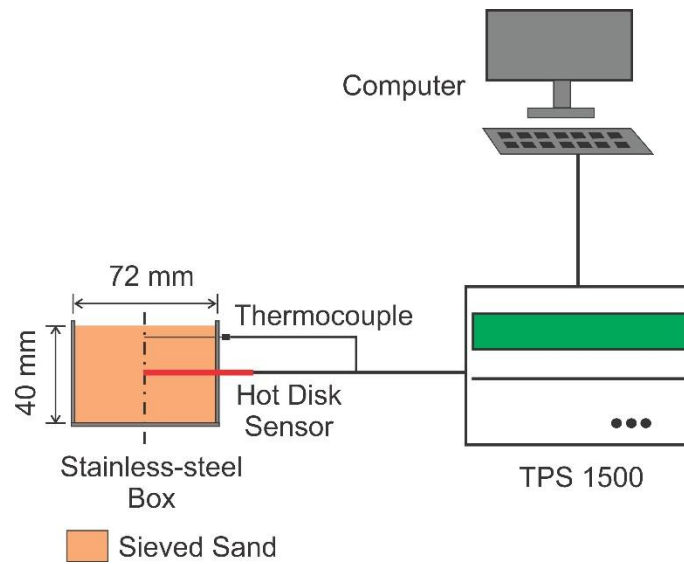
Figure A.3: Schematic of the TPS apparatus, containing TPS 1500, stainless-steel box (sample holder) filled with sieved sand, Hot Disk sensor (Mica), thermocouple, and computer.

Table A.1: TPS experimental parameters for each sand particle diameter.

d_p [mm]	Measurement Time [s]	Relaxation time [s]	Power [mW]	Sample Depth [mm]	Sensor Type [-]	Sensor Radius [mm]	T [°C]
0.125<d_p<0.250	320	11520	150	20	Mica	14.61	19
							86
							175
							269
0.425<d_p<0.600	320	11520	150	20	Mica	14.61	22
							85
							172
							264
1.180<d_p<2.000	320	11520	150	20	Mica	14.61	22
							85
							173
							267

A.2. LTE Criterion Development

Kaviany [6] and Oliveira and Kaviany [7] present a framework for developing case-specific LTE criteria. They indicate that LTE can be assumed when the characteristic time associated with heat transfer at the scale of a representative elementary volume (REV) is much greater than that at the scale of a single particle:

$$\tau_{REV} \gg \tau_p \tag{A.5}$$

To evaluate τ_p in this case, it is necessary to consider the energy in a sand particle at equilibrium with the air flowing past it:

$$m_s C_{p_s} \frac{\partial T_s}{\partial t} = A_{s,sp} h_{sg} (T_\infty - T_s) \tag{A.6}$$

Equation (A.6) is valid if the Biot ($Bi=h_{sg}d_p/k_s$) number is much less than one [8]. Using $m_s=\rho_s V_{sp}$, ∂T_s is approximated by (T_∞-T_s), and ∂t is the particle-scale characteristic time (τ_p) gives:

$$\tau_p = \frac{\rho_s C_{p_s}}{h_{sg}} \left(\frac{V_{sp}}{A_{s,sp}} \right) \tag{A.7}$$

To evaluate Equation (A.5), d_p is taken as the REV characteristic length scale and u_g as the Darcy air velocity. Thus, the REV characteristic time (τ_{REV}) for the sand particles to equilibrate with the gas is:

$$\tau_{REV} = \frac{d_p}{u_g} \tag{A.8}$$

Assuming the particle to be spherical such that ($A_{s,sp}/V_{sp}$)=6/d_p, Equation (A.5) can now be rewritten for our specific case:

$$\frac{6h_{sg}}{u_g \rho_s C_{p_s}} \gg 1 \tag{A.9}$$

Equation (A.9) can be evaluated by (*i*) C_{ps} provided by the measurement (see Section 3.2.3, Chapter 3) taken at the average temperature (Equation (3.20), Chapter 3), and (*ii*) h_{sg} provided by the optimized value from the inverse modelling results.

A.3. Dominant Heat Transfer Processes

Conduction versus convection dominance was analyzed through a time scale analysis. An energy balance was considered based on purely conductive and purely convective processes, respectively:

$$\rho_s C_{p_s} \frac{\partial T}{\partial t} = k_s \frac{\partial^2 T}{\partial x^2} \tag{A.10}$$

$$\rho_s C_{p_s} \frac{\partial T}{\partial t} = \rho_g C_{p_g} u_g \frac{\partial T}{\partial x} \tag{A.11}$$

Assuming $\partial T=(T-T_0)$, $\partial t=\tau_{cond}$, and $\partial x=\delta_w$ and rearranging the terms, Equation (A.10) becomes:

$$\tau_{cond} = \frac{\delta_w^2}{\alpha_s} \tag{A.12}$$

where δ_w is the thickness of the heat wave, τ_{cond} is the characteristic time associated with conduction, and $\alpha_s=k_s/\rho_s C_{ps}$. Following the same procedure for Equation (A.11) and adopting a characteristic time associated with convective processes $\partial t=\tau_{conv}$:

$$\tau_{conv} = \frac{\rho_s C_{p_s}\delta_w}{\rho_g C_{p_g} u_g} \tag{A.13}$$

Thus, conduction and convection dominance can be analyzed by the ratio:

$$\frac{\tau_{cond}}{\tau_{conv}} = \frac{\rho_g C_{p_g} u_g \delta_w}{k_s} \tag{A.14}$$

If $\tau_{cond}/\tau_{conv} << 1$, conduction is the dominant heat transfer mechanism, if $\tau_{cond}/\tau_{conv} >> 1$ otherwise convection dominates, and if $\tau_{cond}/\tau_{conv} \approx 1$ then the two processes are equally important.

A.4. Mixed Convection

In low Darcy air fluxes, mixed convection (buoyancy in forced convection) might happen and thus its influence needs to be investigated. A Darcy-modified Rayleigh number (Ra) [9] was then calculated through the inverse modelling results in Section 3.4.2, Chapter 3:

$$Ra = \frac{(k_p D)g\gamma(T_{avg} - T_w)}{v_g \alpha_g} \tag{A.15}$$

Here, $\gamma=((T_{avg}+T_w)/2)^{-1}$ for ideal gases, $v_g=\mu_g/\rho_g$, and $\alpha_g=k_g/\rho_g C_{pg}$. v_g and α_g were taken at T_{avg}, i.e., the centerline experimental average temperature calculated by Equation (3.20), Chapter 3. T_w is the wall temperature and was estimated based on the analysis of heat losses (see sections 3.2.2 and 3.4.1, Chapter 3):

$$\frac{E_s(U=0) - E_s(U_{avg}=1.7)}{t_f - t_0} = U_{avg}A_{s,cl}(T_{avg} - T_w) \qquad (A.16)$$

E_s was calculated by Equation (3.18) in Chapter 3 and used here to investigate the numerical energy loss based on the energy difference when $U=0$ W m^{-2} K^{-1} (adiabatic conditions) and $U_{avg}=1.7$ W m^{-2} K^{-1} (see section 3.4.1).

References

[1] A. D6539, Standard test method for measurement of pneumatic permeability of partially saturated porous materials by flowing air, in, ASTM International, West Conshohocken, PA, 2000 (2006).

[2] ASTM-E1269-11, Standard test method for determining specific heat capacity by differential scanning calorimetry, in, ASTM International, West Conshohocken, PA, 2011.

[3] S.E. Gustafsson, Transient plane source techniques for thermal conductivity and thermal diffusivity measurements of solid materials, Review of Scientific Instruments, 62(3) (1991) 797-804.

[4] S. Lagüela, P. Bison, F. Peron, P. Romagnoni, Thermal conductivity measurements on wood materials with transient plane source technique, Thermochimica Acta, 600 (2015) 45-51.

[5] Y. Yang, T.G. Voskuilen, T.L. Pourpoint, D.R. Guildenbecher, J.P. Gore, Determination of the thermal transport properties of ammonia borane and its thermolysis product (polyiminoborane) using the transient plane source technique, International Journal of Hydrogen Energy, 37(6) (2012) 5128-5136.

[6] M. Kaviany, Principles of Heat Transfer in Porous Media, Springer, 1995.

[7] A.A.M. Oliveira, M. Kaviany, Nonequilibrium in the transport of heat and reactants in combustion in porous media, Progress in Energy and Combustion Science, 27(5) (2001) 523-545.

[8] F.P. Incropera, Fundamentals of heat and mass transfer, John Wiley, 2007.

[9] A. Bejan, K.R. Khair, Heat and mass transfer by natural convection in a porous medium, International Journal of Heat and Mass Transfer, 28(5) (1985) 909-918.

Appendix B: Supplementary Material for "The Role of Local Thermal Non-Equilibrium in Modelling Smouldering Combustion of Organic Liquids"

B.1. TG/DTG and DSC Experiments

Figure B.1 shows TG/DTG and DSC experiments for bitumen conducted at 10, 20, 30, and 40 K min^{-1} under N_2 and air atmospheres. Figure B.1a,b will be explained in details as an example. Bitumen does not show a significant mass loss (Figure B.1a) from ambient to 563 K (290 ℃) under either air or N_2, which indicates that both water and light hydrocarbons are not present in large quantities. DTG (Figure B.1a) along with DSC data (Figure B.1b) also do not capture any significant heat absorbed at this region (apart from the one absorbed due to the heat capacity of the material) for both atmospheres.

Between 563 and 843 K (290-570 ℃), pyrolysis reactions take place and a rapid decrease in mass loss is observed (Figure B.1a). DTG shows a large and unique peak in this region either under N_2 or air, and DSC under N_2 describes a representative endothermic behaviour. At this stage, bitumen decomposition occurs, producing volatiles, maltene (liquid), alsphaltene (solid), and char [1]. Note that the mass loss under N_2 and air in Figure B.1a shows the same behaviour and magnitude until approximately 803 K (530 ℃), which indicates that pyrolysis reactions are independent of atmosphere.

Between 803 and 843 K (530-570 ℃), TG under N_2 keeps losing mass, whereas the one under air reaches a plateau. This feature is characterized by a competition between pyrolysis and fuel oxidation reactions that occur in TG under the presence of an oxidizer (air). DSC data (Figure B.1b) under air reveal a slightly exothermic behaviour at this region, which suggest that the net heat released by fuel oxidation is slightly higher than the total net heat absorbed by pyrolysis reactions. Under N_2, pyrolysis reactions tend to produce more volatiles, resulting in more mass consumption, whereas under air, the competition with fuel oxidation yields a high amount of solid/liquid residue (e.g., char, maltene, asphatene, etc), creating the plateau in the mass loss.

After 843 K (570 ℃), TG under N_2 reaches a minimal with no more relevant fuel consumption, leaving a hydrocarbon residue. DSC data show a negative increase in the heat flow caused by the heat capacity of the residue. Under air, TG data show one more decomposition step caused by the oxidation of this residue. DTG indicates a peak between 843 and 1163 K (570-890 ℃) and DSC data show a strong exothermic peak at this region. After 1163 K (890 ℃), the total consumption of the fuel is achieved. Note that the temperature ranges at which these reactions are taking place may change depending on the heating rates adopted (see Figure B.1c-h).
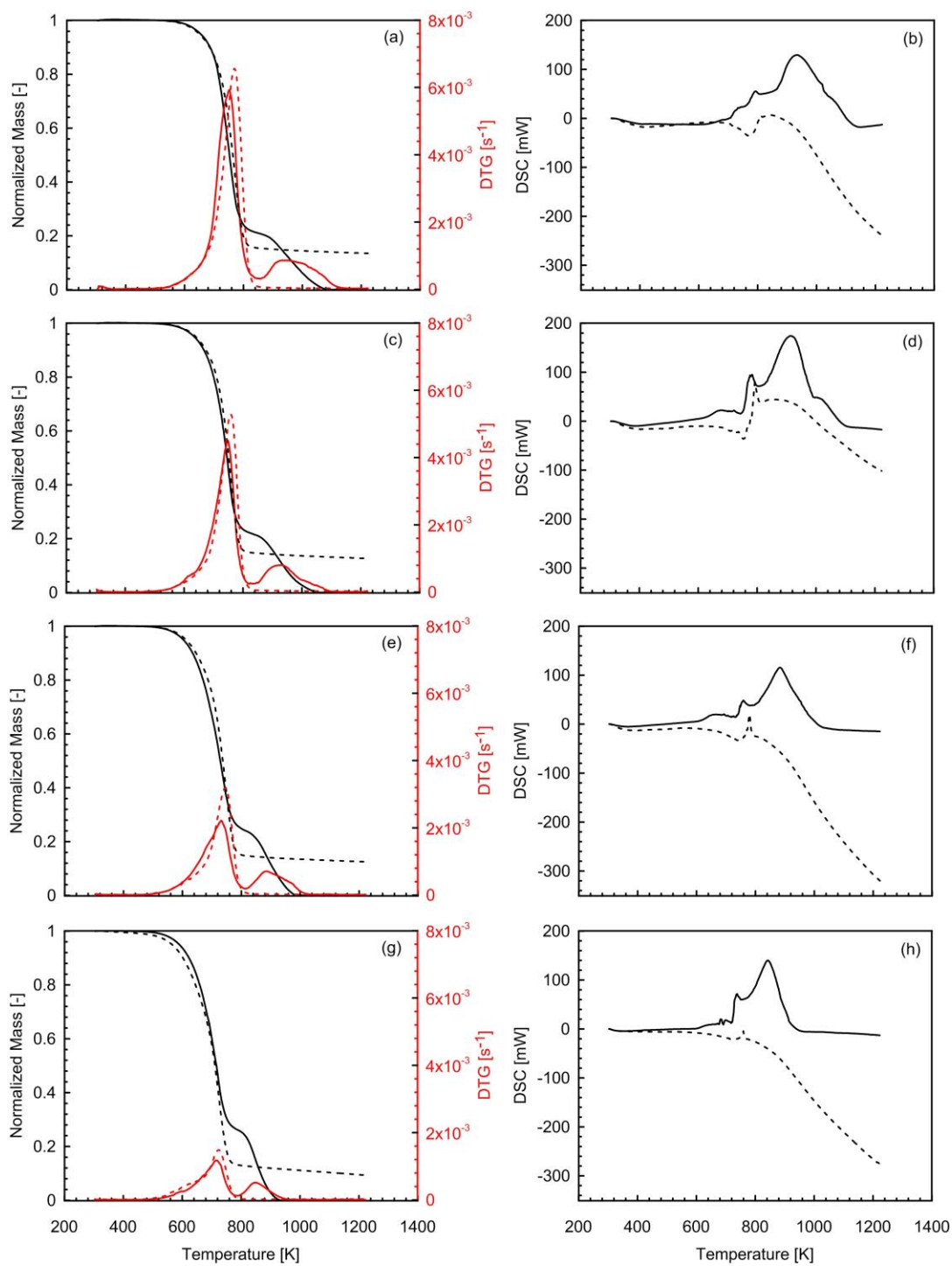
Figure B.1: (a, c, e, g) TG (black), DTG (red), and (b, d, f, h) DSC under air (solid line) and N_2 (dashed line) at (a, b) 40 K min^{-1}, (c, d) 30 K min^{-1}, (e, f) 20 K min^{-1}, (g, h) 10 K min^{-1}.

B.2. Kinetic Mechanism

The 2-step kinetic mechanism developed in Chapter 4 (Equation (4.3)) for bitumen smouldering was based on TG, DTG, and DSC results presented in Figure B.1. The Arrhenius parameters (A_i and E_i) for each reaction (i) presented in Table 4.2 were obtained by the use of Kissinger method along with TG experiments:

$$-\frac{E_i}{R_g} = \frac{d\left(ln\frac{\beta}{T_{p,i}^2}\right)}{d\left(\frac{1000}{T_{p,i}}\right)} \tag{B.1}$$

$$A_i = \frac{\beta E_i}{R_g T_{p,i}^2} exp\left(\frac{E_i}{RT_{p,i}}\right) \tag{B.2}$$

Further information on the derivation of Equations (B.1) and (B.2) can be found in [2, 3]. Figure B.2 describe a plot of $ln(\beta/T_{p,i}^2)$ against ($1000/T_{p,i}$) under N_2 and air at different heating rates (β) (Table 4.2, Chapter 4); T_{pi} corresponds to the temperature at which the reaction rate for each reaction (i) in DTG curve (Figure B.1) is maximum. The slope of -(E_i/R_g) is used to calculate E_i, Equation (B.1), through a linear fit of four experimental points. Once the value of E_i is known, A_i can be calculated by substituting E_i into Equation (B.2).
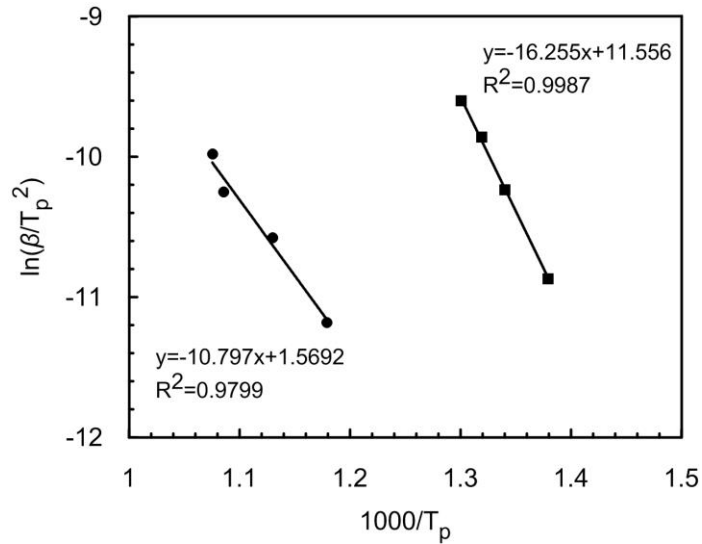
Figure B.2: Correlation between heating rates and peak temperatures based on Kissinger method: (●) air; (■) N₂; (solid lines) linear fit.

B.3. Model Calibration

Model parameters such as A_c, v_{O2}, v_c, and U were adjusted to match peak temperature and front velocity (A_c and v_c), experimental O_2 consumption (v_{O2}), and the shape of the temperature profile behind the smouldering front (U). Note that A_c calculated from Kissinger method (Table 4.2) resulted in a non-self-sustaining smouldering front; hence, its value was adjusted. Equation 4.10 was used to calculate the errors associated with changes in the peak temperature, front velocity, temperature versus time, and temperature versus distance. Figure B.3 shows five groups of adjusted parameters systematically chosen for testing in the model. Groups 1 (non-self-sustaining) and 5 resulted in the highest average NRMSD (30-80%), Groups 2 and 4 showed average NRMSD equal 15% and Group 3 described the lowest average NRMSD (13%). Thus, Group 3 (U=13 W m^{-2} K^{-1}, log(A_c)=4.9, v_c=0.55, v_{O2}=1.7 kg O_2 kg fuel^{-1}) was chosen as the final set of adjusted parameters to implement into the model.
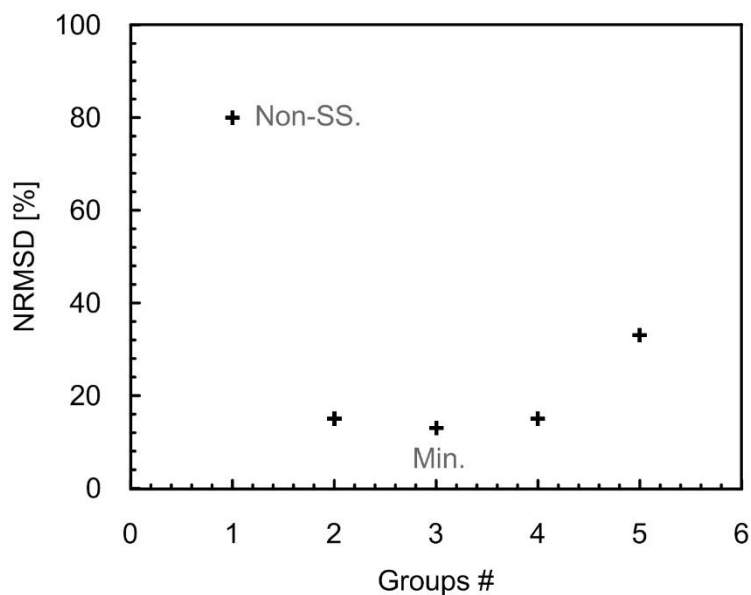
Figure B.3: Average NRMSD for five groups of adjusted parameters: (1) U**=16 W m^{-2} K^{-1}, log(A_c)=3, v_c=0.6, v_{O2}=0.5 kg O$_2$ kg fuel^{-1}; (2)** U**=5 W m^{-2} K^{-1}, log(A_c)=6, v_c=0.4, v_{O2}=3 kg O$_2$ kg fuel^{-1}; (3)** U**=13 W m^{-2} K^{-1}, log(A_c)=4.9, v_c=0.55, v_{O2}=1.7 kg O$_2$ kg fuel^{-1}; (4)** U**=13 W m^{-2} K^{-1}, log(A_c)=6, v_c=0.6, v_{O2}=1 kg O$_2$ kg fuel^{-1}; and (5)** U**=9 W m^{-2} K^{-1}, log(A_c)=4, v_c=0.5, v_{O2}=1 kg O$_2$ kg fuel^{-1};**

References

[1] M. Cinar, L.M. Castanier, A.R. Kovscek, Combustion Kinetics of Heavy Oils in Porous Media, Energy & Fuels, 25(10) (2011) 4438-4451.

[2] H.E. Kissinger, Reaction kinetics in differential thermal analysis, Analytical Chemistry, 29(11) (1957) 1702-1706.

[3] K.-Y. Li, X. Huang, C. Fleischmann, G. Rein, J. Ji, Pyrolysis of Medium-Density Fiberboard: Optimized Search for Kinetics Scheme and Parameters via a Genetic Algorithm Driven by Kissinger's Method, Energy & Fuels, 28(9) (2014) 6130-6139.

Appendix C: Mesh Analysis and Conservation of Energy and Mass

C.1. Mesh Analysis

In COMSOL Multiphysics, the time step is controlled by Backward Differentiation Formula (BDF), which allows the user to select the initial (0.001 s) and maximum (10 s) time steps, whereas the mesh size is defined by the user. Thus, a mesh convergence was conducted and is presented in Figure C.1 and Table C.1.
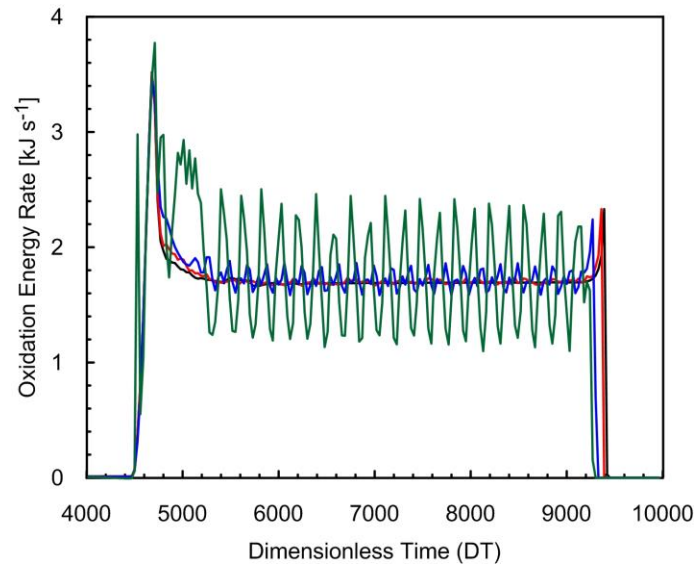

Figure C.1: Oxidation energy rate changing with mesh size: (green) 0.500 mm, (blue) 0.280 mm, (red) 0.125 mm, and (black) 0.100 mm.

Table C.1: Average Error of the Energy Released by Oxidation for Different Meshes

Mesh [mm]	Average Error [%]
0.500	12
0.280	5
0.125	2
0.100	< 2

The criterion used was based on the average error of the oxidation energy rate (Equation (5.11), Chapter 5) for mesh sizes varying from 0.50 to 0.10 mm (Figure C.1). A converged mesh was assumed to have average error less than 2 % (Table C.1). Therefore, mesh size=0.10 mm was used for all the simulation presented in this thesis.

C.2. Mass and Energy Balance

A mass balance was conducted based on the numerical mass loss [kg]:

$$m_b = \int_{0.1}^{0.45} (\rho_b + \rho_c) A_{cs} dx \qquad (C.1)$$

and mass loss rate [kgs^{-1}]:

$$\frac{dm_b}{dt} = \int_{0.1}^{0.45} (R_b \rho_b + R_c \rho_c) A_{cs} dx \qquad (C.2)$$

integrated over the length of the contaminated region (x=0.35 m) for the base case (0.058 m s^{-1}, 15% saturation, 20.4 % O$_2$), where ρ_b and ρ_c are the concentrations [kg m^{-3}] of bitumen and char, respectively, and A_{cs} is the cross-sectional area of a cylindrical column. The results of Equation (C.1) were compared with the total mass of fuel available ($m_{av}=\rho_{b0}V$=57.165x($\pi(0.08^2)$x0.35)=0.402 kg), where $\rho_{b0}=\rho_b S_b \phi$ and V is the cylindrical volume of the contaminated region. Equation (C.1) resulted in m_b=0.402 kg, which matches with m_{av}; thus, mass is conserved.

Figure C.2a shows the mass loss and mass loss rate calculated by Equations (C.1) and (C.2). Before air flux is turned on (DT<0), the temperature is still low and pyrolysis is weakly activated with a slight decrease in mass loss. Mass loss rate shows a relatively weak peak at this region. When the air flux is initiated (DT=0), a rapid decrease in the mass loss is observed as a result of much higher temperatures, activating pyrolysis and oxidation reactions, which results in total fuel consumption; mass loss rate is mostly constant (DT>0) at this region (with minor instabilities at the boundaries).

The conservation of energy was analyzed by Figure C.2b. The numerical pyrolysis (E_{pyr}) and oxidation (E_{oxid}) energies calculated by the integration of Equations (5.11) and (5.12) (Chapter 5) resulted in 0.652 MJ and -8.575 MJ, respectively (Figure C.2b). The energies available for pyrolysis $E_{av,p}$=(1.62)x(0.402)=0.651 MJ and oxidation $E_{av,o}$=-38.73x0.402x0.55=-8.570 MJ, resulted in similar values. Then, the global energy balance was calculated by summing all the energy components in Figure C.2b, resulting in a numerical error less than 2%; therefore, it can be considered that energy is conserved.

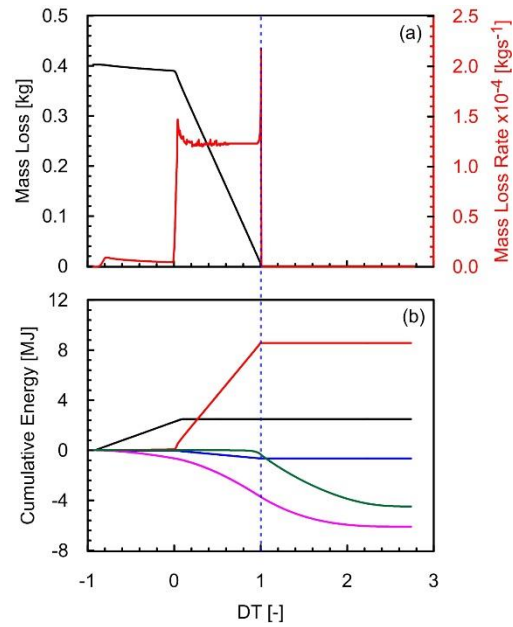**Figure C.2: (a) Numerical mass loss (black) and mass loss rate (red) and (b) cumulative energy rate versus Dimensionless Time (DT) for base case simulation. Colours in (b) show the cumulative energy for each component: (black) heater, (red) oxidation, (blue) pyrolysis, (magenta) loss, and (green) out. Dashed blue line shows the end of the column (DT=1) when energy starts leaving the system.**

Appendix D: Sensitivity Analysis to extra smouldering Experiments under Weak and Extinction conditions

D.1. Experiments

Seven smouldering experiments were conducted in a stainless-steel column (Figure D.1) under robust and weak (near extinction) conditions to test the model limitations (Table D.1). Experimental setup and methodology are similar to previous work (Chapters 4 and 5). The column contained 0.10 m of clean sand (d_p=0.88 mm) below the heater and a 0.35 m layer of a mixture of sand and bitumen (density (ρ_b)=1030 kg m^{-3}, PG 58-28, McAsphalt Industry Limited) above it. Ten thermocouples spaced 0.035 m apart were assumed to measure the solid (sand/bitumen) temperature along the column center-line every 2 seconds. The apparatus was insulated to minimize heat losses. Each experiment was initiated by powering the resistive heater until the temperature of the first thermocouple (x=0.12 m) reached 400 ℃. Then, air injection at a fixed rate was supplied, which initiated smoldering. The heater was then switched off while the air was maintained.
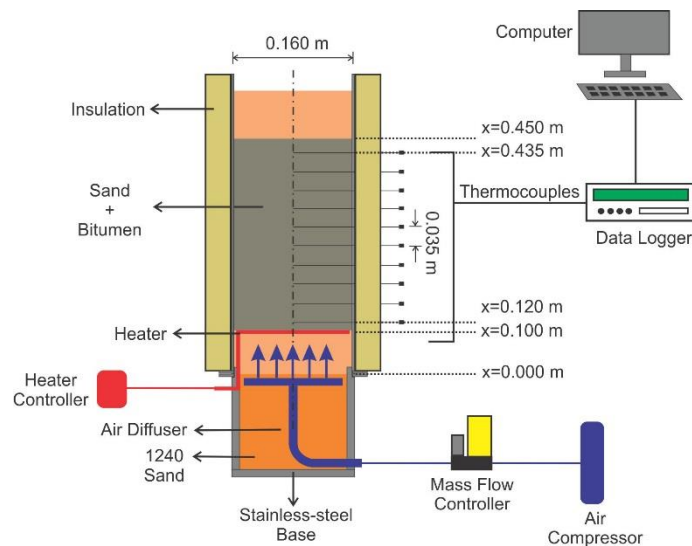

Figure D.1: Schematic of the experimental apparatus.

These experiments were used to identify the model limitations. The influence of U and ΔH_c was analyzed in the robust experiments (Exp. #1-3). For the weak cases (Exp. #4-7), a sensitivity of only ΔH_c was conducted. The final values of U and ΔH_c were calibrated to experimental results based on a fitting methodology developed in Chapter 4. The model calibration involved minimizing the error, Equation (D.1), between the model prediction (*num*) and the experiments (*exp*) presented in Table D.1, giving equal weight to four aspects of the fit: average peak temperature (T_p), smouldering front velocity (v_f), temperature versus time plots ($T(t)$), and temperature versus distance profiles ($T(x)$). The best fitted values of U and ΔH_c for each experiment are presented in Table D.1.

$$ERROR[\%] = \frac{1}{4}\left|\frac{T_{p,exp} - T_{p,num}}{T_{p,num}}\right| + \frac{1}{4}\left|\frac{v_{f,exp} - v_{f,num}}{v_{f,num}}\right| + \frac{1}{4}NRMSD_{T(t)}$$
$$+ \frac{1}{4}NRMSD_{T(x)}$$
(D.1)

Table D.1: Smouldering experiments.

Exp. # [-]	u_g [m s^{-1}]	Regime[c] [-]	S_b [%]	t_g [s]	t_h [s]	Repeats [#]	SS [-]	U[d] [W m^{-2} K^{-1}]	ΔH_c[d] [MJ kg^{-1}]
1	0.025	Robust	15	4926	5357	1	Yes	5	50.35
2[a]	0.058	Robust	15	4532±378[b]	4865±300[b]	3	Yes	13	42.60
3	0.083	Robust	15	5077	5329	1	Yes	18	34.86
4	0.025	Weak	10	4677	5110	1	Yes	13	77.46
5	0.058	Weak	10	5486	6004	1	Yes	13	61.97
6	0.025	Weak	5	5100	5700	1	No	13	89.10
7	0.058	Weak	5	5890	6370	1	Yes	13	92.95

[a] Base case; [b] 95% confidence interval; [c] Robust: far from extinction, Weak: near extinction; [d] Calibrated according to Equation (D.1).

D.2. Robust Regime

The one-dimensional numerical model assumed a constant heat of oxidation (ΔH_c) and constant heat loss coefficient (U). Both terms have strong effect in the global energy balance, altering energy added into and removed from the system. Fitting experimental data is challenging and may be affected by experimental conditions such as air flux, fuel saturation, heat losses on the column walls, and combustion efficiency. Such conditions may require numerical values of the heat loss coefficient and heat of oxidation that vary in both space and time. Thus, the fitting methodology presented in Section D.1 was employed to identify the best (still constant) values of U and ΔH_c that fit the experiments presented in Table D.1.

Figure D.2a-c show the case presented in Chapter 4 where four parameters were fitted using experimental data at 0.058 m s^{-1} (Exp. #2, Table D.1). Thus, these parameters were used to predict (without any fitting) experiments at 0.025 m s^{-1} (Exp. #1) and 0.083 m s^{-1} (Exp. #3). The predictions described very good agreement with experiments in terms of T_p and v_f (Figure D.2j) and overall shape of the temperature curves at 0.058 m s^{-1} (Figure D.2b) and 0.083 m s^{-1} (Figure D.2c). At 0.025 m s^{-1} (Figure D.2a), although a good agreement in T_p was reached (Figure D.2j), v_f and cooling region do not agree with the experiment. In fact, the predicted temperatures cool down much faster than the experiment. This suggests that, at low air fluxes $U=13$ W m^{-2} K^{-1} overestimates heat losses, affecting the overall energy balance. Equation (D.1) described an average ERROR=26% at 0.025 m s^{-1}, 13% at 0.058 m s^{-1}, and 9% at 0.083 m s^{-1}.

In order to verify the influence of radial heat losses on low and high air fluxes, different U values were tested. The minimization of Equation (D.1) resulted in the best values of U presented in Figure D.2d-f. Figure D.2d (0.025 m s^{-1}) indicates that a lower U (5 W m^{-2} K^{-1}) considerably improves the shape of the cooling region, although only slightly improving v_f (Figure D.2k) and average ERROR (21%). Figure D.2f shows low sensitivity to U at high air fluxes (0.083 m s^{-1}, $U=18$ W m^{-2} K^{-1}), slightly improving the average ERROR (8%), with negligible changes in v_f (Figure D.2k). Thus, although minor improvements were noted, smouldering front velocity is quite insensitive to changes in U in the robust regime.

Finally, a sensitivity analysis on the heat of oxidation (ΔH_c) was conducted; U was kept constant at 13 W m^{-2} K^{-1}. Differences in ΔH_c might be related to the combustion efficiency with changes in air flux. Figure D.2g-i and Figure D.2l show the excellent agreement with experiments. Moreover, T_p and v_f demonstrated to be highly sensitive to changes in ΔH_c, as expected. The average ERROR decreased to 10% at 0.025 m s^{-1}, 11% at 0.058 m s^{-1}, and 6% at 0.083 m s^{-1}. Note that ΔH_c decreases when air flux increases, which indicates that the combustion reaction is more efficient at high air fluxes (due to high O_2 mass flux), needing less energy from the fuel to propagate. Moreover, Figure D.2l indicates that experimental and predicted T_p follows the same trend (i.e., quite insensitive to air flux), contrary to the trends showed in Figure D.2j-k (i.e., increasing with increased air flux).
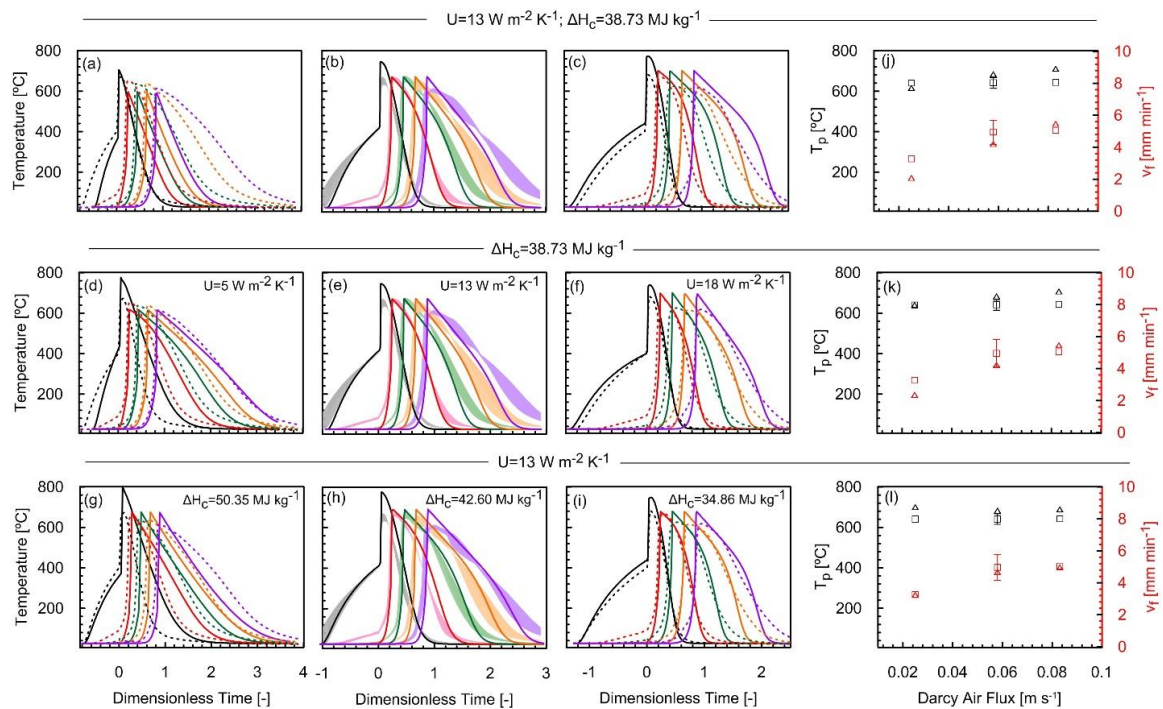

Figure D.2: (a-i) (Dashed line) Experimental and (solid line) numerical sand/bitumen temperature versus Dimensionless Time (DT). Colours show thermocouple positions (x) from 0.12 to 0.40 m with 0.07 m intervals. (b, e, f) The shadings encompass three experimental repeats. (a, d, g) Exp #1; (b, e, h) Exp. #2, and (c, f, i) Exp. #3 (Table 4). (j-l) Peak temperature and smouldering front velocity versus Darcy air flux: (■) experimental and (▲) numerical data. The error bars denote the variation observed in three repeats of Exp. #2, Table D.1.

D.3. Weak Regime

Since varying U resulted in only slightly improvements in T_p and overall shape of the temperature curves (negligible improvements in v_f) for the robust regime (Section D.2), the weak cases describe a sensitivity only for ΔH_c. Figure D.3a-e present Exp. #4-7 (Table D.1) compared with predicted temperatures using the calculated ΔH_c=38.73 MJ kg^{-1} and a constant U=13 W m^{-2} K^{-1} calibrated in Chapter 4.

Experiments suggest that self-sustaining smouldering occurs even under weak conditions such as the combination of low air flux (0.025 m s^{-1}) and low saturation (10%), Figure D.3a, and very low fuel saturation (5%) at 0.058 m s^{-1} (Figure D.3d). Moreover, note that Figure D.3c show non-self-sustaining conditions at 0.025 m s^{-1}, 5% saturation, but when air flux is increased to 0.058 m s^{-1}, self-sustaining smouldering is achieved due to the increase in the O_2 mass flux.

Predicted temperatures show a smouldering front that is not self-sustaining in Figure D.3a and Figure D.3d, contrary to experiments. This suggests that ΔH_c=38.73 MJ kg^{-1} might not provide the energy necessary to overcome heat losses, resulting in extinction; Figure D.3b-c describe similar behaviour. In Figure D.3b, although the front is self-sustaining in both numerical and experimental cases, heat losses are quite high, quickly cooling the trailing edge of the temperature curves. Equation D.1 indicates that the average ERROR was 99% (Figure D.3a), 33% (Figure D.3b), 63% (Figure D.3c), and 48% (Figure D.3d).

Figure D.3e-h show very good agreement between predicted and experimental temperatures by varying ΔH_c. The average ERROR decreased to 15% (Figure D.3e), 15% (Figure D.3f), 22% (Figure D.3g), and 8% (Figure D.3h). High values of ΔH_c (sometimes two times higher than the base case value) were required to improve the fitting of the experimental data. Although this seems inappropriate, it is due to a compensation effect on heat losses. Since U was kept constant, ΔH_c had to increase. Similar behaviour would be achieved if a constant ΔH_c was applied with varying U. However, v_f would never match since its quite insensitive to U. Figure D.4 show good match for v_f and reasonable match for T_p. Note that experimental and numerical v_f reaches a maximum and then decreases when saturation increases; similar trend is described in Figure 6.6, Chapter 6.
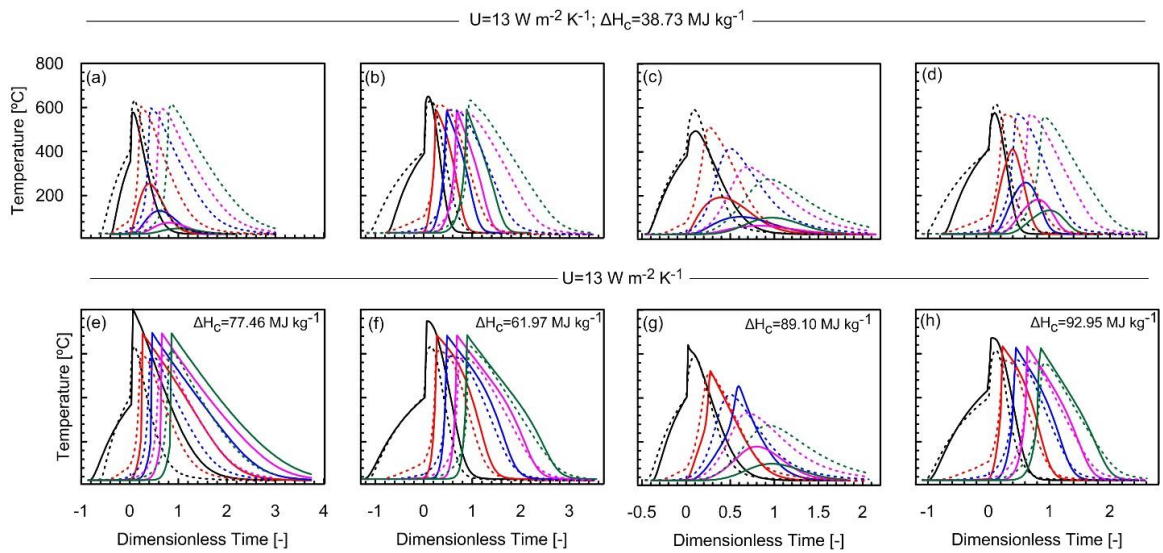
Figure D.3: (a-h) (Dashed line) Experimental and (solid line) numerical sand/bitumen temperature versus Dimensionless Time (DT). Colours show thermocouple positions (x) from 0.12 to 0.40 m with 0.07 m intervals. (a, e) Exp #4; (b, f) Exp. #5, (c, g) Exp. #6, and (d, h) Exp. #7 (Table D.1).
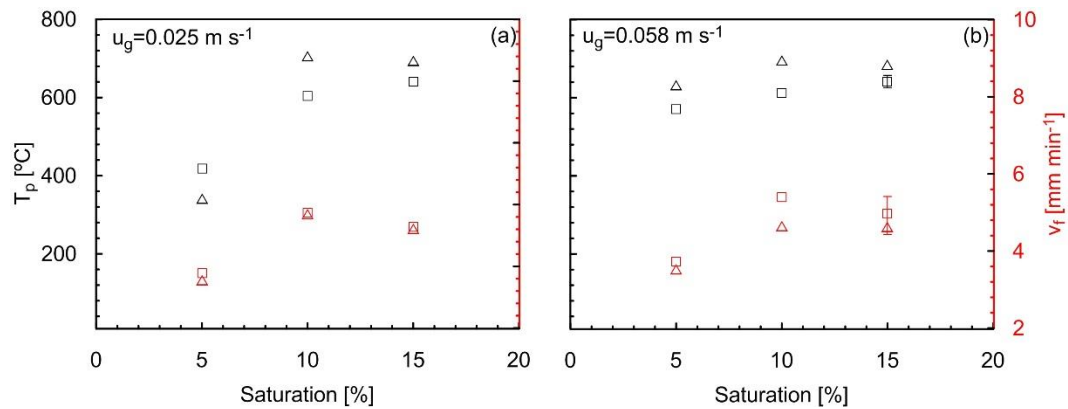

Figure D.4: Peak temperature and smouldering front velocity versus saturation: (■) experimental and (▲) numerical data. (b) The error bars denote the variation observed in three repeats of Exp. #2 (Table D.1). ΔH_c values are presented in Figure D.3

Curriculum Vitae

Name:	Marco Aurelio Bazelatto Zanoni
Post-secondary Education and Degrees:	Federal University of Espirito Santo (UFES) Vitoria, Espirito Santo, Brazil 2005-2010 B.A.
	Federal University of Espirito Santo (UFES) Vitoria, Espirito Santo, Brazil 2010-2012 M.Sc.
	The University of Western Ontario London, Ontario, Canada 2013-2018 Ph.D.
Honours and Awards:	R. M. Quigley Award (2013) Petrobras Award of Technology (2013)
Related Work Experience	Teaching Assistant The University of Western Ontario 2013-2018
	Research Assistant The University of Western Ontario 2013-2018

Publications:

M.A.B. Zanoni, H. Massard, M.F. Martins, S. Salvador, Application of inverse problem and thermogravimetry to determine the kinetics of oil shale pyrolysis, High Temperatures - High Pressures, 41(3) (2012) 197-213.

M.A. Bazelatto Zanoni, H. Massard, M. Ferreira Martins, Formulating and optimizing a combustion pathways for oil shale and its semi-coke, Combustion and Flame, 159(10) (2012) 3224-3234.

M.A.B. Zanoni, J.L. Torero, J.I. Gerhard, Determination of the interfacial heat transfer coefficient between forced air and sand at Reynold's numbers relevant to smouldering combustion, International Journal of Heat and Mass Transfer, 114 (2017) 90-104.